THE UNIVERSITY of ADELAIDE

Radar Measurements of Gravity Wave Characteristics in the MLT

Andrew John Spargo

Thesis submitted for the degree of
Master of Philosophy
at
The University of Adelaide
Faculty of Sciences
School of Physical Sciences
Department of Physics

Supervisors:
Prof. Iain M. Reid and Dr. Andrew D. MacKinnon

February 2016

Originality declaration

I certify that this work contains no material which has been accepted for the award of any other degree or diploma in my name, in any university or other tertiary institution and, to the best of my knowledge and belief, contains no material previously published or written by another person, except where due reference has been made in the text. In addition, I certify that no part of this work will, in the future, be used in a submission in my name, for any other degree or diploma in any university or other tertiary institution without the prior approval of the University of Adelaide and where applicable, any partner institution responsible for the joint-award of this degree.

I give consent to this copy of my thesis, when deposited in the University Library, being available for loan and photocopying, subject to the provisions of the Copyright Act 1968.

I also give permission for the digital version of my thesis to be made available on the web, via the University's digital research repository, the Library Search and also through web search engines, unless permission has been granted by the University to restrict access for a period of time.

Signed: .....

Andrew John Spargo

February 2016

Abstract

This thesis examines medium frequency (MF) partial reflection and very high frequency (VHF) meteor radar estimates of wind variances and covariances in the altitude range 70-100 km. The quantities estimated form the components of the Reynolds Stress Tensor (RST) for an atmospheric flow; non-zero values of them are are considered to arise in the presence of propagating gravity waves and/or turbulence. Vertical fluxes of horizontal momentum, which correspond to the covariance of horizontal and vertical wind fluctuations, are of particular interest.

A 14-year data set of Full Correlation Analysis (FCA) velocities from the large-aperture Buckland Park MF radar was firstly probed for long-term trends in wind variance. A negative trend in the wind variance due to waves with periods in the range 20-480 minutes during summer was found to coincide with a weakening of the wind jet around 70 km altitude. This result adds to a very limited collection of studies of gravity wave activity trends in the middle-upper atmosphere.

Potential biases in a number of RST component measurement techniques were then investigated. A simple computer model was created, in which the spatio-temporal distributions of effective beam positions (EBPs) from multi-beam MF Doppler and meteor radar experiments were used to estimate the RST components of a gravity wave field with known input parameters. Systematic biases were found in both techniques if insufficient integration times were used. These biases could be removed entirely from the meteor technique by increasing the integration time, although the Doppler techniques slightly underestimated horizontal variances and horizontal-vertical covariances, and overestimated vertical variances, regardless. However, the Doppler estimates, especially vertical-horizontal covariances, were seen to be substantially less affected by random errors than the meteor estimates.

RST components from historical multi-beam MF Doppler campaigns were then estimated. Hybrid Doppler Interferometry (HDI) had been applied during these campaigns to estimate the EBP. The results were compared with those obtained from a simpler older technique (in which interferometric measurements of the beam position were not available), and were found to be in reasonable agreement. Noteably, the results also indicate that reasonable RST component estimates can be attained by simply applying interferometry to a vertically transmitted beam.

A setup of a similar multi-beam MF Doppler experiment using the Buckland Park radar is then described, along with the procedure used to correct for receiver gain differences. It is intended that this configuration will be used in future, in conjunction with the co-located meteor radar, for an intercomparison of MF and meteor radar estimates of RST terms.

Acknowledgements

I'd firstly like to thank my supervisors, Em. Prof. Iain Reid and Dr. Andrew MacKinnon. I'm grateful for the guidance Iain's given me over the last few years, the countless hours of inspiring discussions we've had, and the empathy he's shown when things weren't tracking well for me. I am also grateful for the travelling opportunities Iain's provided me; these include two trips to the AAD in Kingston, Tasmania (the second of which was supported by ATRAD) and a trip to Canberra, ACT for the AIP conference. I thank Andrew for going out of his way to teach me many handy computing/electronics tricks over the years, and for allowing me to get as much as possible out of the radar install at Kingston. I also collectively thank my supervisors for the feedback they provided on my thesis drafts.

I thank Chris Adami, for patiently helping me set up the MF radar on numerous occasions, and for putting in the effort to clearly explain much of what goes into running and configuring a radar system. As I understand, much of this assistance was given during his own time.

I thank Dr. Jonathan Woithe, for the years of tireless hardware and software help. At times I've bombarded him with questions I should've known the answers to, but he's nonetheless always taken the time to answer them comprehensively, and has often added in related snippets of advice along the way. I feel priveleged to have learned so much from him.

I thank Dr. John French, for all he's taught me on the Spex, and for all his efforts in getting the installation of the Spex underway in Adelaide.

I thank Dr. Damian Murphy, for all the support he gave Andrew MacKinnon and I during the meteor radar installation at Kingston, and for providing data from the Davis MF and meteor radars. I also thank Dr. Peter Love for his assistance during this installation.

I thank Dr. David Holdsworth, for fielding some questions on the 1997-98 HDI campaigns.

I thank Neville Wild, for the assistance in setting up the TDR experiment in August 2014.

I thank Ramona Adorjan for all the IT support.

I'd also like to thank other past and present members/visitors of the Space and Atmospheric Physics group, many of whom I've enjoyed some great discussions with. These include Dr. Stuart Anderson, Tom Chambers, Jake "Jaek" Clark, Simon Curtis, Dr. Alex Dinovitser, Dr. Bron Dolman, Assoc. Prof. Murray Hamilton, Dr. Mike Hatch, Andrew Heitmann, Dr. Andrew Klekociuk, Dr. Sujata Kovalam, Nicky Luo, Andrew Malouf, Li Na, Dr. Ray Oermann, Dr. David Ottaway, Dr. Som Kumar Sharma, Nadia Steyn, Liam Twigger, Em. Prof. Bob Vincent, and Dr. Joel Younger.

I thank Michelle, Michael, Luke, Nanna, Nonna and Dino for the great family times, and for putting

up with my absence from many of them during the last two years.

Finally, I thank my wonderful parents, John and Agnese, for their unwavering affability, and for their support and encouragement in everything I've ever taken on. I dedicate this thesis to them.

Contents

List of Figures

List of Tables

Chapter 1

Introduction

This thesis investigates radar measurements of the energy and momentum transport by gravity waves in the Mesosphere-Lower-Thermosphere (MLT). A strong focus is given to the limitations of radar measurements of the vertical flux of horizontal momentum associated with gravity waves. Accurate measurements of this parameter are currently of great importance to global climate models.

The effect gravity waves have on the temperature structure and wind field of the MLT is discussed in the first section of this chapter. This section goes on to briefly describe the nature of two sources of radio wave scatter in the MLT—partially reflecting irregularities and ablating meteor trails—which are exploited in this thesis to provide wind velocity estimates. In the second section, the derivation of gravity wave parameters from the radial component of those velocity estimates is described, along with a discussion of the difficulties encountered thus far in doing so.

1.1 The MLT

Earth's atmosphere is conventionally divided into layers with boundaries defined by the turning points in the vertical temperature profile. The different layers are suffixed with "sphere" and turning points with "pause". A representation of these layers is shown in Fig. 1.1; the MLT is defined as the region between about 60 and 110 km in altitude. It constitutes the upper and lower parts of what are usually referred to as the middle atmosphere and ionosphere, respectively.

1.1.1 Temperature/wind field structure and its production

The global-mean temperature in the MLT decreases with altitude up to the mesopause, and then increases into the thermosphere. On average, this part of the atmosphere is nearly in radiative equilibrium; the cooling with altitude above the stratopause and the warming above the mesopause can be explained in terms of the variable levels of absorption of solar radiation and infrared emission by the atmospheric constituents. However, as the model zonal-mean climatologies in Fig. 1.2 show [Richter et al., 2008], the temperature profile actually varies in a complicated manner with latitude and season. A significant departure from radiative equilibrium also occurs around the high-latitude mesopause, which, despite insolation levels, is cooler during summer than in winter.

The earliest observations of mesospheric temperatures at a polar latitude were made by Crary

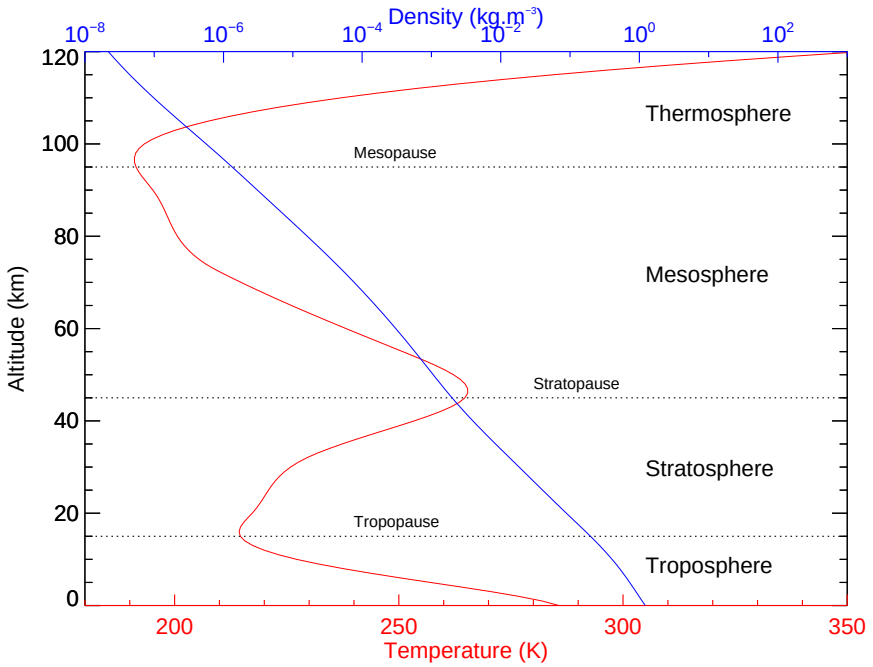

Fig. 1.1: Atmospheric temperature (red) and density (blue) profiles from the NRLMSISE-00 model, for 45°S around the time of the Southern Hemisphere autumnal equinox (late March).

[1950]. These showed clear evidence of a cold summer and warm winter mesopause. Taking into account these and existing observations of the stratosphere, Kellogg and Schilling [1951] devised a circulation model of the atmosphere up to 120 km in altitude, and attributed the radiative equilibrium departures in the high-latitude mesosphere to rising/sinking motions over the poles. This is in agreement with the present understanding. The caveat in the model was the existence of the strong meridional motions required to satisfy flow continuity; to conserve angular momentum, these would result in zonal motions much larger than those that had been observed at the time. In fact, the inferred zonal motions accelerated westward during summer and eastward during winter with altitude unabated. As recent model climatologies show in Fig. 1.3 [Richter et al., 2008], the winds actually decelerate and reverse between altitudes of 60 and 80 km, depending on the latitude and season.[1] Examples of wind climatologies at middle and high latitudes considered in this work can be found in Figs. 4.5 and 4.9 respectively.

To reconcile the unexpectedly small zonal motions, Haurwitz [1961] proposed that frictional forces on the zonal wind result in the necessary meridional motions. A similar process was later coined "Rayleigh drag" by Leovy [1964]. Although the drag mechanism explained the meridional flow, it was only sufficient to decelerate the zonal motions to zero, not reverse them. The source of the drag was also unknown at the time (e.g., Dunkerton [1982]).

Somewhat in parallel with these studies, the presence of irregularities in mesospheric wind fields and meteor trail observations became known. They were interpreted as internal atmospheric gravity waves in a landmark paper by Hines [1960]. In particular, Hines suggested that gravity waves:

1. have the ability to transport energy upwards from their source region in the lower atmosphere;

[1]This process is often referred to as the "closing" of the mesospheric wind jets.

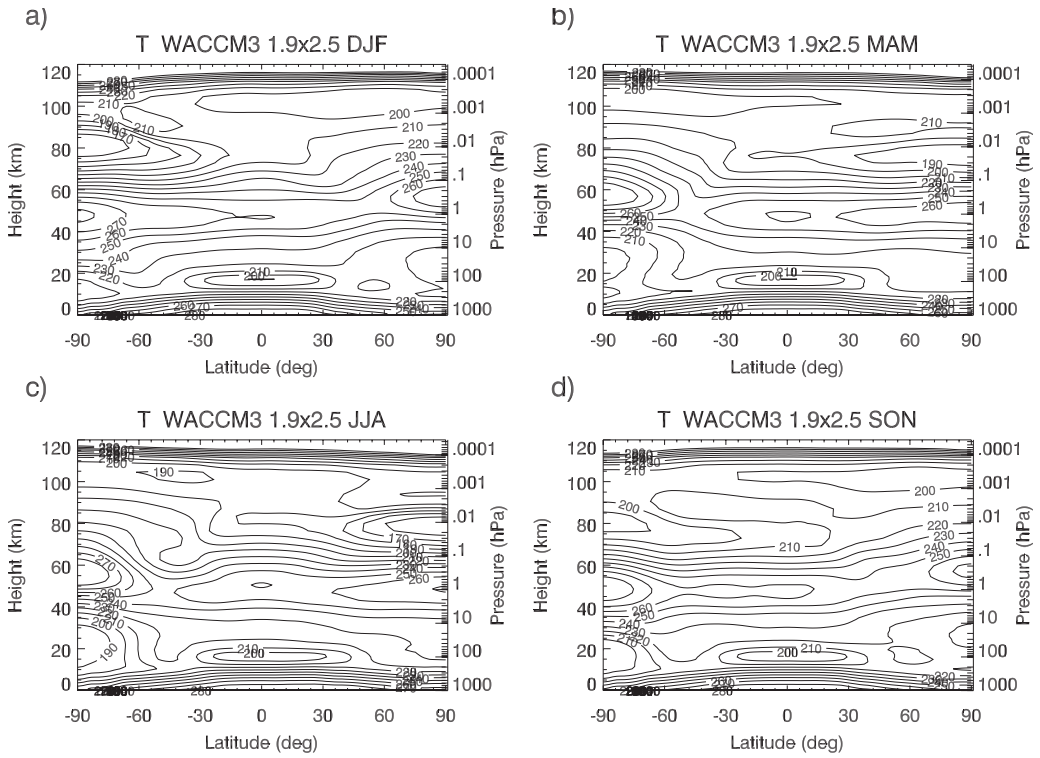

Fig. 1.2: 30-year climatology of WACCM3 temperatures with height and latitude (from Richter et al. [2008], Fig. 4). Each plot represents a different season (which are indicated in the plot titles).

2. will, through conservation of energy, increase in amplitude with height as a result of decreasing density;

3. will "saturate"[2] at some threshold altitude, and simultaneously deposit their energy through the production of turbulence.

Gravity wave theory developed rapidly following Hines' paper. As an example relevant to this thesis, Bretherton [1966] and Booker and Bretherton [1967] showed that a vertical flux of wave energy will be accompanied by a vertical flux of wave momentum, and that this momentum will be transferred to the wind in the presence of a shear flow. They also showed that gravity waves will interact with the wind in such a way as to be absorbed by the flow when the wave's phase velocity is equal to the wind's. This is a process often referred to as "critical level absorption".

The role played by gravity waves in controlling the circulation was largely clarified by Lindzen [1981]. He showed that the phase velocities of waves propagating to the mesosphere are sharply limited by critical level absorption in the troposphere and stratosphere. The waves that do reach the mesosphere consequently have a phase velocity spectrum that is "biased away" from the wind profile's. It was suggested that the momentum divergence associated with the waves' saturation results in a body force on the wind, tending to accelerate it towards the waves' phase velocity. This acceleration is synonymous with that earlier envisaged to be provided by Rayleigh drag, except that it also has the capability of reversing the flow. The body force is balanced by a Coriolis torque (an acceleration of

[2] A detailed review of gravity wave saturation theory can be found in Fritts [1984].

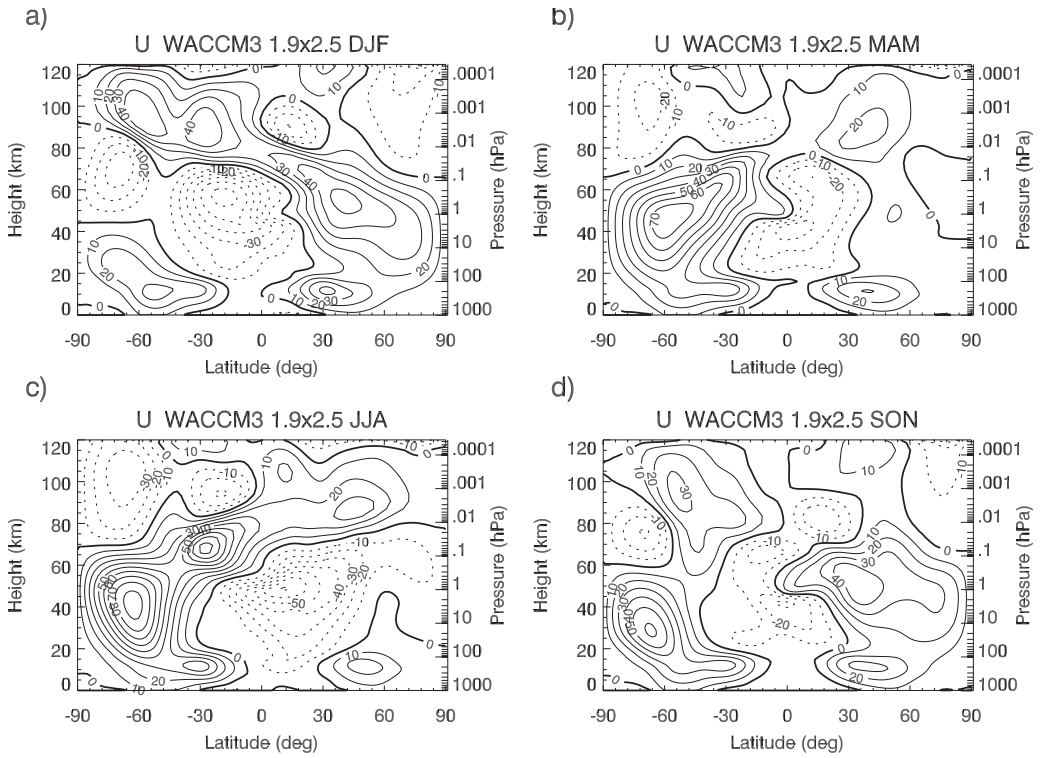

Fig. 1.3: As per Fig. 1.2, but for zonal winds (from Richter et al. [2008], Fig. 3)

the meridional wind[3], in this case) sufficient to satisfy the continuity requirements for vertical motions over the poles, and hence the observed temperature distribution.

There was considerable interest in measuring gravity wave momentum transport in the MLT once its importance in controlling the mean circulation was realized. The relevant measurable stresses can be conveniently parameterized as components of the Reynolds stress tensor (herein RST) per unit mass:

$$\frac{\tau_{ij}}{\rho} = \langle u_i' u_j' \rangle \tag{1.1}$$

which is a 3×3 matrix of the covariances of the fluctuating Cartesian components of the wind velocity. An individual entry of $\langle u_i' u_j' \rangle$ represents the net momentum flux per unit mass in direction $\hat{x}_i$ across a plane perpendicular to $\hat{x}_j$ [AMS Glossary, 2012]. The terms that are important in determining body forces in the atmosphere are the covariances between the horizontal and vertical velocities; these are usually referred to as "vertical fluxes of horizontal (zonal or meridional) momentum". Formally, the zonally-averaged body force required to produce a net meridional circulation is given by:

$$\langle F_x \rangle = -\frac{1}{\rho} \frac{\partial(\rho \langle u'w' \rangle)}{\partial z} = f \langle v \rangle \,, \tag{1.2}$$

where u, v and w represent wind velocities in the zonal, meridional and vertical directions respectively, and $f = 2\Omega \sin\phi$ is the Coriolis parameter, where Ω is the (Earth's) rotational angular frequency and ϕ is the latitude. The angled brackets in this equation denote a zonal average, and in eqn. 1.1, an

[3]The meridional wind is driven from the summer to the winter pole, in what is usually referred to as the "Brewer-Dobson" circulation in the stratosphere.

ensemble (e.g., temporal or spatial) average. A similar equation can be derived for $\langle F_y \rangle$.

The vertical flux of horizontal momentum terms were first measured directly in the MLT by Vincent and Reid [1983], using radar techniques. The same techniques (with some refinements) were applied extensively in the years that followed (see Sect. 1.2). The general motivation of the earlier studies was to quantitatively clarify the contribution gravity waves made to the momentum budget in the MLT, relative to other longer-period oscillations (such as tides and planetary waves). Later studies sought to determine the importance of different gravity wave scales (e.g., Reid and Vincent [1987]), and investigate the interaction between gravity wave momentum fluxes and tides (e.g., Fritts and Vincent [1987]), and the 2-day wave (e.g., Murphy and Vincent [1998]).

At present, there exists a need to improve the poorly-constrained parameterization of small-scale gravity waves in global climate models (GCMs). It is acknowledged in the modelling community that, while the gravity wave momentum fluxes in recent high-resolution GCMs show excellent agreement with those from radar and satellite, a large fraction of the small-scale momentum flux in the models remains unresolved [Alexander et al., 2010]. Observational efforts to improve this parameterization have still not yet been able to quantify all of the relevant scales globally. Moreover, the major sources of gravity waves in the atmosphere are only known qualitatively; secondary sources, which may well contribute substantially to the vertical transport of horizontal momentum, are poorly understood [Fritts et al., 2014]. These problems continue to motivate major observational campaigns to quantify gravity wave dynamics and effects, from their sources to regions of dissipation (e.g., the Deep Propagating Gravity Wave Experiment [Fritts et al., 2015; Bossert et al., 2015]).

As inferred above, ground-based radars have the ability to provide valuable information on the momentum fluxes due to gravity waves of scales smaller than those resolvable in GCMs. However, as will be discussed in Sect. 1.2, radar techniques which rely on line-of-sight Doppler velocities to estimate these quantities (which constitute all of those experiments mentioned above) suffer from some significant limitations. A focus of this thesis (Chapters 5 and 6) is to further understand the accuracy and precision of the RST components from these techniques—specifically, those that obtain their scatter from partial reflection and meteor ablation in the MLT. Recently, there has also been much interest in using these techniques (and many others) to quantify the effects of anthropogenic climate change in the MLT-region; a preliminary long-term analysis of such radar data sets is taken up in Chapter 4. Before delving into the measurement limitations, the mechanisms for partial reflection and meteor scatter in the MLT are briefly discussed.

1.1.2 Radio wave scattering mechanisms

In general, the scattering or reflection of a wave arises from inhomogeneities in the refractive index n of the propagation medium. For radio-frequency waves in the atmosphere, the refractive index is given approximately by [Gage and Balsley, 1980]

$$n - 1 = \frac{3.73 \times 10^{-1} e}{T^2} + \frac{77.6 \times 10^{-6} P}{T} - \frac{N_e}{2N_c}\,, \tag{1.3}$$

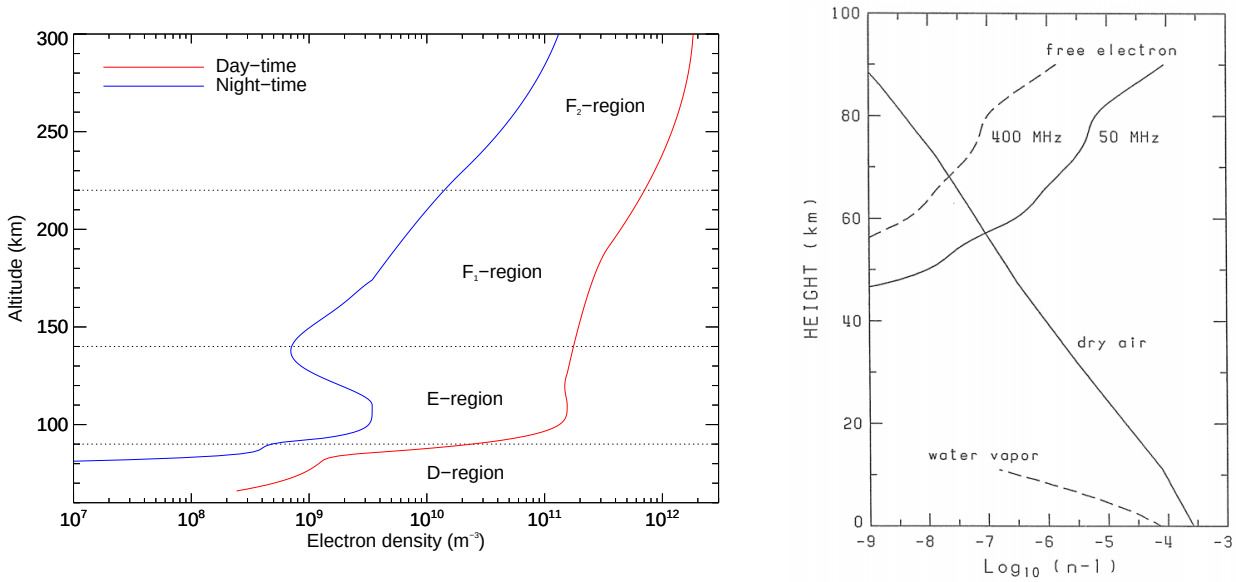

Fig. 1.4: Left: atmospheric electron density profiles from the International Reference Ionosphere (IRI-2012), for 45°S around the time of the Southern Hemisphere autumnal equinox (late March). Day-time and night-time profiles were evaluated at 12:00 and 00:00 LT, respectively. Right: Height profiles of water vapour, dry air, and free electron contributions to the refractive index (from Sato [1988]).

where e is the partial pressure of water vapour (mb), P the atmospheric pressure (mb), T the absolute temperature (K), N_e the number density of free electrons (m^{-3}), and N_c the critical plasma density (m^{-3}). The first and second terms describe the contribution from the density fluctuations of bound electrons in wet and dry air respectively; the former dominates the contribution in regions of high humidity (i.e. the lower troposphere), and the latter in drier regions (i.e. the mid-troposphere up to the stratosphere). The third term represents the contribution from free electrons, which dominates above about 50 km (see right panel in Fig. 1.4). Variability of the free electron density and hence refractive index on small spatial scales (in the range of tens to hundreds of metres) gives rise to essentially all radio wave scatter considered in this thesis.[4]

The free electrons (and positive ions) themselves predominantly arise from the ionisation of the atmospheric constituents by incoming short-wave solar radiation, electrons (> 30 keV), protons (> 1 MeV), and galactic cosmic rays. Ionisation levels are seen to vary substantially with altitude and time of day, as indicated in the left panel of Fig. 1.4, and with solar activity. The traditional nomenclature [Silberstein, 1959] for the different "regions" of the ionosphere, which has been widely adopted in the modern literature, is also shown in Fig. 1.4; attention here will be restricted to sources of radio wave scatter in the D-region and lower part of the E-region.

The ionisation levels in the D-region are determined by a balance of photoionisation/corpuscular ionisation and recombination processes (which are reviewed in e.g., Rishbeth and Garriott [1969]). D-region ionisation usually peaks with photoionisation around mid-day, and falls markedly overnight. For most practical purposes, the D-region is considered a day-time attenuator of radio waves; the

[4] As an aside, note that the refractive index *decreases* with increasing with electron density, and can be less than unity.

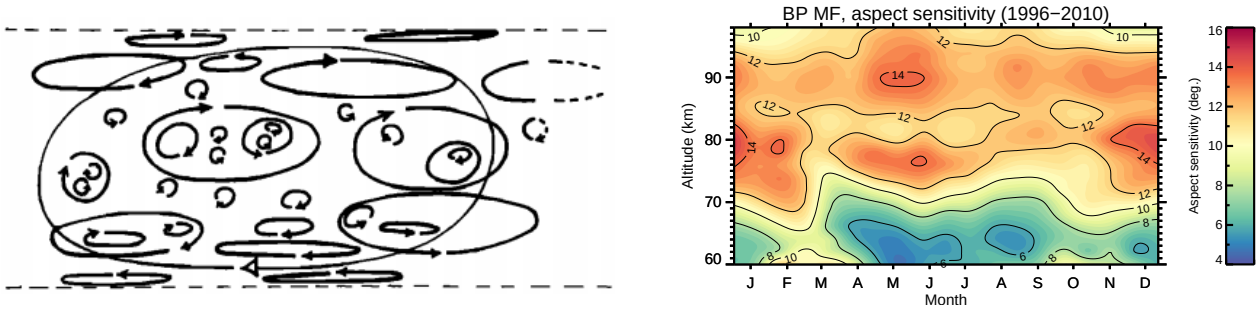

Fig. 1.5: Left: a schematic diagram of the scattering "layer" model proposed by both Woodman and Chu [1989] and Hocking [1989]. Right: 14-year climatology of FCA aspect sensitivities observed at Buckland Park (see Sect. 3.1). It should be noted that lower values actually correspond to higher degrees of aspect sensitivity.

neutral densities there are sufficient to dampen, through collisions, the oscillation of electrons set in motion by a passing radio wave. This level of attenuation decreases with frequency. Much like in the higher parts of the ionosphere, the D-region will also totally reflect radio waves whose frequency is equal to the plasma frequency $f_p = \sqrt{\frac{N_e e^2}{\epsilon_0 m_e}}$, where N_e is the electron number density, e is the charge of an electron, and m_e is the electron mass (e.g., Ratcliffe [1972]). A very weak coherent scattering of upward (not necessarily vertically) propagating radio waves, originally referred to as partial reflection, is seen to occur for waves below their height of total reflection.

Partial reflection

As both Reid [2015] and Hocking [2011] mention in recent reviews, the nature of the scatterers causing the partial reflection of radio waves from the D-region is not fully understood. The coherent scatter is thought to arise from some combination of three processes; namely, Bragg scatter, Fresnel scatter and Fresnel reflection. Bragg (or turbulent) scatter occurs when variations in electron density with scales of half the radar wavelength are projected onto the radio wave vector. Fresnel scatter results when many electron density irregularities are present within a radar range resolution cell [Röttger, 1989], which have a large correlation distance in the plane perpendicular to the wave vector and are random in the plane parallel. Fresnel reflection is a special case of Fresnel scatter, occuring when a single, thin (compared to the radar wavelength) electron density irregularity exists along the axis of the wave vector, with a large correlation length in the plane perpendicular.[5]

It is generally accepted that these irregularities form as a result of turbulence acting on gradients in the electron density (see, e.g., Lesicar et al. [1994] and references therein). It is also known that the scatter tends to be strongly anisotropic close to the zenith, and more isotropic at off-zenith angles greater than about 10° (e.g., Hocking [1987]). A variety of models have been proposed to explain the anisotropic-isotropic progression, although none have yet been widely accepted. As an example, Woodman and Chu [1989] and Hocking [1989] independently conceived the idea that scattering "layers"

[5]Note that, as it is defined, "partial reflection" strictly refers to Fresnel reflection. However, in the literature, "partial reflection" is almost always used in place of what may be some combination of these three processes.

are composed of thin "sheets" of anisotropic turbulence at their edges, with more isotropic turbulence within (see left panel of Fig. 1.5).

A related problem concerns whether or not the scatter is due to turbulence (i.e., "volume" scatter), or discrete scattering points. This hypothesis was relevant to Imaging Doppler Interferometry (IDI)[6] investigations of the MLT (e.g., Roper and Brosnahan [1997]). The reviews by both Reid [2015] and Hocking [2011] give little credence to this view.

The implications of the anisotropic-nature of the scatterers, and the notions that the scatter is caused by turbulence, are profound. Finite-width radar beams that are transmitted at small off-zenith angles often appear to be "shifted" towards the zenith on reception—an effect usually referred to as "aspect sensitivity" (an example of its height and seasonal variation is shown in the right panel of Fig. 1.5). Moreover, in the presence of horizontally inhomogeneous turbulence, the "magnitude" of the refractive index irregularities in the volume illuminated by the radar may not be fixed, and so the returns may be biased to one (or multiple) subset(s) of the beam volume. If these irregularities change with time or move with respect to the radar, the "effective position" of the beam will change with time. Such fluctuations in beam position are pertinent to the results presented in Chapters 5 and 6.

Meteoroid ablation

An independent source of ionisation in the MLT-region, which also has the ability to partially and totally reflect radio waves, arises from the ablation of meteoroids (which are referred to as "meteors"). The majority of meteor trails detectable by radar typically extend over a height range of 10-15 km, centred around 85-90 km, and are derived from meteoroids with masses less than 10^{-5} kg (radius $\sim$ 0.01 m) [Ceplecha et al., 1998]. The meteoroids are sourced from both a sporadic background and (to a lesser extent) the material associated with meteor shower events. No discussion of the radio wave scattering process from meteor trails is given here; Ceplecha et al. [1998] provide a detailed overview. As an aside, it should be noted that only underdense[7] meteor echoes are utilised in this work.

For reasons which will be discussed in the next section, of interest in this thesis are the temporal and spatial statistics of the detections that may be provided by a ground-based meteor radar—especially the symmetry of the spatial distribution with azimuth at any given time. These are largely controlled by variations in the flux of sporadic meteors into the atmosphere, which varies seasonally and diurnally (reasons for this are not considered here; see e.g., the modelling of the meteor radiant distribution in Janches et al. [2006]). An example of the net effect of these variations on the meteor detection rate at a fixed location are shown in Fig. 1.6; data in this case is from the 33 MHz meteor radar at Davis, Antarctica (68.6°S, 78.0°E). Meteor trails here are mainly detected between altitudes of

[6]IDI [Adams et al., 1985] is an analysis technique which measures the radial velocity and position of individual scatterers in a radar beam volume, assuming that each scatterer is at a discrete position and corresponds to a unique Doppler shift. It is not discussed any further in this thesis.

[7]In which case, the electron density of the ionisation trail is sufficiently low that the radio wave penetrates the trail entirely.

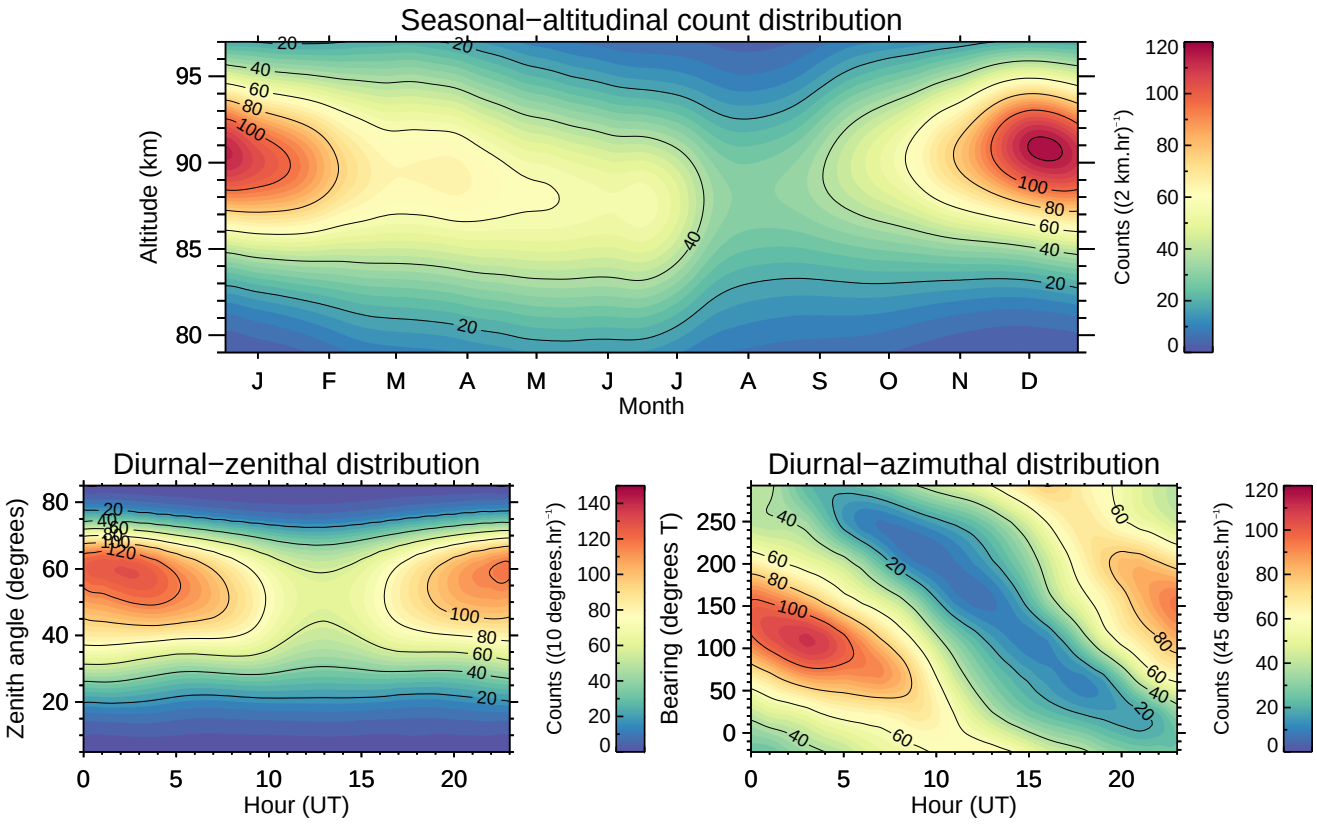

Fig. 1.6: 9-year climatology (26-Jan 2005 - 29-Oct 2014) of meteor detection rate distributions for the Davis 33 MHz meteor radar with time of year and altitude (top panel), time of day and zenith angle (lower left) and time of day and azimuth angle (lower right).

about 80 and 98 km, reaching a maximum in early summer and a minimum in early spring. There is a variation with zenith angle, peaking at about 60° (which is largely an artefact of the viewing geometry, and to a smaller extent, the intensity distribution of the transmitted radar beam), and a pronounced diurnal variation with azimuth. In particular, the azimuthal distribution is, most of the time, highly asymmetric.

The operation mechanism of a meteor radar, and some of the analyses pertinent to this thesis applied on the received signals, are summarized in Sect. 2.2.

1.2 The remote sensing of Reynolds stress

A summary of the problems encountered in using radar techniques to measure components of the Reynolds stress tensor in the atmospheric wind field will now be discussed.

Suppose that a radar has supplied a population of n radial velocity measurements of scatterers in the atmosphere at positions (θ, ϕ). Assuming that the neutral wind has advected the scatterers, the radial velocities can be represented as a system of linear equations:

$$\boldsymbol{V_{rad}} = \boldsymbol{A}\boldsymbol{v}\,, \tag{1.4}$$

where $\boldsymbol{V_{rad}} = [V_{rad_1}, ..., V_{rad_n}]^{\mathrm{T}}$, $\boldsymbol{A}_{i*} = [\sin\theta_i \sin\phi_i, \sin\theta_i \cos\phi_i, \cos\theta_i]$, and $\boldsymbol{v} = [u, v, w]^{\mathrm{T}}$, and

$i = 0, ..., n-1$ is an index. It is clear that at least three radial velocity measurements at different (but known) positions are required to invert this equation, and hence determine the three components of the wind velocity vector.

It is also possible to account for linear shears in the wind field. Following Browning and Wexler [1968] (their eqn. (2)), expanding the mean horizontal components of the wind field as a truncated Taylor series leads to the system of equations in eqn. (1.4), with the modifications:

$$\boldsymbol{v} = \left[u,\, v,\, w,\, \frac{\partial u}{\partial y} + \frac{\partial v}{\partial x},\, \frac{\partial v}{\partial y} - \frac{\partial u}{\partial x},\, \frac{\partial u}{\partial x} + \frac{\partial v}{\partial y}\right]^{\mathrm{T}} , \text{ and}$$

$$\boldsymbol{A}_{i*}^{T} = \begin{bmatrix} \sin\theta_i \sin\phi_i \\ \sin\theta_i \cos\phi_i \\ \cos\theta_i \\ \frac{r_i}{2} \sin 2\phi_i \sin^2\theta_i \\ \frac{r_i}{2} \cos 2\phi_i \sin^2\theta_i \\ \frac{r_i}{2} \sin^2\theta_i \end{bmatrix} ,$$

where r_i is the radial distance to the ith scatterer. Clearly, at least six independent measurements are required for a solution in this case.

In practice, eqn. (1.4) is often overdetermined, and is typically (e.g., Vandepeer and Reid [1995]) solved by least squares (e.g., Aster et al. [2005]),

$$\boldsymbol{v} = (\boldsymbol{A}^T \boldsymbol{W}^{-1} \boldsymbol{A})^{-1} \boldsymbol{A}^T \boldsymbol{W}^{-1} \boldsymbol{V_{rad}} , \tag{1.5}$$

where $\boldsymbol{W} = \mathrm{diag}\left(\sigma_1^2, ..., \sigma_n^2\right)$ is a diagonal matrix whose entries are weights for scaling the system of equations. These would typically be the variances in the entries of $\boldsymbol{V_{rad}}$.

If the wind field varies spatially or temporally, a non-zero perturbation term for the ith radial velocity can be represented as

$$V'_{rad_i} = V_{rad_i} - \langle V_{rad} \rangle , \tag{1.6}$$

which can be squared and written in terms of the Reynolds stress tensor components:

$$\boldsymbol{V'^2_{rad}} = \boldsymbol{A'} \boldsymbol{v'} , \tag{1.7}$$

where $\boldsymbol{V'^2_{rad}} = [V'^2_{rad_1}, ..., V'^2_{rad_n}]^{\mathrm{T}}$, $\boldsymbol{v'} = \left[\langle u'^2 \rangle, \langle v'^2 \rangle, \langle w'^2 \rangle, \langle u'v' \rangle, \langle u'w' \rangle, \langle v'w' \rangle\right]^{\mathrm{T}}$, and

$$\boldsymbol{A'^T_{i*}} = \begin{bmatrix} \sin^2\theta_i \sin^2\phi_i \\ \sin^2\theta_i \cos^2\phi_i \\ \cos^2\theta_i \\ \sin^2\theta_i \sin 2\phi_i \\ \sin 2\theta_i \sin\phi_i \\ \sin 2\theta_i \cos\phi_i \end{bmatrix} ,$$

where the angled brackets denote an average over the space and time spanned by the n samples. This of course may be weighted and solved as per eqn. (1.4) in eqn. (1.5); Thorsen et al. [1997] were the first to do so for radar beams with arbitrary "brightness" functions.[8] Vincent and Reid [1983] earlier introduced a momentum flux estimator exploiting a special case of eq. (1.7), in which look directions were chosen to cancel unwanted terms in $\boldsymbol{A'}$. For example, by steering two radar beams in the East and West directions at equal zenith angles (yielding a so-called "complementary coplanar beam arrangement"), one can derive the expression

$$\langle u'w' \rangle = \frac{\langle V'^2_{rad}(\theta) \rangle - \langle V'^2_{rad}(-\theta) \rangle}{2 \sin 2\theta}, \tag{1.8}$$

where $\langle V'^2_{rad}(\theta) \rangle$ and $\langle V'^2_{rad}(-\theta) \rangle$ are mean radial velocity perturbations in the East and West directions, respectively. A similar expression can be derived for $\langle v'w' \rangle$. Vincent and Reid applied the estimator to multi-beam data from the Buckland Park MF array; it has since been applied in several works using radars at a variety of sites (e.g., for mesospheric studies a VHF radar at Andøya (69.3°N, 16.0°E) [Reid et al., 1988], the Jicamarca MST radar (12.9°S, 76.9°W) [Fritts et al., 1992], the MU radar in Shigaraki (34.9°N, 136.1°E) [Nakamura et al., 1993], and more recently the Andenes MF radar (69.3°N, 16.0°E) [Placke et al., 2014]). An important digression to make here, which will be returned to in Chapters 5 and 6, is that fluctuations in the beam position (presumably due to turbulent irregularities moving through the volume illuminated by the radar) were not directly accounted for in any of these studies.

Hocking [2005] later demonstrated an apparently successful application of the Thorsen et al. [1997] technique to the radial velocity distributions from meteor radars. A key merit of this application is the much lower cost of the system components relative to those of the large phased array MF radars that had made the measurements in the years prior. If it could be shown that their estimates of the vertical fluxes of horizontal momentum were valid, it would make practical sense to widely distribute these radars for routine measurements. Following Hocking [2005]'s work, meteor radars have been used in several studies for RST component estimation (e.g., Antonita et al. [2008], Clemesha and Batista [2008], Clemesha et al. [2009], Beldon and Mitchell [2009, 2010], Liu et al. [2013], Andrioli et al. [2013b, 2015], and de Wit et al. [2014a, 2014b]).

There are legitimate reasons for concern (see below) over the RST component extraction capability of the method; to this end, a number of authors have also supplemented their observations with modelling studies to assess the method's accuracy and precision [Fritts et al., 2010a,b; Vincent et al., 2010; Placke et al., 2011a; Fritts et al., 2012a,b; Andrioli et al., 2013a], and some have gone on to suggest post-analysis empirical correction routines to reduce biases in the derived stresses (e.g., Placke et al. [2011b] for the removal of vertical shear-induced variance, and Andrioli et al. [2013a] for the removal of tide and planetary wave stress). In particular, Vincent et al. [2010]'s study suggests that it is impossible to even measure momentum fluxes of the correct sign using conventional meteor radar (regardless of the averaging time used), with predicted detection rate-dependent uncertainties of 250-

[8] The "brightness" function refers to a normalized angular and Doppler-frequency power spectral density (see Thorsen et al. [1997]'s eqn. (3)). Qualitatively, it describes the power received by a radar as a function of viewing angle, and is a weighting function for the measured Doppler velocity.

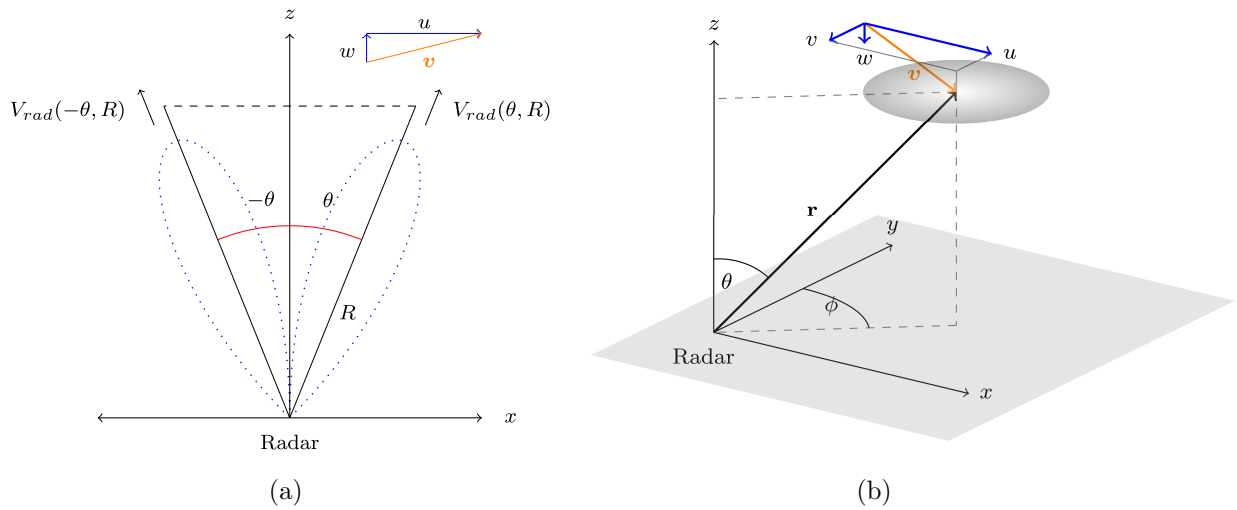

Fig. 1.7: Geometry of the (a) Vincent and Reid [1983] and (b) Thorsen et al. [1997] radar techniques used to determine momentum fluxes and (in the case of (b)) other RST components. Example polar diagrams for the receive beams are plotted in (a) and a "brightness" function for a scatterer is plotted in (b).

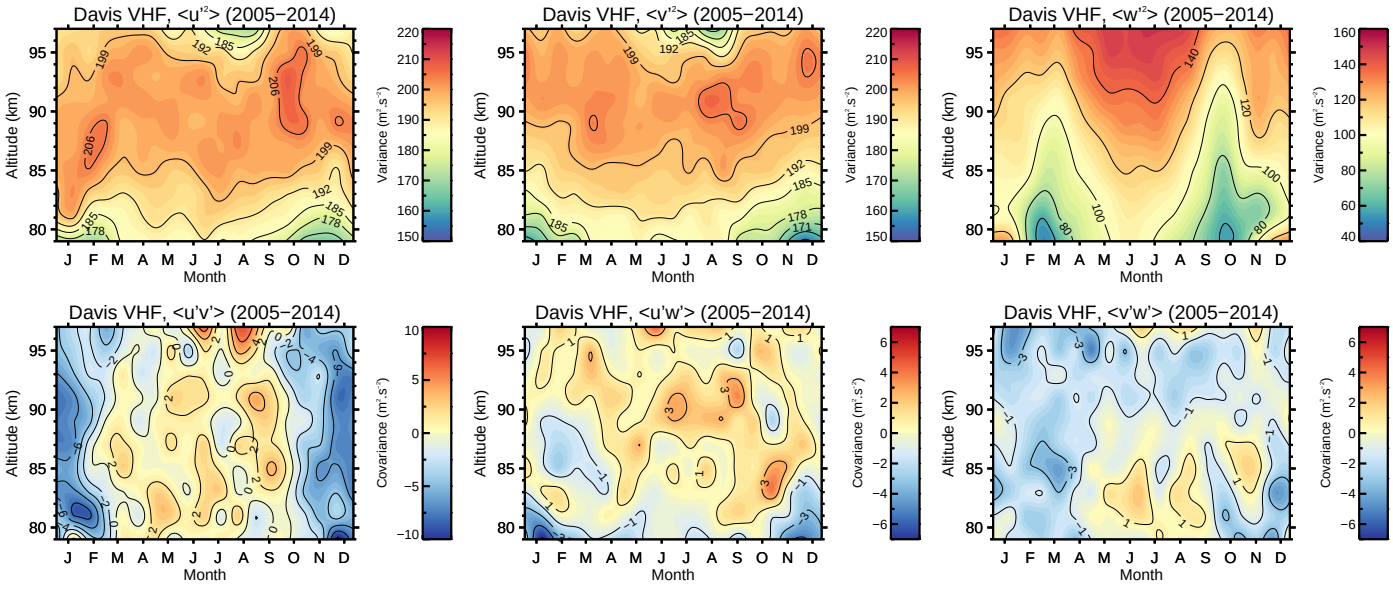

Fig. 1.8: A climatology of Reynolds stress tensor components from the 33 MHz meteor radar at Davis.

1250%. This study did not consider the effects of a vertical shear in the wind velocity nor tidal and/or planetary wave effects or their removal from the radial velocity distribution; doing so, presumably, would have further deteriorated the estimates.

Reid [1987] considers in detail the assumptions needed for an accurate estimate of momentum fluxes (and the other RST terms) using various "pencil-beam" configurations of an MF Doppler radar, which are in general also valid for radar systems with arbitrary "brightness" distribution functions, including meteor radars. Briefly, if a complementary coplanar beam arrangement is considered, like that used for the Vincent and Reid [1983] estimator, the wind field need only be statistically homogeneous in the volume spanned by the two beams (i.e., in such a way that perfect "anemometers" located anywhere in

the volume in the same range bin would measure the same RST terms, given the same time averaging).[9] For a non-complementary beam arrangement, such as that implied by the azimuthally asymmetric meteor distribution in the lower panels of Fig. 1.6, estimates of the flux terms will only converge to the true values for wave scales much larger than the probed volume.

An example climatology of RST terms derived from the 33 MHz meteor radar at Davis, evaluated using the Thorsen et al. [1997] technique (see Sect. 6.2 for a full description of the methodology), is shown in Fig. 1.8.[10] A sensible way to test the meteor-derived momentum fluxes is to compare the estimates to those of a co-located system which applies the well-established Vincent and Reid [1983] estimator, or alternatively the Thorsen et al. [1997] inversion on a system which obtains good radial velocity estimates at approximately opposite azimuths. Placke et al. [2014] does the former for the Andenes MF and meteor radars, and in summary, obtains satisfactory agreement for $\langle u'w' \rangle$ and poor agreement for $\langle v'w' \rangle$. However, this paper only compares broad climatological features in its assessment of the agreement between the techniques (over 20-day averages), does not remove tidal/planetary wave effects from the radial velocities prior to evaluating the stress terms, and (as mentioned earlier) does not account for fluctuations in the MF radar's beam position.

This thesis investigates the accuracy of multi-beam Doppler radar measurements of momentum fluxes, and other components of the RST. This is done as a precursor to using the Doppler radar measurements to assess the accuracy of the same estimates from a co-located meteor radar. In particular, substantial fluctuations in the beam positions measured by the Doppler radar are found and accounted for; these fluctuations have been neglected in previous studies.

1.3 Scope of thesis

This chapter has reviewed the momentum transport property of small-scale gravity waves, the role the transport plays in controlling the general circulation of the MLT, and the shortcomings of current parameterization of the waves in climate models. It pointed out that radar investigations of gravity waves have and will continue to provide measurements to improve these parameterizations. Two types of radio wave scattering mechanisms exploited in this thesis, those due to partial reflection and meteor ablation, were outlined. The present status of radar measurements of gravity wave momentum transport in the MLT was then briefly reviewed.

Chapter 2 gives a detailed overview of the radar systems used in this thesis: the Buckland Park MF array, and various meteor radars. In particular, some results of modelling the polar diagram of the BP MF array are shown, which may prove fruitful in the future if funds become available to refurbish the

[9] This statement has been recently recast for a meteor radar application in Fritts et al. [2012a]; quoting from their conclusion, "...momentum flux estimates are challenging for meteor radars because of the large number of meteors required to adequately resolve differences in radial velocity variances at opposite azimuths".

[10] It is beyond the scope of this thesis to explain these features in a geophysical context. However, it is noted that the variances show few qualitative similarities with the season-adjusted climatologies for a northern hemisphere polar location, Andenes, reported in Placke et al. [2011a]. The vertical fluxes of horizontal momentum also show limited agreement in terms of structure (although absolute values are similar).

array. The results of a procedure used to estimate the complex gain discrepancies between receivers on the array are then presented.

Chapter 3 describes the analysis techniques applied in the thesis to raw MF radar data, and includes a brief discussion on the known sources of error in the wind velocity estimates derived from the techniques.

Long term variations in the winds and gravity wave energies derived from two radar data sets (as have been previously mentioned, the BP MF array and the Davis meteor radar), are examined in Chapter 4.

In Chapter 5, the Reynolds stress extraction capabilities of MF Doppler and meteor radar techniques are assessed. This is done through the use of a computer model, which simulates a wind field with gravity wave-induced perturbations, and samples it with spatiotemporal distributions of samples of the techniques' recorded measurements.

In Chapter 6, Reynolds stress terms from campaigns conducted with the Buckland Park MF during 1997-1998 are evaluated and analysed. Attention is given to the agreement between Doppler techniques using off-vertical and solely vertical transmitted beams. An experiment configuration for the BP MF which will be used in future to assess the momentum flux estimations from the BP meteor radar is then presented. This chapter also raises some important questions about the accuracy of the wave energies estimated in Chapter 4.

Chapter 2

Instrumentation

2.1 The Buckland Park MF array

The Buckland Park medium frequency (BP MF) array, located on a nearly-flat coastal plain about 36 km NNW of the Adelaide CBD (34.6°S, 138.5°E), consists of 89 crossed-dipole antennas arranged on a rectangular grid with a circular outline. The antennas are used as the transmitting and receiving elements of a 1.98 MHz radar. The array was constructed in the late 1960s, principally to study the characteristics of the ground diffraction pattern produced by radio wave scatter from the ionosphere, and to be used as the receiver for a low frequency radio telescope. It is presently used to routinely measure wind velocity and electron density profiles over the altitude range $\sim$ 50-100 km.

In this section, a few aspects of the history of the system and an overview of the operation of its present implementation are provided. A survey of antenna impedances and cable quality profiles for each of the 178 elements of the array, which indicate a substantial limitation in the number of elements available for use, is then briefly presented. It should be noted that in the formative stages of this work, an effort was made to clarify which of the antennas and cable pairs should preferentially be refurbished to bring the radar into a state in which it could be used to steer narrow Doppler beams in hardware (see Sect. 3.2 and 3.3). The implementation of this work was put on hold in early 2015 because of limited funding, and the considerable merit inherent in simply using the array in its unrefurbished state for steering a Doppler beam in both hardware and software (see Sect. 6.4). The work involved modelling the polar diagram of the array and its beamsteering capabilities for different scenarios of antenna refurbishment, and a summary of it is shown in Sect. 2.1.4. Finally, the results of a procedure used to calibrate the gains of each receiver to a common value are described (which are pertinent to the results presented in Sect. 6.4).

2.1.1 Brief historical overview

Construction of the array commenced in 1965, and first results were obtained in 1968. Initially, the 178 elements of the array were configured for reception on 1.98 MHz or 5.94 MHz, and transmission was performed using separate four-element arrays (one for each of the reception frequencies). The reduction in SNR and angular sensitivity on reception as a result of the broad transmit beam was not ideal, but implementing a transmit capability on all receivers was not financially feasible early on

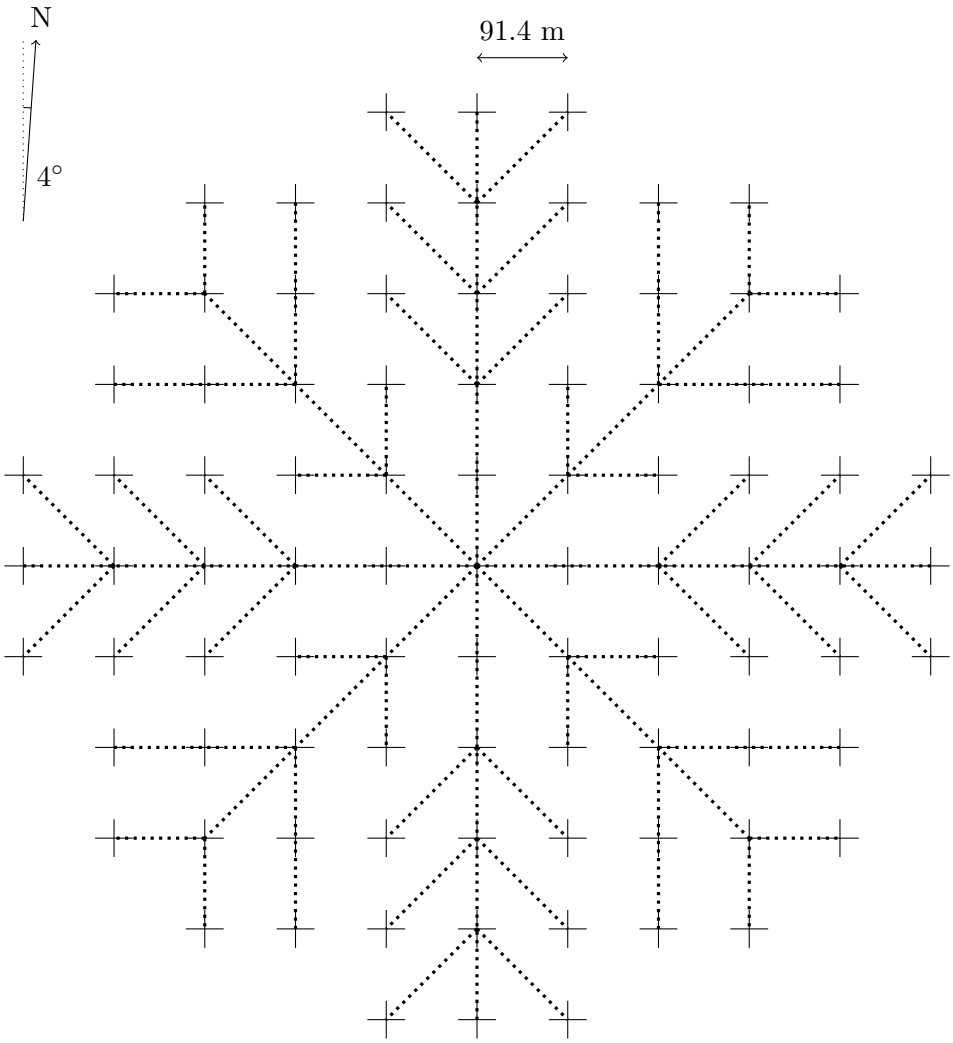

Fig. 2.1: A diagram indicating the layout of the Buckland Park MF array antennas. The underground cables to each antenna are shown as grey dotted lines. For ease of viewing the antennas are not drawn to scale; each antenna element is actually twice as long as shown.

[Briggs, 1993].

The first results presented by Briggs et al. [1969] and Golley and Rossiter [1970] using the FCA (Sect. 3.1) provided an early indication of the so-called "triangle-size effect" (TSE). This refers to the underestimation of the wind velocity inferred from the velocity of the ground diffraction pattern; the velocity underestimation decreases when the spacing between the receiving antennas is increased. In these early studies, emphasis was placed on interpretation of returns from the E- and F-regions, although some consideration was given to the much weaker partial reflections from the D-region. The D-region returns lacked the fringes associated with the more specular returns from the E- and F-regions, being random and more variable with time [Felgate and Golley, 1971].

Interest in using the FCA to determine wind velocities grew during the 1970s. A number of studies comparing the velocity estimates with the co-located Adelaide Meteor System [Weiss and Elford, 1963] and inferring the tidal and planetary wave influences on the mean winds were published during this time (e.g., Stubbs [1973], Stubbs and Vincent [1973], Stubbs [1976], and Vincent and Stubbs [1977]). These records mark the beginning of a long-term data set of D-region winds that extends to the

present. The early wind studies typically utilised three antenna groups for reception, arranged in a near-equilateral triangle, with each group consisting of four adjacent antennas connected in parallel. Pulse repetition frequencies in the range of 50 Hz were used, and coherent integration of consecutively received signals from a given range was applied on reception to increase the SNR. The radar was also used for MF studies of meteors [Brown, 1976] and imaging of ionospheric irregularities [Briggs and Holmes, 1973] during this period.

Beamsteering in reception (achieved by insertion of phase-delay cables of appropriate length between the antennas and receiving system) was first applied from the late 1970s. In such experiments, the receive beam was typically steered to a zenith angle of 11.6° (the first null in the polar diagram of the array). This found application in the study of the scattering characteristics of irregularities in the D-region (e.g., Hocking [1979], Hocking and Vincent [1982], and Lesicar and Hocking [1992]), studies of turbulence energy dissipation rates (e.g., Vincent and Ball [1981] and Hocking [1983]) and momentum fluxes (e.g, Vincent and Reid [1983], Reid and Vincent [1987], Fritts and Vincent [1987], and Murphy and Vincent [1993, 1998]).

From 1989-1995, an extensive upgrade and refurbishment of the array took place, with a principal aim of enabling transmission on all 178 elements, as well as reception (thus converting the array into a "true" Doppler radar). This involved replacing the original receive-only baluns with baluns capable of handling peak transmitter powers of $\sim$ 5 kW, replacing sections of damaged air-cored transmission lines with solid-cored cable, and replacing most of the dipoles' copper wire with new hard-drawn copper wire [Reid et al., 1995].

Providing power amplifiers (PAs) for each of the 178 elements was not economically feasible. Fortunately, design studies [Vandepeer, 1993] showed that satisfactory beam patterns to zenith angles of at least 30° could be obtained if all 89 dipoles on one orientation were phased in adjacent groups of three. To this end, three 10-channel solid-state transmitter subsystems were constructed. Each of the 30 power amplification (PA) modules on these could be electronically phased in increments of 8.5° (which enabled beamsteering resolution of $\sim$ one-half beamwidth of the full array), which enabled easy implementation of rapid beamsteering on transmission. For reception, a modular 10-channel system was constructed, which was later expanded to a 16-channel system [Holdsworth and Reid, 2004b].

Vandepeer and Reid [1995] used the new programmable hardware and software beam steering capabilities to implement Time Domain Interferometry (TDI) experiments, as did Holdsworth for Hybrid Doppler Interferometry (HDI) analysis between 1997 and 1999. Fig. 6.1 shows an example of how PA modules may be allocated to groups of antennas for a beamsteering experiment. The routine FCA analysis was configured to run on two sets of receiving triangles of differing size ("small" and "large"; see Sect. 4.2) from March 1997 [Holdsworth and Reid, 2004b]. The array was also used for Differential Absorption Experiments (DAE) [Holdsworth et al., 2002], and parts of the array were extensively refurbished between 1999 and 2003 for meteor work [Grant, 2003].

The array has predominantly been run in a vertical-beam spaced antenna configuration for D-region wind and electron density studies since the meteor work in 2003. The transmitting system installed during the 1995 upgrade was replaced in June 2009, and the receiving system was upgraded during

March 2011. Unfortunately, maintenance of the array to the required standard (e.g., Grant [2003]) has proven difficult, especially in recent years. Despite a considerable amount of maintenance work performed on the array in late 2005, the ongoing deterioration of the array's antennas and transmission lines has progressed to the point where, today, $\sim 2/3$ of the antenna/cable pairs require refurbishment to be brought back into use (see Figs. 2.3 and 2.4). Fortunately, the remaining useable antennas still allow for a variety of useful experiment configurations, such as that considered in Chapter 6.

2.1.2 Present system overview

The 89 crossed half-wave (at 1.98 MHz) dipole antennas are separated by ~ 91.4 m (0.6λ at 1.98 MHz) (shown in Fig. 2.1). The "North-South"-oriented rows of antennas are parallel to a line with bearing of about 356°T (the magnetic North in 1967), and the "East-West" perpendicular to these. The land the array is situated on is almost flat (the maximum gradient averaged over the array is $\sim$ 0.2% toward the North-East).

Each of the dipoles are centre-fed, suspended atop ~ 10 m high wooden poles. The antenna elements are 2 mm-thick hard-drawn copper wires, cut to physical lengths of 71.6 m. Adjacent antenna arms are connected to each other by 19.8 m sections of insulating glass fibre rope (which serve the purpose of keeping the antenna elements parallel to the ground).

The antennas are connected to the central laboratory by coaxial cable, most of which is buried. The buried component is comprised of 70/75 Ω air-cored Aeraxial coaxial cable, and the above-ground 75 Ω Belden 8213 RG-11/U coaxial cable. The above-ground section is routed in plastic conduit (to reduce UV-induced deterioration), while the buried section is not. Each cable has an electrical length corresponding to a half integer multiple of the array wavelength, ranging from $\frac{1}{2}\lambda$ for the centre element, to $\frac{9}{2}\lambda$ for the most distant elements. The excess cable is reeled in a hut adjacent to the central laboratory. Each cable is terminated by a connection to an antenna patchboard in the central laboratory. There is a separate patchboard for the two antenna orientations; each has a BNC coaxial connector to each of the corresponding 89 antennas.

At 1.98 MHz, individual antennas exhibit an impedance of 28 Ω. They are impedance-matched to their 70/75 Ω transmission line by means of a balun [Lewallen, 1985], which contains circuitry to serve both antenna orientations. The balun for each crossed-dipole is mounted at the top of the corresponding wooden antenna pole. The balun connection feeds on those elements with non-integer cable lengths are also reversed, so as to remove their antenna's 180° phase offset relative to those with integer cable lengths.

The current radar's transmitting and receiving system consists of the following components (all of which are located in a laboratory adjacent to the centre element of the array):

- A digital transceiver, comprising a 6-channel complex digital receiver and an exciter;
- A 48 kW transmitter, comprising three 8-channel solid state modules;
- a PC running Linux for controlling the radar, configuration of the radar's transmit and receive parameters, and analysis of the acquired raw data;

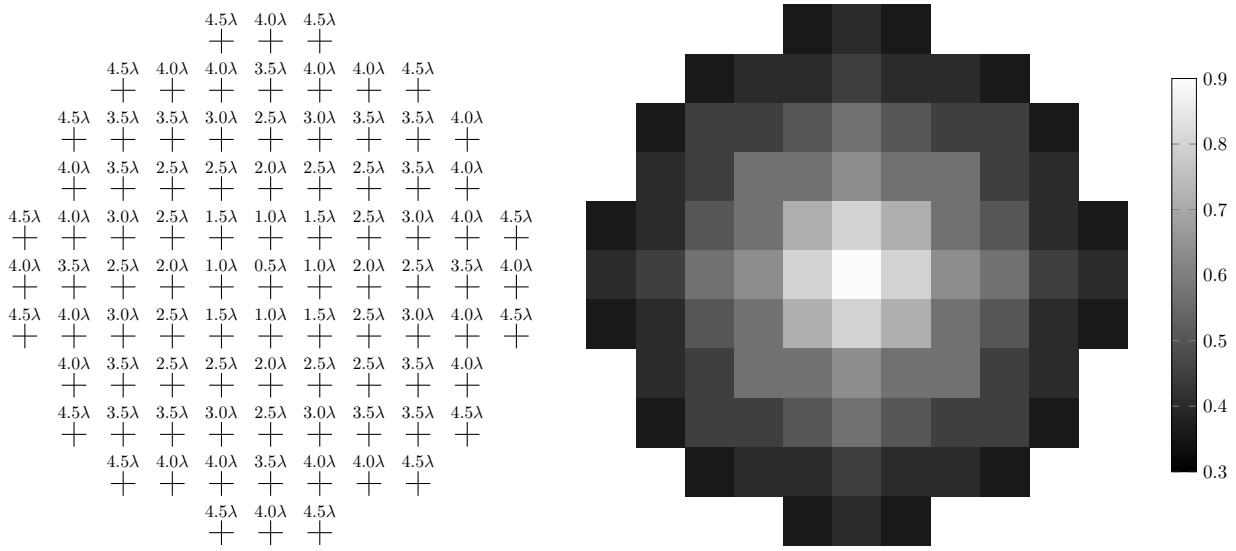

Fig. 2.2: A diagram indicating the electrical length in wavelengths of the transmission line to each antenna (left), and the associated apodization function (right). A value of "1" on the apodization plot corresponds to zero attenuation. NB: the array elements here are not drawn to scale.

The system, as operated between 1995 and 2011 (and the system which the results presented in Chapters 4 and 6 used), is described by Reid et al. [1995]. Briefly, the radio frequency (RF) exciter in the transceiver generated an RF signal (1.98 MHz) modulated by a Gaussian envelope with the desired pulse width. This was sent to a specifiable group of channels in the transmitter (each of which has a power amplification (PA) module, a phase control module (PCM) and a transmit/receive (T/R) switch), where it was amplified and its phase appropriately adjusted as required, before being transferred to a transmission line and radiated via an antenna. The radar was modified in 2011 to a 4-channel APAC system [ATRAD Pty. Ltd., 2006], and the transceiver was upgraded to a 6-channel digital transceiver in June 2015 by C. Adami and the author.

Each of the PAs are designed to operate with a load of three 75 Ω transmission line/antenna pairs in parallel. The T/R switch on each channel allows any antenna groups used for transmission to also be used for reception, though receive-only groups may be designated. For reception on a given channel, the analogue signal of a particular range gate from an antenna group is firstly passed through a RF bandpass filter, and converted to an intermediate frequency (5.3 MHz) via a second bandpass filter. It is then digitized for subsequent processing. Only Doppler shifted signals will give rise to a time-varying signal.

Cable length (λ at 1.98 MHz)	0.5	1.0	1.5	2.0	2.5	3.0	3.5	4.0	4.5
Attenuation (dB at 1.98 MHz)	0.49	0.99	1.48	1.99	2.48	2.99	3.48	3.97	4.45

Table 2.1: Transmission line attenuation parameters for the Buckland Park MF array [Vandepeer, 1993].

2.1.3 Antenna/transmission line surveys

As mentioned in Sect. 2.1.1, the antennas and transmission lines are subject to deterioration over time. To aid in the selection of working antennas appropriate for particular analyses and to assist in the direction of future array maintenance work (see next section), three surveys of each element of the array were performed:

1. Measurement of the Voltage Standing Wave Ratio (VSWR) across a sweep of frequencies adjacent to the radar's operating frequency;
2. Acquisition of a transmission line Time Domain Reflectometry (TDR) (see below) trace;
3. Visual inspection of an antenna's components from the ground (not discussed here).

Comments on measurement procedures and interpretation of results

The VSWR measurements were obtained by connecting a VIA (Vector Impedance Analyser) Bravo! unit to the patchboard BNC connector of each antenna element, and programming the unit to scan the VSWR of a 75 Ω transmission line across the frequency range [1.78, 2.18] MHz at uniform increments of 4 kHz. Assuming a lossless transmission line, the resultant signal propagating down it is given by a solution to the Telegrapher's equations:

$$V(z) = V^+ \left(e^{-i\beta z} + \Gamma e^{i\beta z} \right)$$
$$I(z) = \frac{V^+}{Z_0} \left(e^{-i\beta z} - \Gamma e^{i\beta z} \right) ,$$

where $V(z)$ and $I(z)$ are, respectively, the voltage and current distributions along the line, z is the the distance along the line, β is the complex propagation constant of the line, V^+ is the amplitude of the "forward-going" wave, Z_0 is the line's characteristic impedance, and Γ is the line's reflection coefficient. The VSWR is defined as the ratio of the maximum and minimum voltages attained along the line,

$$\mathrm{VSWR} = \frac{V_{\max}}{V_{\min}} = \frac{1 + |\Gamma|}{1 - |\Gamma|} ,$$

and so values of 1 indicate zero reflection of the "forward-going" wave and hence delivery to the load impedance ("impedance-matched"), and values > 1 indicate increasing amounts of wave reflection.

Ideally, the VSWR of a radar transmission line should be close to 1 at its operating frequency, and large elsewhere. In this work, antennas with VSWR $\lesssim 1.5$ at 1.98 MHz (which is a threshold largely derived from experience) are taken to be in "good-condition". Large values of VSWR can generally be taken to indicate variations in cable characteristic impedance, a damaged/faulty balun, a damaged/fallen antenna element, or some combination thereof.

TDR traces were taken principally to obtain spatial information on the likely contributors to poor VSWR profiles, in order to distinguish transmission line and antenna element faults. To facilitate the measurements, an HP 8112A pulse generator was arranged to transmit square pulses of temporal

width 100 ns and a repetition rate of 2 kHz into the patchboard BNC connector of the antenna element in question. A Tektronix TDS 1002 oscilloscope was placed in series with the circuit to sample the signal. The expectation was that any discontinuity in characteristic impedance along the length of a transmission line would cause the partial reflection of a transmitted pulse. Its location could be discerned by assuming that its distance d could be given to first approximation by $d = \frac{1}{2}vt$, where t is the time of an increase in voltage, and v is the speed of the signal in the cable.

In a given TDR trace, rises in voltage could be expected at a time of ~ 0 (the transmitted pulse) and at the time corresponding to the distance of the balun. Any major peaks closer than the expected distance of the balun could probably be attributed to a fault of some kind. Grant [2003] takes a decidedly more thorough approach than this, considering the effect of each component in the circuit on signal risetime, accurately determining the range of impedance discontinuities, distinguishing the types of discontinuities, and estimating the level of water ingress into the cables. Nonetheless, the simpler approach outlined here was sufficient to qualitatively identify cable faults.

Results

The VSWR profiles and TDR traces for each element are shown in Figs. 2.3 and 2.4 respectively. As a broad overview, the VSWR plots indicate that the array has deteriorated the most in the Eastern half, with essentially no reliable dipoles in columns 10 and 11. The far Northern and North-West sections of the array also contain few useable dipoles. Overall, the West and South-West sections contain the highest consistency of reliable dipoles. It also generally appears that there are more North-South oriented dipoles available (coloured blue) than there are East-West (red).

The TDR traces attribute the failure of many of the dipoles in columns 10 and 11 to cable faults (as many of them do not appear to show a substantial reflection at the expected balun location). A noteworthy train of cable failures quite close to the centre of the array (dipoles 4-5–6-5), and some elements nearby) is also evident. Without doing a systematic analysis, the cluster of what appeared to be mostly reliable North-South oriented dipoles around this section was anticipated to be the best part of the array to use for forming a narrow transmit beam with minimal grating lobe influence (as discussed in the next section, this would require a large array with as few as possible antenna separations greater than a radar wavelength). To estimate which cable(s) would be the most economical to replace, the array's polar diagram was modelled for each plausible replacement scenario.

2.1.4 Modelling of the array's transmit polar diagram

The polar diagram of the array was modelled using `EZNEC+ v5.0.63` (`www.eznec.com`). Briefly, each antenna dipole was represented as a 2 mm diameter copper wire of length 71.6 m, positioned 10 m above a flat `Real/MININEC` ground (the East-West oriented dipoles were arbitrarily positioned at heights of 10.01 m, so as to not intersect with the North-South dipoles situated at a height of exactly 10 m). Each dipole was divided into 8 finite elements, and the "source" for each antenna was specified as a "split-source" over the 4th and 5th elements.

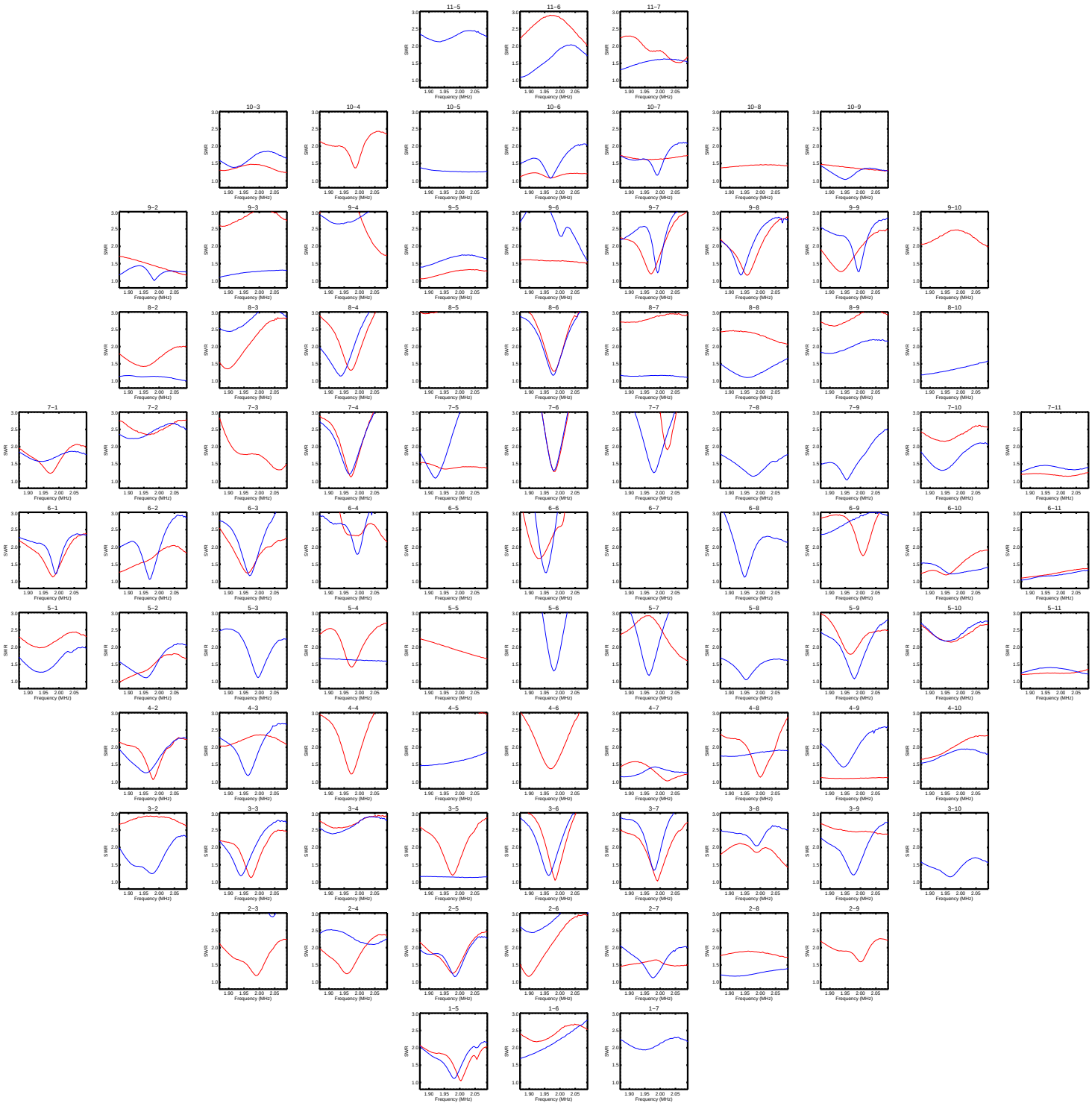

Fig. 2.3: A profile (1.78-2.18 MHz) of the SWR of each antenna-transmission line pair for the BP MF array. The measurements were performed using a VIA Bravo! Vector Impedance Analyser most recently by the author on 30-Jul 2015. The plots have been positioned to represent the locations of the corresponding crossed-dipole pairs. Results for the North-South oriented antennas are shown in blue, and red for the East-West oriented. "Good" antennas here (e.g., 7-6) are deemed to be the ones that show a minimum SWR of less than about 1.5 at the operating frequency of the radar (1.98 MHz). This would imply a well-matched transmission line and antenna element.

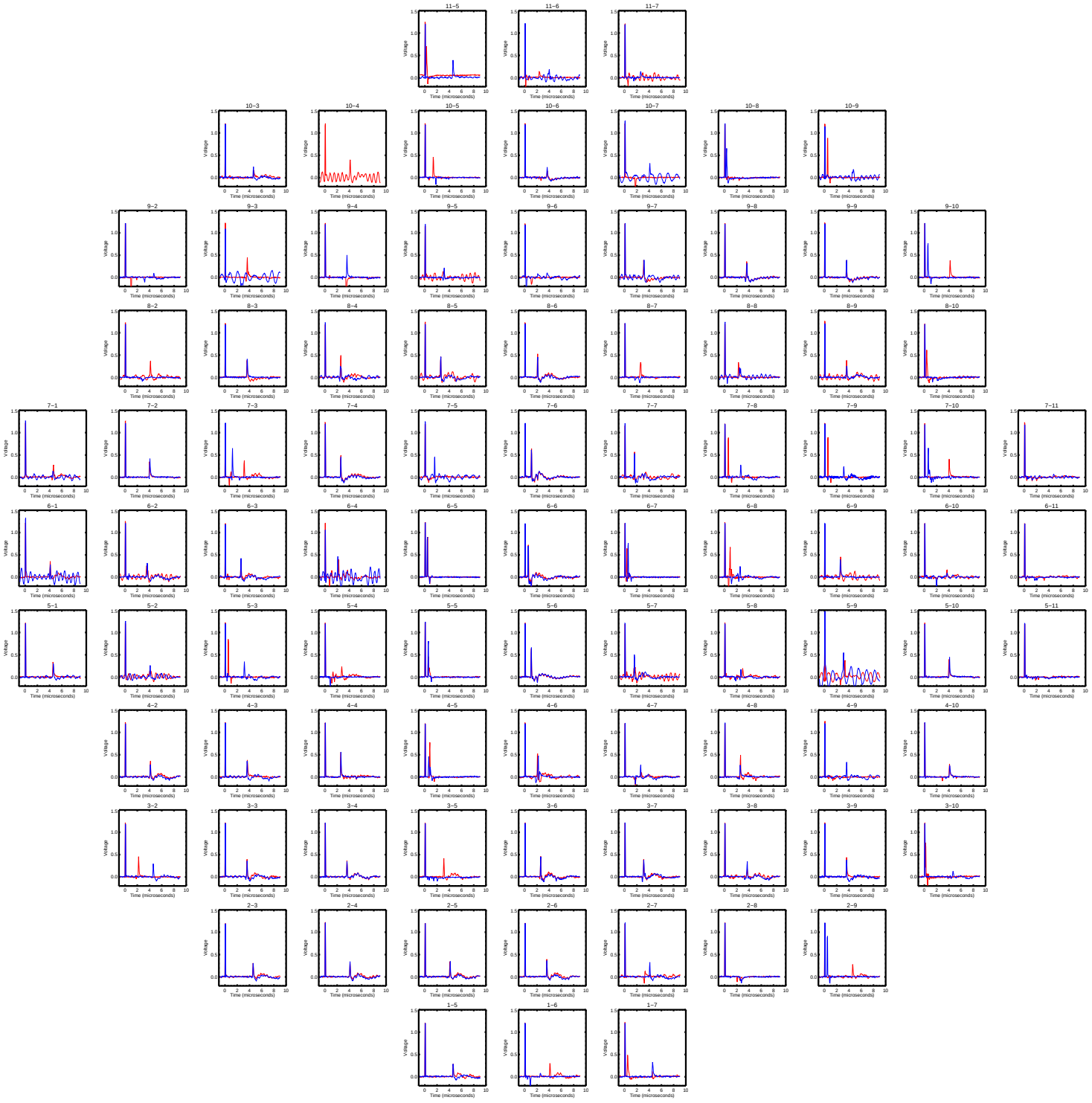

Fig. 2.4: TDR traces for each transmission line of the BP MF array, again with the plots positioned to represent the crossed-dipole pair locations, and with North-South oriented antennas shown in blue and East-West in red. The measurements were performed by the author on 27-Aug 2014 and 4-Sep 2014. The "good" transmission lines here (e.g., 7-6) should show a peak at the expected distance (i.e. time) of the balun, and no peaks between the zero-time and balun peaks.

The chosen ground was given a conductivity of 0.0303 S.m^{-1} and a dielectric constant of 20 (which is regarded as a "Very Good" quality by e.g., Cebik [date unknown]). As Hocking [1981] discusses, the ground at Buckland Park consists of a layer of sand (3-5 m thick) above a salty water table. These materials will have differing dielectric constants, and so multiple reflections of down-propagating waves will occur. The conductivities and dielectric constants of these ground materials have never been measured; it is suspected (somewhat naïvely) that their combined effect is to produce a ground with similar characteristics to that used here.

The "sources" were specified to provide a voltage of arbitrary absolute amplitude, oscillating at a frequency of 1.98 MHz. The relative amplitude of each source was adjusted based on the known signal attenuation level for each transmission line length (Table 2.1, and shown graphically in Fig. 2.2). To steer the beam and hence verify the radar's beamsteering capability, the phase of the signal at each dipole was varied linearly along the columns or rows of the array as necessary (for "North-South" or "East-West" steering respectively); the required phase difference φ between any two elements was evaluated as $kd\sin\psi$, with $k = \frac{2\pi}{\lambda}$ as the radar wavenumber, d as the antenna separation, and ψ as the zenith angle at which to form the centre lobe of the beam (see Sect. 3.3 for a brief introduction to radar interferometry).

Models of the one-way transmit polar diagram were produced for different realizations of the availability of North-South oriented antennas in the South/South-West section discussed previously. The polar diagram qualities were deduced subjectively only; the rough requirements on them were:

1. To have an approximately circular main lobe;
2. To have a Full-Width at Half Maximum (FWHM) of less than about 20°;
3. To have as few possible grating lobes above -15 dB within 20° of the centre of the main lobe;
4. To not have any grating lobes above -20 dB within a few degrees of the zenith when steering the beam "North-South" or "East-West".

None of the plausible configurations fully satisfied these requirements. The most satisfactory polar diagram produced is shown in Fig. 2.6, and the associated antenna configuration in Fig. 2.5. The proposed configuration consists of 39 "North-South" oriented antennas. The modelled beam is reasonably circular, narrow (FWHM of $\sim 20°$), and contains grating lobes at levels that may be acceptable for steering the beam in the "East-West" plane. The configuration is also reasonably satisfactory from an economic point of view, as at the time of writing it only requires the replacement of three transmission lines. However, a number of the antennas allocated for use here clearly have unsatisfactory VSWR profiles (e.g., 2-3, 8-5). These would need to be refurbished before the outlined experiment could proceed.

As mentioned in Sect. 2.1.2, the power amplifiers (PAs) presently installed are designed to operate with three antennas connected in parallel. Bearing this in mind, a proposal of antenna groupings for PAs 1-14 is shown. This could be made slightly more efficient if the designated beam steering angle was such that the phase difference along subsequent columns was 90°; this way, the single antenna in

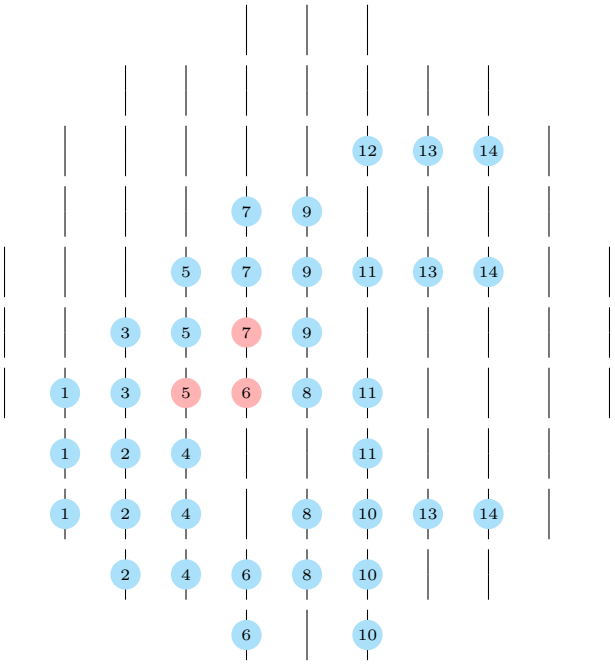

Fig. 2.5: Proposed antenna configuration for the formation of a narrow Doppler beam in hardware, with a polar diagram that should at least be adequate for steering in the "East-West" plane. Elements coloured red are those for which a cable replacement is assumed. An example of how the available PAs might be assigned to particular groups of antennas is also indicated by the number on each unit.

"group 12" could be contracted to the third element of "group 3", since these group's phases would be aliased. However, this phasing would place the centre lobe of the beam at a zenith angle of nearly 25°, which, due to aspect sensitivity, is probably too large to be useful.

It was intended that this entire configuration would be used to form a Doppler beam on transmission, and that all groups would be combined into a single receive channel with the same phasing applied in hardware to form an identical receive beam. DBS analysis (Sect. 3.2) would then be performed on the raw data from that single receive channel. Another approach would be to set aside some of the transmit groups for reception on independent channels, with a spatial distribution appropriate for performing HDI (Sect. 3.3). An optimal configuration for this, taking into account different scenarios of transmission line replacement, is beyond the scope of this thesis.

This concludes the work done on prescribing an antenna configuration for a narrow-beam DBS experiment. Due to financial constraints, no refurbishment work was deemed feasible, and attention was to be re-directed into investigating the capability of the unrefurbished array to produce reasonable momentum flux estimates. HDI analysis on a vertically transmitted beam was deemed feasible; as discussed in Sect. 3.3, this required the gains on each receiver channel to be calibrated to the same value. The procedure used to do this is described in the following section.

2.1.5 Receiver channel calibration

The interferometric radar technique (HDI) described in Sect. 3.3 requires accurate and precise estimates of the spatial variation of the amplitude and phase of a received signal. Components of the

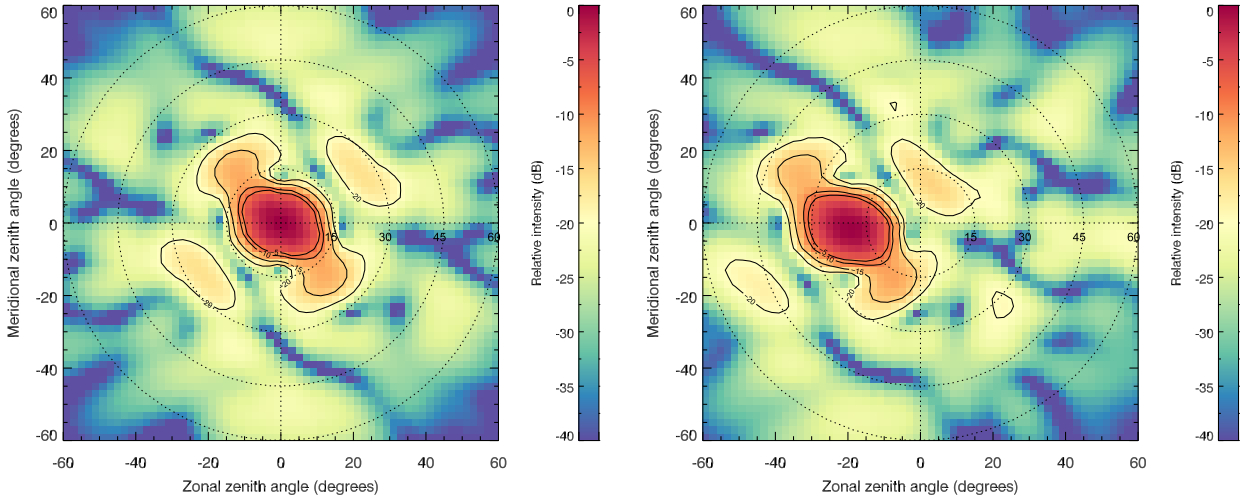

Fig. 2.6: One-way transmit polar diagrams for the antenna configuration proposed in Fig. 2.5. The left panel incorporates equal phasing at each transmitter, and in the right panel the phase progresses by $\sim 74.3°$ per element to the right along the rows, so as to steer the beam $\sim 20°$ West of the zenith.

Buckland Park MF, such as the antennas, transmission lines and T/R switches, may add unknown phase delays or advancements to the received (and transmitted) radio signals; moreover, the radar has an apodization function arising from the increasing levels of transmission line attenuation with distance from its centre (Fig. 2.2). A method of measuring and compensating for the phase and amplitude differences of each receiver channel is therefore needed.

A procedure similar to that described in Holdsworth and Reid [2004b] has been applied in this work. It involved the calculation of complex gain calibration terms from ensembles of data from an arbitrarily-selected reference channel and all other channels under consideration. Such gain terms can be represented in polar form as

$$g_{jk} = A_{jk}\, e^{-i\phi_{jk}}\,,$$

where $A_{jk} = \langle A_j / A_k \rangle$ is the ratio of the zero-lag autocorrelation function amplitudes of receivers j and k, and ϕ_{jk} is their zero-lag cross correlation function phase. As Holdsworth and Reid [2004b] mention, it is best to acquire zero-lag interpolants for both of these values, so as to remove the noise correlated between receiver channels from the acquired statistics. Interpolation was performed over lags [-2,-1,1,2] in this work.

The procedure aims at being applicable to raw data from essentially any vertical beam experiment conducted with the radar. One caveat here is that the received signals will invariably contain contributions from irregularities and/or tilts in the backscattering surfaces. These will lead to fluctuations in the effective beam position and hence[1] in the measured channel phase differences (see Sect. 3.3). It is beyond the scope of this work to compensate for these, so it is assumed on average that the effective beam position is centred on zenith, such that the mean phase difference between any two calibrated

[1]Note that the projection of the radio wave vector on the separation vector between the receivers in question would need to change for this to occur.

receiver pairs will equate to zero. As the results of this work (along with Holdsworth et al. [2004b] and Holdsworth and Reid [2004b]) show, time averaging of a day or more is needed to obtain a well-defined phase difference distribution, and even then substantial variation about the mean exists.

A second problem with using raw experimental data is that the backscatter characteristics may change with altitude. In particular, at higher altitudes ($\gtrsim$ 90 km, depending on the pulse length used) the radar pulse's tail may be totally reflected. If the E-region has non-zero tilt, a bias from the the true mean phase difference of a receiver pair in question will be observed. Care must also be taken to ensure that the receiver amplitudes are not saturated by such total reflections, as this would lead to a bias in the measured amplitude ratios. On this basis, only data from range gates centred below 90 km have been used in this analysis.

Amplitude ratio and phase difference histograms acquired from four days of raw data in early July 2015 are shown in Fig. 2.7, and the associated receiver configuration in Fig. 6.11. Receiver 1 is used as the reference here. The data shown includes that from range gates 78-88 km inclusive (in 2 km increments), with SNR $>$ 10 dB (following Holdsworth and Reid [2004b]), and solar elevation angle $>$ 10° (i.e, day-time data only). The 10° solar elevation and lower height cut-offs were somewhat arbitrarily selected; it was superficially noted that data outside of this range rarely attained SNRs $>$ 10 dB. It should also be noted that the form and mean ratios/differences did not appear to vary significantly with time.

The amplitude histograms show that the dynamic range of Receivers 2, 3, 4 and 6 are above that of Receiver 1 (and the opposite for Receiver 5), which is conceivable, given the relative transmission line lengths. The phase histograms show a marked phase difference between Receivers 1-4, 1-5 especially, and 1-6. Interestingly, the circular standard deviation of the phase difference distributions also appears to increase with antenna separation. The cause of this is unclear.

An attempt has also been made to isolate the phase differences inherent in the T/R switch–transmission line–antenna chain from the digital receivers themselves. To do this, a signal with fixed amplitude and phase needed to be directed into the receivers—i.e., a radar signal without the modulating effects of atmospheric backscatter. An experiment was set up in which a Gaussian-shaped pulse (with an arbitrary "length" of 500 m) was transmitted from the "Tx drive" output on the RF exciter module, attenuated, and passed through a 1:6 splitter. Each of the six outputs were connected into a given receiver channel. A pulse repetition frequency of 50 Hz was used, and four coherent integrations were performed on the sampled time series (also arbitrary). Ideally, each channel would show an identical amplitude and phase.

A sample of the calibration signal recorded on each of the six channels is shown in Fig. 2.8. It can be seen that the mean phase of channels 1-3 and 4-6 agree quite closely, although there is a noteable separation of the order of 15° between these two groups. These two groups of receivers are associated with two independent three-channel receiver modules, and the observed discrepancy was explained as being a design artefact [private communication, C. Adami, July 2015].

The mean receiver amplitude ratios and phase differences from the two techniques are summarized in Table 2.2. The phase differences in all cases are of the same sign, although there appears to

be a noteworthy contribution from system components other than the receivers themselves. This comparison aside, the gain discrepancies accounting for the entire receiver chain have been used to calibrate the receivers used in the configuration.

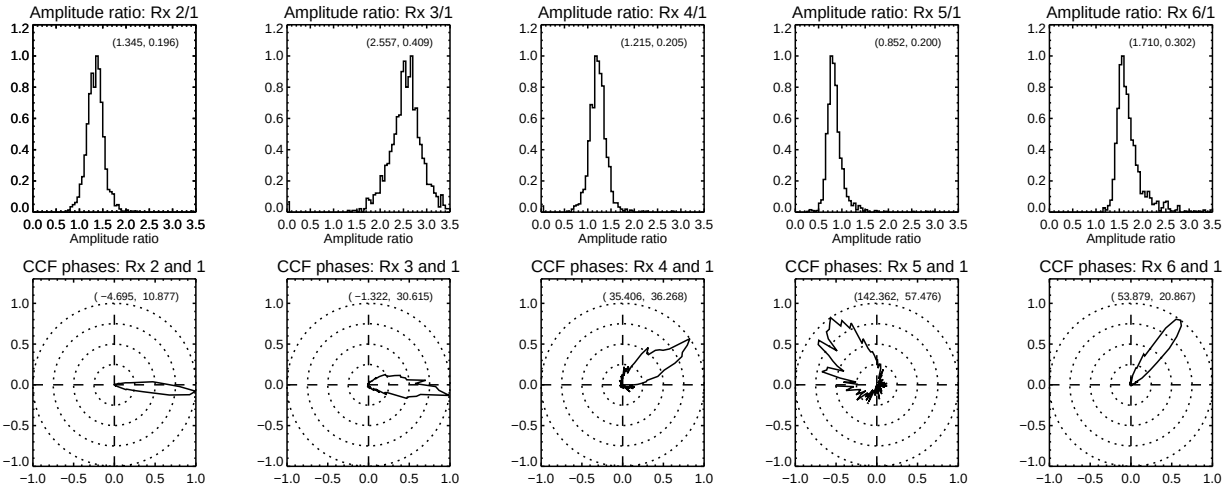

Fig. 2.7: Histograms of receiver amplitude ratios (upper panels) and phase differences (lower panels), for the receiver configuration shown in Fig. 6.11. These correspond to four days of day-time (solar zenith angle $> 10°$) data from 03-Oct—06-Oct 2015 inclusive, from range gates 78-88 km inclusive. Means and standard deviations of the quantities are shown in the upper-right corner of each plot in the form (μ,σ). Note that the shown standard deviation for the phase result is a circular standard deviation, given by $\sqrt{-2\ln R}$, where $R = \frac{1}{n}\sqrt{\sum_{i=0}^{n-1}(\cos^2\phi_i + \sin^2\phi_i)}$, n is the number of points in the time series and ϕ_i is the ith phase.

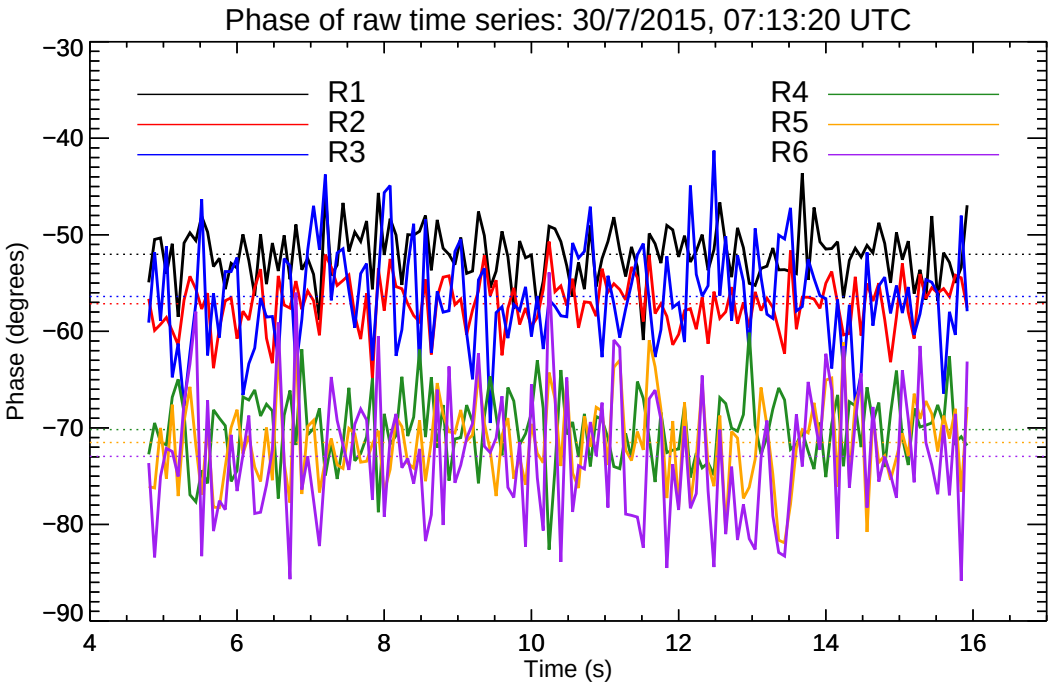

Fig. 2.8: Time series of the phases recorded on the six receiver channels when identical signals of fixed amplitude and phase were fed to them.

Pair	A_{jk}	A'_{jk}	ϕ_{jk}	ϕ'_{jk}
1-2	1:1.345	1:1	-4.695	5.123
1-3	1:2.557	1:1	-1.322	4.374
1-4	1:1.215	1:1	35.406	18.159
1-5	1:0.852	1:1	142.362	19.493
1-6	1:1.710	1:1	53.879	20.933

Table 2.2: A summary of the measured gain discrepancies between Receivers 2-6 and 1 (the reference). Primes denote the results from the second experiment described in the text (results independent of antenna, transmission line and T/R switch effects).

Site name	Location	Freq.	Power	Uptime	Avg. counts
Buckland Park	34.6°S, 138.6°E	55 MHz	40 kW	10-Feb 2014 –	7255 day^{-1}
Kingston	43.0°S, 147.3°E	55 MHz	40 kW	10-Jun 2014 – 16-Feb 2015	6475 day^{-1}
Davis Station	68.6°S, 78.0°E	33 MHz	7.5 kW	27-Jan 2005 –	9717 day^{-1}
Darwin	12.5°S, 130.8°E	33 MHz	7.5 kW	15-Nov 2005 –	13460 day^{-1}

Table 2.3: Summary of the utilised meteor radars. The count rates shown for a particular radar are averages over the number of unambiguous detections acquired between 00:00 and 23:59 UTC on days the radar was operating. "Present" was valid as at 17 May 2015.

2.2 All-sky interferometric meteor radar

Data from meteor radars produced by ATRAD Pty. Ltd. are used in this thesis for mean wind evaluation (Davis 33 MHz, Chapter 4) and for modelling of the sampling of gravity wave-perturbed wind fields (Buckland Park 55 MHz, Chapter 5). Of particular interest in the latter analysis is the precision and accuracy of the angle-of-arrival retrievals from the radar. In this section, the angle-of-arrival estimation procedure and associated uncertainties are discussed, along with a brief description of the operation procedure of the radar (following Younger [2011] and McIntosh [2009]). It should also be noted that climatologies of wind velocities and covariances were acquired from other similar radars at locations specified in Table 2.3; the results from Buckland Park and Darwin are presented in Appendix D.

2.2.1 System operation overview

Broadly, the radar system is comprised of the following components:

- a transceiver unit for generation and modulation of transmitted pulses and amplification of received signals;
- a folded crossed-dipole antenna for transmission, and five receive antennas arranged in the interferometric layout recommended by Jones et al. [1998] (see Fig. 2.9), connected to the

Parameter	Value
Max. duty cycle (uncoded pulse)	5%
Max. duty cycle (coded pulse)	8.3%
Max. PRF	20 kHz
Pulse length (HPFW)	0.1-9 km
Receiver filter width (HPFW)	18-404 kHz

Table 2.4: General ATRAD all-sky interferometric meteor radar specifications (adapted from Younger [2011] and Holdsworth et al. [2004a]).

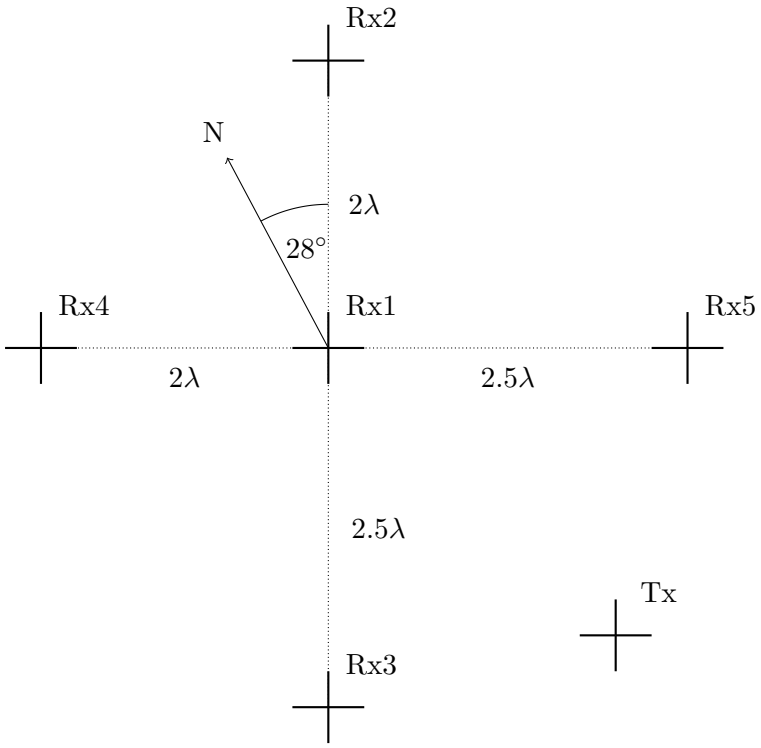

Fig. 2.9: Arrangement of antennas for the Buckland Park meteor radar (NB: the transmit antenna location is approximate).

transceiver via 50 Ω transmission lines;

- a "control" PC, serving basically the same purpose as the MF's PC.

Signal transmission

The carrier signal at the operating frequency of the radar is produced by a synthesizer in the transceiver, in the form of a ±3 V continuous wave. Pulse width modulation is used to generate a signal envelope of the desired height and width; this is applied to the carrier signal, and the product is amplified to ±6 V.

The modulated pulse is sent to a 6-way splitter, and each of the split signals are amplified (the amplification is system-dependent; for the Buckland Park implementation, 4 kW amplifiers are used). The six amplified signals are combined, and then split into two transmission lines, each of which is

Fig. 2.10: Photographs taken while tuning one of the receiver antennas of the meteor radar installed at Kingston. Data from this radar has been utilized in Bossert et al. [2015], shown in Appendix A. Installation was perfomed during May-June 2014 by C. Adami, P. T. Love, D. J. Murphy, A. D. MacKinnon, and the author. Left: a receive antenna. Right: a closer photograph of the balun, which is used to match the antenna to its transmission line.

connected (and impedance-matched, through the use of a balun) to one of the 200 Ω arms of the transmit antenna. Circular polarization of the desired handedness is obtained by incorporating a phase delay of 90° into one of the transmission lines.

Signal reception

A signal sampled by a 200 Ω receive antenna, which in typical meteor detection cases has an amplitude of a few microvolts, is firstly transferred to a transmission line impedance-matched to the antenna. It is then passed through an amplifier with a bandpass filter (for noise removal), which increases the signal's SNR by about 20 dB.

At the transceiver, it is again amplified and bandpass filtered (to a degree controlled by the acquisition PC) and mixed with a reference signal of a fixed frequency (135 MHz for the 55 MHz Buckland Park system) to produce new signals with frequencies equal to the sum and difference of the fixed and received signals (heterodyne reception). The higher frequency signal is removed by means of a bandpass filter, and the lower frequency signal is amplified, again with adjustable gain.

This signal is then transferred to a detector stage, where it is mixed with (80 MHz) I (in-phase) and Q (quadrature) reference signals (the Q reference having a phase delay of 90° relative to I). The mixed signals are passed through a Butterworth filter with adjustable bandwidth (18.1-404 kHz); the bandwidth used here is selected to maximise the signals' SNR, based on the pulse length used. Finally, the I and Q signals are fed to a data acquisition card.

Echo detection and selection

Following application of an interference filter to remove the presence of coherent "sharp bursts", the raw time series are probed for features which resemble the expected scatter from an ablating meteor and subsequently diffusing trail. This process, including the rigorous criteria needed for rejecting possible meteor candidates, is described in Holdsworth et al. [2004a].

2.2.2 Parameter estimation

Radial drift velocity

Radial drift velocities for echo candidates satisfying the mentioned acceptance criteria are estimated by computing the slope of a linear least squares fit to the CCFs of all possible receiver pairs over lags [-2,-1,1,2]. The time series used in computing the CCFs is restricted from 0.015 seconds after the "start time" to the "end time", so that the effects of the noise floor, Fresnel oscillations or the velocity of the meteoroid itself (as Holdsworth et al. [2004a] discusses) can be minimized.

Echo candidates with poor CCF phase fits or computed radial velocities in excess of 200 $\mathrm{m.s}^{-1}$ are rejected from the subsequent height and angle-of-arrival analysis.

It should also be noted that the technique for determining a radial drift velocity from a meteor candidate is identical to that used in eqn. (3.14) for DBS.

Angle-of-Arrival

The receive antennas of a standard interferometric radar should be spaced closely enough to avoid ambiguity in their CCF phases, while still being kept separated enough to avoid the effects of noise induced by their mutual coupling. The former condition requires that $|d| \leq \frac{\lambda}{2}$, and for a VHF meteor radar (according to measurements reported in Jones et al. [1998]) the latter requires $|d| > \frac{3\lambda}{2}$ (where d is the antenna separation and λ is the radar wavelength).

Jones et al. [1998] overcame these conflicting requirements by proposing a configuration like that shown in Fig. 2.9; it allows an estimate of the phase difference at virtual pair separations of 4.5λ (for decreased noise) and 0.5λ (to resolve ambiguity in the 4.5λ estimate). These phase differences, respectively, are obtained by differencing and combining the phase difference estimates at spacings of 2.5λ and 2λ (i.e., $\varphi'_{4.5\lambda} = \varphi_{2.5\lambda} - \varphi_{2\lambda}$, and $\varphi'_{0.5\lambda} = \varphi_{2.5\lambda} + \varphi_{2\lambda}$). The $\varphi'_{4.5\lambda}$ candidate closest to $\varphi'_{0.5\lambda}$ is then used to evaluate ψ using eqn. (3.18).

Holdsworth et al. [2004a] suggested some improvements to this method, which have been implemented in the analysis presented here:

- Use the "physical" $\varphi_{4.5\lambda}$ in preference to the "virtual" $\varphi'_{4.5\lambda}$ (since the latter is expected to have a larger relative error);
- Estimate the possible values for ψ using $\varphi_{2\lambda}$ (denoted $\psi_{2\lambda}$), then select the value of $\varphi_{2\lambda}$ that minimizes $|\sin\psi_{2\lambda} - \sin\psi_{0.5\lambda}|$, and use it to find the value of $\varphi_{4.5\lambda}$ that minimizes $|\sin\psi_{4.5\lambda} - \sin\psi_{2\lambda}|$. Doing this reduces the probability of measurement error in $\varphi'_{0.5\lambda}$ causing an incorrect selection of a $\varphi_{4.5\lambda}$ candidate (since there is greater angular spread in the $\varphi_{2\lambda}$ candidates).

Following these corrections, an unavoidable mutual coupling-induced error still arises in the $\varphi_{4.5\lambda}$, $\varphi_{2.5\lambda}$ and $\varphi_{2\lambda}$ estimates. Using simulations based on measured mutual impedance parameters from the Buckland Park meteor radar, Younger et al. [2013] predicted angle-of-arrival estimate errors of less than $\pm 0.5°$. Part of this error is in the form of a slowly-varying bias across the field of view, which if removed can reduce the total error to $\pm 0.2°$.

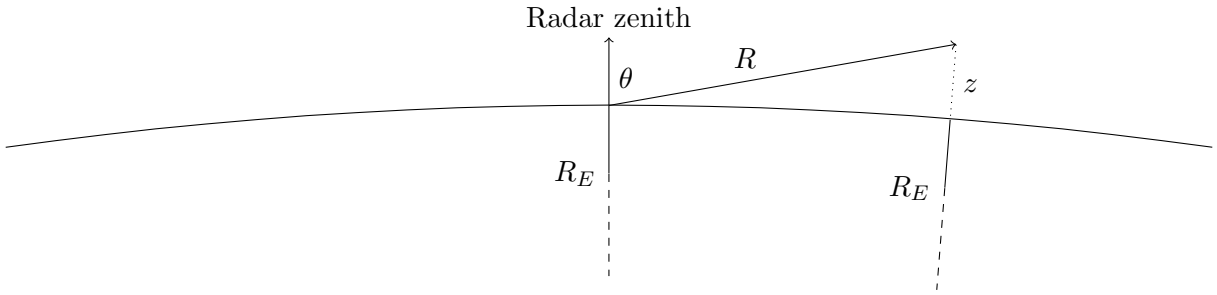

Fig. 2.11: A scale diagram indicating the geometry used to determine the height of a meteor echo at a zenith of 80° and a true altitude of 110 km.

It is also likely that other as yet unquantified phase measurement errors will contribute to biases/errors in the obtained angle-of-arrival estimates. It is thought that the net effect of these leads to approximately Gaussian-distributed errors in the angle-of-arrival of around ±1° [private communication, J. P. Younger, October 2015]. The magnitude of this error is relevant to the results presented in Chapter 5.

"True" meteor range and height

The PRFs used are commensurate with the time taken for a radar pulse to propagate from the transmitter (to a meteor trail and) back to the receiver, so the reception of pulses after the transmission of a subsequent pulse (range aliasing) occurs for meteors past a range threshold of $R_{amb} = \frac{c}{2f_{PRF}}$. Thus range de-aliasing is needed; it is done by producing a range ensemble for each candidate:

$$R_n = R + nR_{amb}\,, n = 0,\ ...,\ N\,,$$

where $N = R_{max}/R_{amb}$, and $R_{max} = 520$ km, assuming a maximum meteor height of 110 km and maximum zenith angle of 80°. A height ensemble is determined (accounting for the Earth's curvature; see Fig. 2.11) using the equation:

$$z_n = \sqrt{R_E^2 + R_n^2 + 2R_E R_n \cos\theta} - R_E\,, \tag{2.1}$$

where the constant R_E is the Earth's radius ($\approx 6,370$ km). Echo candidates are rejected if $z_n \notin [70, 110]$ km ("height unresolvable") or if there are two or more candidates in the [70,110] km interval ("height ambiguous").

Mean wind velocity

Initial wind estimates are computed using by least squares solving eqn. (1.4) (without fitting for a vertical wind velocity) for a given distribution of radial velocities and angle-of-arrival directions. As per Holdsworth et al. [2004a], no estimate is evaluated if there are less than six meteors available in a given height/time bin. The radial projection of the mean winds is then subtracted from the radial velocity recording for each meteor. Those meteors whose absolute residual exceeds 25 m.s^{-1} are rejected, and the least squares solution is re-evaluated. This process repeats until no more rejections

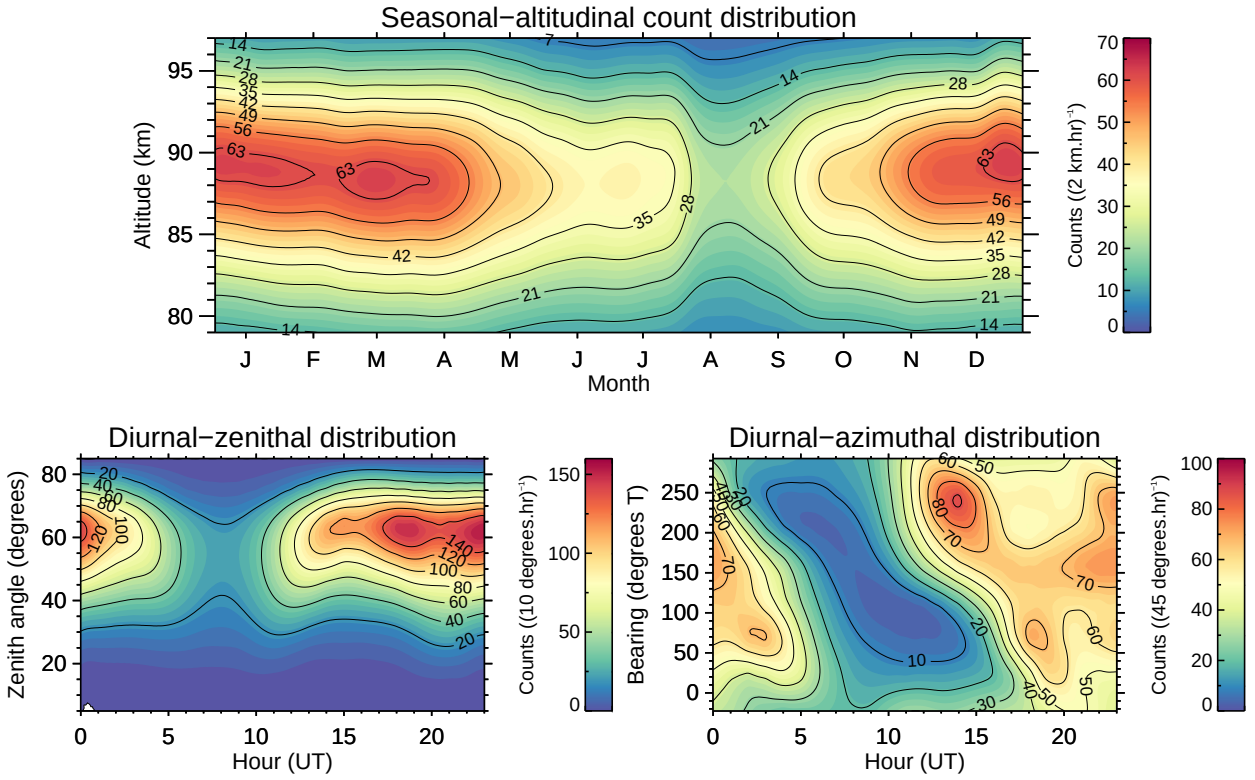

Fig. 2.12: Climatology (04-Apr 2014 - 30-Sep 2015) of count rate distributions for the 55 MHz Buckland Park meteor radar with time of year and altitude (top panel), time of day and zenith angle (lower left) and time of day and azimuth angle (lower right).

occur, or until the number of remaining meteors drops below six. In the latter case, no estimate is evaluated.

In this work, all meteor analyses involving the computation of wind velocities or stress terms only utilize meteors between zenith angles of 15° and 80°. Below this limit, spurious radial velocities due to the larger relative contribution from vertical velocities are likely to result, and above, large height determination errors due to angle-of-arrival uncertainties (e.g., Fritts et al. [2012a]).

2.2.3 Typical coverage

Example climatologies of meteor detection rate distributions from the Buckland Park radar are shown in Figs. 2.12 and 2.13. The variation in detection rate with season and time of day can be attributed to the meteor radiant distribution (e.g., Janches et al. [2006]). The diurnal variation in azimuthal detection rate is especially expected to have an impact on the radar's ability to measure wind covariances, as discussed in Sect. 1.2, and implicitly modelled in Chapter 5.

2.3 Summary

This chapter has provided an overview of the Buckland Park (BP) MF radar and other meteor radar systems utilised in this thesis.

In particular, surveys of the quality of the antennas in the MF radar were described. These included

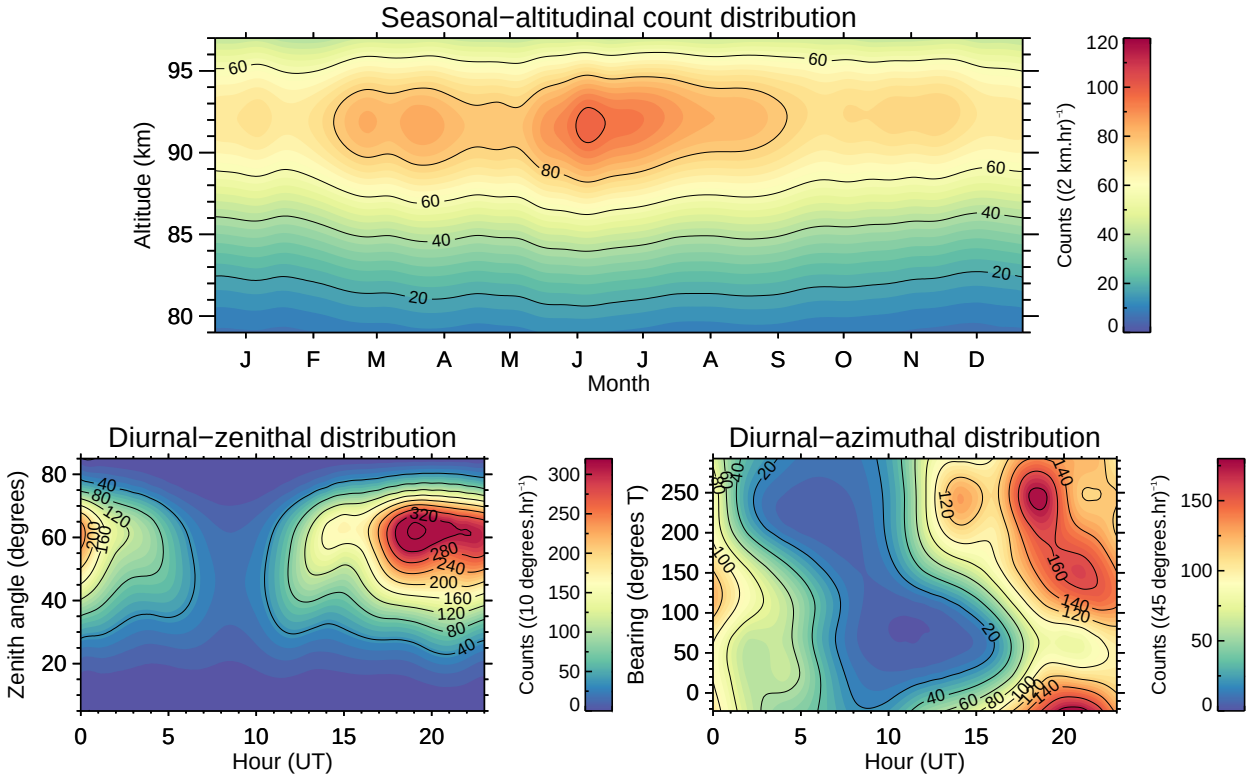

Fig. 2.13: As per Fig. 2.12, but for the 33 MHz Darwin meteor radar (14-Nov 2005 - 31-May 2015).

measurements of the Standing Wave Ratio (SWR) of each antenna (depicting the level of impedance matching between the antenna element and transmission line pairs) and a Time Domain Reflectometry (TDR) trace of each transmission line (which identified "breaks" in the lines, in the form of sudden changes in refractive index). The surveys indicated that $\sim 2/3$ of the antennas in the array require refurbishment to be brought back into use. The number of available antennas was generally considered inadequate for Doppler beamsteering on transmission, due to the suspected grating lobe influence.

The antenna array was then modelled in software, and attempts were made to optimize the transmitted beam pattern for Doppler beamsteering, with the restriction that only several transmission lines could be replaced. A refurbishment plan was proposed on this basis. Due to financial constraints, this has not yet been implemented.

An antenna configuration using the array in its present state has instead been proposed for Doppler studies, and is further elaborated upon in Sect. 6.4. Results from a receiver gain calibration procedure were presented, which will be utilised prior to applying interferometric techniques to the data from this configuration.

The next chapter describes the three analysis techniques that are applied in this thesis to data from spaced antenna receivers on the BP MF.

Chapter 3

Spaced antenna techniques

This chapter provides a description of the FCA, DBS and HDI techniques. While not addressed in this thesis, an understanding of the wind velocity estimation biases common to the three techniques at MF/HF frequencies is needed to justify their use on the BP MF array; findings in this area are briefly mentioned at the end of the chapter.

3.1 The Full Correlation Analysis (FCA)

The Full Correlation Analysis (herein denoted "FCA") first appeared in Briggs et al. [1950]. It is a technique that analyses the data from spatially separated radio receivers using correlation techniques to estimate the horizontal velocity components and spatial properties of a (far-field) ground diffraction pattern. Such a pattern is typically produced by the partial reflection of a vertically transmitted radar beam by atmospheric scatterers (see Sect. 1.1.2). Since the horizontal velocities of the pattern and scatterers are equivalent, the procedure provides a wind velocity estimate if it is assumed that the scatterers are advected by the neutral wind. The FCA can also be used to estimate scatterer shape and size characteristics (e.g., Lesicar and Hocking [1992] for the mesosphere) since the spatial properties of the pattern and scatterers are Fourier Transform pairs.

The software implementation of the FCA used in this work has been provided as part of a package supplied by ATRAD [Holdsworth and Reid, 2004b]. The package has been used here to derive data sets of wind velocities (Chapter 4) and scatterer aspect sensitivities (Chapter 6) from the Buckland Park MF radar. The derivation of these parameters using the FCA, discussed at length in excellent reviews by Briggs [1985] and Holdsworth [1995], is briefly reviewed here.

The FCA assumes that the spatio-temporal correlation functions of pairs of spatially separated receivers have the form of a family of similar ellipsoids. In terms of the ground diffraction pattern $f(x, y, t)$, such a (real) spatio-temporal correlation function may be represented as

$$\rho(\xi, \eta, \tau) = \frac{\langle f(x, y, t)\, f(x + \xi, y + \eta, t + \tau) \rangle}{\langle |f(x, y, t)|^2 \rangle}\,, \tag{3.1}$$

where ξ, η and τ are zonal, meridional and temporal lags respectively, and, for simplicity, $f(x, y, t)$ is assumed to have zero mean. If the functional form of $\rho(\xi, \eta, \tau)$ is assumed ellipsoidal, in the frame of

reference moving with the pattern it may be represented as

$$\rho(\xi', \eta', \tau) = \rho\left(A(\xi'^2 + B\eta'^2 + K\tau^2 + 2H\xi'\eta')\right) , \tag{3.2}$$

where the factors A and B account for "elongation" of the pattern in the zonal and meridional directions respectively, K is the constant for its temporal variability, and H allows for systematic tilt of the pattern in the xy-plane. Assuming that the pattern is moving at a fixed velocity V at a bearing of ϕ, the spatial lags in the stationary frame are represented by the Galilean transformation:

$$\xi = \xi' + V_x\tau\,,\ \eta = \eta' + V_y\tau\,, \tag{3.3}$$

where $V_x = V\sin\phi$ and $V_y = V\cos\phi$. Supposing now that the pattern is sampled in the stationary frame by an arbitrarily-spaced array of receivers with separation vectors $\boldsymbol{r}_{ij} = [\xi_{ij}, \eta_{ij}]$ (as is done practically), the cross correlation function for a given receiver pair may be written as

$$\rho(\xi_{ij}, \eta_{ij}, \tau_{ij}) = \rho\left(A(\xi_{ij} - V_x\tau_{ij})^2 + B(\eta_{ij} - V_y\tau_{ij})^2 + K\tau_{ij}^2 + 2H(\xi_{ij} - V_x\tau_{ij})(\eta_{ij} - V_y\tau_{ij})\right) , \tag{3.4}$$

which has the "form"

$$\rho(\xi_{ij}, \eta_{ij}, \tau_{ij}) = \rho(A\xi_{ij}^2 + B\eta_{ij}^2 + C\tau_{ij}^2 + 2F\xi_{ij}\tau_{ij} + 2G\eta_{ij}\tau_{ij} + 2H\xi_{ij}\eta_{ij})\,. \tag{3.5}$$

The coefficients A-H must be evaluated to be able to obtain the wind velocity and spatial characteristics of the pattern. Briggs [1985] suggests a way of doing this using least squares techniques, which has been implemented in the package used here. The equations obtained by equating coefficients of $\xi_{ij}\tau_{ij}$ and $\eta_{ij}\tau_{ij}$ in eqns. (3.4) and (3.5),

$$AV_x + HV_y = -F \text{ and} \tag{3.6}$$

$$BV_y + HV_x = -G\,, \tag{3.7}$$

may then be solved simultaneously to determine V_x and V_y. These velocities, coined the FCA "true" velocities, account for both anisotropy and random temporal variations in the ground diffraction pattern, provided the assumption that the temporal autocorrelation function has the same functional form as the spatial correlation function is valid.

Of particular interest in this work is the typical coverage of the MLT winds acquired by the FCA (applied to Buckland Park MF data). The software implementation used here assigns error codes to wind estimates associated with raw signals that fail to satisfy certain criteria. Describing these criteria is beyond the scope of this work; a full listing of them is given in a recent review by Reid [2015]. An example climatology of FCA acceptance rates for ordinary-mode transmission is shown in Fig. 3.1.

Additionally, two spatial characteristics of the scatterers that the FCA parameterizes are of interest in Chapter 6. The first is a measure of the elongation of the characteristic ellipse, the so-called "axial-ratio", defined as

$$R_{ax} = \sqrt{\frac{\frac{A}{C} + \frac{B}{C} + r}{\frac{A}{C} + \frac{B}{C} - r}}\,, \tag{3.8}$$

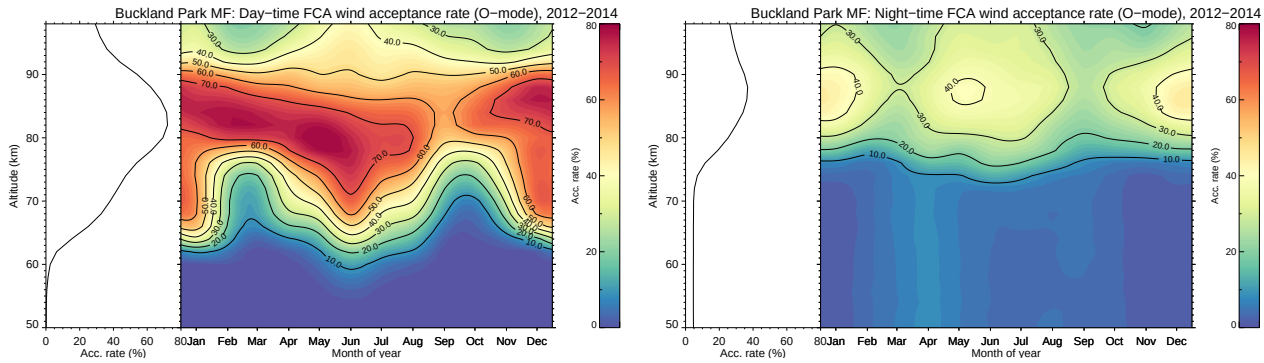

Fig. 3.1: Acceptance rates for ordinary (O)-mode transmission on the BP MF. Day-time (solar elevation $\geq 0°$) rates are shown on the left, and night-time (solar elevation $< 0°$) on the right.

where $r = \sqrt{(\frac{A}{C} - \frac{B}{C})^2 + 4\frac{H}{C}^2}$. The second is the major axis of the characteristic ellipse, termed the "pattern scale". It is defined as

$$S_{0.5} = r_{maj} = \sqrt{\frac{2\tau_{0.5}^2}{\frac{A}{C} + \frac{B}{C} - r}}\,, \tag{3.9}$$

where $\tau_{0.5}$ is the so-called "fading time", which is the time taken for the mean autocorrelation function (i.e., averaged across each receiver) to fall to half its maximum value. These two quantities can be used to define the aspect sensitivity of the scatterer(s), if the polar diagram of the scatterer(s) is assumed Gaussian.[1] The aspect sensitivity is given by (e.g., Holdsworth and Reid [1995])

$$\theta_s = \sin^{-1}\sqrt{\frac{\sin^2\theta_{sb}\sin^2\theta_b}{\sin^2\theta_b - \sin^2\theta_{sb}}}\,, \tag{3.10}$$

where θ_b is the e^{-1} half-width of the radar polar diagram, $\theta_{sb} = \frac{0.22\lambda\sqrt{R_{ax}}}{S_{0.5}\sqrt{\ln 2}}$ is the e^{-1} half-width of the product of the radar and backscatter polar diagrams, and λ is the radar wavelength. In the case of an off-zenith beam, this information may also be used to evaluate the effective beam angle [Czechowsky et al., 1988] via:

$$\theta_e = \sin^{-1}\left(\frac{\sin\theta_a}{1 + \frac{\sin^2\theta_b}{\sin^2\theta_s}}\right)\,, \tag{3.11}$$

where θ_a denotes the zenith angle the beam is steered to on transmission.

3.2 Doppler Beam Swinging (DBS)

DBS was first described and applied in an atmospheric context by Woodman and Guillen [1974]. The technique uses the spectra of received backscatter signals, usually combined across an array of receivers for increased beam directivity, to estimate a beam power P, SNR ($\frac{S}{N}$), radial Doppler velocity V_{rad}, and spectral (or velocity distribution) width σ_v. Each of these quantities are of interest in this work. They may be computed from the combined signal's autocorrelation function $C(\tau)$ and

[1] For example, Hocking et al. [1986] assumes that the scatterer polar diagram is of the form $P(\theta) = e^{\frac{\sin^2\theta}{\sin^2\theta_s}}$.

its derivatives; the power is defined as

$$P = C(0_{\#})\,, \tag{3.12}$$

(where the subscript $_{\#}$ indicates an interpolation over nearby points—e.g., lags [-2,-1,1,2]), the SNR

$$\frac{S}{N} = 10\log_{10}\left(\frac{P}{C(0)}\right)\,, \tag{3.13}$$

the Doppler velocity

$$V_{rad} = -\frac{\lambda}{4\pi\delta}\,\tan^{-1}\frac{\Im(C'(0_{\#}))}{\Re(C'(0_{\#}))}\,, \tag{3.14}$$

where λ is the radar wavelength, δ is the time gap between subsequent samples, $\Re$ and $\Im$ denote the real and imaginary operators respectively, primes denote time derivatives, and the spectral width

$$\sigma_v = \frac{|C''(0_{\#})|}{C(0)}\,. \tag{3.15}$$

The theoretical variance in this estimate, if a narrow Gaussian signal spectrum is assumed, is given by [Doviak and Zrnič, 1993]

$$\mathrm{var}\,(V_{rad}) = \frac{\lambda^2}{4n\delta^2}\left[\frac{\sigma_{vn}}{4\sqrt{\pi}} + 2\sigma_{vn}^2\,\frac{N}{S} + \frac{1}{12}\left(\frac{N}{S}\right)^2\right]\,, \tag{3.16}$$

where $\sigma_{vn} = \frac{2\sigma_v\delta}{\lambda}$ and $\frac{N}{S}$ is the inverse of the SNR.

In order to estimate component wind velocities, DBS has (in the past) been applied to scatter from vertically and obliquely received beams (e.g. Vincent and Reid [1983]). As discussed in Sect. 1.1.2, a correction for aspect sensitivity is generally needed to assign the obtained V_{rad} to the correct off zenith angle; the next technique discussed considers one way of doing this.

3.3 Hybrid Doppler Interferometry (HDI)

HDI [Holdsworth and Reid, 1998] applies DBS on a receive beam "synthesized" in the direction of an interferometrically-derived estimate of the effective beam position (EBP). It uses either Post-set Beam Steering (PBS) [Röttger and Ierkic, 1985] or the more computationally efficient Post Statistics Steering (PSS) [Kudeki and Woodman, 1990] to estimate the EBP. PBS and PSS are fundamentally the same; in the interests of brevity, an implementation of the PSS technique is be described here.

Consider an arbitrary spatial arrangement of n antenna receivers (as may be done in typical implementations of HDI) sampling plane radio wave fronts with the geometry indicated in Fig. 3.2. Specify a matrix $\boldsymbol{S} = [\boldsymbol{s}_1, ..., \boldsymbol{s}_n]^{\mathrm{T}}$, containing the complex time series from each receiver. The phase difference φ_{ij} measured between any two receivers with spatial separation $\boldsymbol{d}_{ij} = [x_{ij}, y_{ij}, z_{ij}]$ is given by

$$\varphi_{ij} = \tan^{-1}\frac{\Im(C_{ij}(0))}{\Re(C_{ij}(0))} = k\,\boldsymbol{d}_{ij}\cdot\boldsymbol{A}\,, \tag{3.17}$$

where $C_{ij}(0)$ is the cross correlation function of the two receivers evaluated at zero lag, $k = \frac{2\pi}{\lambda}$ is the radar wavenumber and $\boldsymbol{A} = [\sin\theta\sin\phi,\ \sin\theta\cos\phi,\ \cos\theta]$. As an aside, if the horizontal component of

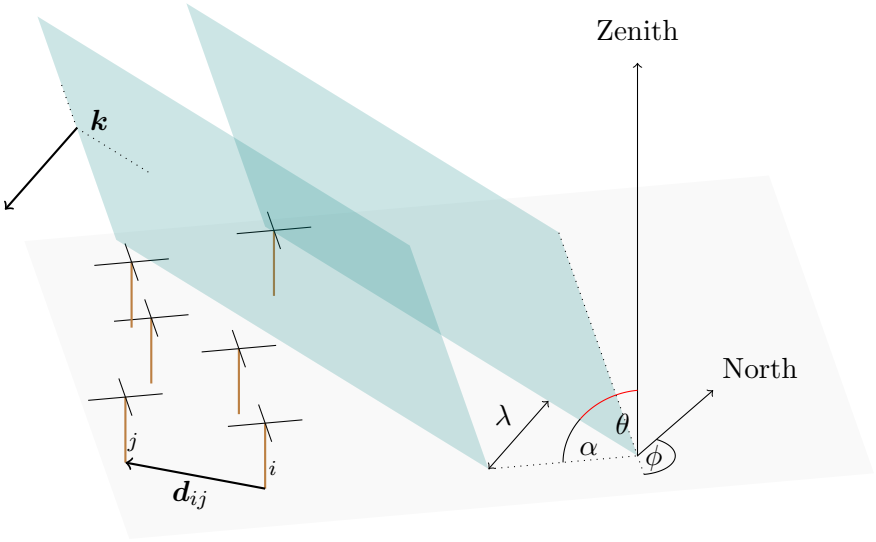

Fig. 3.2: A three-dimensional schematic of an arbitrary distribution of antenna receivers sampling two phase fronts of a plane radio wave, totally reflected from a scatterer at a zenith angle θ (elevation angle α) and a bearing of ϕ. The measured phase difference between any two receivers is the dot product of their separation vector $\boldsymbol{d}_{ij}$ and the wave vector $\boldsymbol{k} = -k\boldsymbol{A}$ (shown schematically only).

the radio wave vector and the antenna separation vector are parallel,

$$\psi = \sin^{-1}\left(\frac{\varphi}{kd}\right) \tag{3.18}$$

where ψ is the zenith angle (conforming with the convention typically used) and d is the antenna separation. Now, one can effectively reverse eqn. (3.17) by multiplying C_{ij} by an appropriate complex gain term. That is, by introducing a phase difference φ'_{ij} between the recorded signals $\boldsymbol{s}_i$ and $\boldsymbol{s}_j$, one can construct a new cross correlation function between the two receivers that would be obtained if the beam was being received in a different direction. This process is known as the "synthesization" of a beam in software.

If each of the n receivers were to be used to synthesize a single beam in a direction with direction cosines $\boldsymbol{A}$, the gain terms could be specified by the vector

$$\boldsymbol{t} = [e^{ik\boldsymbol{A}\cdot\boldsymbol{d}_1}, ..., e^{ik\boldsymbol{A}\cdot\boldsymbol{d}_n}]^{\mathrm{T}}, \tag{3.19}$$

and the autocorrelation function of the synthesized signal by [Kudeki and Woodman, 1990; Palmer et al., 1990]

$$\Sigma = \boldsymbol{t}\left\langle \boldsymbol{S}\boldsymbol{S}^{\dagger}\right\rangle \boldsymbol{t}^{\dagger}, \tag{3.20}$$

where † represents a Hermitian conjugate and the term $\left\langle \boldsymbol{S}\boldsymbol{S}^{\dagger}\right\rangle$ represents the cross correlation functions of every possible combination of receiver pair signals. Signal power (and Doppler velocity) may then be estimated from Σ using standard DBS analysis. Equation (3.20) may be simply iterated over multiple directions to obtain a spatial distribution of DBS parameters; in the HDI analysis implemented on the Buckland Park MF, iteration is done over a uniform grid of positions, usually within the expected

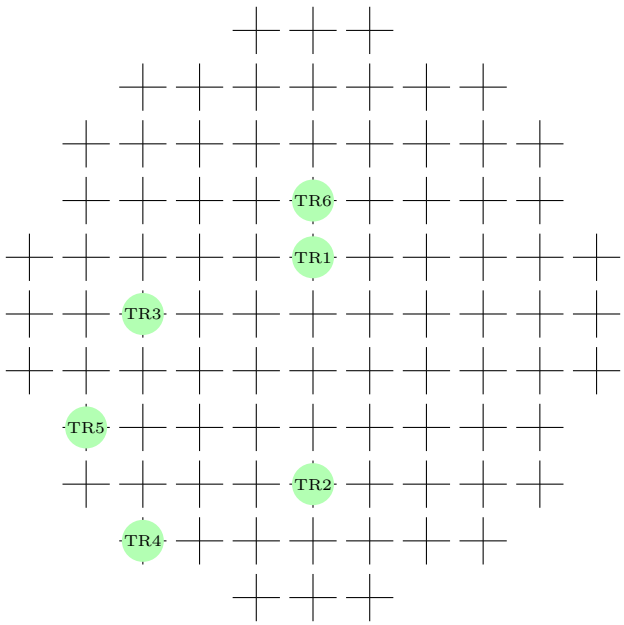

Fig. 3.3: Transmitter and receiver configuration used in acquiring the time series in Fig. 3.4.

FWHM of the transmitted beam(s). An example of such an analysis performed on a raw time series is shown in Fig. 3.4. The transmitted beam in this case was vertical, with transmitter/receiver locations shown in Fig. 3.3.

The EBP is then assigned to the peak of a two-dimensional Gaussian fit to the spatial power distribution (lower left panel of Fig. 3.4) in the vicinity of the direction of peak power. Finally, a beam is synthesized in the direction of the EBP, and all of the standard DBS parameters from Sect. 3.2 are estimated.

As discussed in Kudeki and Woodman [1990], a crucial assumption of PSS (and for that matter, any radar interferometric study) is that the gains of each receiver are calibrated to be equal; such a calibration was performed in Sect. 2.1.5.

The software used to perform the HDI analysis reported in this work (Chapter 6) was also provided as a part of a package supplied by ATRAD. From a raw radar signal, the software evaluates a power, SNR, radial velocity, EBP, spectral width, and aspect sensitivity parameter, using the methodology previously outlined. The scenarios under which the analysis will fail on any given data record are summarized in Table 3.1; wherever products of the analysis have been reported in this thesis (e.g., in Chapter 6), only data with an error code of 0 (i.e., no error) have been used in their derivation.

3.4 A note on wind estimation biases at MF/HF

The accuracy of spaced antenna wind estimation techniques at MF/HF frequencies has attracted controversy in the past (this is reviewed in detail in Reid [2015], and is discussed very briefly here). Much of the controversy stemmed from the elementary analyses applied in the original measurements, and the adoption of quality control measures based on experience in applying the analysis rather than

Code	Error
1	Low dynamic range, or interference rejection
2	SNR < -6 dB
3	Off zenith beams: projected horizontal velocity based on EBP and radial velocity > 200 m.s^{-1}
4	Maxima in power estimates too close to edge of synthesized beam directions to estimate EBP
5	Azimuth angle of EBP not within 45° of the transmitted beam azimuth
6	Zenith angle of EBP < 0
7	Zenith angle of EBP > transmitted beam azimuth
8	Insufficient good power estimates with synthesized beam angle to estimate the EBP

Table 3.1: Error codes for the ATRAD HDI analysis.

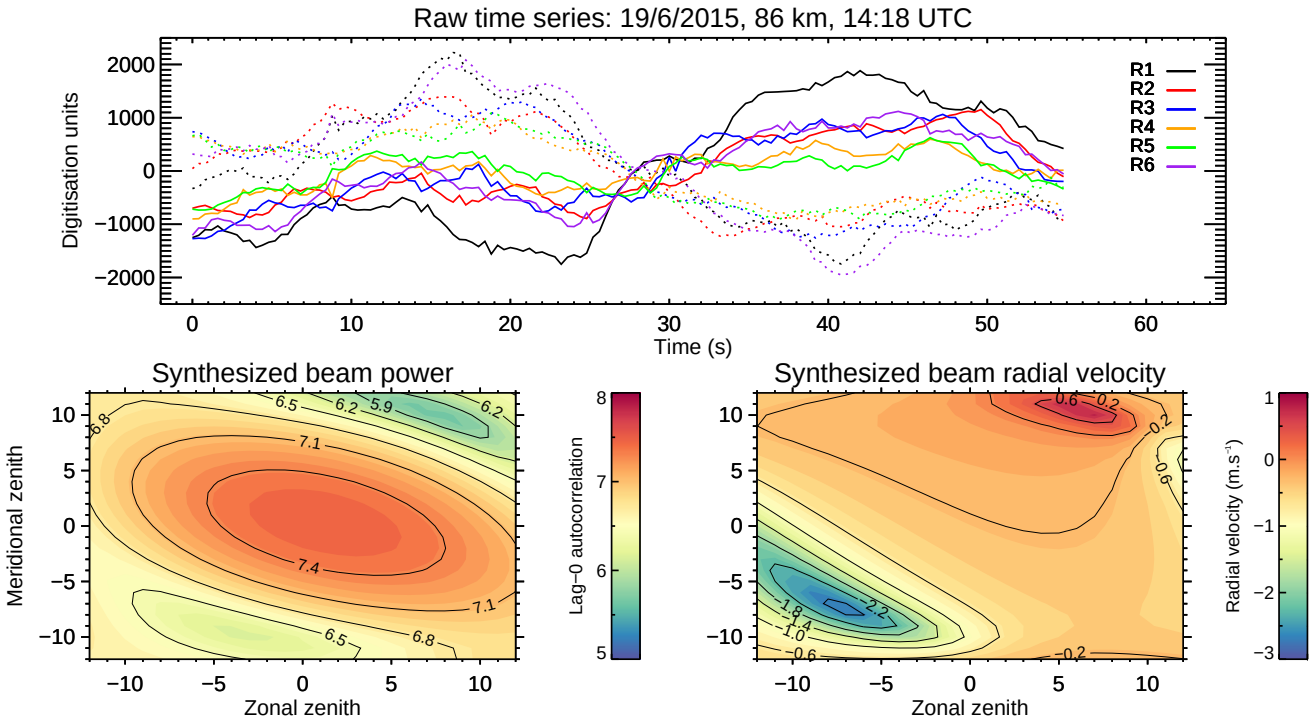

Fig. 3.4: A randomly-selected raw time series from the BP MF (top panel) and the HDI-derived synthesized beam powers (lower left) and radial velocities (lower right). In the top panel, the in-phase component is shown as a solid line, and the quadrature phase dotted.

theoretical considerations. Perhaps the most noteworthy scrutiny the FCA, DBS and IDI[2] techniques faced was in the 1990's, following the results of the Arecibo Initiative in Dynamics of the Atmosphere (AIDA) '89 campaign [Hines et al., 1993]. The authors of this work argued that the partial reflection

[2]Note that IDI, as discussed briefly in footnote 6 on page 8, is distinct from HDI, which was developed after the AIDA '89 campaign.

IDI-derived winds they had obtained above 80 km were biased toward the phase velocity of internal gravity waves—in much the same way as total reflection-derived winds would be, as proposed by e.g., Hines and Rao [1968].

This argument assumed that specular reflection, as opposed to isotropic Bragg scatter, was the dominant contributor to the radar returns above 80-85 km. In response, Kudeki et al. [1993] argued that there was no independent evidence of this being the case for MF/HF radar echoes. Through a modelling study, they predicted that flow field inhomogeneities could contaminate shorter-period statistics of IDI-derived results in a similar way, and that results time-averaged over periods greater than about one hour were unaffected. Sürücü et al. [1995] subsequently included the effects of anisotropic scatterers in a related modelling study, and concluded that wind estimation biases would arise from the sampling of an anisotropic scattering volume perturbed by gravity waves, but that they would not necessarily be toward the gravity wave phase speed, and were much smaller than those found in the AIDA campaign (15 $\mathrm{m.s^{-1}}$ vs. 40 $\mathrm{m.s^{-1}}$).

Holdsworth and Reid [1995, 1997] also numerically modelled the spaced antenna FCA, using a parameterization of aspect sensitive volume scatter with discrete scatterers. Evidence of an underestimation of the winds due to the triangle size effect (TSE) was determined, although no evidence of a bias in the direction of gravity wave phase speeds was found.

Nonetheless, the FCA is still known to exhibit a height-dependent underestimation of the mean wind, and to a greater extent than that predicted by the TSE. These are clearly evident from e.g., recent intercomparisons of FCA-derived winds with those from a meteor radar [McIntosh, 2009]. Reid [2015] considers some reasons for this, but ultimately notes that the source of the height-dependence in the bias still needs to be resolved. Accounting for the effects of this bias in the FCA results presented in Chapters 4 and 6 was considered beyond the scope of this thesis.

3.5 Summary

This chapter has briefly described the FCA and HDI techniques. The FCA is applied in the next Chapter to a long-term spaced antenna data set from the BP MF, and both techniques are applied to estimate Reynolds stress terms in Chapter 6.

Chapter 4

Long-term study of gravity wave variances

In this Chapter, a preliminary analysis of the long-term trends and solar cycle influence of wind velocities and gravity wave variances derived from 14 years of Buckland Park MF routine FCA velocities and 9 years of winds from the Davis 33 MHz meteor radar, is presented. The later chapters in this thesis are concerned with assessing the abilities of the discussed radar techniques to measure gravity wave variances and momentum fluxes; in this context, it is interesting to consider evidence that these quantities may be changing in response to anthropogenic global warming. Moreover, there has been no study published suggesting deficiencies in the horizontal wind or variance estimate capability of the FCA or meteor technique[1] that undermine their utility for long-term trend measurement.

In the first section, a very brief review of the recent studies of wind field gravity wave activity trends in the MLT-region is provided. The antenna configuration and experiment parameters used for the Buckland Park MF study are then described, followed by the analysis method for the two different radars, and a discussion of the trend results.

4.1 Introduction

The measurement of long-term trends in the ionosphere has been of great interest since Roble and Dickinson [1989] predicted the cooling effect that a doubling of CO_2 and CH_4 mixing ratios would have on regions above the stratosphere. An "emerging pattern" of long-term trends in temperatures and electron densities, derived from both observational and modelling studies, was presented by Laštovička et al. [2006, 2008]. The observed trends have been explained as being compatible with an increase in greenhouse gas concentrations, with probable secondary influences from stratospheric ozone depletion, long-term changes in solar geomagnetic activity, and changes of the Earth's magnetic field [Laštovička et al., 2012].

A study that appears to be raising some controversy in the community is that of Oliver et al. [2013]; in analysing 30 years of noon-time temperature data from the Millstone Hill incoherent scatter radar (MHISR), they (as did Holt and Zhang [2008]) measured a neutral cooling rate of 50 K/decade at 375 km. This (1) represents an overcooling with respect to the theory of Roble and Dickinson [1989], and (2) far exceeds the cooling implied by the modest declines in density observed by satellites at the

[1] Regarding the meteor technique, only longer term variances are being referred to here—that is, variances evaluated from the mean winds only, not via an inversion of eqn. (1.7) for all radial velocities in a sample. See Sect. 4.3 for details.

same altitude. Oliver et al. [2013, 2014] reconcile (1) by suggesting that the cooling may have been caused by a climate-shift-induced increased flux of gravity waves into the thermosphere[2], and (2) by noting that an O density increase observed by the MHISR at 120 km would counteract the density decrease implied by the cooling around 375 km. Laštovička [2015] disputes these hypotheses, arguing that the temperature trends observed by Oliver et al. [2014] were biased by including only noon-time measurements, and incorrectly notes that all other studies of O density at 120 km contradict Oliver's findings. In reply, Oliver et al. [2015] stood by the claim that radiative cooling by greenhouse gases alone could not have caused the noon-time overcooling.

Regardless of the "true" magnitude and cause of the ionospheric cooling above Millstone Hill, the extent to which wave activity has changed in the upper atmosphere, both as a consequence of change in the lower and middle atmosphere and as a possible driver of other trends in the upper atmosphere, remains an unsolved problem [Qian et al., 2011]. It is clear that a more widespread study of trends in short period ionospheric gravity wave fluxes is needed to address this. Such studies may also assist in the interpretation of the considerable body of analyses of wind trends in the upper atmosphere (see e.g., Laštovička et al. [2008] and Laštovička et al. [2014] for recent reviews).

The only studies to date reporting trends in gravity wave parameters are summarized in Table 4.1. Of particular interest here are the wind and gravity wave variance trend relationships presented in Hoffmann et al. [2011]. Briefly, above Juliusruh during summer, they found a steady increase in westward winds near 75 km [Keuer et al., 2007] that was correlated with an increase in the gravity wave variances at about 80 km. They attributed the variance increase to the reduced filtering of eastward propagating gravity waves imposed by the wind trend (see Sect. 1.1.1). They noted the simulations by Becker [2009] as a suggestion for a cause of the increasing variance, which indicate that the altitude of the gravity wave drag will shift downward in the event of gravity wave amplification in the extratropical troposphere. Offermann et al. [2011] also comment on the wind trends reported in Keuer et al. [2007] in the context of the long-term increase they saw in their own OH temperature variances. They suggested, as did Offermann and Koppmann [2013] in a subsequent review, that the results were consistent with the zonal wind being driven by gravity wave dissipation.

Along with adding to the existing studies of wave variance in the upper atmosphere, the analysis presented here aims to assess the validity of the hypothesis of Hoffmann et al. [2011].

4.2 Data set characteristics

The Buckland Park MF FCA wind data considered here begins on 11-Apr 1996 and ends on 04-May 2010, and spans the altitude range 70-98 km inclusive (see Fig. 4.2 for a time series of the daily acceptance rate of individual records). Beam transmission (pertaining to the FCA at least) was solely vertical, performed using up to 20 groups of 3 "North-South" oriented antennas. The FCA was applied to signals received on a "small" triangle of crossed-dipole antennas, similar to the TR1-3 and R11-13 groups outlined in bold in Fig. 4.1. The location of these reception groups did vary throughout

[2]by way of inducing a divergent downward heat flux [Walterscheid, 1981].

Study	Data set	Duration	Relevant findings
Oliver et al. [2013]	Millstone Hill (46.2°N, 71.5°W) incoherent scatter radar	1966-2012	Enhancement of gravity wave intensities around 350 km
Hoffmann et al. [2012]	Andenes (69.3°N, 16.0°E) MF radar (FCA)	1999-2011	Reduction of GW variances from 80-88 km, no significant solar cycle correlation
Hoffmann et al. [2011]	Juliusruh (54.6°N, 13.4°E) MF radar (FCA)	1990-2010	Enhancement of GW variances above 80 km (and weak solar cycle correlation), increase in mean westward wind and its velocity at 75 km (summer)
Offermann et al. [2011]	Wuppertal (51.3°N, 7.2°E) / Hohenpeissenberg (47.8°N, 11.0°E) OH rotational temperatures	1994-2009	Enhancement of nocturnal gravity wave activity around 87 km
Li et al. [2010]	Hawaii (19.5°N, 155.6°W) Rayleigh lidar temperatures	1997-2007	Enhancements of GW variance in upper stratosphere during 2001-02 and winter 2005-06
Jacobi et al. [2006]	Collm (52.1°N, 13.2°E) LF drift measurements	1984-2003	Clear decadal oscillation in GW variances in phase with solar cycle (85-110 km)
Gavrilov et al. [2004]	Hawaii (22.0°N, 159.3°W) MF radar (FCA)	1990-2000	Possible correlation between GW variances and SOI
Gavrilov et al. [1999]	Shigaraki (34.9°N, 136.1°E) MU radar (DBS)	1986-1997	”
Gavrilov et al. [1995]	Saskatoon (52.2°N, 107.1°W) MF radar (FCA)	1979-1993	Negative correlation between GW variances and solar cycle/geomagnetic activity

Table 4.1: A summary of studies analysing long-term trends in MLT-region gravity wave (GW) activity. Note that a number of unpublished papers presented at the 2013 CAWSES-II Symposium, cited in Laštovička et al. [2014], are not included here. Also, note that the Hoffmann et al. [2012] presentation included updated results from Hoffmann et al. [2011].

the period considered (as necessitated by antenna failures/refurbishment and transmitter availability [Holdsworth and Reid, 2004b]), though their spacing was consistent. Other experiment parameters used are shown in Table 4.2.

It should be noted that the FCA was, from 02-Mar 1997 through to 04-May 2010, applied to

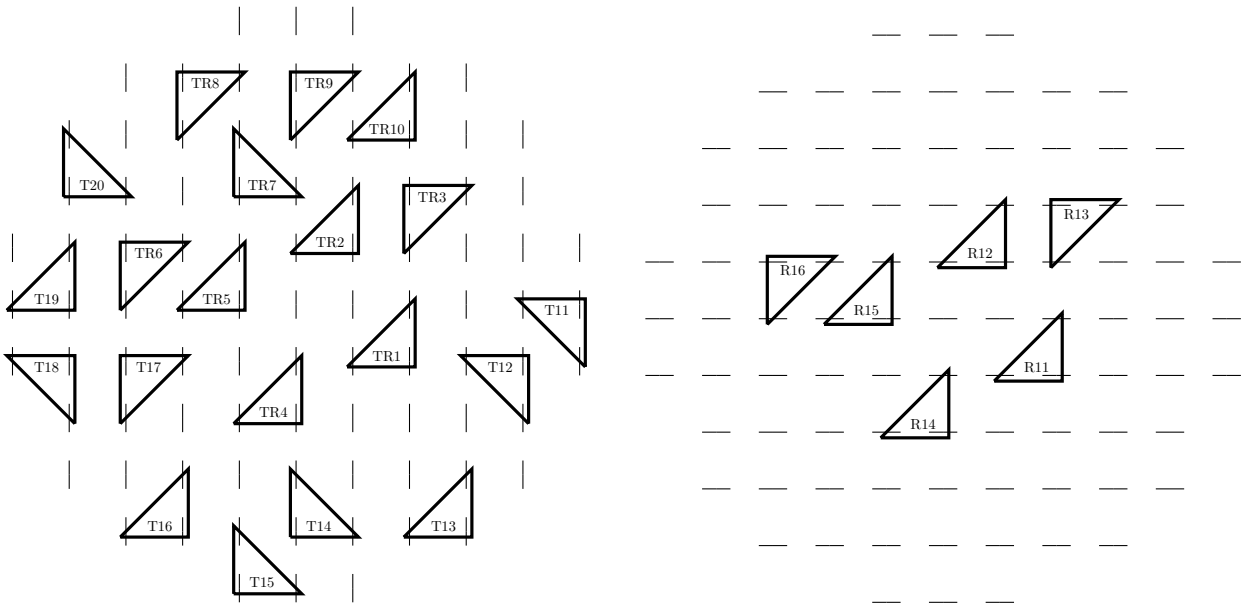

Fig. 4.1: Initial antenna configuration used for the routine BP MF observations. Here, "TR" refers to transmit-receive groups, "T" to transmit-only groups, and "R" to receive-only groups. The "small" triangle of receivers used for the long-term studies here encompassed receivers with spacings similar to TR1-3.

a "large" triangle of crossed-dipoles (using groups similar to the TR 1,5,9 trio in Fig. 4.1). To preferentially choose the data set from the smaller configuration for a long-term analysis requires some justification, in light of the triangle size effect. While it is acknowledged that the velocity estimates from the smaller configuration may more substantially underestimate the true wind velocity, it is argued that the smaller configuration will have produced fewer spurious velocity estimates and higher mean acceptance rates, and hence more statistically significant trends. Additionally, the FCA has been applied to signals received at spacings similar to the "small" configuration historically (see Sect. 2.1.1). An original goal of this work was to assimilate the older data (dating back to 1973) into the "small" 1996-2010 analysis, as it seemed reasonable to expect the dynamic range of the two data sets to be the same. Preliminary observations (not presented here) indicate that this is not the case, and that more care is required in the combining of the data sets. Nonetheless, a comparison between the concurrent "small" and "large" data sets is another obvious extension to the analysis presented here.

The experiment parameters used for the Davis 33 MHz meteor radar are identical to those described in Sect. 2.2. The data set considered begins on 26-Jan 2005 and ends on 29-Oct 2014, and spans the altitude range 80-94 km inclusive. A plot of the percentage of hourly wind records accepted in each day of the data record is shown in Fig. 4.3 (the criteria for successful wind velocity evaluation are described in Sect. 2.2.2, from pg. 33).

The complete time series used for the trend estimations reported in this study have been included for reference in Appendix E.

Parameter	Value
Peak power (kW)	25.0-82.5
No. antennas	30-75
Sampling range (km)	50-102 (70-102)
Sampling resolution (km)	2
Range bin size (km)	4
Beam $\frac{1}{2}$-power $\frac{1}{2}$-width (°)	5.0-8.4
PRF (Hz)	100 (20)
No. CI	40 (8)
No. samples per beam	280
No. Rx	16
No. Tx	20

Table 4.2: Parameters used over 1996-2010 for the small-triangle FCA experiment. Where applicable, night-time values are bracketed (and day-time un-bracketed).

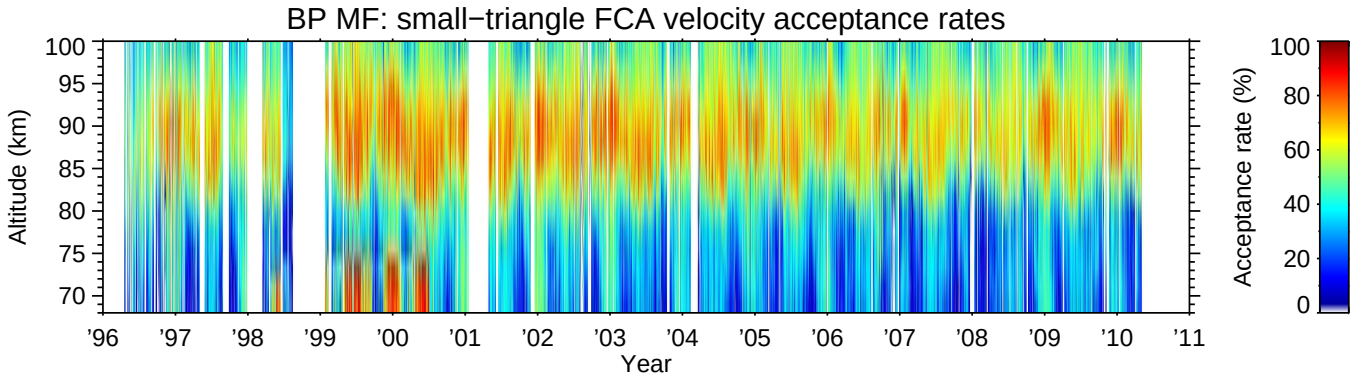

Fig. 4.2: Acceptance rates for the small-triangle FCA experiment. The rates shown have been computed on a 24-hour time and 2 km range grid.

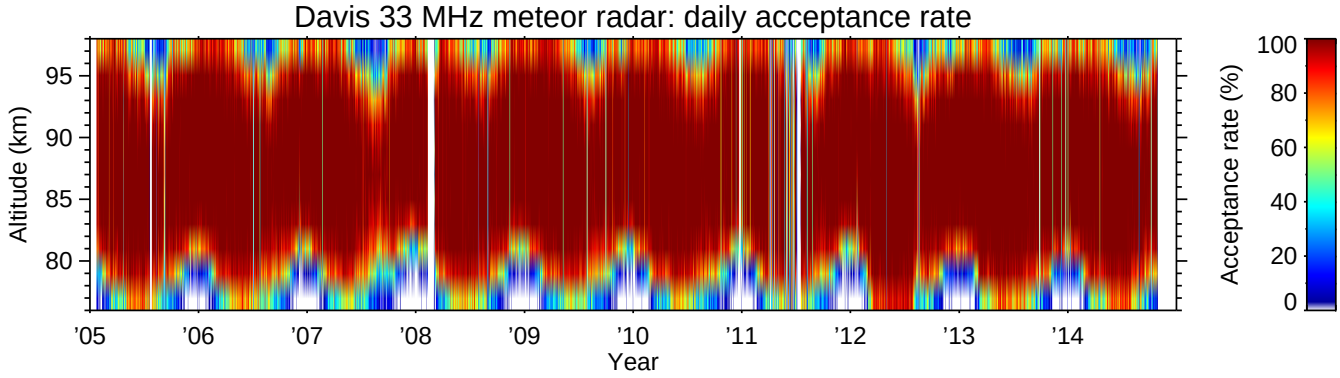

Fig. 4.3: Wind acceptance rates for the Davis 33 MHz meteor radar (for one-hour bins). The rates are shown on a 24-hour time and 2 km height grid.

4.3 Analysis technique

4.3.1 MF radar FCA velocities

True FCA horizontal velocities were extracted from records of typical length 112 seconds, and were firstly averaged into bins of length one hour, to be used subsequently in defining the mean wind, tidal and planetary wave fields in the vicinity of each record. Only velocities with no reported error (see Sect. 3.1) were included; despite this, some clear outliers in one or both of the component velocity distributions were often present. It is plausible that some of the outliers may have been a genuinely geophysical artefact (e.g. a result of transient turbulence and/or gravity wave activity). Attempting to distinguish between genuine and spurious velocity estimates was considered beyond the scope of this work, so in the interests of reducing the possibility of the corruption of individual hourly averages, a procedure needed to be devised to remove the outliers.

The procedure used was based on Principal Component Analysis. For each hourly time series, the covariance matrix of the component velocities,

$$\boldsymbol{R}_{uv} = \begin{bmatrix} \langle (u - \langle u \rangle)^2 \rangle & \langle (u - \langle u \rangle)(v - \langle v \rangle) \rangle \\ \langle (v - \langle v \rangle)(u - \langle u \rangle) \rangle & \langle (v - \langle v \rangle)^2 \rangle \end{bmatrix}, \tag{4.1}$$

was evaluated. The eigenvectors $\boldsymbol{v}$ of $\boldsymbol{R}_{uv}$, given by the solutions to $\boldsymbol{R}_{uv}\boldsymbol{v} = \lambda\boldsymbol{v}$ (where λ are the eigenvalues), are oriented along the axis of the data's so-called "error ellipse". Along this axis, the components of the data have zero correlation. The "error ellipse" can be constructed in parametric form as:

$$x(t) = \sigma \sqrt{|\lambda_0|} \cos t$$
$$y(t) = \sigma \sqrt{|\lambda_1|} \sin t\,,$$

where σ is the number of standard deviations the ellipse is to represent, and t is the parameter. In this study, the points falling outside this ellipse were removed from the analysis; this process was repeated until all remaining points were within the ellipse (see Fig. 4.4 for an example application). The value of σ was set to 2.5; an inspection indicated that doing so resulted in the removal of most "significant" outliers, without causing the method to iteratively remove all points considered; however, it is acknowledged that this selection is somewhat arbitrary.

Following the evaluation of hourly averages, the 112-second records were binned into windows of length 48 hours, with the centres of adjacent windows separated by 6 hours. The tidal and planetary wave fields for each bin were defined by least-squares fitting a sum of sinusoid functions with periods T = [1/3, 1/2, 1, 2] days (see Sect. 5.1.3 and eqn. (5.4)) to the hourly-averaged winds within 48 hours of the centre of the bin under consideration. The fits were subsequently subtracted from the 112-second wind estimates.

The bins were then partitioned into non-overlapping "continuous" segments greater than six hours in length. The "continuity" requirement was for there to be no temporal gap greater than an hour

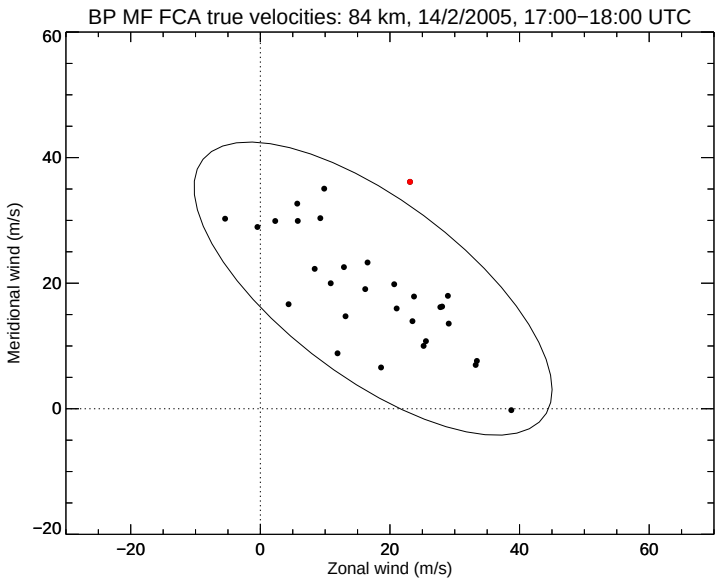

Fig. 4.4: Example of the outlier rejection procedure used in this study, on a randomly selected hour of measurements. The point outlined in red, which is outside the 2.5σ ellipse shown, would be rejected from the evaluation of the mean for each component.

in any segment longer than 6 hours. Two independent copies of the time series in each segment were then interpolated to a 10-minute grid, and were convolved with Kaiser filters in the time domain with bandpasses of [20,120] minutes and [120,480] minutes respectively. It was assumed that this convolution would produce time series with variances corresponding to gravity wave activity at the frequencies between the bandpasses. Average variances for each segment (and for each of the two filters) weighted by the number of points in the corresponding segments were then evaluated for the 48 hour window in question; this process was repeated across all windows. Finally, monthly- and seasonally-averaged winds and variances were computed from the 48-hour windows.

A minimum "continuous" segment length of six hours was chosen in the interests of satisfying two conflicting requirements: having a segment long enough to not substantially filter variations of timescales up to about eight hours, while not having a minimum segment length so large as to exceed typical scales of fluctuation in the FCA true velocity acceptance rates. As shown in Fig. 3.1, mean acceptance rates are significantly lower overnight than during the day at altitudes 80-90 km, and are essentially zero overnight below about 75 km, while still remaining above around 50% during the day down to altitudes of about 65 km. In general, this would make a minimum segment length of around (say) 12 hours impractical over most of the considered altitude range.

It should be noted that this procedure will lead to variances that are biased toward values at the times of largest acceptance rates for a given altitude (which, as discussed, will be towards values at day-time measurements). It is straightforward to avoid this source of bias in mean wind estimates—for example, Holdsworth and Reid [2004b] do so by averaging "two-minute" FCA winds into hourly and subsequently fortnightly bins with equal weights; the requirement for good time resolution generally makes this impossible for variance estimation though. To explain any long-term variance trends in the context of long-term wind variations, mean winds here are also computed over the same window

lengths, presumably with the same biasing present.

Following Hoffmann et al. [2012], the long-term trends in the seasonally averaged winds and variances were computed by solving a multivariate linear regression of the form

$$y = at + bF_{10.7} + c\,, \tag{4.2}$$

where y is the quantity under investigation, a, b and c are the regression coefficients, t is time, and $F_{10.7}$ is a proxy for the solar cycle phase (in this work, the Merged Solar Radio Flux at 10.7 cm has been used).[3] The regression was performed using IDL's in-built `regress` function, with a 1-sigma error estimate also evaluated for each coefficient.

A solar cycle correlation has been allowed for in the fits of both the winds and variances to ensure the consistency of the trend analysis with Hoffmann et al. [2011]. As an aside, a relationship between the zonal/meridional wind and the solar cycle has been suspected since Sprenger and Schminder [1969] found a positive correlation between them. However, as detailed reviews by Jacobi [1998] and Iimura et al. [2011] indicate, its form does not appear to be spatially or temporally consistent, with evidence of positive, zero and negative correlations reported across a variety of sites for different seasons. As for variances, no conclusive results have yet been reported, other than those in the very sparse observations indicated in Table 4.1.

4.3.2 Meteor radar radial velocities

Mean wind velocities were estimated from hour-long bins of data using the technique outlined in Sect. 2.2.2. Tidal and planetary wave fields were fitted to and subtracted from the hourly averages. The remaining analysis was essentially identical to that performed on the FCA winds, with the only distinction being the sole use of a [2,8] hour bandpass on a copy of the hourly-averaged winds prior to a variance calculation.

4.4 Results and discussion

4.4.1 Buckland Park MF radar

Climatologies of the mean winds determined as described above are shown in the upper panels of Fig. 4.5. Their features are quite typical for those of a mid-latitude site, as discussed in Sect. 1.1.1. Below about 80 km, the zonal winds are westward in summer and eastward in winter, transitioning around the equinoxes. The westward summer zonal winds decrease with altitude, and reverse to an eastward flow around 85 km. The eastward winter zonal winds decrease with altitude, but remain eastward at least to heights just above the mesopause. The meridional winds are significantly weaker than the zonal winds, and show a more complex variation with season and altitude. They are briefly equatorward during summer and generally poleward during the non-summer months.

The corresponding variances are shown in the middle and lower panels of Fig. 4.5. Across most of the height range examined, the variances in both period bands show a combination of an annual

[3] This is available at `http://lasp.colorado.edu/lisird/tss/noaa_radio_flux.html`.

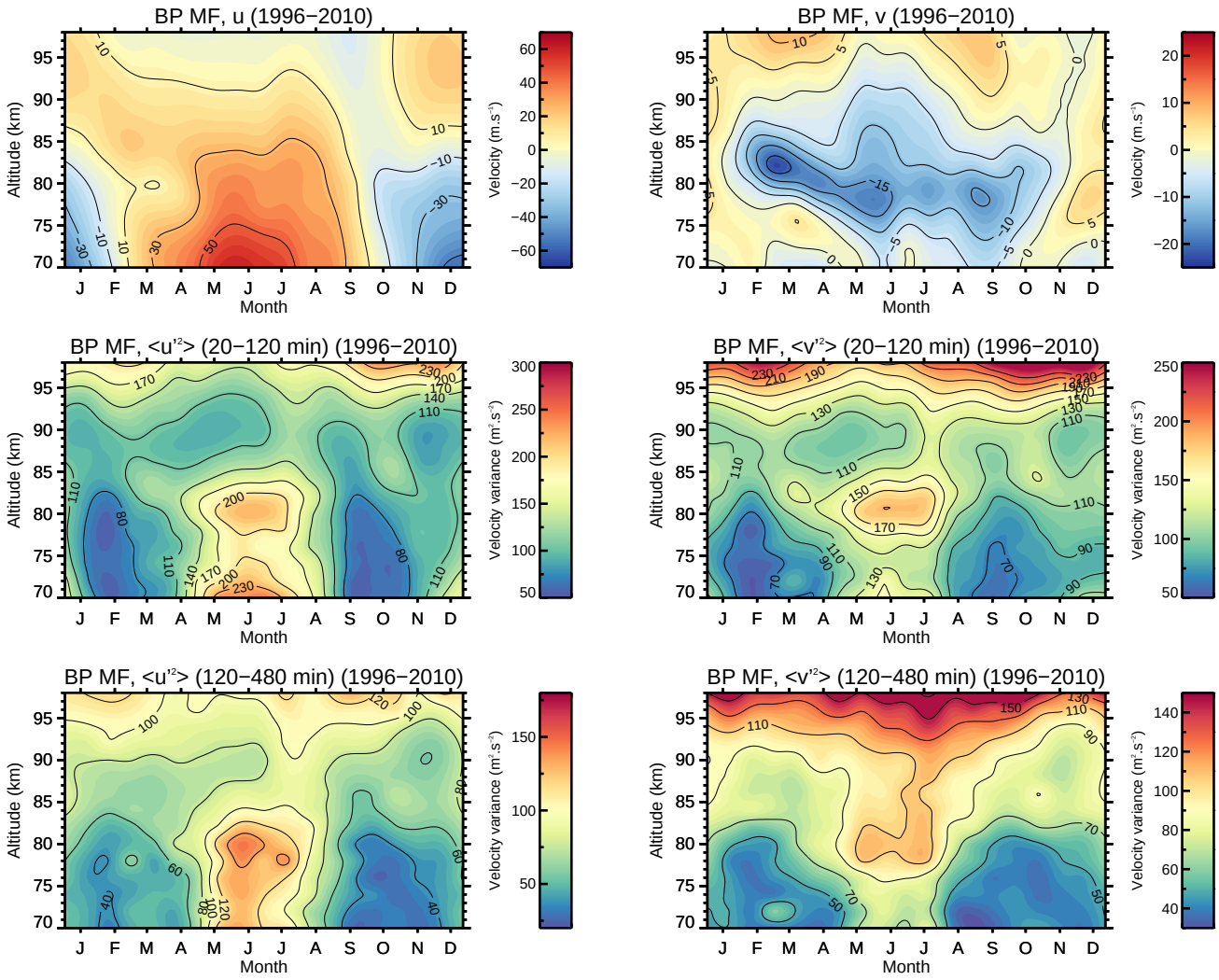

Fig. 4.5: 14-year climatologies of the "true" wind velocities (upper panels), shorter period gravity wave variances (middle panels), and longer period gravity waves (lower panels) for the small-triangle FCA data set. Each plot shows non-oversampled 20-day averages of the corresponding 48-hour averages wrapped into a single year, at 2 km height intervals.

and semiannual variation, with minima at the equinoxes and maxima at the solstices. The winter maximum is considerably larger than the summer maximum, especially below about 85 km. The zonal variances are also of the same order as the meridional. These features are largely consistent with those reported from climatologies of other mid-latitude sites, such as Juliusruh [Hoffmann et al., 2010] and Hawaii [Gavrilov et al., 2004].

The evaluated long-term and solar cycle regression coefficients for the mean winds are shown in Fig. 4.6. A noteworthy result here is the indication of a weakening of the summer, and especially winter, wind jets. The magnitude of the summer westward velocity decline reaches 0.6 ± 0.9 m.s^{-1}.yr^{-1} at 72 km, and the winter eastward velocity decline reaches 2.3 ± 1.4 m.s^{-1}.yr^{-1} at 74 km. The winter trend is remarkably consistent with altitude; only above 88 km does it become statistically insignificant. The summer zonal trend becomes negative above about 90 km, which implies a deceleration of the

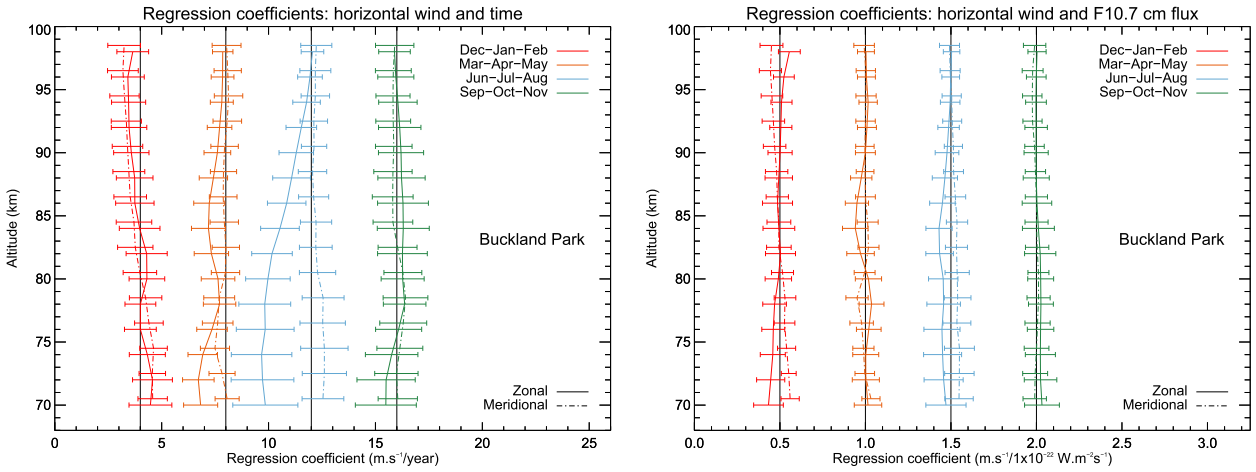

Fig. 4.6: Evaluations of the regression coefficients a (time, left panel) and b (solar flux, right panel) for the zonal and meridional winds at Buckland Park. The profiles for different seasons have been translated horizontally. The error bars shown correspond to 1σ error estimates.

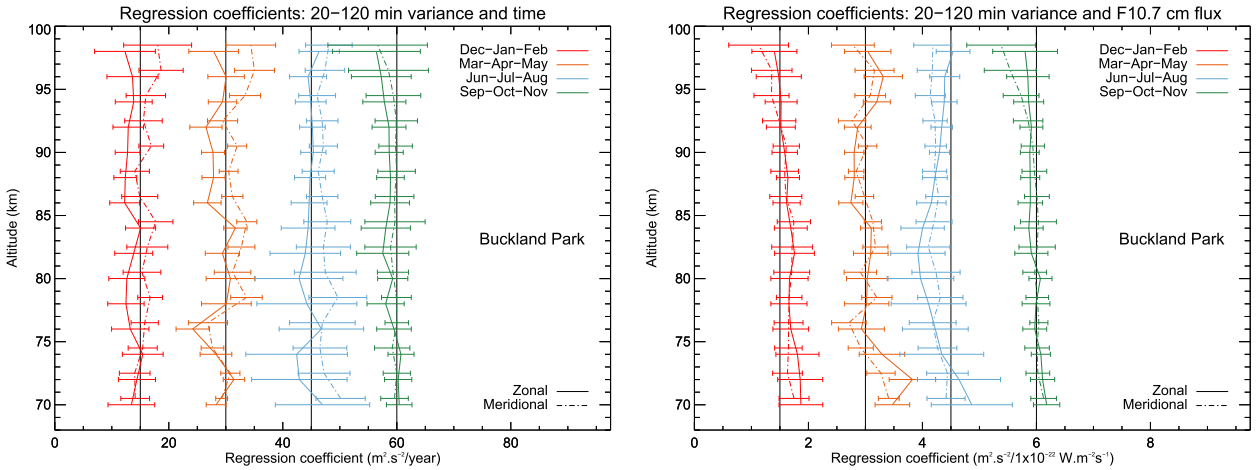

Fig. 4.7: As per Fig. 4.6, but for variances in the period range 20-120 minutes.

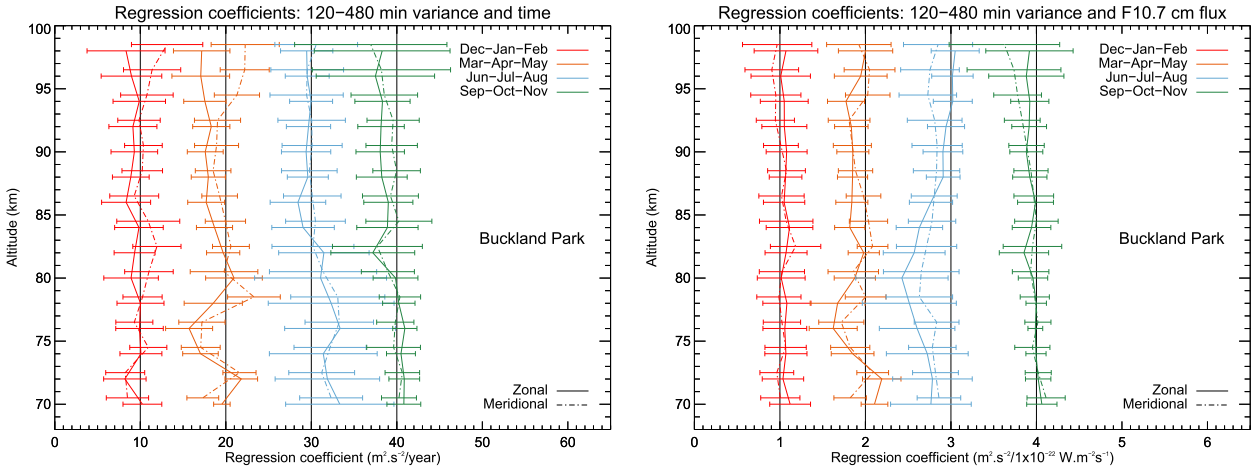

Fig. 4.8: As per Fig. 4.6, but for variances in the period range 120-480 minutes.

"lower thermospheric" eastward wind at these heights. Statistically significant trends are also noted in the autumnal equinox wind velocities around 70 km, though are less relevant given the rapid seasonal variation of the daily mean wind velocity at this time. No consistent significant trends are seen in the meridional velocities, nor is there evidence of a consistent relationship between either of the velocity components and the F10.7 cm flux.

Regression coefficients for the short (20-120 minute) and long (120-480 minute) period variances are shown in Figs. 4.7 and 4.8 respectively. The trends in summer short period zonal component are generally of a decreasing (though insignificant) nature; the maximum decrease reached is 2.5 ± 3.2 $m^2.s^{-2}.yr^{-1}$ at 80 km. The meridional result does not appear to be consistent with altitude. The trends in winter, though not significant over any extended height range, appear to be of an increasing nature, especially in the meridional component. The winter variances, in both period bands, appear to be negatively correlated with the F10.7 cm flux around 80 km. No such significant correlation is noted in any of the other components across an extended altitude range.

The cause of the winter wind trends is not clear at present. Interestingly, the summer zonal wind and variance trend results are of the opposite sign to those reported in Hoffmann et al. [2011]. Applying the inverse of their argument, it may be that the decreased westward winds around 70-75 km have preferentially removed more eastward propragating gravity waves from the spectrum, and consequently reduced the wave variance above (since eastward propagating waves are expected to dominate the mesospheric spectrum during summer). This would also imply a decreased eastward wave drag in the wave dissipation regime (above $\sim$ 85 km), which the wind results appear to show evidence of. Unfortunately, it is likely that some of the day-time results above $\sim$ 90 km have been contaminated by total reflection and/or group retardation (e.g., Reid [2015]). If this is true, the velocity estimates would not be representative of the mean wind velocity. Before this has been examined, the trends at these heights cannot be assumed valid.

4.4.2 Davis station VHF meteor radar

Climatologies of the mean winds and variances from the Davis 33 MHz meteor radar are shown in Fig. 4.9. The qualitative features of these are largely similar to those of the high-latitude MF radar climatologies presented in Dowdy et al. [2007]. The winds (upper panels) below about 90 km are westward in summer and eastward during winter, with an abrupt transition around the equinoxes. The reversal of the summer mean winds appears to occur a few km higher here than it does at Buckland Park. There is also very little decrease in the eastward wind velocity with altitude during winter. The meridional wind is considerably weaker than the zonal wind, and equatorward during much of the year, this being strongest during summer. It reverses to a poleward wind, predominantly above 86 km, during winter. Both components of the 2-8 hour gravity wave variances show what appears to be a semiannual variation across most of the observed height range, with minima around the equinoxes and maxima at the solstices. As with Buckland Park, the winter solstice maximum is much stronger than the summer maximum.

The temporal and solar cycle regression coefficients for the horizontal winds are shown in Fig. 4.10.

A significant decrease in the zonal wind during summer is apparent, peaking at -1.6±1.3 m.s^{-1}.yr^{-1} around 89 km. This occurs approximately at the same height as that of the reversal of the wind from westward to eastward. There also appears to be a significant positive correlation between the zonal wind and the F10.7 cm flux during summer. No significant trends or solar cycle correlations are seen during any other seasons. There are no significant trends in the 120-480 minute variances (Fig. 4.11), although there is possible evidence of a decrease below about 87 km during summer. There is no solar cycle correlation of note in the variances.

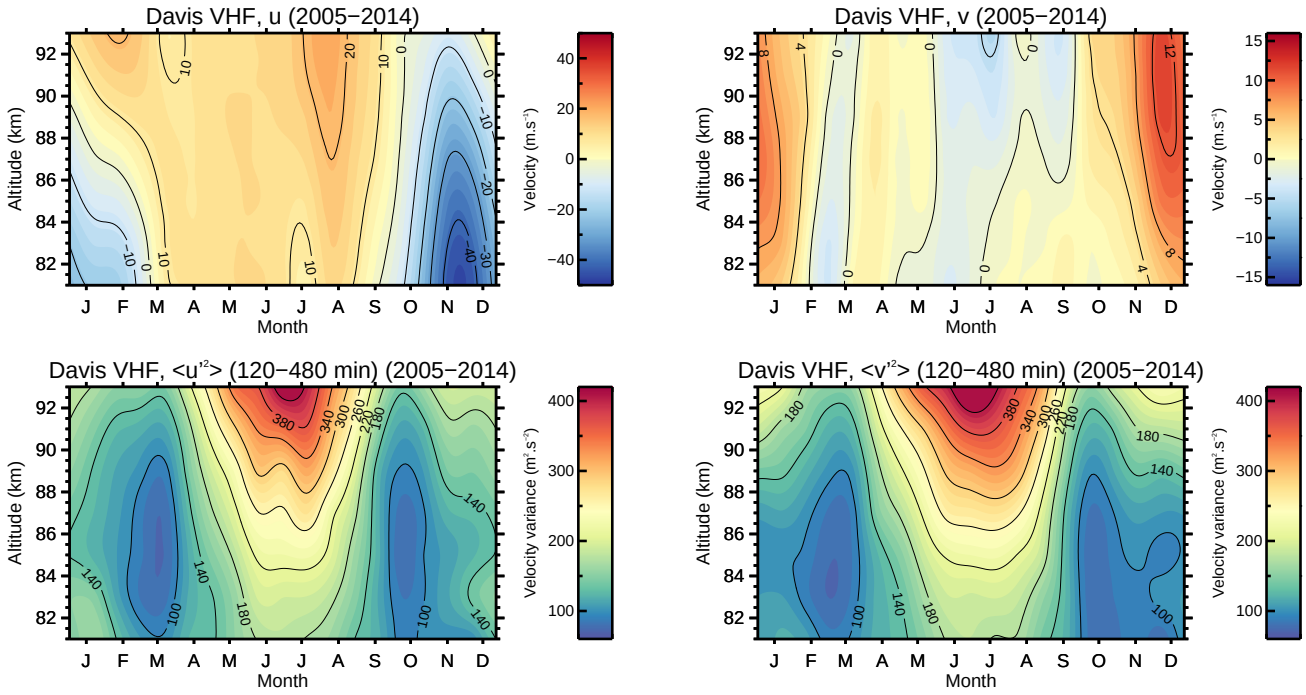

Fig. 4.9: As per Fig. 4.5, but for the Davis 33 MHz meteor radar.

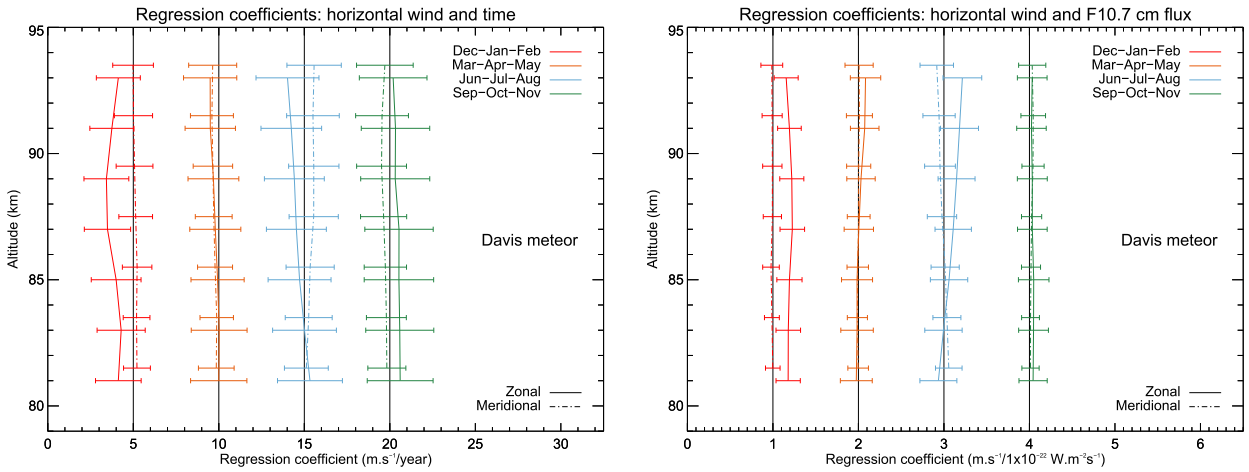

Fig. 4.10: As per Fig. 4.6, but for the 33 MHz meteor radar at Davis.

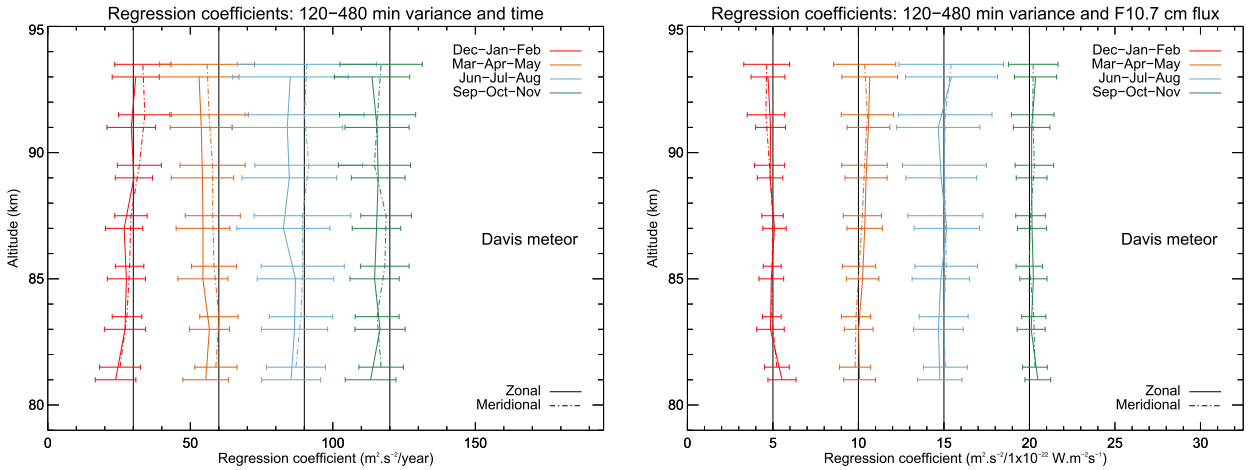

Fig. 4.11: As per Fig. 4.10, but for variances in the period range 120-480 minutes.

4.5 Summary and recommendations for future work

The long-term trends and solar cycle influence in MLT-region winds and gravity wave variances derived from routine Buckland Park MF radar FCA (1996-2010, using a small receiver triangle) and 33 MHz meteor radar data from Davis (2005-2014) have been investigated. The Buckland Park data indicates a reduction in the velocities of the summer and winter jets from 70-80 km, and possibly a reduction in the zonal variances during summer. The winter variances between about 80 and 85 km show a negative correlation with the F10.7 cm solar flux; at other heights and during other seasons, no consistent solar cycle correlation is observed. At Davis, the summer zonal velocity between 85 and 90 km is seen to decrease, and between about 80 and 95 km, to be positively correlated with the solar cycle. In both components of the winds and variances, there appears to be no evidence of a solar cycle correlation during any other seasons.

The trends observed during summer at Buckland Park are opposite to those reported for Juliusruh in Hoffmann et al. [2011]. It is not known if the inverse of their explanation for their observations applies here (that is, whether or not the observed eastward summer wind trend has filtered more eastward propagating gravity waves from the spectrum and subsequently reduced the variance above). More widespread study of the long-term trends in winds and associated wave variances is recommended, although it is unclear if consistent long-term trends in either of the parameters will emerge.

A next step for the Buckland Park study is to ensure the consistency of these wind and variance trends by comparing them with those deduced from the FCA performed with larger receiver separation. The older observations (dating back to 1973) recorded on a small receiver triangle should then be assimilated into the data set presented here.

With regard to the Davis 33 MHz meteor radar study, an MF radar at the same location has also supplied a long-term (1994-present) data set of FCA velocities. These should ultimately be compared to those from the meteor system. Difficulty in reconciling the polarization used on the Davis MF radar [private communication, D. J. Murphy, June 2015] has resulted in these data not being shown here.

It should also be noted that other techniques for trend estimation (which go beyond simple mul-

tivariate linear regression) are available and have been applied in the past to time series similar in nature to those considered here. For example, Merzlyakov et al. [2009] and Portnyagin et al. [2006] applied autoregressive techniques to several MLT-region wind time series to determine the timing of statistically significant "structural changes" in the long-term trends. Such analyses have suggested that apparently stable wind trends in the MLT may periodically change sign, and may exhibit different levels of correlation with certain parameters in the lower atmosphere (e.g. the Southern Oscillation Index) depending on the trend sign. This analysis employed in this Chapter should ultimately be extended in a similar way.

Chapter 5

Modelling of RST component extraction techniques

To correctly interpret Reynolds stress tensor component measurements from the aforementioned radar techniques, it is crucial to know the magnitude of the likely biases in the estimates, and the dependence of the biases on the geophysical conditions and temporal/spatial sampling distribution. A number of recent computer simulation studies (see below) have quite exhaustively clarified these quantities for the meteor radar technique. However, no such analyses exist for the 5-beam or vertical-beam HDI techniques.[1] Hence it is not clear at this point if the fluctuations observed in the beam position (see, e.g., Sects. 3.3 or 6.3.2) will have a detrimental effect on the analysis.

To this end, a simple computer model of the 5-beam Doppler and vertical-beam HDI radar techniques has been created, in which monochromatic gravity and tidal waves with known parameters are propagated over the field of view of a "radar", which samples radial wind velocities with spatiotemporal distributions of the respective radar techniques. An identical assessment of the meteor radar technique, using recorded spatiotemporal distributions from the Buckland Park meteor radar, has also been performed. The approach used has parallels to those used in recent modelling assessments of the meteor and incoherent scatter radar techniques, as follows:

- Fritts et al. [2010a], who evaluated the abilities of a new meteor radar on Tierra del Fuego (53.8°S, 67.8°W) to measure gravity wave momentum fluxes. The wind fields simulated included mean winds, diurnal and semidiurnal tides, and propagating gravity waves with variable phase angles and time-varying amplitudes, and the scattering locations used were based on observed meteor distributions;

- Fritts et al. [2012a], who employed the same tests as Fritts et al. [2010a] on a new meteor radar on King George Island (62.1°S, 58.7°W), and three more conventional meteor radars;

- Andrioli et al. [2013a], who employed tests similar to those in Fritts et al. [2010a] (tides with finite vertical wavelengths and 2-day Rossby waves were also included) on a meteor radar in Cachoeira Paulista (23°S, 14°W);

[1] It should be noted that Murphy [1992] used a time-varying wind field to simulate the effects of pointing angle variations on momentum flux extraction capability of the 5-beam Doppler technique, although he only considered the case of a single gravity wave, and assessed only the Vincent and Reid [1983] estimator.

- Nicolls et al. [2012], who applied an approach similar to that used in Fritts et al. [2010a] to narrow-beam fixed-look phased array radars;
- Vincent et al. [2010], who used a Monte Carlo-based simulation of monochromatic gravity waves with random phases, propagation directions and amplitudes to assess the ability of a meteor radar to measure mean winds and momentum fluxes;

This chapter describes the implementation of the model and the utilised test wind fields, and discusses the implications of the quality of the recovered parameters from the respective techniques. Particular attention is given to the recovered vertical fluxes of horizontal momentum.

5.1 Model description

The model follows the following basic workflow (the steps are described in more detail in the subsequent subsections):

1. Specify a wind field analytically;
2. Acquire an ensemble of scattering positions and times (and add Gaussian-distributed uncertainties to a copy of the positions);
3. Evaluate radial projections of the wind velocity at the *non*-noise-influenced positions/times;
4. Evaluate the RST components by inverting the fluctuating radial velocity components at the noise-influenced positions/times;
5. Evaluate the RST components "directly" using the variances/covariances of the wind field at some arbitrary fixed position;
6. Loop back to 1., and repeat for a different realization of the wind field/different uncertainties in the scattering positions;
7. Investigate the mean and standard deviation of the biases between the results of 4. and 5.

5.1.1 Wind field specification

The wind field in the model is composed of a fixed background velocity (resembling a "mean flow") and a superposition of linear waves (which can resemble gravity, Rossby or tidal waves). It is parameterized in space and time as the velocity vector:

$$\boldsymbol{v} = \overline{\boldsymbol{v}} + \sum_{i=0}^{n-1} \boldsymbol{v}_i' \sin\left(\boldsymbol{\kappa}_i \cdot \boldsymbol{r} - \omega_i t\right) , \tag{5.1}$$

where $\overline{\boldsymbol{v}} = [\overline{u}, \overline{v}, 0]$ is the fixed background velocity vector, n is the number of included waves, $\boldsymbol{v}_i' = [U_i, V_i, W_i]$, $\boldsymbol{\kappa}_i = [k_i, l_i, m_i]$ and ω_i are the vectors of component wave amplitudes, wave vectors and angular frequencies respectively for the i^{th} wave, $\boldsymbol{r} = [x, y, z]$ is the Cartesian position vector, and t is the time since some arbitrary zero.

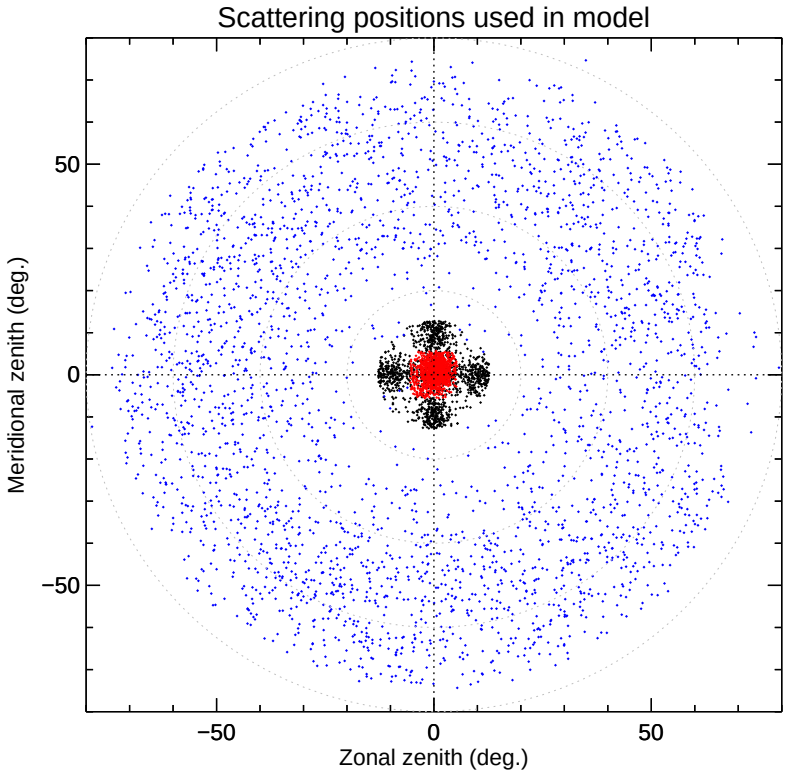

Fig. 5.1: A 48 hour sample of scattering position data used in the model (black: 5-beam Doppler, red: vertical Doppler, blue: meteor). See text for details.

Prior to a simulation, the background wind vector, the number of waves to include, and the horizontal perturbation amplitude v_h, propagation direction ϕ, ground-based phase speed c_p, and ground-based period T for each wave are specified. The remaining parameters in (5.1) are computed using the dispersion and polarization relations (shown in Appendix C). The radial component of the wind field is then evaluated at a set of positions (scattering locations) and times corresponding to those recorded in real samples of Buckland Park MF Doppler/VHF meteor radar measurements (see Fig. 5.1). For simplicity, the wave parameters are evaluated and re-sampled at a fixed height. A "flat-Earth" coordinate system is also assumed, so that

$$\boldsymbol{r}_j^{\mathrm{T}} = \begin{bmatrix} z \tan\theta_j \sin\phi_j \\ z \tan\theta_j \cos\phi_j \\ z \end{bmatrix} , \tag{5.2}$$

where j represents the position index, and θ and ϕ are the usual definitions of zenith and azimuth of the scattering locations.

5.1.2 Scattering locations

1.98 MHz 5-beam Doppler technique

As will be described in more detail in Sect. 6.3.1, during the 1997 and 1998 experiments this technique involved the transmission of a single vertical beam and four off-zenith beams (nominally at

azimuth angles corresponding to the Cardinal directions), each with a half-power half-width of 5.7°. The radar maintained a fixed pointing direction during each analysis interval and iterated to the next beam at the start of the subsequent interval, with an analysis interval length of two minutes. HDI was applied to the acquired raw data to estimate EBPs; the EBPs at a range of 88 km from the June 1998 experiment have been used as input "scattering positions" in the model for this technique. The temporal order of the points was preserved, in hope to best account for the effects on the beam position of structures in electron density propagating over the radar's field of view.

Since only data with zero error code (see Sect. 3.3) were selected, some of the points in the resulting dataset were missing. To fill in these gaps and hence make the off-vertical beam dataset "continuous" (i.e., to have the four beams present in each 10-minute steering cycle) the azimuth angles of the off-vertical beams were firstly wrapped to a common origin (by subtracting from them their nominal azimuth angle). The "wrapped positions" were then assigned to the four off-vertical beams in temporal order, and were unwrapped by re-adding the nominal azimuth angle of the beam the position had been assigned to. The vertical beam positions were simply assigned to subsequent two-minute records in their temporal order.

A configuration solely utilizing data acquired from the vertical beam was also considered in the model. This resembles an analysis that could be applied on systems with no (practical or otherwise) capability for beamsteering on transmission. Experimental data of such a form is also considered in Chapter 6. Vertical transmission in that experimental case was only applied for two minutes per 10-minute steering cycle, and so a 10-minute analysis interval has been used to represent it here.

1.98 MHz vertical beam Doppler technique

From April 1997 through to January 1998, outside of 5-beam Doppler campaign periods, FCA and HDI analyses were applied to the raw data from (solely) vertically transmitted beams, with a two-minute analysis interval. The HDI-derived EBPs at a range of 88 km from 20-Jun 1997 to 15-Jul 1997 have been used as scattering positions to model this technique. As per the vertical beams from the 5-beam technique, the temporal order of the positions was preserved. Once again, the data were derived from beams with a half-power half-width of 5.7°.

55 MHz all-sky meteor technique

This radar transmitted an all-sky beam, and during 2014 and 2015 attained a maximum average count rate of around 60 hr^{-1} 2 km^{-1} bin at the peak of the meteor distribution. Unlike, for example, the SAAMER and DrAAMER radars discussed in Fritts et al. [2012a] and the Trondheim Meteor Radar discussed in de Wit et al. [2014a], this radar was not originally designed to obtain a large number of meteor detections near the zenith, and so in this respect closely represents more traditional meteor radar systems. The distribution on average peaked at a zenith angle of about 54°.

Effective beam position data with zero error code recorded during May 2014 at altitudes between 88 and 90 km were used as scattering positions in the model for this technique.

"Naïve" 5-beam Doppler technique

The only reported MF 5-beam Doppler momentum flux estimates in the literature do not incorporate direct estimates of the EBP. They are referred to here as "naïve" because the EBP was either assumed equal to the apparent beam position (e.g., Vincent and Reid [1983]), or estimated indirectly but with no consideration given to its temporal variability (e.g., Fritts and Vincent [1987], who inferred the EBP from the mean ratios of Doppler and SA wind velocities; Reid and Vincent [1987], who estimated the EBP using multi-site climatological values of aspect sensitivity; and Murphy and Vincent [1993], who used co-located values of aspect sensitivity calculated from the SA-derived pattern scale.). In this work, the model of the "naïve" analysis uses radial velocities evaluated at the same positions and times as those in the standard 5-beam Doppler technique, but they are assumed to be located at fixed zenith angles in the appropriate Cardinal directions. The fixed zenith used here was 9°, which was evaluated from eqn. (3.11) by assuming an apparent beam direction of 12°, a beam half-power half-width of 5.7° and an aspect sensitivity of 10°.

Errors

Errors of the form

$$\begin{bmatrix} \epsilon_{xj} \\ \epsilon_{yj} \end{bmatrix} = \sigma\,\theta_j \begin{bmatrix} \epsilon_1 \sin\phi_j \\ \epsilon_2 \cos\phi_j \end{bmatrix} , \tag{5.3}$$

where ϵ_{xj} and ϵ_{yj} are the errors along the x- and y-direction cosines respectively, ϵ_1 and ϵ_2 are two numbers drawn from a Gaussian distribution with unit variance, and σ is the desired standard deviation of the distribution, are added to the direction cosines of each scattering position. A σ value of 1° is used to represent the meteor technique (see discussion on page 32). The wind field is evaluated at the points without the error, and in the inversions described in the subsequent section, they are interpreted to be at locations corresponding to the positions *with* the added error.

There currently exists no estimate of the EBP errors that would be obtained from an application of PSS/HDI to Buckland Park MF radar data. An attempt was made by Klövekorn [1992] to directly measure the phase errors at individual antennas due to their mutual coupling, although this proved inconclusive[2]. To provide a crude estimate of the EBP error for this work, a basic simulation of the AOA measurement procedure of the Buckland Park MF array was created. It takes as an input a single representative estimate of the phase measurement error of all antennas in an arbitrary receiver configuration. These errors are added to the phases that would be measured by the spatially separated antennas of the configuration, were a single plane wave with arbitrary propagation direction to be

[2]Briefly, Klövekorn [1992] set up an experiment on the Buckland Park MF array in which a given signal could be received on a group of antennas at exactly the same time (i.e., so that each antenna would ideally measure an equal phase). The "instrumental" phase errors were deduced by summing the phase delays relative to one of the antennas around a closed loop of antennas (in the absence of phase measurement error, they would sum to zero). In doing so, phase errors between 0.02° and 8° were determined for different summation paths. It was postulated that these errors *may* have been representative of the true phase estimation error, but that a more detailed analysis was clearly needed.

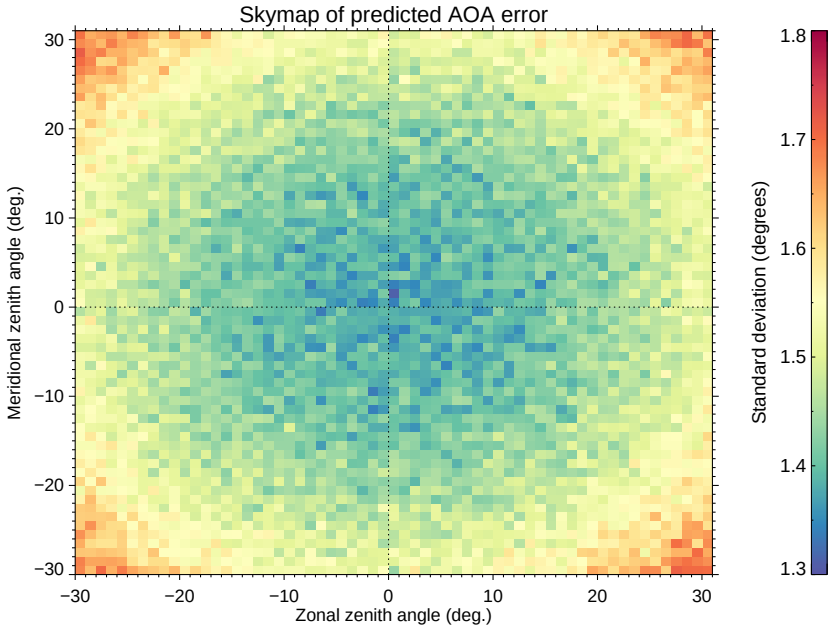

Fig. 5.2: A rough estimation of the 1-sigma error that would be obtained in AOA measurements using the Buckland Park MF radar. See text for details.

incident on the array. The spatial distribution of phase differences is then used to estimate the wave propagation direction (i.e., the "AOA") by least-squares inversion of eqn. (3.17). A grid of wave propagation directions is iterated over, and a number of realizations of phase errors for each antenna are used at each grid point.

Fig. 5.2 shows the standard deviation in each AOA sample, for Gaussian-distributed phase errors of standard deviation 20°, and a receiver configuration corresponding to that in Fig. 6.1 (which was used in the 1997-1998 Doppler experiments). This phase measurement error distribution was chosen to approximately replicate the distribution of the cross-correlation phases of antenna pairs shown in Fig. 2.7. 1000 realizations of antenna phase errors were used here to compute the standard deviation in the AOAs at each grid point. For this phase measurement error distribution, it can be seen that AOA errors of standard deviation 1.3-1.4° will occur around the zenith, and will increase rather uniformly with zenith angle.

On this basis, a σ value of 1.5° has been used to represent (an upper estimate of) the uncertainty in the scattering location of MF Doppler measurements. This figure is strictly preliminary, and it is stressed that more effort needs to be channeled into measuring it directly, before the results presented in this Chapter can be considered to be truly representative of the Buckland Park MF's EBP measurement capability.

Radial velocity measurement uncertainties have not yet been incorporated in this model.

5.1.3 Estimation of RST components

The spatial distribution of radial velocities at this point will contain contributions from the gravity and tidal waves specified in eqn. (5.1). Contributions from the latter are not desired in the RST component estimates here (see Sect. 1.1.1 for details). To remove them, a method similar to that

devised in Andrioli et al. [2013a] is applied; it firstly involves estimating the "background mean" wind field, by partitioning the radial velocity data into non-oversampled windows of width one hour. Eqn. (1.4), in a modified form accounting for shears in the wind field, is then inverted for each window. The tidal wave contributions are removed from each radial velocity by subtracting from them a time-dependent radial projection of a least squares fit to the resulting "background mean" wind time series y of the form:

$$y = \sum_{i=0}^{n-1} \cos \frac{2\pi}{T_i}(t - \phi_i)\,, \tag{5.4}$$

where T is an n-element array of periods (in this work, [1/3, 1/2, 1, 2] days) and ϕ is an n-element array of phases (in this case giving the time at which the ith component maximises). It should be acknowledged that Fritts et al. [2010a, 2010b, 2012a, 2012b] used an "S-transform" Gaussian wavelet fit to estimate diurnal and semidiurnal tidal components from meteor radar time series. While this approach does allow for amplitude and phase modulation of the tidal components in the time series, the Andrioli et al. [2013a] approach is applied here on the basis of the ease of its implementation.

The RST components are then estimated from the residuals by inversion of eqn. (1.7); i.e., the technique of Thorsen et al. [1997]. Note that the selection of the length of data over which this inversion is to be applied is clearly a compromise of increasing time resolution (shorter windows) and correctly sampling longer-period and/or larger scale fluctuations (favouring longer windows). The effect of the data length on the bias in the returned RST component estimates was tested and is discussed in Sect. 5.3.

5.2 Test cases

Two different wind field "configurations" have been used in the model, and are summarized in Table 5.1. The first case considers a single gravity wave of horizontal amplitude 20 m.s^{-1} propagating to the North-East; all RST components will take on non-zero values, with $\frac{\langle u'^2\rangle}{\langle v'^2\rangle} \approx 2$, and $\frac{\langle u'^2\rangle}{\langle w'^2\rangle} \approx 30$ over the periods considered. The horizontal and vertical perturbation components will also be out of phase (as $m \propto -\sqrt{k^2+l^2}$, and $k, l > 0$)—i.e. $\langle u'w'\rangle, \langle v'w'\rangle < 0$. The second case considers an ensemble of 37 smaller-amplitude waves propagating in uniformly-distributed directions in the Eastern sector; here only $\langle u'^2\rangle$, $\langle v'^2\rangle$, $\langle w'^2\rangle$ and $\langle u'w'\rangle$ will take on non-zero values, with $\frac{\langle u'^2\rangle}{\langle v'^2\rangle} \approx 1$, and $\frac{\langle u'^2\rangle}{\langle w'^2\rangle} \approx 15$. The waves will have a net propagation direction due East, so $\langle u'w'\rangle < 0$. The two configurations are intended to emulate the limiting cases observed in real mesospheric wind fields: the first obviously a case in which a single well-defined monochromatic wave dominates the spectrum, and the second in which a spectrum of equal-amplitude waves from an isotropic source propagate with component directions opposite to that of the background wind.

With exception to the final case discussed (Fig. 5.8), the simulations were performed over a sequence of gravity wave periods, so as to test the sensitivity of the techniques to waves of differing scales. A total of 200 realizations were performed at each period, in order to obtain a distribution of the measured RST component biases. At the start of each realization, the initial phases of all waves

Case	v_0 (m.s^{-1})	ϕ_0 (°)	n_{waves}	v_h (m.s^{-1})	ϕ (°)	c_p (m.s^{-1})
1	30	45	1	20	55	50
2	0	-	37	$[3_1, ..., 3_{37}]$	$[0_1, 5_2, ..., 180_{37}]$	$R_1 \times [50_1, ..., 50_{37}]$

Table 5.1: A summary of the gravity wave parameters used in the different test wind field cases. The subscript i on a given parameter denotes the value of the parameter for the ith wave in a specific case. R_1 refers to a random number derived from a uniform probability distribution with bounds $[1, 2]$. The remaining quantities are defined in Sect. 5.1.1.

considered were assigned a random value in the interval [0,2π). In the case of the second configuration, the periods of each of the 37 waves in a given realization were varied slightly, by obtaining periods from the equation $T_i = R_2 \times T_i$, with R_2 being selected from a uniform distribution with bounds ($\frac{3}{4}$,$\frac{5}{4}$). This was essentially done to make the wave field more "random". The phase speeds of the waves in the second configuration were determined as indicated in Table 5.1.

In each realization, diurnal and semidiurnal tides with fixed amplitudes of 15 and 20 m.s^{-1} respectively were also superposed onto the wind field. Their horizontal wavelengths and phase speeds were adjusted to resemble those of real atmospheric tides (i.e., with horizontal wavelengths equal to the ratio of the Earth's circumference and the tidal mode number, and phase speeds such that a full cycle of a given tidal component would be completed in the ratio of 24 hours and the tidal mode number). The spatial variability of the tides was included so that the tide-induced bias of the RST components (particularly those derived from the meteor technique) could be inferred (it is assumed that the subtraction of the fit in eqn. (5.4) will remove most of the temporal variability).

5.3 Results and discussion

5.3.1 Single gravity wave

The biases between the 5-beam Doppler (herein 5BD) and meteor "true" and estimated RST components for a wind field with a single gravity wave (Case 1), plotted against the gravity wave's period, are shown in Fig. 5.3. Each panel shows a mean value of the "true" components across all the periods examined. Each result is the average of all 2-hour blocks in a 48-hour time series, over 200 wave field realisations and scattering position errors. The error bars shown depict the standard deviation in the bias of the estimates across all samples. On the whole, it is clear for such a wave field that both techniques will statistically measure the sign of all RST components correctly, although there are some noteworthy deficiencies.

The 5BD technique estimates vertical variance ($\langle w'^2 \rangle$) with good precision and horizontal (co)variances ($\langle u'^2 \rangle$, $\langle v'^2 \rangle$, $\langle u'v' \rangle$) with comparatively poor precision. This is clearly a consequence of the relative radial weighting of said components in the distribution of the technique's sampling locations. The performance of the meteor technique is much the opposite, which is likely due to the fact that position of its samples are centred on much higher zenith angles. As an aside, a number of other EBP

uncertainties for the Doppler techniques were trialled (not shown here), and it was determined that the underestimation scales with the magnitude of the uncertainty.

The 5BD technique also substantially underestimates $\langle u'^2 \rangle$, $\langle v'^2 \rangle$, $\langle u'v' \rangle$, and this underestimation increases with the gravity wave period (and hence spatial scale, for a fixed phase speed). The meteor technique slightly underestimates these horizontal components, and tends to quite substantially overestimate $\langle w'^2 \rangle$.

The relative performance of the techniques appears to be similar for vertical fluxes of horizontal momentum ($\langle u'w' \rangle$, $\langle v'w' \rangle$), with the 5BD generally obtaining better precision. However, the 5BD has a tendency to underestimate these components, especially at low and high gravity wave periods.

Noting the form of the uncertainties applied to the EBPs of these techniques, it is straightforward to explain their underestimation of horizontal variances and momentum fluxes, and overestimation of vertical variances. Considering a two-dimensional case of solely zonal and vertical motions, eqn. (1.7) can be rearranged to give $V'^2_{rad} = \langle u'^2 \rangle \sin^2\theta + \langle w'^2 \rangle \cos^2\theta + \langle u'w' \rangle \sin 2\theta$. Adding Gaussian-distributed noise to θ will clearly increase $\langle |\theta| \rangle$, for small θ. If V'^2_{rad} is valid for the correct position (i.e., without the positional noise), $\langle \sin^2\theta \rangle$ and $\langle \sin 2\theta \rangle$ will be erroneously large, and $\langle \cos^2\theta \rangle$ erroneously small. On inversion, the obtained estimates for the coefficients of these terms will be erroneously small and large, respectively.

The 5BD technique also appears to obtain very low accuracy and precision when the wave period considered does not sufficiently exceed the time taken for a full 5-beam cycle (10 minutes). This likely indicates an aliased sampling of the wave field.

5.3.2 "Spectrum" of waves

5BD and meteor technique biases for a spectrum of waves propagating in the Eastern sector (Case 2) are shown in Fig. 5.4. Estimates are a product of the same sampling scheme (24 2-hour windows, 200 realizations per period) as in Fig. 5.3. Overall, there appears to be considerably more variability in the biases for both techniques, relative to the monochromatic wave case.

Again, the 5BD technique substantially underestimates $\langle u'^2 \rangle$ and $\langle v'^2 \rangle$, and slightly overestimates $\langle w'^2 \rangle$. No RST components derived using the meteor technique appear to be biased, although precision is poor, notably for $\langle u'w' \rangle$ and $\langle v'w' \rangle$; it appears that the technique will statistically not even measure fluxes of the correct sign. The 5BD estimates $\langle u'w' \rangle$ and $\langle v'w' \rangle$ with relatively good precision, although it does suffer from an underestimation of the non-zero $\langle u'w' \rangle$. It is also interesting to note that the precision of the 5BD technique tends to increase with wave period, whereas the opposite is seen for the meteor technique.

The increase in bias standard deviations with complexity of the wave field (i.e., comparing the results of the Case 1 and 2 wave fields) are consistent with results reported in Vincent et al. [2010], Fritts et al. [2012a], and Andrioli et al. [2013a] for the meteor technique, and those postulated in Nicolls et al. [2012] for the Poker Flat ISR (which considered scattering at fixed positions at zenith angles $< 20°$). It is likely that this is a result of the failure of the assumption of statistical homogeneity of the wind field over the area (or volume) under investigation (see Sect. 1.2, pp. 13 for details). Given

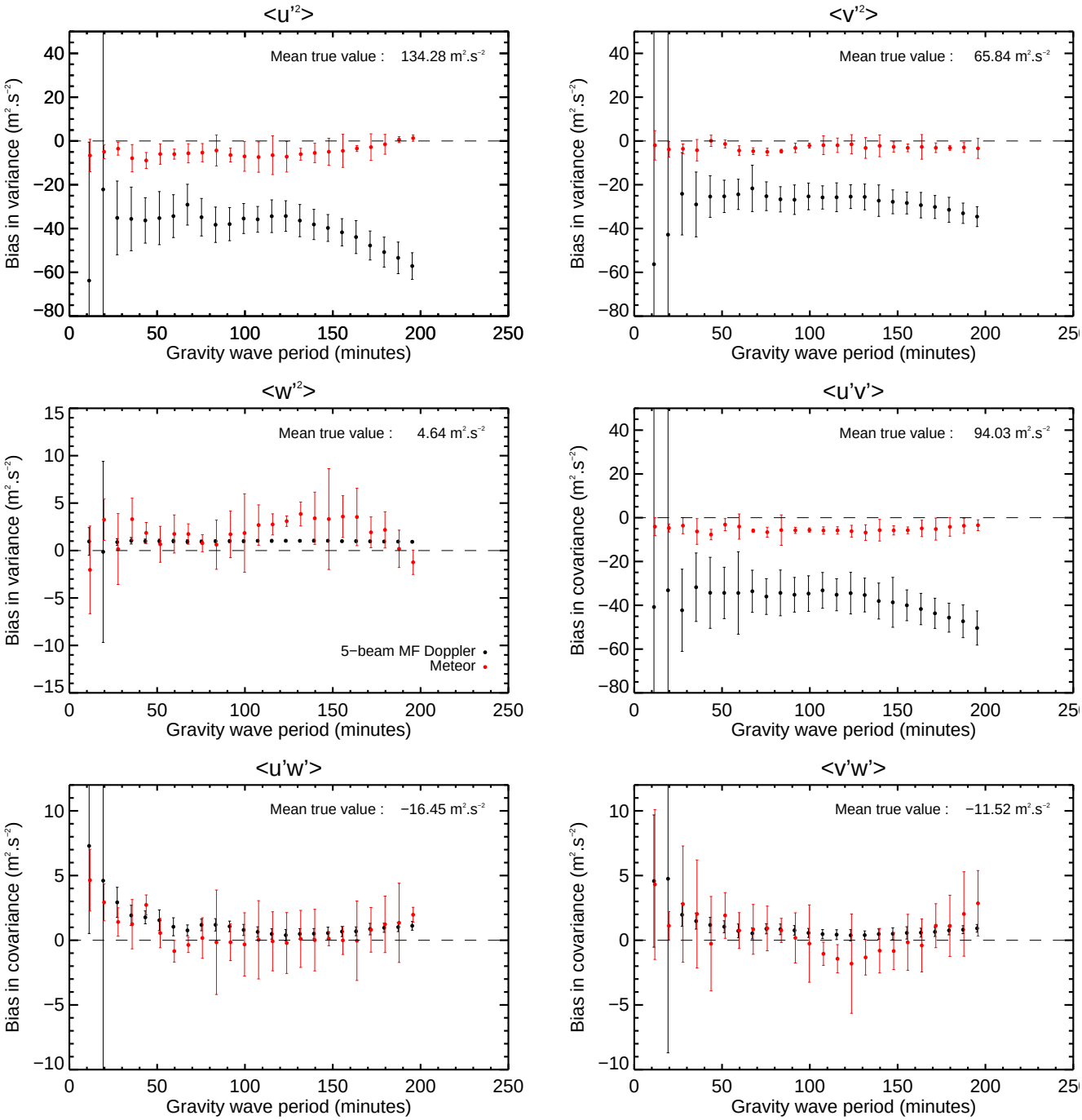

Fig. 5.3: A comparison of the biases in the model stress terms extracted from the MF 5-beam Doppler and VHF meteor radar techniques over a 48 hour period, for the "Case 1" wave field. Doppler results are shown in black, and meteor in red. The error bars show the standard deviation in the bias determined over 200 realizations of the initial gravity wave phase/scattering position error.

its larger observation area, the meteor technique is more susceptible to this than the 5BD.

5.3.3 Effects of window length

The analysis approaches described so far have considered rather "standard" binning of the samples in time—i.e., the performing of an analysis over a window of length several hours (here, 2), and

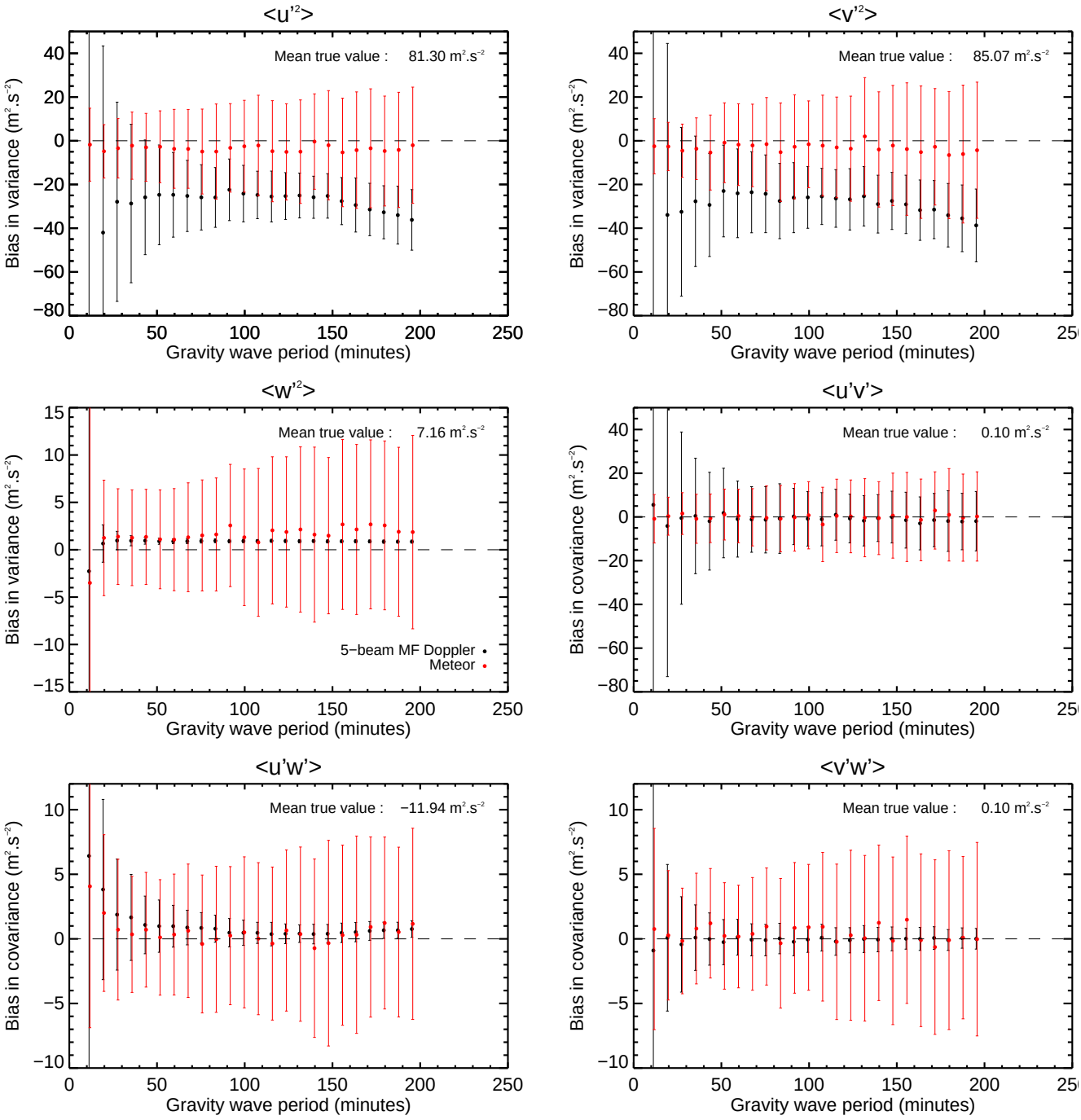

Fig. 5.4: As per Fig. 5.3, but for the Case 2 wave field.

averaging the results of a collection of adjacent windows (here, 24) if improved statistics are needed. There are obvious merits to this approach in this application: namely, the wave field needs to be stationary for the second-order statistics derived from it to be valid; this is more probable for a shorter window. Moreover, if a technique's data acceptance rate varies over an analysis window, as is the case for both the meteor and (to a lesser extent) the 5BD techniques, the obtained statistics will be biased towards those times with higher acceptance rates, if smaller "subset" windows are not used.

However, the increasing underestimation of the 5BD technique (for essentially all RST components) for waves of periods $\gtrsim$ 2 hours likely indicates an inadequate sampling of larger scale waves, which is

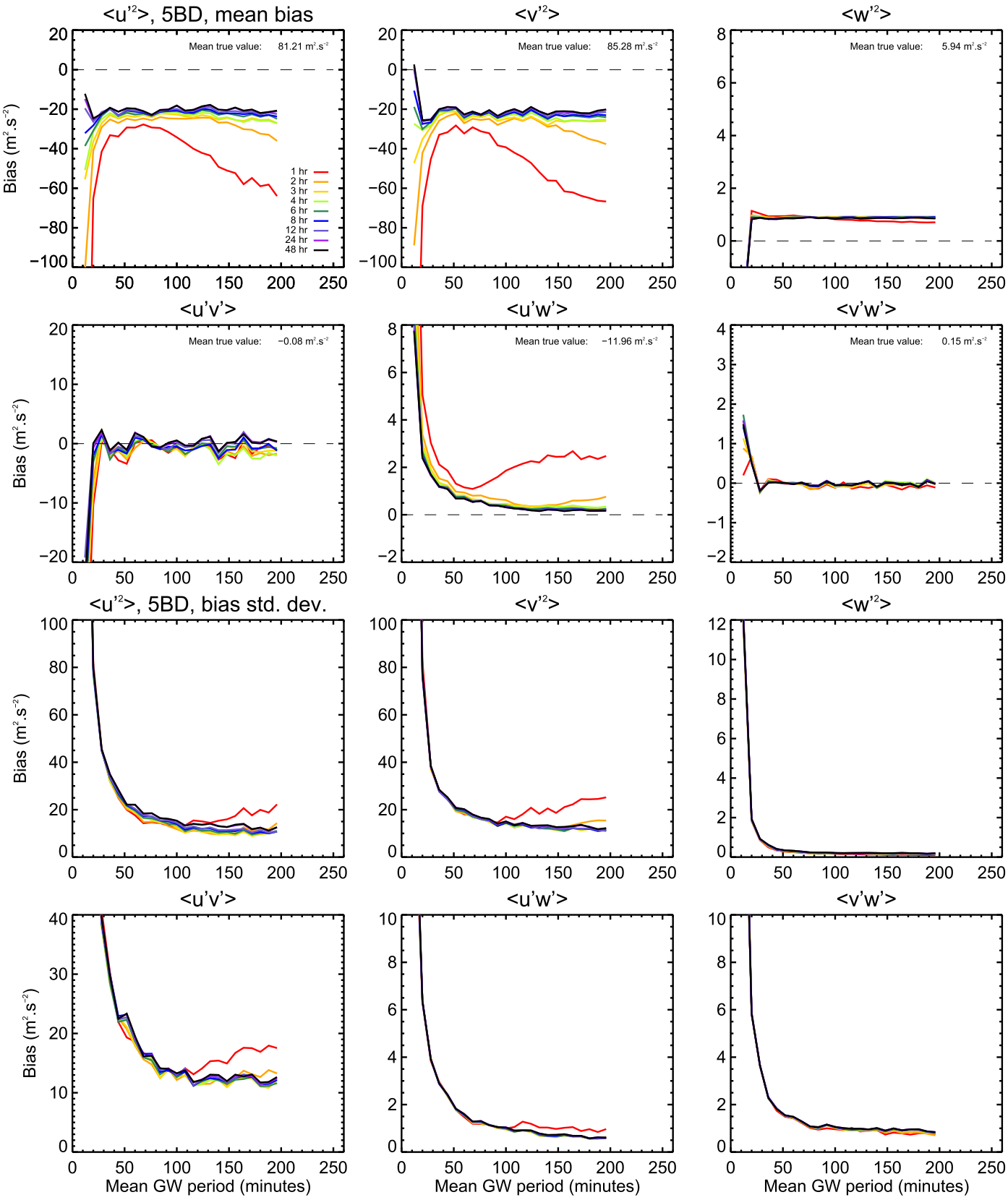

Fig. 5.5: A comparison of biases in the extracted RST estimates for different integration times (1, 2, 3, 4, 6, 8, 12, 24 and 48 hours), for scattering positions from the 5-beam Doppler technique, as a function of mean gravity wave period in minutes, for a spectrum of waves propagating in the Eastern sector (Case 2). Averages over 200 realisations of initial gravity wave phases for each period are shown in the upper 6 plots, and the standard deviations over the same realisations are shown in the lower 6.

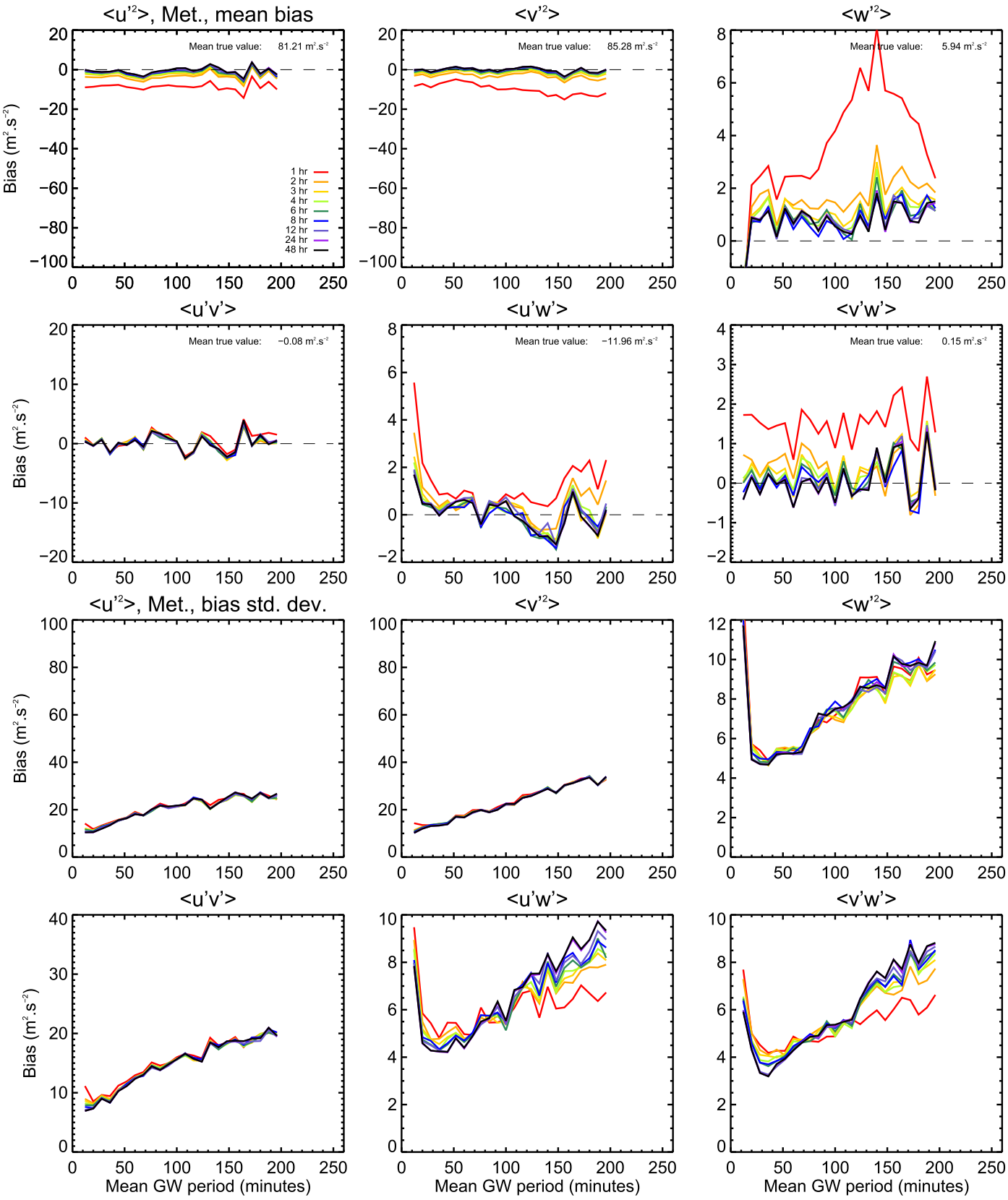

Fig. 5.6: As per Fig. 5.5, but for the all-sky meteor technique.

clearly a consequence of the window length being used. Interestingly, the meteor technique, at least in the results presented so far, does not appear to be susceptible to this.

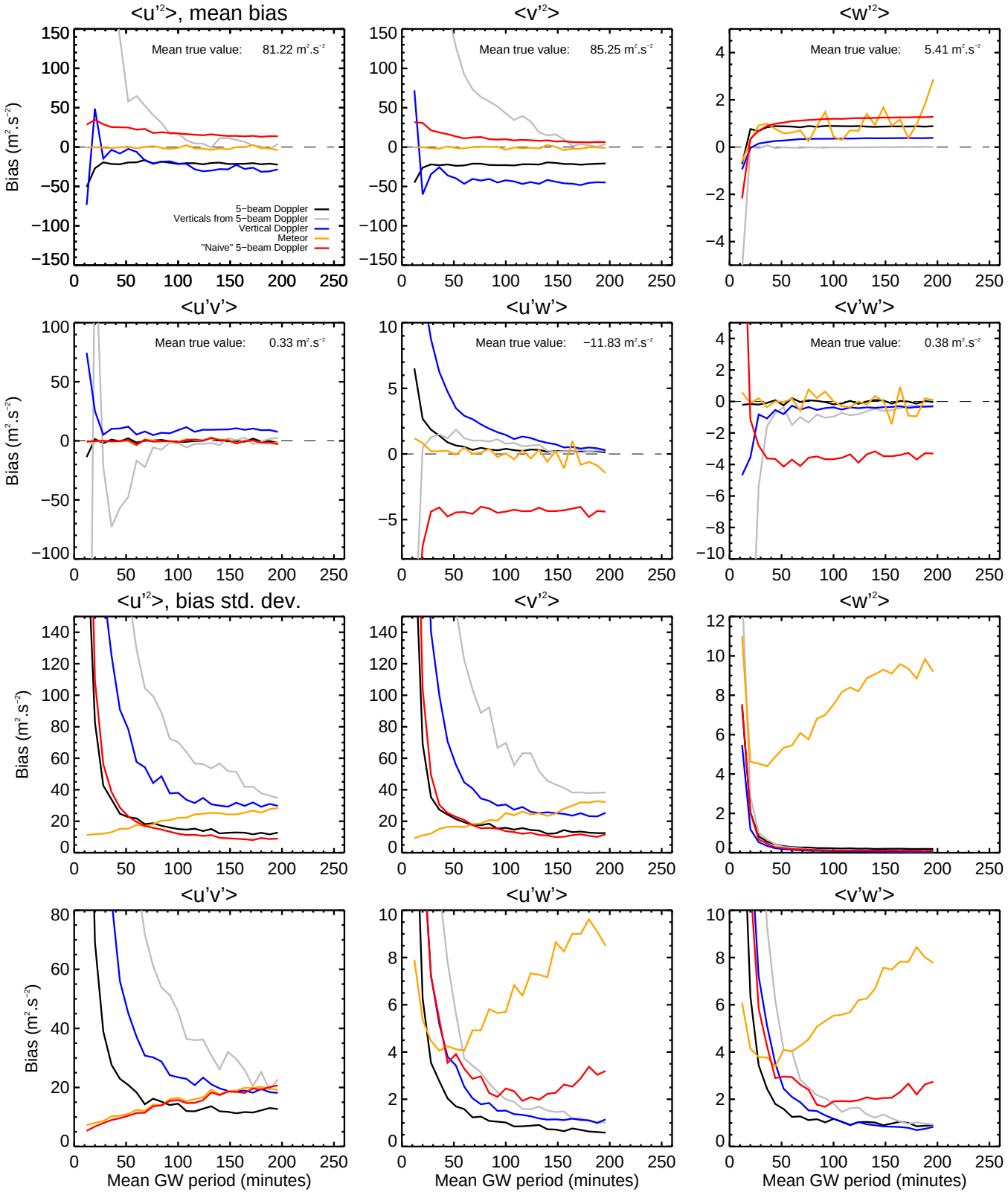

Fig. 5.7: A comparison of biases in the RST components extracted from the 5BD (black), the vertically transmitted subset of the 5BD (gray), vertical-beams only (blue), the meteor technique (orange), and the N5BD (red). Mean biases are shown in the upper six panels, and bias standard deviations in the lower six.

The upper panels of Figs. 5.5 and 5.6 show the effect of window length on mean RST component biases extracted from the 5BD and meteor techniques respectively, in a similar format to the results in Figs. 5.3 and 5.4, for the Case 2 wave field. Windows of length 1-48 hours are investigated. Increasing the window length generally reduces the size of the biases in the extracted RST components, though the level of improvement diminishes rapidly once windows much longer than the maximum gravity wave period considered are used. The bias reduction is most prevalent for horizontal variance and momentum flux estimates using the 5BD technique, at large mean wave periods.

The lower panels of the figures show the standard deviation in the mean bias (again, for 200 realizations at each period). Generally, they indicate little dependence of measurement precision on window length. Increasing the window length beyond two hours has a negligible effect on the standard deviation in all 5BD RST component biases. The precision of the meteor technique momentum flux results appears to be inversely related to the window length, and all other quantities from this technique appear to be unaffected by window length.

On the basis of the results presented in this work, it is assumed that the use of longer windows for Doppler and meteor techniques will at least lead to more accurate (though not necessarily more or less precise) RST components. Only windows of length 48 hours are used herein (i.e., the full length of the 48 hour sample of data, rather than the average computed from subsets within it).

A fixed "integration time" of 48 hours has been used in this work, as this was the longest reasonably continuous sample of 5BD data available from the discussed campaigns. It should be noted that the integration time required for accurate estimates of RST components has been investigated previously, and the findings clearly demonstrate its dependence on the radar technique and/or system used and the region of the atmosphere being probed. Kudeki and Franke [1998] determined, for a perfect dual-beam "anemometer", that at least 16 days of integration is needed to reliably estimate a momentum flux in the stratosphere, if one assumes that the flux represents a fraction of around 1% of the mean horizontal and vertical variance. Accounting for the effects of measurement noise and finite spatial correlation of the wind fluctuations (as would be relevant in the case of using a radar receiving volume scatter from multiple locations), Thorsen et al. [2000] came to a similar conclusion.[3] Vincent et al. [2010], in their modelling assessment of the meteor technique, argued that integration times of over a month are necessary for accurate momentum flux measurements, in approximate agreement with the findings of Kudeki and Franke [1998] for the dual-beam technique. Fritts et al. [2012a] independently assessed the meteor technique, and argued that the large-amplitude monochromatic gravity waves often observed in the MLT-region would result in stronger correlations between component velocity fluctuations (i.e. larger ratios of momentum flux to mean variance) than Kudeki and Franke [1998] assumed, and hence that the relevant required integration time would be reduced (by around a factor of 20). Dutta et al. [2005] and Anandan et al. [2014] have also assessed the abilities of VHF radars in the troposphere to estimate momentum fluxes,[4] and reported required integration times of 15-16

[3]Assuming, for the case of the coplanar radar beam technique, that the beam off-zenith angles are 13°.

[4]Dutta et al. [2005] used a 5-beam Doppler technique with the VHF radar at Gadanki (13.5°N, 79.2°), and Anandan et al. [2014] used a configuration of up to 64 beams with the MU radar.

hours and 8-9 hours respectively.

5.3.4 Other Doppler techniques

Figure 5.7 shows a comparison of RST estimate biases using Doppler and meteor techniques. The Doppler techniques are broken into four groups: the 5BD, the vertically transmitted subset of the 5BD (i.e. a single measurement per 10 minutes) (herein denoted V5BD), one using only vertically transmitted beams (herein VBD), and one using the previously discussed "naïve" version of the 5BD (herein N5BD). The V5BD and VBD results imply that it is basically impossible to obtain accurate horizontal variance estimates for waves of short periods without applying beamsteering on transmission. The accuracy of these two techniques are notably better for momentum flux estimates, though are still generally poorer than those of the 5BD and meteor.

The N5BD results generally show good precision, but substantial overestimates of variances and vertical fluxes of horizontal momentum. The $\langle u'w' \rangle$ estimates in this case are particularly poor, with an overestimate of the order of 30%. It is also interesting to note that the N5BD technique estimates $\langle u'v' \rangle$ with characteristics more similar to the meteor technique than the other Doppler techniques. A reason for this is not clear.

The two vertical beam mean biases display a number of surprising features, that have not yet been reconciled. Firstly, the V5BD bias for $\langle u'^2 \rangle$ and $\langle v'^2 \rangle$ measurements is notably smaller than that for the 5BD and VBD (although the bias in the standard deviation is higher) at high wave periods. Secondly, and similarly, the V5BD bias for $\langle w'^2 \rangle$ is less than that for 5BD and VBD.

The relationship between the precision of the vertical techniques and the 5BD is easier to understand: the precision of the V5BD is lower than the VBD (especially so at low gravity wave periods), which is likely a consequence of the lower sampling rates, given the similar spatial distribution of the techniques' EBPs. The precision of the VBD is lower than the 5BD for all quantities except $\langle w'^2 \rangle$, and this appears to be a consequence of the mean zenith angle of the EBPs of these techniques.

To test the four techniques' abilities on a "wider" spectrum of gravity waves, the 37 individual periods of the waves in Case 2 were modified to be selected from a uniform distribution with bounds $(6, 180)$ minutes. Fig. 5.8 shows histograms of the biases for 10,000 phase and positional error realizations, with the same colour scheme as for the techniques shown in Fig. 5.7. The first two entries of the arrays in the upper-right corner of each plot indicate the mean and standard deviation of each distribution. A third statistic, given by $1.4826 \times$ MAD, where MAD is the median absolute deviation of the distribution, is also given; it corresponds approximately to the standard deviation of the distribution subject to the outlier robustness of the MAD, and if the distribution itself were Gaussian [Rousseeuw and Croux, 1993]. This has been shown along with the "actual" standard deviation since a few large outliers were present in some of the bias samples—especially those of the Doppler techniques, as the figures imply.

The implications of these results do not differ significantly from those showing a wave scale dependence. The 5BD and VBD again underestimate horizontal variances, overestimate vertical variances, and slightly underestimate momentum fluxes. The V5BD tends to overestimate the horizontal vari-

ances, and provide reasonably accurate but very imprecise estimates of the other RST terms. The meteor technique again estimates most components accurately, although obtains poorer precision than the 5BD for momentum fluxes. The N5BD again also overestimates variances and vertical fluxes of horizontal momentum, and estimates $\langle u'v' \rangle$ with precision and accuracy similar to the meteor's.

5.4 Summary and recommendations for future work

A computer model has been created, in which the relative RST component extraction capabilities of Doppler and meteor-based techniques were assessed. The model's wind field included gravity wave effects of variable complexity, and fixed tidal parameters. The tidal effects were removed by subtraction of radial projections of least-squares harmonic fit parameters of the wind field. First-order wind shears were also projected onto and subtracted from the radial velocity field. The RST components were estimated from the residual wind field using the inversion technique specified by Thorsen et al. [1997]. The model used distributions of scattering positions from Doppler and meteor experiments to simulate the techniques' spatiotemporal sampling, and incorporated Gaussian-distributed errors of 1.5° and 1° in the techniques' positions respectively.

The results showed that the Doppler technique, when used in a 5-beam configuration and with HDI applied to determine the EBP, will underestimate horizontal variances and momentum fluxes, and overestimate vertical variances (by factors of $\sim$ 30-40% and 5-20%, respectively). If no interferometric capability is available and the EBP is estimated using an aspect sensitivity climatology, substantial overestimates of all RST components will result, save $\langle u'v' \rangle$. Precision of RST components in such a case should remain unaffected. The meteor technique will generally estimate all RST components accurately, although will obtain poorer precision in momentum flux estimates than will the 5-beam technique. Identical tests on vertical beam Doppler techniques also indicates the necessity of steering a beam on transmission if momentum flux estimates are desired; if this is not done, less precise and more biased measurements will result. Nonetheless, it may still be possible to obtain useful measurements from MF radar systems with interferometric (but no transmission beamsteering) capability, as per the Thorsen et al. [1997] paper.

A rather crude method was used in this work to estimate the contribution of phase measurement errors to EBP determination errors for the Doppler techniques. The reported uncertainties (Gaussian-distributed with standard deviation 1.5°) are likely overestimates, since the phase difference errors used to derive them incorporated both instrumental errors and geophysical variations in the beam position. This in turn may have made the Doppler technique RST biases reported here excessive. A better value of the phase measurement error could be deduced by injecting a radar signal of known phase directly into the antennas constituting given receiver channels. The EBP errors used here for the meteor technique (Gaussian-distributed with standard deviation 1°) are probably representative of the true error; however, a more accurate figure may be obtained by comparing the meteor positions determined by co-located meteor radars (e.g., the 33 and 55 MHz radars at Davis).

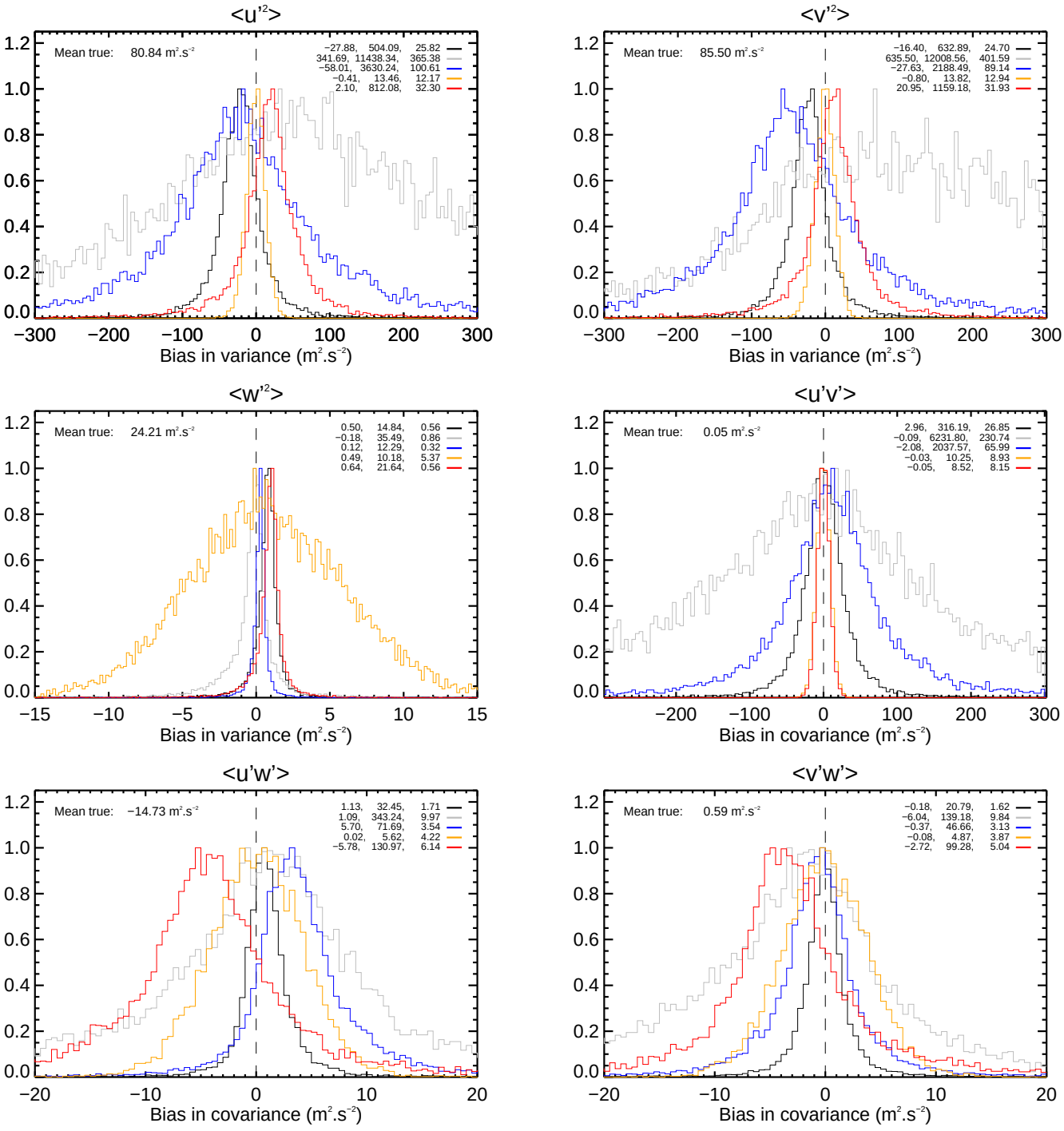

Fig. 5.8: Histograms showing the bias in the RST components, evaluated using the 5BD, the vertically transmitted subset of the 5BD, vertical-beams only, the meteor technique, and the N5BD. The colour scheme used is the same as that in Fig. 5.7. The mean, standard deviation and standard deviation evaluated from a sample's median absolute deviation (see text for details) are also indicated in that order in three-element arrays in the upper right of each plot.

Chapter 6

HDI experiments with the Buckland Park MF

6.1 Introduction

In this Chapter, the inversion technique of Thorsen et al. [1997] (eqn. 1.7) is applied to MF radar HDI (Sect. 3.3) radial velocities measured from a set of multi-beam Buckland Park MF radar experiments, to acquire RST component estimates. This analysis has been conducted with a number of aims in mind. They are:

1. To verify that the 5-beam Doppler technique can extract vertical fluxes of horizontal momentum that are physically reasonable;

2. To predicate the existence of any biases in the spaced antenna (SA)-derived variance and covariance terms in the horizontal wind, obtained during the routine analysis run adjacent to the Doppler experiments[1];

3. To verify experimentally that the early analysis of momentum fluxes using MF Doppler radar (e.g., Vincent and Reid [1983], Fritts and Vincent [1987], Reid and Vincent [1987], and Murphy and Vincent [1993]) were not biased by not explicitly accounting for the effective beam position (EBP)[2];

4. To provide a set of RST component measurements which may be of use in verifying estimates of the same parameters from a meteor radar.

The technique used to obtain components of the RST (starting from the obtained distributions of radial velocities measurements) are firstly described, and then descriptions of the experiment parameters and results from each set of experiments are given. The experiments were conducted as part of dedicated momentum flux measurement campaigns during 1997 and 1998.

[1] This is of particular importance to the validity of the long-term trends in FCA-derived variances discussed in Chapter 4.

[2] Reid and Vincent [1987] implicitly accounted for the EBP by inferring it from a multi-site climatology of aspect sensitivity measurements, as did Murphy and Vincent [1993] by calculating the EBP from the SA-derived pattern scale.

6.2 Analysis technique

The analysis performed here on HDI radial velocities follows the methodology applied to model Doppler data in Chapter 5, in that RST components are estimated from the data in several, in this case three, independent ways. The first of the techniques used data from all available beams, and assumed that the EBPs derived from HDI were the "true" beam positions (i.e., Chapter 5's "5BD"). The second aimed to replicate that done in the "naïve" earlier analysis, in which the azimuth of the received beam was assumed the same as that transmitted, and that its zenith angle was reduced by atmospheric aspect sensitivity (i.e., Chapter 5's N5BD). The third analysis was confined to data from the vertical beam (i.e., Chapter 5's V5BD).

The second technique required that SA-FCA-derived pattern scale data exist in the routine analysis run adjacent to the Doppler experiments. Each of the analyses also required the pre-determination of tidal components in the measured velocities, which were projected onto the radial velocities (if they were Cartesian components, as in the first and third techniques) and subtracted from them prior to evaluating any stress terms (see Sect. 5.1.3). The full list of steps used to determine the mean winds and RST components are described in separate sections below. Justification for certain steps is given where appropriate.

Mean wind velocity determination

1. Partition the two-minute resolution data from a given campaign, as well as the SA-FCA data adjacent to it, into 2-hour blocks, with the centre of each block displaced by 2 hours from the adjacent one (the remaining steps pertain to *each* separate 2-hour block);

2. Using the pattern scale and axial ratio information derived from the SA-FCA analysis, calculate circularly averaged values of θ_s (see Sect. 3.1, pg. 38 for a description of θ_s, θ_e and θ_a);

3. Calculate the altitude of each Doppler measurement (from the recorded line-of-sight ranges) using two different techniques:

   (a) Simply assume that the zenith angle of the return is equal to the HDI-derived θ_e.

   (b) i. Interpolate a θ_s value from the averaged SA-FCA data at an altitude corresponding to the range of the Doppler measurement (assuming $\theta_a = \theta_e$). The interpolant should be determined from a block of data centred on the time of interest, with a block width of the order of a few days. In this study, a block length of 14 days has been used, given the high variance observed in θ_s on short time scales;

   ii. Use the interpolant to calculate an SA-FCA-derived θ_e;

   iii. Use the acquired θ_e to calculate the "true" altitude of the Doppler measurement from its original range (note that this is a circular argument: one needs to know the altitude the Doppler measurement is actually at to interpolate the correct θ_s, but the θ_s is needed a-priori to be able to determine the altitude. This methodology was considered adequate, though is subject to the following as yet unchecked assumptions:

- the block-averaged θ_s changed slowly with height, and;
- θ_a was small enough such that the difference between the "true" altitude and the altitude determined from θ_a was insignificant.)

4. Using the two sets of altitudes calculated in Step 3, partition each block into 2 km-width bins, with the lowest bin starting at 70 km and the highest at 96 km[3]. For brevity, call the set of bins pertaining to those measurements with altitudes derived from the HDI-based θ_e "A", and those from the second method "B";

5. By applying an inversion of eqn. (1.4) (with shear terms included) on A, estimate the mean horizontal and vertical winds. Scale the system equations with the radial velocity variances evaluated using eqn. (3.16). If less than 10 measurements exist across all available beams, consider the wind estimate for this block as "missing". If calculating winds based on a single beam (e.g., the vertical beam), only compute if at least 3 measurements exist. Refer to these as $\langle \boldsymbol{v}_A \rangle$[4].

6. Evaluate mean radial velocities for each nominal beam direction in B. Remove points more than 3 standard deviations from the means, and recalculate the means.[5] Refer to them as $\langle V_{rad_{Bi}} \rangle$ (for the ith beam direction). If there are less than 2 points in a given beam, consider this measurement as "missing" and do not perform any further analysis on it;

7. Simultaneously solve eqn. (1.4) for pairs of off-zenith beams of opposite azimuths, to obtain an estimate of the mean horizontal and vertical winds from B. Adjust θ_a only for the local value of θ_s (i.e., do not apply any correction to the apparent azimuthal angle). Refer to the wind estimates as $\langle \boldsymbol{v}_B \rangle$.

RST component determination

1. Re-partition the two-minute resolution Doppler and SA-FCA data into 48-hour blocks, with the centre of each block displaced by 6 hours from the adjacent one (the remaining steps pertain to *each* separate 48-hour block);

2. Perform a least squares fit for (Cartesian) tidal/planetary wave components in $\overline{\boldsymbol{v}_A}$. The fit should be performed over a window encompassing data in the vicinity of the block currently being analysed. In this study, a window width of 4 days (centred on the current block) was used. It should be noted that, for simplicity (see discussion in Sect. 5.1.3, pg. 64), this step assumes stationary tidal and planetary wave effects;

[3]Suitable altitude limits in this case were determined from the radial velocity acceptance rate profiles (Fig. 6.3).

[4]Here, different combinations of beams in A were used to calculate the mean winds (e.g., using only the vertical beam. See next section for details).

[5]It should be noted that the outlier removal part of this step was omitted in the Chapter 5 model. It was included here in the interests of removing outliers likely caused by interference. Its effect has not been systematically tested.

3. Subtract a radial projection of the fitted components from the individual radial velocity records in A;

4. Estimate the RST components from the residuals by inverting eqn. (1.7). Again, scale the system of equations with the radial velocity variances;

5. Repeat steps 2 and 3 for the mean radial velocity time series $\langle V_{rad_{Bi}} \rangle$;

6. Simultaneously solve eqn. (1.8) to evaluate $\langle u'w' \rangle$ (and similarly for $\langle v'w' \rangle$).

A very similar analysis has also been applied in this work to the radial velocities from meteor radars. In that case, hourly mean winds were determined as outlined in Sect. 2.2.2. Steps 1-4 under "RST component determination" were then followed.

6.3 The 1997-1998 experiments

These experiments comprised four periods (during July, September and October 1997, and June 1998) in which all available elements of the Buckland Park MF array were phased to form identical transmit and receive beams in five directions: one vertical, and four at small off-zenith angles in the Cardinal directions. The experiments were conducted with the intention of measuring momentum fluxes using the Vincent and Reid [1983] estimator [Holdsworth and Reid, 2004b].

6.3.1 Data set characteristics

An example of one of the antenna configurations used for HDI experiment campaigns is shown in Fig. 6.1. The configuration utilised a total of 20 groups (60 antennas) for transmission and 16 groups (48 antennas) for reception. As with the long-term FCA data set (Sect. 4.2), the configuration was varied slightly during and between campaigns to compensate for antenna failures. The radar transmitted/received on a two-minute archiving interval, with data acquisition lengths of 112 seconds. The phase at each PA on transmission was changed at the beginning of each archiving interval, so as to steer the transmitted beam through the sequence of directions specified in Table 6.1, along with other parameters used during the 1997 experiments.

Models (produced using `EZNEC+ v. 5.0.63`; see Sect. 2.1.4) of the transmit and receive polar diagrams of the Fig. 6.1 antenna configuration are shown in Fig. 6.2. In both cases, the signal phase has been progressed by about 48° per row to the right, so as to steer the beam 13° West of the zenith. As in the real experiment, the three antennas constituting each group have been driven with an equivalent phase, which has been evaluated for the centroid of each group. The main lobe of the transmit beam is approximately circular with a half-width of around 6°. There appears to be some influence of side/grating lobes in the opposite sector of the sky, although it is likely that these are too far off-zenith to result in ambiguous radial velocities. The receive polar diagram (constituting TRs 1-10) is slightly wider, with a half-width of around 10°, and again contains side/grating lobe influences that are not expected to be of major concern.

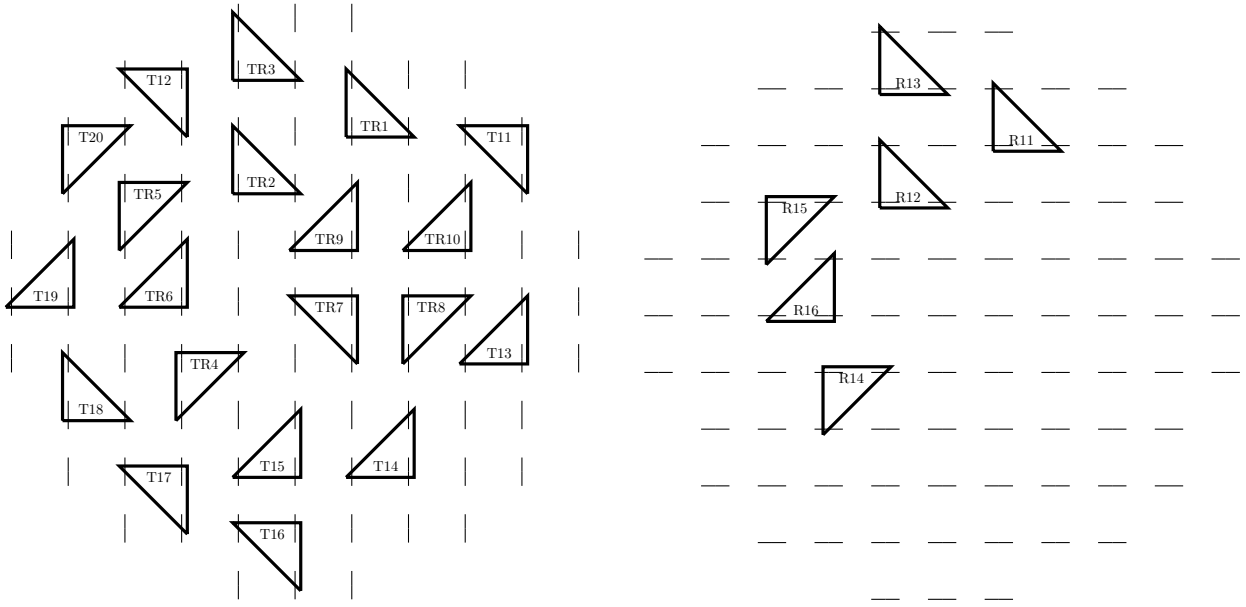

Fig. 6.1: Antenna configuration used for the BP MF during the June 1998 HDI experiment. Here, "TR" refers to transmit-receive groups, "T" to transmit-only groups, and "R" to receive-only groups.

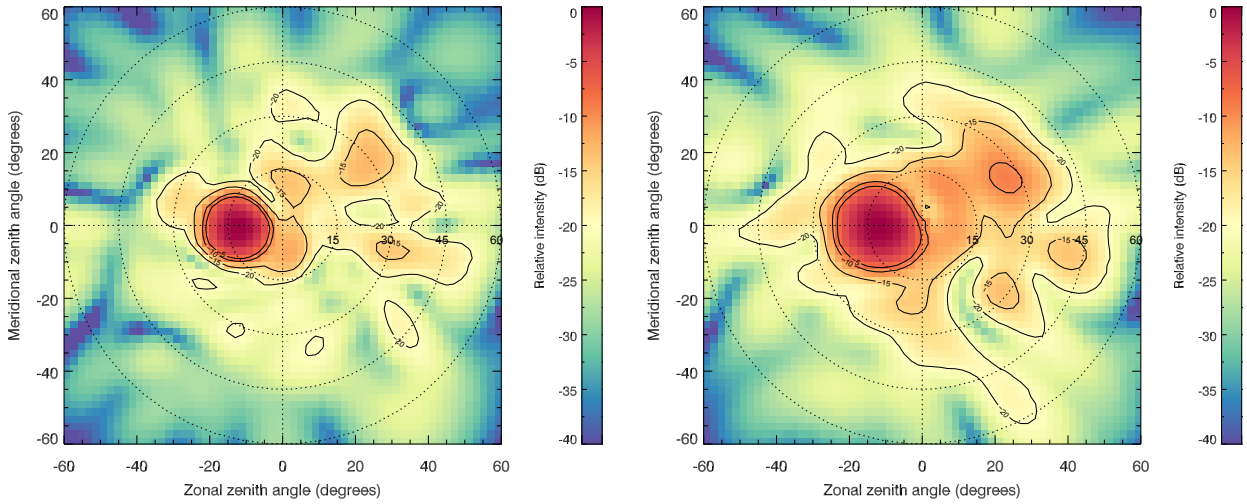

Fig. 6.2: Modelled one-way transmit polar diagram for the antenna configuration proposed in Fig. 6.1 (left) and the receiver polar diagram used to steer a beam in software (right).

Acceptance rate profiles for the radial velocities during the four campaigns are shown in Fig. 6.3. Good acceptance rates ($> 75\%$) were generally obtained during the day across all ranges examined up to 90 km, and overnight between 80 and 90 km. The overnight data below 80 km is still included in the analysis presented here, and so the reported RST terms at these altitudes will be biased towards the day-time results. The October 1997 and June 1998 results are still analysed as a single campaign, despite the clear radar down-times.

Parameter	Value
Sampling range (km)	50-102 (70-102)
Sampling resolution (km)	2
Steering sequence (θ, °)	[0, 12, 12, 12, 12]
Steering sequence (ϕ, °T)	[0, 0, 90, 180, 270]
Beam $\frac{1}{2}$-power $\frac{1}{2}$-width (°)	5.7
PRF (Hz)	100 (20)
No. CI	20 (4)
No. samples per beam	280
No. Rx	16
No. Tx	20

Table 6.1: Parameters used in the 1997 Doppler experiments. Where a given parameter is varied during the day and night, its night-time value is shown in parentheses. The parameters used in June 1998 were identical, except all off-vertical beams were steered to zenith angles of 13°.

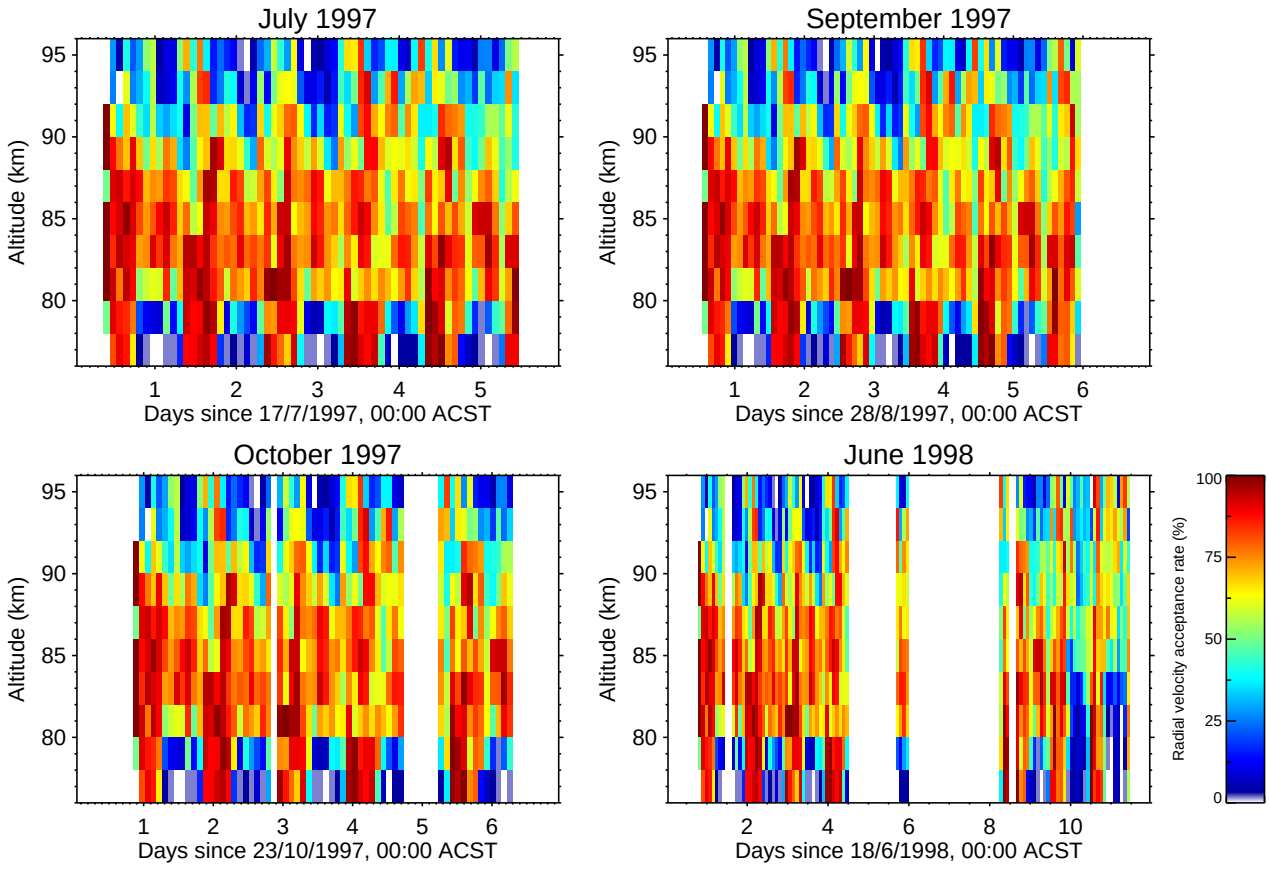

Fig. 6.3: Radial velocity acceptance rate profiles for the four HDI campaigns. Results are plotted on a 2 km range and 2-hour altitude grid.

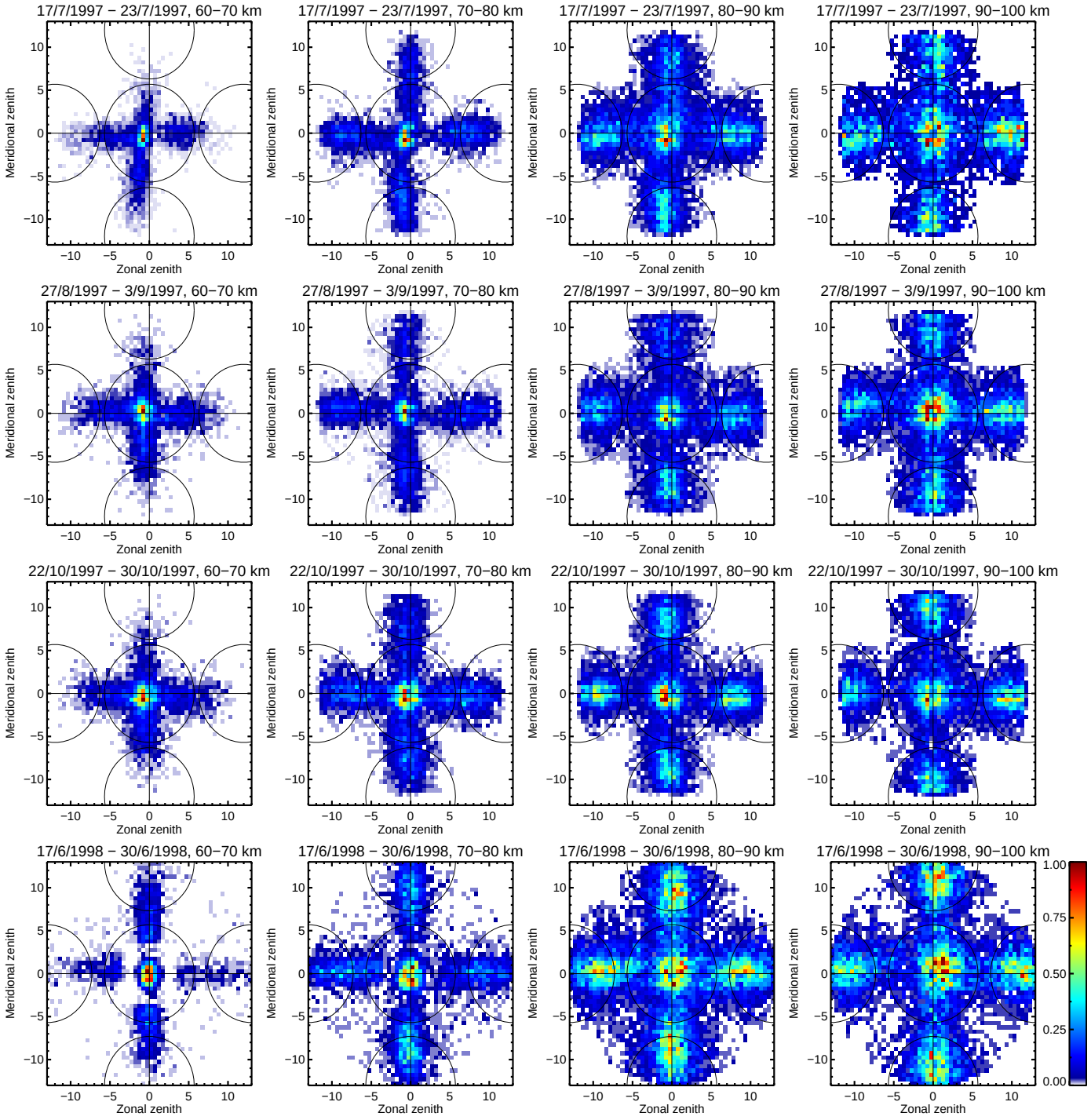

Fig. 6.4: Histograms of the 5BD EBPs determined by HDI at selected ranges for the four Doppler experiments (each row pertains to a given campaign, and each column a given range). The thin black circles approximately denote the half-power half-width contours of the transmitted beams (5.7° in all cases shown).

6.3.2 Results and discussion

Effective beam positions

Histograms of the EBPs at 60, 70, 80 and 90 km in each of the four campaigns are shown in Fig. 6.4. It is clear that, in many cases (especially in the lower height regions, where the atmosphere

is expected to be more aspect sensitive) the EBP is not within the half-power half-width region of the transmitted beam. A remarkable spread in azimuth of the off-vertical beams is also observed, which is not expected on the basis of aspect sensitivity. The azimuthal spread is likely associated with the (relatively large) angular shifts in peak beam intensity expected when turbulent fluctuations in electron density do not fill the beam volume. This phenomenon could also explain the observed spread in the received position of the vertically transmitted beam. It should be noted that these results are consistent with the spread observed by Vandepeer [1993] in mean angles of arrival (determined using PBS as opposed to HDI) with the same radar system.

The vertical beam EBPs (especially in the lower range gates) during the 1997 experiments also appear to have a non-zero mean zenith. This is indicative of an error in the receiver phase calibration used at the time. However, it is surprising to note that there is little evidence of the same error in the data from a range of 90-100 km. The error from the lower heights could be removed using Holdsworth and Reid [2004b]'s receiver gain calibration procedure outlined in Sect. 2.1.5, although it has not yet been possible to do this for the data presented here.

Mean winds, aspect sensitivities, and horizontal stresses

Mean vertical profiles of the retrieved winds and horizontal stresses are shown in Figs. 6.5 (for the July and August 1997 campaigns) and 6.6 (for the October 1997 and June 1998 campaigns). Horizontal variances derived from coincident SA-FCA data (using the technique outlined in Chapter 4 sans bandpassing) are also shown. Aspect sensitivities determined during each campaign from the SA-FCA pattern scale and the HDI EBPs[6] are shown for reference. The error bars in each plot correspond to the standard deviations of results constituting each campaign period.

All the zonal wind results show features that are consistent with the expected wind climatology at the respective times of year. The Doppler techniques have a tendency to underestimate those provided by the FCA. This contrasts with other comparisons of the FCA with independent radar techniques (e.g., Holdsworth and Reid [2004a], who showed a tendency of the FCA to underestimate IDI-derived winds, and McIntosh [2009], who found that the FCA underestimates meteor radar-derived winds). The agreement between the three Doppler techniques is generally good between about 86 and 90 km (which is also roughly where the acceptance rates maximise) and poor elsewhere. On average, the 5BD and N5BD winds agree more closely than those from the V5BD.

Agreement between the four techniques on the meridional wind is poorer. While the 5BD and N5BD techniques agree well, they generally have a different form to the FCA-derived winds, and some very large discrepancies are evident (e.g., ~ 30 m.s^{-1} around 80 km in July 1997). The V5BD winds generally only agree with those of the other Doppler techniques between 86 and 90 km (with a notable exception in the July 1997 campaign).

The agreement between the FCA and HDI aspect sensitivities is generally poor and inconsistent; HDI overestimates that from the FCA during August 1997, but underestimates it during October

[6]In this case, eqn. (3.11) was rearranged for θ_s, and the positive root was taken.

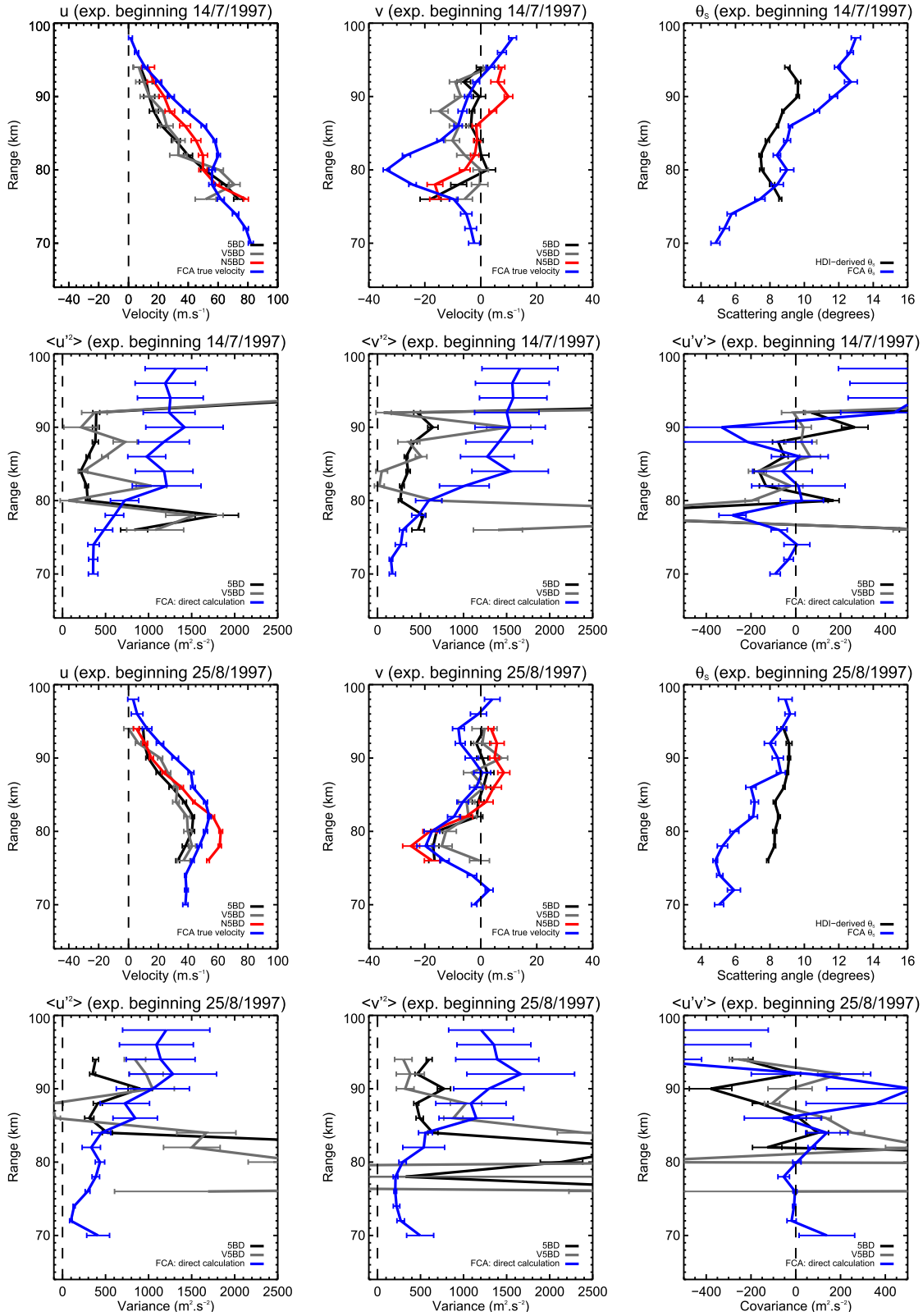

Fig. 6.5: Average vertical profiles of the results from the July and August 1997 Doppler experiments. See text for details.

1997. No comparisons between such two techniques have yet been reported; a more systematic analysis clearly needs to be undertaken to comment further on these discrepancies.

The agreement between the 5BD and V5BD variances is generally favourable between about 80 and 90 km (with exception to the $\langle u'^2 \rangle$ result during August 1997). The V5BD results have considerably

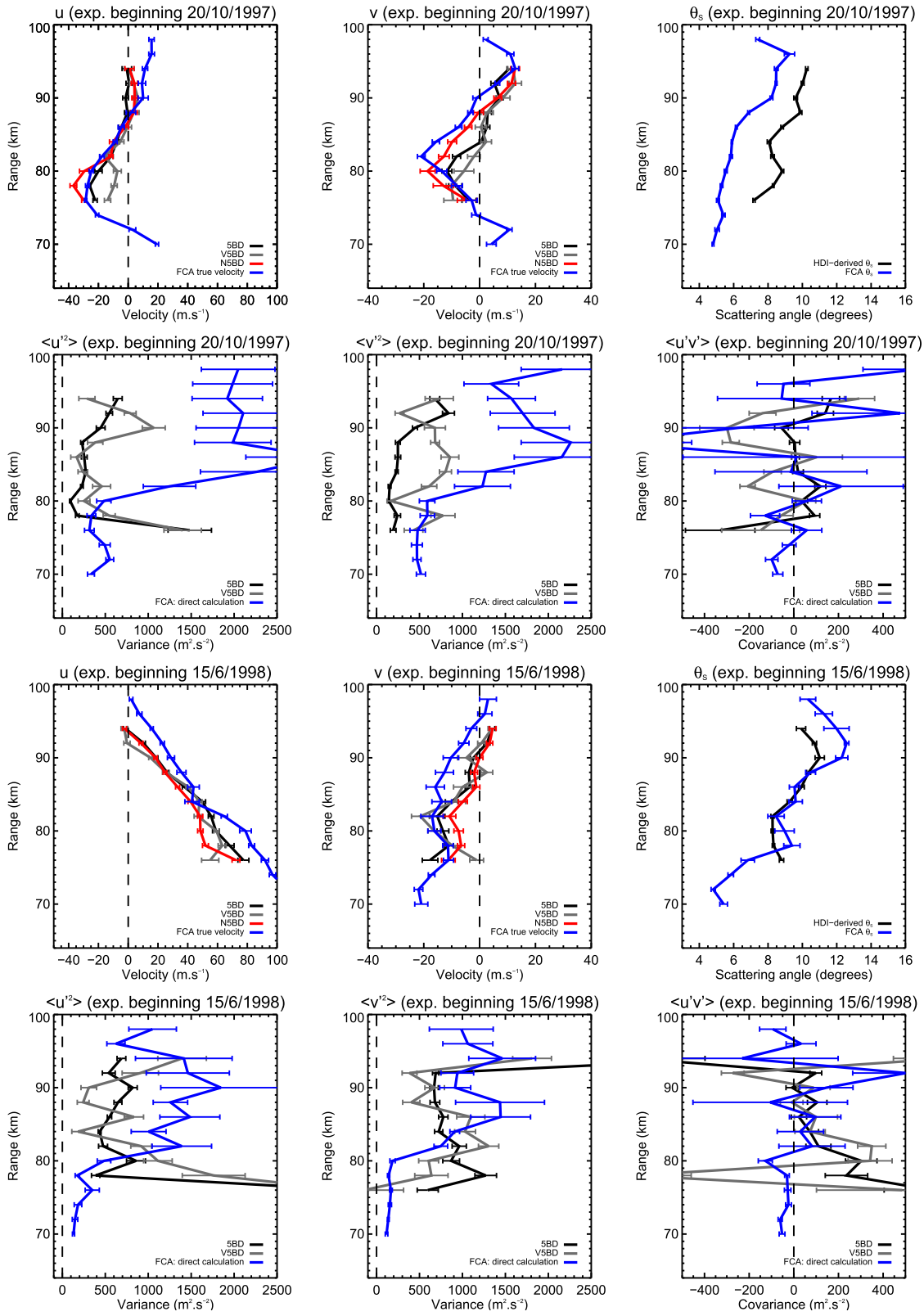

Fig. 6.6: As per Figure 6.5, but for the October 1997 and June 1998 experiments.

more variability with altitude, which is likely false, and is consistent with predictions from the Chapter 5 model.

An important result is that the Doppler techniques generally underestimate the variances provided by the SA-FCA. In Chapter 5 it was predicted that both the 5BD and V5BD would underestimate the true horizontal variance (by around 35%), and that such an underestimation would increase with

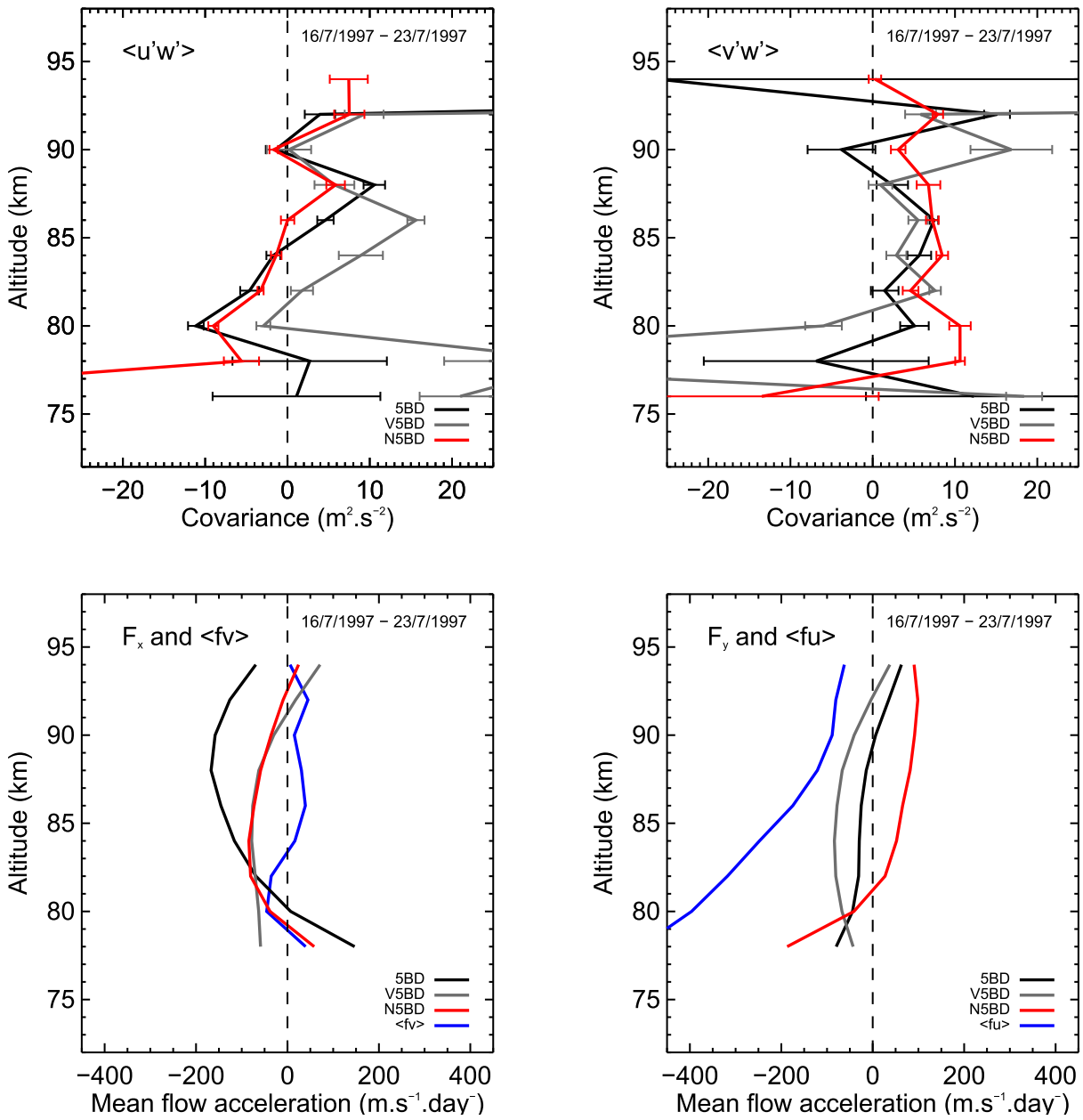

Fig. 6.7: Vertical profiles of the vertical fluxes of horizontal momentum obtained from the July and 1997 Doppler experiments (top panels) and inferred body forces and Coriolis torques (lower panels).

the EBP uncertainty. Assuming the FCA variances are accurate, the discrepancies shown here are relatively larger than the predicted ones (especially for $\langle v'^2 \rangle$ in July 1997 and both $\langle u'^2 \rangle$ and $\langle v'^2 \rangle$ during October 1997), and it seems unlikely a larger EBP uncertainty than that used for the Doppler techniques in Chapter 5 (1.5°) is justified. Therefore, other contributors to the observed discrepancy are likely. It is not clear what these may be; they are at least not associated with filtering of the true wave variances imposed by the techniques' sampling times, since these (unlike in the Doppler vs. meteor radar case) are equivalent.

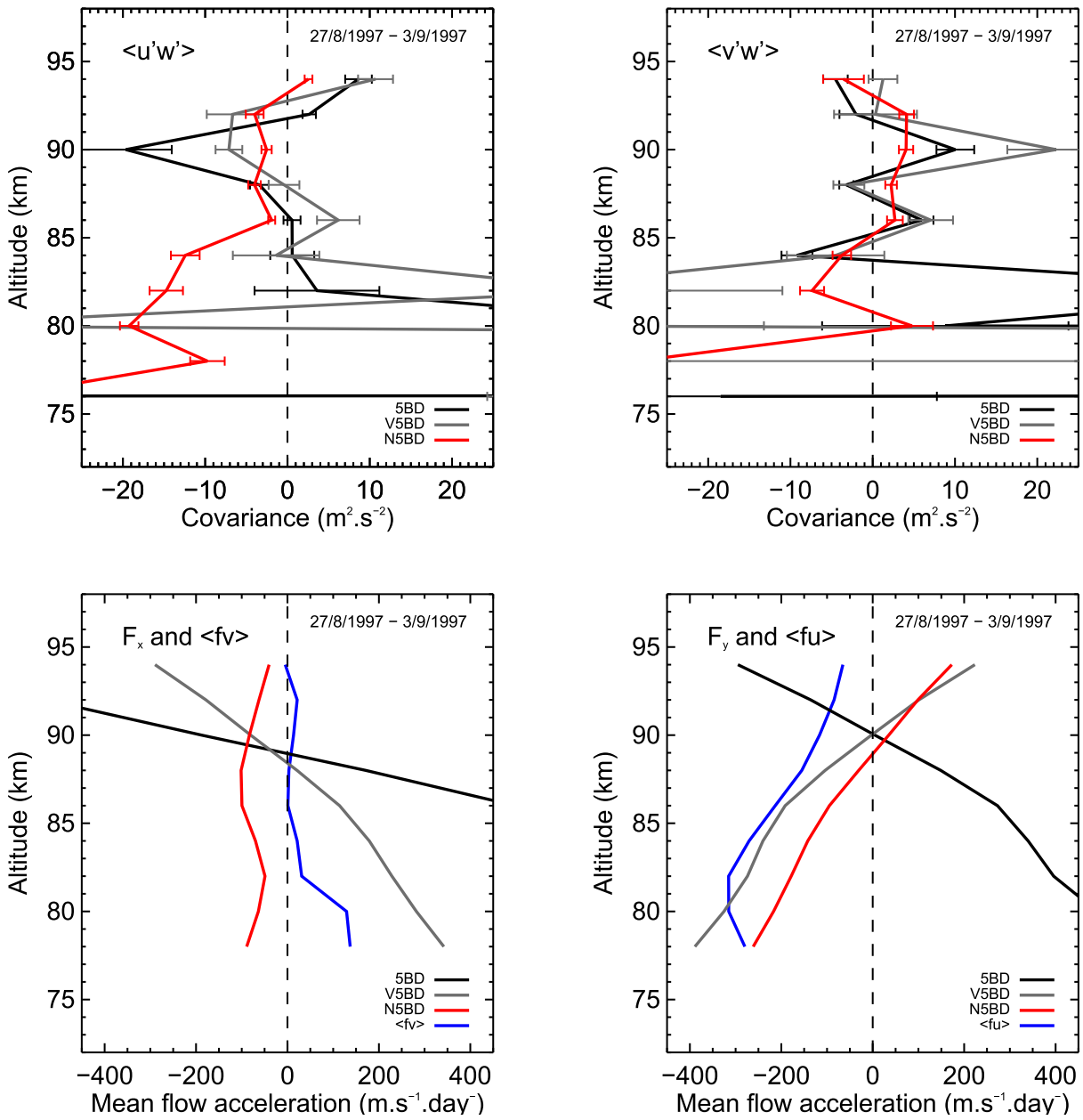

Fig. 6.8: As per Fig. 6.7, but for the August 1997 campaign.

Momentum fluxes and body forces

Mean profiles of the vertical fluxes of horizontal momentum for the four campaigns and three Doppler techniques are shown in the top panels of Figs. 6.7 - 6.10. In addition, preliminary calculations of the inferred body forces and Coriolis torques from the mean wind profiles are shown in the bottom panels of the figures. The body forces were evaluated from eqn. (1.2), using densities derived from the NRLMSISE-00 model (at the same time of year of the measurements, at Buckland Park's location). Following Reid and Vincent [1987],[7] a function has been fit to the density-weighted profiles so as to reduce the effects of measurement noise on their derivatives. The function of choice in this work was a quartic polynomial; it seemed to be able to adequately replicate most of the major features in the momentum flux profiles. It also lead to smaller least-square residuals than lower order polynomials,

[7] They fitted a polynomial to the density-weighted profiles.

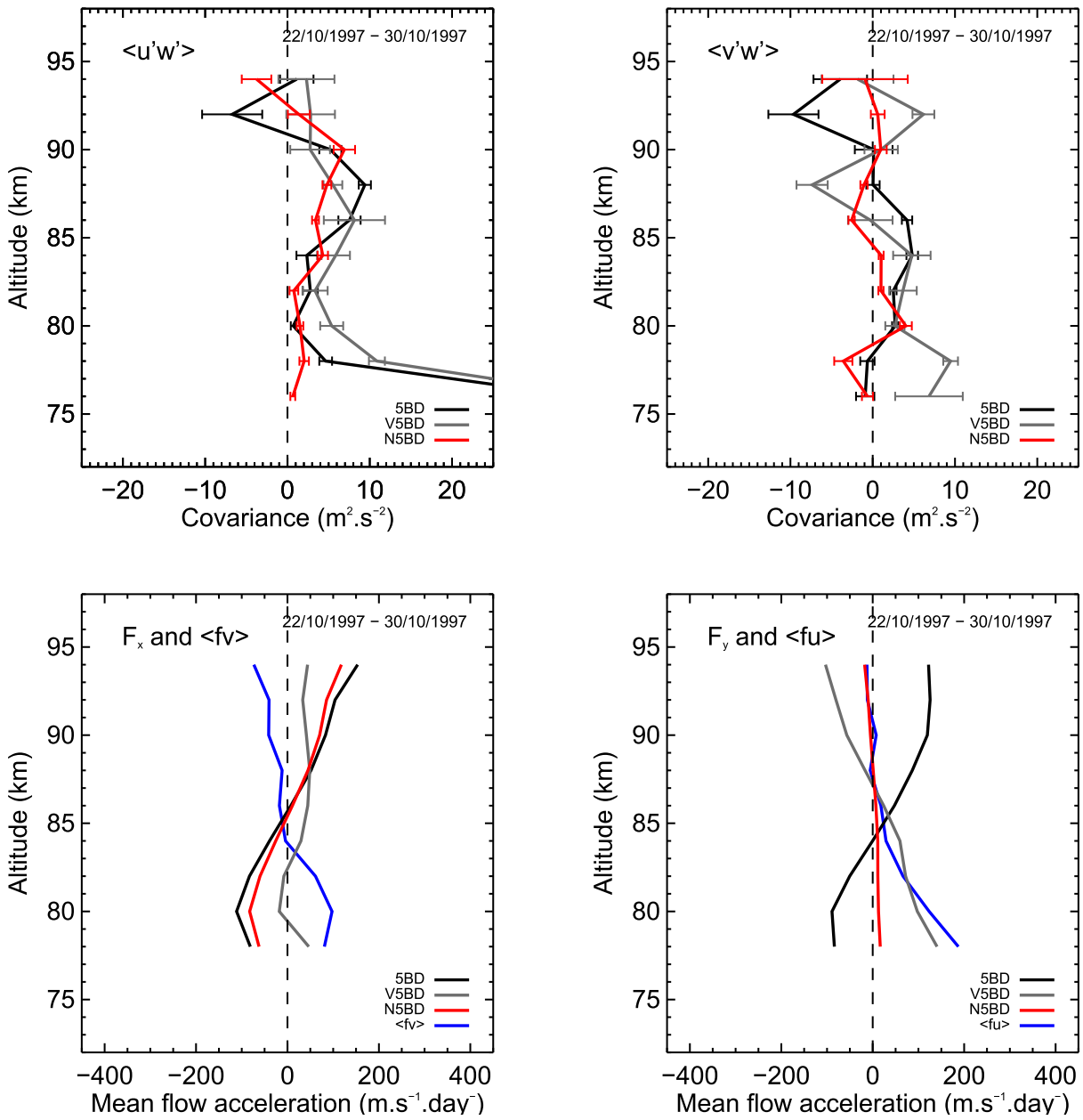

Fig. 6.9: As per Fig. 6.7, but for the October 1997 campaign.

and lacked the spurious "edge-effects" associated with higher orders.

In general, there is a good level of agreement between the three techniques, particularly for measurements of $\langle u'w' \rangle$ between 86 and 90 km. The $\langle u'w' \rangle$ measurements close to this height range show a marked vertical structure, with sign reversals in the flux occurring in the July 1997 and June 1998 campaigns. The inferred body forces in both of these cases are also predominantly westward, which is consistent with a deceleration of eastward MLT winds during winter.

The agreement between the mean inferred body forces and Coriolis torques is generally poor, in both the zonal and meridional planes. Some of these discrepancies may be explained by noting that the relation between the two quantities is only valid for a zonal average. Additionally, the results presented here are centred on the winter months; during this time, planetary waves can propagate into the MLT [Andrews et al., 1987], saturate and contribute to the body force. Only the body force

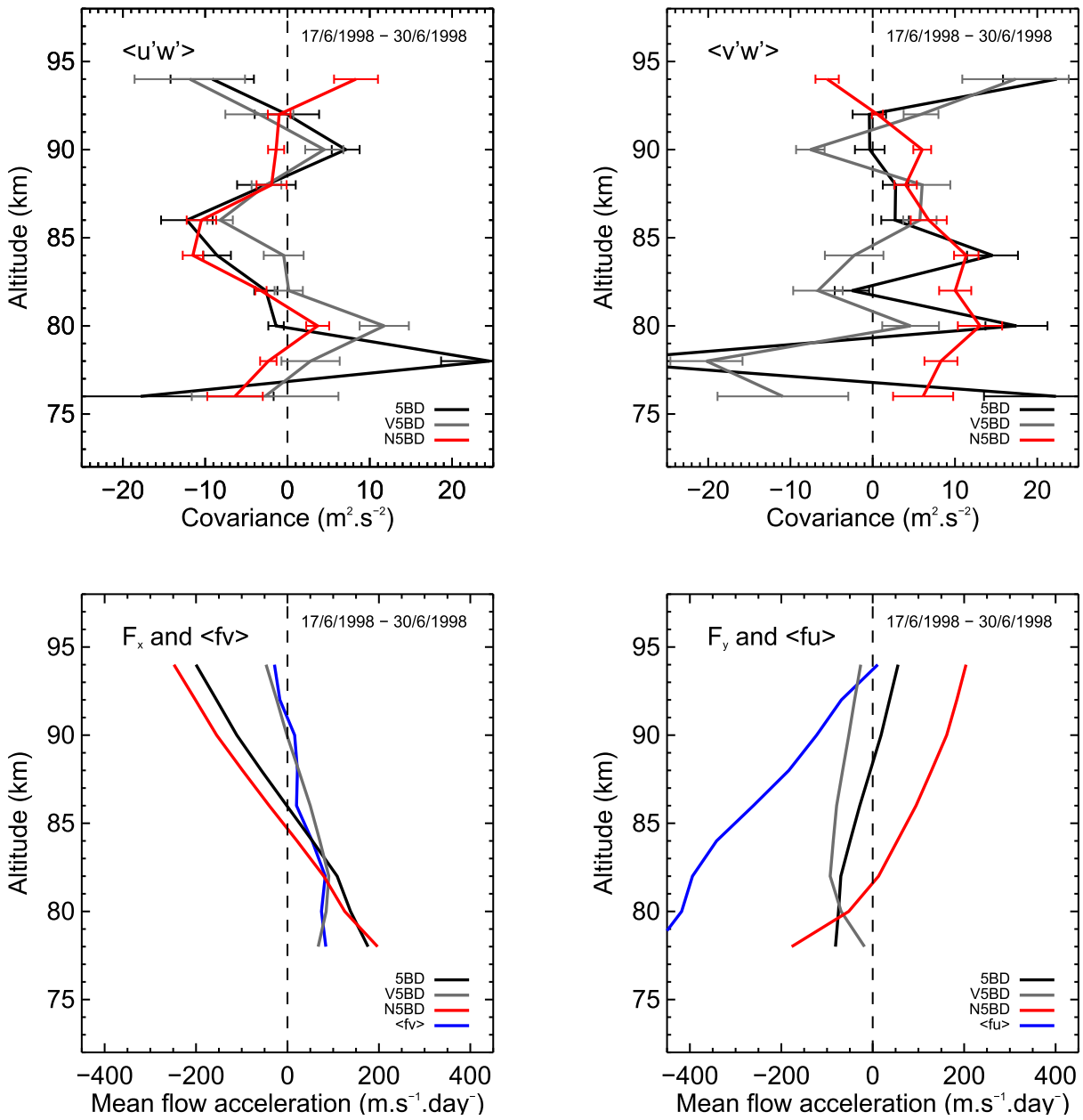

Fig. 6.10: As per Fig. 6.7, but for the June 1998 campaign.

contributions from gravity waves have been considered here.

Other studies of the same intercomparisons have mixed conclusions. Reid and Vincent [1987] compare Coriolis torques and inferred body forces using measurements derived from the Buckland Park MF radar, essentially encompassing all seasons and, as in this study, having measurements taken as part of dedicated campaigns lasting several days. They noted that the zonal body force was usually of the correct sense to balance the Coriolis torque due to the meridional wind, though the agreement varied from excellent (e.g., May 1982, their Fig. 12h) to poor (e.g., July 1982, their Fig. 12j). Hall et al. [1992] used 17 days of measurements from the Saskatoon MF radar (summer, 1989) to perform a similar comparison, and found good agreement between the zonal body force and meridional torque, but poor agreement in the orthogonal plane. Frame et al. [2000] also considered this intercomparison, using one month of data from the Buckland Park and Christchurch (New Zealand)

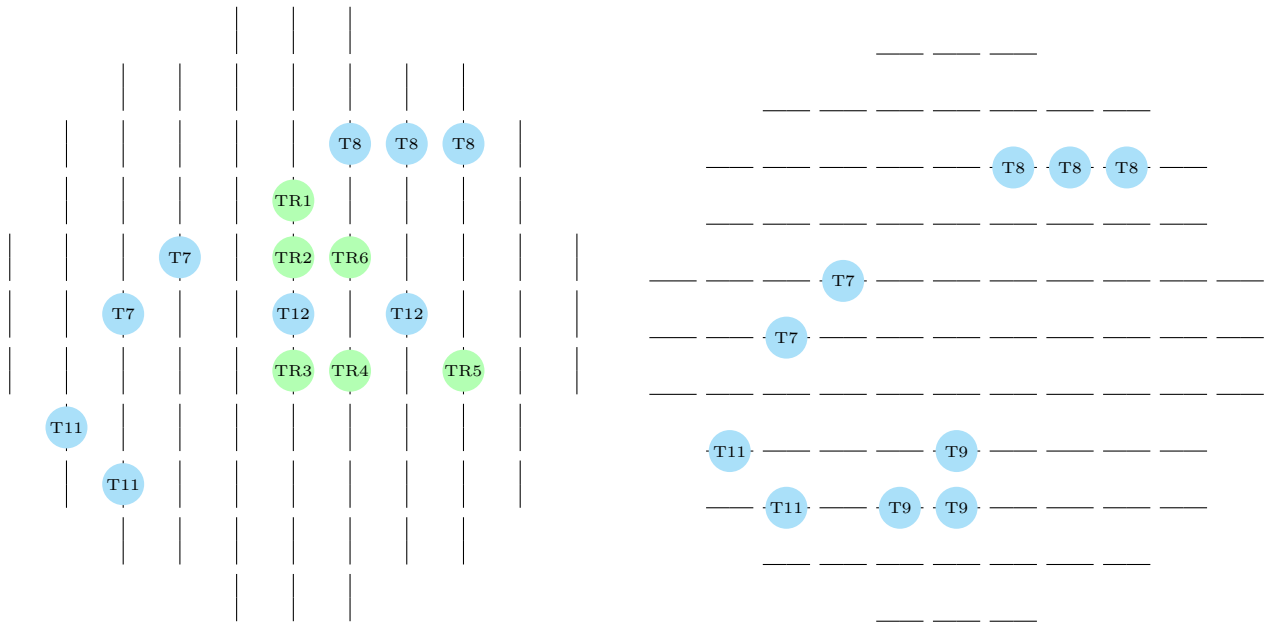

Fig. 6.11: Transmitter and receiver configuration used in the October 2015 HDI experiments reported in this work (Sect. 6.4). Transmit-receive antennas are shown in green, and transmit-only groups are shown in blue.

MF radars (May 1992). They obtained good agreement between the gravity wave-driven body forces and Coriolis torques in the zonal and meridional directions at Christchurch, but inconsistent results at Adelaide. In a more recent study employing DBS on the Saura MF radar, Placke et al. [2015] notes good agreement between body forces and Coriolis torques during summer in the MLT, but not during winter (as done here, attributing the winter result to planetary wave contributions to the momentum flux).

In the analysis reported here, only HDI radial velocities/EBPs with no reported error (see Table 3.1) have been used as inputs to inversions for wind/RST component estimation. Doing so should have removed the likelihood of radial velocities derived from a sample suffering from a lack of beam directivity from entering the analysis. It is hoped that the detrimental effect any remaining points satisfying the "zero-error" criteria but still corresponding to a beam of poor directivity (whatever the reason) will have been reduced by weighting the inversions with the radial velocity variances. Whereas the ATRAD error codes only consider SNR/power/EBP, the variances are proportional to the squares of the spectral width and SNR reciprocals (though it is difficult to conceive a scenario resulting in high power, anomalously large spectral width, and a well-defined EBP that will return a non-representative mean radial velocity). It should be noted that a number cases of "zero-error" and anomalously large radial velocity variance were observed, but their genesis is yet to be determined.

6.4 Future work

The next step in this work is to compare HDI estimates of RST components with those of a co-located meteor radar, now that a clear indication of the ability of the 5-beam Doppler technique to measure physically reasonable momentum fluxes has been established. To this end, an experiment

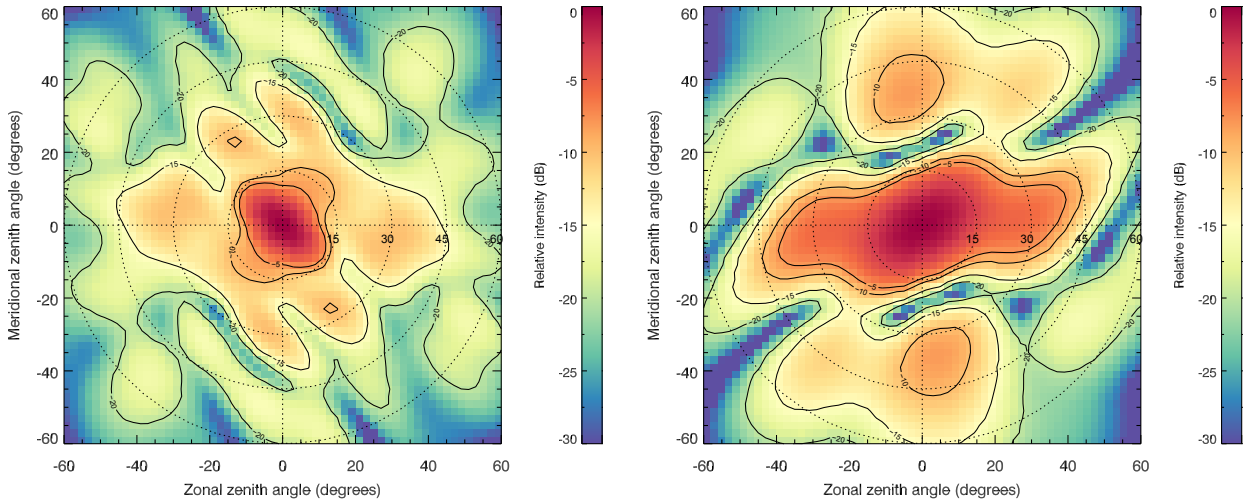

Fig. 6.12: Modelled one-way transmit polar diagram for the antenna configuration proposed in Fig. 6.11 (left) and the receiver polar diagram used for steering a beam in software (right).

on the BP MF array has recently been configured for HDI studies, with an antenna configuration shown in Fig. 6.11. The configuration utilises six individual antennas close to the centre of the array for reception (which are also used as transmit antennas) and 19 other elements for transmission. Beamsteering is applied on transmission to form a symmetric 5-beam arrangement (as done in the 1997-98 studies) with a tentatively-selected off-zenith beam angle of 10°.

Transmit and receive polar diagrams for this configuration are shown in Fig. 6.12. The transmission function is clearly less ideal than that used in the 1998 experiments, radiating relatively large amounts of power at zenith angles up to 45° with an anisometric main lobe. The receive polar diagram is also of an undesirable shape, again with an anisometric main lobe and large grating lobes close to the Cardinal directions. Nonetheless, in light of the V5BD results presented in this Chapter, it is thought that such a polar diagram will still be sufficient for RST component extraction if transmit beams are confined to small off-zenith angles (e.g., $\lesssim 10°$), such that the power received from transmit grating lobes remains low.

This experiment was configured in early October 2015. It was originally intended to show a preliminary comparison of RST component measurements from this radar and the co-located meteor system in this work; problems encountered in obtaining good radial velocity acceptance rates in the off-zenith beams have delayed this analysis. Also, in late September 2015, the connector to one of the receive antennas on the BP meteor radar began to intermittently fail, manifesting in a substantially decreased meteor detection rate. These problems have rendered the RST estimates unrepresentative of the respective techniques, and so must be resolved before the experiment can proceed.

It should be noted that Placke et al. [2014] recently compared 4-year climatologies of momentum flux estimates afforded by the Saura MF array and Andenes meteor radar (which are separated by $\sim$ 25 km). The comparison was qualitative; the structures in the climatologies of $\langle u'w' \rangle$ showed some similarity, and the $\langle v'w' \rangle$ climatologies showed marked differences. In their analysis of the MF radar data, they also employed the original Vincent and Reid [1983] estimator for momentum flux

evaluation, and did not apply interferometry to determine an EBP. In their defence, the Saura MF radar transmits and receives on a considerably narrower beam than does the BP MF (3.2° [Placke, 2014] vs. 5.7°), and so the effects of aspect sensitivity on the beam position are reduced. Moreover, both modelling and observational work conducted here shows that "naïvely" assuming a fixed beam position may not be detrimental at least to the sense of the obtained results.

An area for improvement of the analysis technique used in this study concerns the quality of the assumption of stationary tides and planetary waves over the window length selected (4 days). Observations of transience in tidal/planetary wave parameters in the MLT-region on this time scale are not new (e.g., Merzlyakov et al. [2005]), and techniques which accomodate the analysis of non-stationary time series are available and have been used before for tidal analysis (see Sect. 5.1.3, pg. 64). These influences should be assessed specifically in this study using some kind of wavelet analysis (S-transform or otherwise), and subsequently projected onto and removed from the radial velocity field.

6.5 Summary

Components of the RST have been derived by applying Thorsen et al. [1997]'s inversion technique to Buckland Park MF radar data, derived from a symmetric 5-beam Doppler experiment run during 1997-98. The analysis mainly sought to compare the accuracies of momentum fluxes obtained when interferometric techniques (in this case, HDI) are used for EBP determination, to the results of older studies in which the EBP and transmitted beam direction were assumed equivalent. The results of the two techniques compared quite favourably, which indicate that accounting for the EBP, while important for improved accuracy, may not be essential. This result is in general agreement with those of the modelling study presented in Chapter 5.

The stresses derived solely from the vertical beam were also compared to those from all five beams. The results from the vertical beam were generally more variable than those from all five, though their structures in their mean vertical flux of horizontal momentum profiles were similar. The level of agreement between the two techniques for horizontal variances was poorer, although means across vertical profiles were still similar.

Very poor agreement was found between Doppler and FCA-derived horizontal variances. The latter almost consistently overestimated the former. The cause of this discrepancy is not clear. It does put a question on the physicality of variances derived directly from FCA horizontal winds, though a more thorough investigation is needed to determine the true nature of their bias.

The body forces inferred from the momentum fluxes derived from the Doppler techniques were also compared to Coriolis torques due to the mean winds. Very poor agreement was noted between these quantities. However, this is not to the detriment of the quality of the derived momentum fluxes, since the quantities are only equivalent when zonally averaged. The results presented were also predominantly from winter months, and so planetary wave contributions to the momentum flux, which were not accounted for here, may have been significant.

Chapter 7

Conclusion

7.1 Thesis summary and conclusions

This thesis has been concerned with measurements of the energy and momentum transport due to gravity waves in the upper part of the Earth's middle atmosphere (60-110 km), otherwise known as the Mesosphere-Lower-Thermosphere (MLT). Such measurements are of great importance to global climate models, which at present use poorly-constrained parameterizations of gravity wave effects in this region and lower parts of the atmosphere. The limitation in the models is largely a consequence of the expense and hence sparse spatial distribution of instruments which can measure energy and momentum fluxes of the relevant scales correctly.

Given the relative inexpensiveness of their system components and their purported ability to measure gravity wave momentum fluxes, it has been hoped that meteor detection radars will play an important role in addressing this problem. To the contrary, recent modelling work showed that these radars cannot measure momentum fluxes to a useful level of accuracy, even with substantial time-averaging. Despite this somewhat undesirable evidence, many workers have continued to utilise momentum flux estimates from these instruments to characterize wave activity in the MLT.

Measurements of gravity wave momentum fluxes have been made before, as part of multi-day campaigns during the 1980s and early 1990s utilising large phased-array Doppler radars. The measurements derived from these campaigns are widely considered as being accurate and representative of gravity wave effects. It was envisaged that re-configuring one of these systems—the Buckland Park medium frequency (BP MF) array (34.6°S, 138.6°E)—for such measurements, and then comparing them with those from a co-located meteor detection radar, would clarify the meteor system's measurement accuracy.

Standing wave ratio and time domain reflectometry measurements on the antennas/transmission lines indicated that array refurbishment would be needed before such an experiment could be re-configured. A refurbishment plan was created by investigating which feasible combination of transmission line replacements would give the array a polar diagram suitable for steering beams to small ($\sim 10^\circ$) off-zenith angles. A suitable polar diagram was found to be attainable with the replacement of three transmission lines, although it was soon realised that such an approach is currently financially untenable.

Attention was redirected into analysing symmetric 5-beam campaign data from the BP MF, from four periods during 1997-1998. The application of Hybrid Doppler Interferometry (HDI) on the received data showed substantial fluctuations in the effective beam position (EBP), despite the transmit beam directions being fixed. Aforementioned momentum flux analyses using the MF array had not considered the effect of EBP fluctuations of this size on the analysis. This raised suspicion concerning the validity of the momentum flux estimates from the technique.

To this end, a gravity wave flux measurement simulation of the Doppler technique was created. This utilised real spatiotemporal distributions of EBPs recorded from the technique, and a wind field with superposed tidal and gravity wave contributions. Additionally, variations on the Doppler technique, including the sole use of vertical beams and a multi-beam experiment with no assumed knowledge of the EBP, were also tested, along with the meteor technique. Gaussian-distributed EBP measurement uncertainties were included for improved realism, though the error magnitudes employed were preliminary and possibly larger than the true uncertainties of the respective techniques. Broadly, the results showed that the 5-beam Doppler technique will slightly underestimate horizontal variances and momentum fluxes, and overestimate vertical variances. If no interferometric capability is available, the 5-beam technique will overestimate all variance and covariance quantities except those between the horizontal wind components. The meteor technique was seen to estimate all aforementioned terms accurately, though with notably less precision on momentum fluxes than the 5-beam technique. Finally, the results demonstrated that the sole use of a vertical beam will not necessarily lead to momentum flux estimates of the correct sign. However, this is not conclusive evidence that such data is not useful, which remains to be determined.

With confidence in the 5-beam Doppler technique's momentum flux measurement capability, a similar analysis was performed on the radial velocity data recorded during the four campaigns. The momentum flux results from the HDI-5-beam data favourably agreed with those in which no interferometric capability was assumed, which in turn agreed reasonably well with those from solely a vertical beam. However, the latter did contain larger fluctuations with altitude, which are thought to be spurious. In attempt to confirm the validity of the momentum flux estimates, mean flow accelerations associated with the estimates were calculated. At least for a zonal average, these are expected to be equivalent to the Coriolis torques due to the orthogonal wind. Very poor agreement was found between the accelerations and Coriolis torques; this has been mainly attributed to contamination from planetary waves.

Horizontal variances and covariances derived from the Doppler techniques were also compared to those estimated directly using Full Correlation Analysis (FCA) horizontal winds. In particular, the Doppler variances tended to substantially underestimate those derived from the FCA—in some cases by a factor of around 70%. This may in part be due to angle of arrival determination errors in the Doppler measurements, though given the size of the underestimations, a secondary contributor is suspected. It is also not clear if this result indicates that the FCA systematically overestimates gravity wave variances.

A similar technique was applied to estimate variances from long-term FCA and meteor radar wind

data sets, and determine any evidence of trends therein. The FCA data set (1996-2010) was from the BP MF, and the meteor's (2005-2014) from the 33 MHz radar at Davis (68.6°S, 78.0°E). At Buckland Park, negative trends (though insignificant at the 1-sigma level) were detected in the magnitudes of the summer and winter wind jets (70-80 km) and in the zonal variances due to waves of periods 20-120 minutes during summer (70-98 km). Notably, these are opposite in sense to those reported for Juliusruh in Hoffmann et al. [2011], though it is not yet clear if the reduction in the westward summer wind has filtered, through critical level absorption, more eastward propagating waves from the gravity wave spectrum. In the Davis dataset, a decrease in the summer zonal wind velocity was observed (between 85 and 90 km), though no statistically significant trends were noted in the variances.

The F10.7 cm flux, a "proxy" for the solar cycle, was also included in the above regressions. Few statistically significant correlations were noted; at Buckland Park, the flux was negatively correlated with the winter variances between about 80 and 85 km, and at Davis, the flux was positively correlated with the summer zonal winds across the observed height range (80-95 km).

As a whole, this thesis has (1) shown a successful evaluation of small-scale gravity wave characteristics using a phased-array Doppler radar, and (2) has presented preliminary evidence of long-term changes in gravity wave activity in the upper atmosphere. (1) confirms that the 5-beam Doppler technique is an adequate candidate for experimentally testing, via a statistical comparison of the results, the momentum flux measurement capability of meteor radars. (2) encourages continued investigation of the signs of gravity wave activity trends in the upper atmosphere.

7.2 Suggestions for future work

A statistical comparison of stress terms afforded by the BP MF and meteor radars is yet to be performed. The antenna configuration for a HDI experiment on the BP MF array was discussed in Sect. 6.4, and gain calibration results for the receiver were shown in Sect. 2.1.5. At the time of writing (October 2015), the discussed configuration is being utilized on the array, with the transmitted beam being steered symmetrically about the zenith in a standard 5-beam arrangement. However, the radial velocity acceptance rates in some of the beams are too low for a stress term analysis to be practical; the cause for this is presently unknown. Additionally, the connector on the fourth receiver of the meteor radar must be replaced; the count rates from the radar are currently in the range of half of that expected for optimal operation. Once these problems have been rectified, an analysis of the data from the two radars following the methodology of that in Chapter 6 could proceed.

The quality of the BP MF's polar diagram (and hence, the results of the above experiment) could be improved by increasing the number of antennas available for use. With little doubt, this will require the replacement of some of the underground transmission lines. A proposition for this is discussed in Sect. 2.1.4.

In Chapters 5 and 6, mean winds were determined by a least squares fit to fields of radial velocities. First order shears were also accounted for in the fitting process. It was originally intended to use these

shear terms to complement the RST component analysis in some way—for example, to see if horizontal variances correlate with gradients across the wind field, and determine if those gradients should be removed prior to RST component estimation. This has not been done yet, and is a recommended avenue for future work. As an aside, the fitting of shear terms also appears to have been omitted from recent studies of MLT-region winds utilizing Doppler velocities, for no apparent reason.

The technique used here for RST component determination also incorporates a subtraction of tidal and planetary wave components, but assumes that those components are stationary. This assumption remains to be verified for the data examined. If it is found to be invalid, a more suitable method of estimating the components should be used (e.g., a wavelet transform, or the related S-transform, which has been used in more recent studies).

The realism of the models presented in Chapter 5 could be improved by incorporating more representative angle-of-arrival measurement uncertainties. That used for the meteor radar in this work ($\pm 1^\circ$), while probably accurate, was a rough guess based on experience, and the value used for the MF radar ($\pm 1.5^\circ$), is probably an overestimate. A more accurate figure for the meteor radar could be obtained by evaluating the variance in the positions of duplicate meteor detections derived from e.g., the 33 and 55 MHz radars at Davis. For the MF array, it would be more valid to determine the phase measurement uncertainty by injecting a radar signal of known phase directly into the antennas connected to the receiver channels in question.

The BP MF FCA data set used for long-term trend estimation should also be extended. As discussed in Sect. 4.2, FCA measurements on a small receiver triangle commenced at BP in 1973. The dynamic range of the data prior to 1996 was noted to be different to that post-1996, and so, in the interests of obtaining realistic trends, it was excluded from the analysis presented here. However, if care is taken in "normalizing" the sensitivity of the instrument for the duration of the observations, there is the promise of an unprecedented FCA data set spanning more than three solar cycles. This would prove an invaluable addition to the ever-growing repository of studies of change in the upper atmosphere.

A more straightforward addition to this study could be made by comparing the long-term trends present in the small- and large-triangle FCA data sets. If the results are consistent, more confidence could obviously be assigned to the entire small-triangle BP data set.

The Davis MF radar has also acquired 21 years of FCA data (commencing 1994). As discussed in the summary of Chapter 4, the polarization the radar was using through most of this period is unclear, and so the data was excluded from this analysis. Rectifying this, while likely extremely tedious, would provide a useful window into any long-term trends in the Antarctic MLT, and also provide a useful comparison to the co-located meteor radar results.

The long-term study's analysis technique should also be extended to one which does not assume static trends. A number of studies exist which employ autoregressive techniques to determine statistically significant "breakpoints" in MLT-region wind and temperature time series trends. These studies have shown conclusively that such trend breakpoints do exist, and that a deeper understanding of their cause may be obtained by correlating them with the signs of trends in various lower atmosphere

indices (e.g., the Southern Oscillation Index). An additional motivation is that no such approach has yet been applied to gravity wave activity trends.

Finally, no explanation has yet been tendered for the discrepancies between the variances derived from the five-beam Doppler and FCA techniques. Determining whether or not the Doppler's underestimation is entirely attributable to angle-of-arrival estimation errors would help with clarifying the validity of the FCA variances. Ultimately, it is not yet even known if long-term trends derived from them are valid, although no evidence to the contrary exists.

Appendix A

Published paper: J. Geophys. Res. Atmos., 120, 9323-9337, 2015

AGU PUBLICATIONS

JGR

Journal of Geophysical Research: Atmospheres

RESEARCH ARTICLE
10.1002/2015JD023197

Key Points:
- Mountain waves penetrate the mesosphere under suitable propagation conditions
- Small-scale gravity waves can attain very large momentum fluxes
- Occurrence of peak momentum fluxes is often dictated by multiscale environments

Correspondence to:
K. Bossert,
Katrina.Bossert@gmail.com

Citation:
Bossert, K., et al. (2015), Momentum flux estimates accompanying multiscale gravity waves over Mount Cook, New Zealand, on 13 July 2014 during the DEEPWAVE campaign, *J. Geophys. Res. Atmos.*, *120*, 9323–9337, doi:10.1002/2015JD023197.

Received 30 JAN 2015
Accepted 20 AUG 2015
Accepted article online 24 AUG 2015
Published online 23 SEP 2015

Momentum flux estimates accompanying multiscale gravity waves over Mount Cook, New Zealand, on 13 July 2014 during the DEEPWAVE campaign

Katrina Bossert[1,2], David C. Fritts[1], Pierre-Dominique Pautet[3], Bifford P. Williams[1], Michael J. Taylor[3], Bernd Kaifler[4], Andreas Dörnbrack[4], Iain M. Reid[5,6], Damian J. Murphy[7], Andrew J. Spargo[6], and Andrew D. MacKinnon[6]

[1]GATS Inc., Boulder, Colorado, USA, [2]Aerospace Engineering Science, University of Colorado Boulder, Boulder, Colorado, USA, [3]Center for Atmospheric and Space Sciences, Utah State University, Logan, Utah, USA, [4]Institute of Atmospheric Physics, German Aerospace Center, Oberpfaffenhofen, Germany, [5]School of Physical Sciences, University of Adelaide, Adelaide, South Australia, Australia, [6]ATRAD Pty Ltd., Thebarton, South Australia, Australia, [7]Australian Antarctic Division, Department of the Environment, Kingston, Tasmania, Australia

Abstract Observations performed with a Rayleigh lidar and an Advanced Mesosphere Temperature Mapper aboard the National Science Foundation/National Center for Atmospheric Research Gulfstream V research aircraft on 13 July 2014 during the Deep Propagating Gravity Wave Experiment (DEEPWAVE) measurement program revealed a large-amplitude, multiscale gravity wave (GW) environment extending from ~20 to 90 km on flight tracks over Mount Cook, New Zealand. Data from four successive flight tracks are employed here to assess the characteristics and variability of the larger- and smaller-scale GWs, including their spatial scales, amplitudes, phase speeds, and momentum fluxes. On each flight, a large-scale mountain wave (MW) having a horizontal wavelength ~200–300 km was observed. Smaller-scale GWs over the island appeared to correlate within the warmer phase of this large-scale MW. This analysis reveals that momentum fluxes accompanying small-scale MWs and propagating GWs significantly exceed those of the large-scale MW and the mean values typical for these altitudes, with maxima for the various small-scale events in the range ~20–105 $m^2 s^{-2}$.

1. Introduction

Gravity wave (GW) momentum transport and deposition throughout the atmosphere have significant impacts on Earth's weather and climate. Momentum deposition causes drag on mean and larger-scale winds, resulting in reversals of the mesospheric jets, an induced residual circulation that impacts mean temperatures from the lower altitudes into the mesosphere and lower thermosphere (MLT), and modulations of larger-scale motions and their mapping to higher altitudes [e.g., *Holton*, 1982, 1984; *Garcia and Solomon*, 1985; *Haynes et al.*, 1991; *Smith*, 2003; *Fritts and Alexander*, 2003; *Kim et al.*, 2003; *Lieberman et al.*, 2010, 2013]. Many studies suggest that GWs having smaller horizontal wavelengths and higher intrinsic frequencies contribute significantly to the total momentum budget [e.g., *Vincent and Reid*, 1983; *Fritts and Vincent*, 1987]. In some cases, small-scale GW momentum fluxes (MFs) are tied to specific sources such as orography and convection [e.g., *Nastrom and Fritts*, 1992; *Pfister et al.*, 1993]. In other cases, strong localized GW packets exhibit no obvious sources and more likely achieve large amplitudes and MFs due to filtering by the larger-scale environments [e.g., *Hertzog et al.*, 2012; *Fritts et al.*, 2002, 2014]. Some modeling studies show that smaller-scale GWs may be significantly influenced by multiscale GW environments [*Eckermann*, 1997]. Despite many studies and valuable insights, much remains to be learned about the multiscale interactions that influence small-scale GW behavior and the character and statistics of small-scale GW contributions to total MFs throughout the atmosphere.

Many studies using individual instruments or instrument suites have contributed to our understanding of GWs at larger and smaller scales. Ground-based instruments such as lidars, airglow imagers, and radars have been used to characterize GW activity [e.g., *Fritts*, 1984, and references therein; *Wilson et al.*, 1991; *Collins et al.*, 1996; *Taylor et al.*, 1997; *Yue et al.*, 2009]. Lidars allow for a vertical and temporal characterization of GWs and profiles of buoyancy frequency and/or background winds that define the GW propagation environment. Airglow imagers provide valuable information on GW horizontal scales, orientations, and propagation directions that are challenging to infer from lidars and radars alone. The more recent Advanced Mesosphere

AGU Journal of Geophysical Research: Atmospheres 10.1002/2015JD023197

Temperature Mappers (AMTMs) also provide temperature images at the OH layer [*Pautet et al.*, 2014], which prove especially valuable in quantifying small-scale GW amplitudes and MFs [e.g., *Fritts et al.*, 2014]. Indeed, various combinations of these instruments have contributed greatly to a broader understanding of GWs over many years [e.g., *Collins and Smith*, 2004; *Williams et al.*, 2006; *Namboothiri et al.*, 1996; *Hecht et al.*, 1997; *Nielsen et al.*, 2012; *Bossert et al.*, 2014; *Cai et al.*, 2014; *Yuan et al.*, 2014; *Ejiri et al.*, 2009; *Simkhada et al.*, 2009] because such combinations of instruments allow for a more complete quantification of GW environments and parameters.

Measurements from various instruments allow for the quantification of mean and variable GW momentum flux within the MLT. Multiple radars from equatorial to polar latitudes have revealed typical mean zonal momentum flux magnitudes of $<u'w'>$ ~1–20 $m^2 s^{-2}$ in the MLT that are anticorrelated with zonal mean winds and with lower (higher) values at lower (higher) altitudes and latitudes [*Vincent and Reid*, 1983; *Fritts and Vincent*, 1987; *Reid et al.*, 1988; *Tsuda et al.*, 1990; *Wang and Fritts*, 1990; *Hitchman et al.*, 1992; *Fritts et al.*, 2010, 2012; *Murphy and Vincent*, 1993; *Nakamura et al.*, 1993]. Global MF averages from satellites have provided previous estimates ranging from ~1 to 8 $m^2 s^{-2}$ in the MLT [*Ern et al.*, 2011]. Local estimates for short-term (~1–6 h) averages using radars are often ~30–60 $m^2 s^{-2}$ or larger, while local estimates employing airglow observations suggest systematic geographic conditions and occasional, very strong events having $<u'w'>$ magnitudes as large as ~900 $m^2 s^{-2}$ [*Fritts et al.*, 2014; *Espy et al.*, 2004]. Finally, satellite measurements have allowed for calculations of the residual-mean circulation and provided estimates of total wave drag (assumed to be due primarily to GWs in the mesosphere) that are similar in form to but somewhat smaller in magnitude than radar measurements at corresponding latitudes and altitudes [*Lieberman et al.*, 2000].

The Deep Propagating Gravity Wave Experiment (DEEPWAVE) research program was conceived to take advantage of the synergism between multiple instruments and performed measurements addressing GW responses to multiple sources throughout a large and active source region. For these purposes, DEEPWAVE employed two new airborne lidars and an AMTM developed specifically for the National Science Foundation/National Center for Atmospheric Research (NSF/NCAR) Gulfstream V (GV) research aircraft. These measurement capabilities were augmented by a second aircraft, the German DLR Falcon having in situ instruments and a downward viewing aerosol Doppler lidar and extensive ground-based measurements extending from the surface to ~100 km on the New Zealand South Island and Tasmania. An overview of the DEEPWAVE program [*Fritts et al.*, 2015] describes the program motivations, measurement and modeling capabilities, performance, and initial results. DEEPWAVE was performed on and over South Island, Tasmania, and the surrounding Southern Ocean and Tasman Sea during June and July 2014, with aircraft operations and program logistics based in Christchurch.

Research reported here addresses GW dynamics observed by the GV Rayleigh lidar, AMTM, and two IR "wing" cameras at altitudes from ~20 to 90 km on Research Flight 22 (RF22) performed on 13 July, one of the 26 GV research flights performed throughout DEEPWAVE. The DEEPWAVE instrumentation and data are described in section 2. Sections 3 and 4 describe the estimates of GW parameters and momentum fluxes. A discussion of the results and our conclusions are provided in sections 5 and 6.

2. Research Data and Instrumentation

DEEPWAVE data employed for this study were collected with the new GV Rayleigh lidar, AMTM, and wing cameras viewing the OH layer to either side of the GV in order to extend the cross-track imaging to ~900 km. A brief description of each measurement capability and data analysis is provided below.

2.1. GV Advanced Mesosphere Temperature Mapper

The GV AMTM is a newly developed IR imager measuring selective lines of the OH (3,1) emission. This bright emission originates from a ~8 km full width at half maximum (FWHM) layer located at ~87 km in altitude [*Baker and Stair*, 1988; *She and Lowe*, 1998] and is widely used as a tracer of the dynamical processes propagating through the upper atmosphere. The AMTM comprises a 320 × 256 pixel IR sensor, a large-aperture telecentric lens system, and a computer-controlled filter wheel to sequentially measure the brightness of the $P_1(2)$ and $P_1(4)$ lines of the OH (3,1) band, as well as the atmospheric background. Combining these three emissions, it is possible to calculate the OH (3,1) rotational temperature for each pixel of an image and "map"

AGU Journal of Geophysical Research: Atmospheres 10.1002/2015JD023197

the mesospheric temperature over a ~120 × 80 km area [*Pautet et al*., 2014]. During the DEEPWAVE flights, the exposure time for each filter was 4 s, providing a temperature measurement every ~16 s, with a typical error of ±2 K for each individual pixel. In the months preceding the campaign, cross calibration was performed by operating the AMTM alongside the well-proven Utah State University Na lidar. The two instruments were in good agreement on individual nights as well as on an average basis. The accuracy relative to the lidar measurements at 87 km was <1 K. In addition to the AMTM, two low-elevation (25° above the horizon) IR imagers were operated on each side of the plane. They only measured the OH emission brightness, but their large field of view (~40 × 30°) allowed to laterally extend the region of the MLT observed from the aircraft and to investigate the large-scale gravity waves covering its surroundings.

2.2. GV Rayleigh Lidar

The Rayleigh lidar is a new facility instrument built at GATs Inc. for the NSF/NCAR Gulfstream V. This lidar and the GV sodium lidar are contained in two standard GV instrument racks. The laser is a diode-pumped Nd:YLF Photonics DS20-351 generating 5 W at a 351 nm wavelength and a 1 kHz pulse repetition rate. The beam is expanded to 20 mm diameter and 0.4 mrad divergence, so that it is eye safe for 0.25 s exposures when it exits the laser windows on the top of the aircraft. The return signal is received using a 0.3 m diameter f/4 Newtonian telescope. The fiber-coupled detector is a 50% quantum efficiency, low-noise photomultiplier tube with a 0.5 nm FWHM interference filter. The returned signal profiles are recorded at 1 s temporal and 37.5 m altitude resolution.

Following the normal Rayleigh procedure, an atmospheric density profile is calculated from the lidar signal profile taking into account the geometric factors. The density is integrated down from a top starting temperature to obtain a temperature profile. For the start temperature, we used the European Centre for Medium-Range Weather Forecasts (ECMWF) model temperature at 71 km interpolated to the aircraft time and position. This calculation assumes that there is no aerosol scatter. Temperature results are shown from 20 to 60 km. At 40 km altitude, the temperature error is ~2 K in a 30 s, 3 km integration.

2.3. GV Sodium Lidar

The sodium lidar is a high spectral resolution system that shares the same racks, telescope, and receiver electronics as the Rayleigh system. The transmitter is a narrowband Toptica continuous wave laser composed of a 18 W Raman fiber amplifier doubled to produce 10 W of 589 nm light with a 10 MHz line width. The laser output light is locked to the D2a feature in the sodium Doppler-free saturation spectrum. We use an acousto-optic amplitude modulator to produce 20 μs square pulses repeating at 1 kHz. This modulator produces a small 80 MHz frequency shift, which we account for in the analysis. This pulsed beam has a 150 km total range and 3 km range resolution.

The receiver is fiber coupled to the telescope. We use a 75% transmission 1 nm bandwidth interference filter and a 40% quantum efficiency photomultiplier tube. This beam is synchronized with the Rayleigh beam to avoid cross talk, and the data are recorded on the same counter board oversampled at 1 s and 37.5 m resolutions. For postprocessing, the counts are averaged in bins of 1 km and 3.2 min (~45 km spatially) and Rayleigh normalized at altitudes from 30 to 35 km using Mass Spectrometer Incoherent Scatter (MSIS). The mixing ratios are calculated from sodium densities and relative background atmospheric conditions based on a scale height calculated from the AMTM temperature and MSIS densities at 87 km.

2.4. Lauder Rayleigh Lidar

The German Aerospace Center (DLR) Rayleigh lidar at Lauder (45.0°S, 169.7°E) is a mobile mesospheric lidar system contained in an 8 foot container. The transmitter comprises a diode-pumped Nd:YAG laser generating 12 W at 532 nm wavelength and 100 Hz pulse repetition rate. Backscattered light is collected using a fiber-coupled 25 inch diameter telescope mirror with a field of view (FOV) of 0.24 mrad. In the receiver the light is distributed between three detectors, a 608 nm Raman channel and low and high rate 532 nm channels. The timing of detected photons is recorded at 2 ns resolution. The temperature is initialized at 95 km. For the nightly average, the count profiles are vertically averaged over a 900 m resolution.

2.5. Kingston Meteor Detection Radar

An ATRAD meteor detection wind radar, capable of measuring wind speeds between heights of 70 and 110 km, operated at Kingston, Tasmania (43.0°S, 147.3°E), from 10 June 2014 through the DEEPWAVE

AGU Journal of Geophysical Research: Atmospheres 10.1002/2015JD023197

measurement program. The radar consisted of a high-power pair of crossed folded dipole antennas for circularly polarized all-sky transmission at the radar frequency of 55.0 MHz and a Mills cross array of five crossed Yagi receiving antennas. Transmitted power was 40 kW peak. Winds were derived at equally spaced heights by least squares fitting a nondivergent wind field to 1 h windows of radial velocity determinations. A general system description of this type of meteor radar is given by *Holdsworth et al*. [2004].

3. Determination of GW Parameters

The observed GWs were characterized using the methods and equations from *Fritts et al*. [2014] and *Fritts and Alexander* [2003], an overview of which is provided here. The GW perturbations are assumed to have the approximate forms given by

$$\widetilde{u},\widetilde{w},\widetilde{T},\widetilde{p},\widetilde{\rho}\sim u',w',\frac{T'}{\overline{T}},\frac{p'}{\overline{p}},\frac{\rho'}{\overline{\rho}}\left(\exp\left[i(kx+mz-\omega t)+\frac{z}{2H}\right]\right) \tag{1}$$

Where u', w', T', p', and ρ' are horizontal and vertical velocity, temperature, pressure, and density perturbations; $\overline{T}$ is the mean temperature; $\overline{\rho}$ is the mean density; $\omega = kc$ is the GW frequency; and H is the scale height. The buoyancy frequency squared is given by

$$N^2=\frac{g}{\overline{T}}\left[\frac{d\overline{T}}{dz}+\frac{9.5K}{km}\right] \tag{2}$$

From the polarization relations in *Fritts and Alexander* [2003], the momentum flux (MF) averaged over a wavelength of a GW can be obtained as follows:

$$\mathrm{MF}=<u'w'>=\frac{1}{2}u'^2\left(\frac{k}{m}\right)=\frac{1}{2}\left(\frac{T'}{\overline{T}}\frac{g}{N}\right)^2\left(\frac{k}{m}\right) \tag{3}$$

The above equation calculates the vertical flux of horizontal momentum. Here $k = 2\pi/\lambda_h$ is the horizontal wave number, $m = 2\pi/\lambda_z$ is the vertical wave number, and λ_h and λ_z are the horizontal and vertical wavelengths, respectively. Equation (3) gives a low-end estimate for MF, as it uses raw temperatures and does not account for phase averaging over the hydroxyl layer. For an ideal GW propagating through the hydroxyl layer, the temperature perturbation, T', can be corrected by dividing by a correction factor, C_F, as $T'\mathrm{corr} = T'/C_F$. The correction factor, C_F, for this ideal case is given in equation (4).

$$C_F=\frac{<T'>}{T'(z_o)}=\exp\left[\frac{-\pi^2 z_{\mathrm{FWHM}}^2}{4\ln(2)\lambda_z^2}\right]=\exp\left[-3.56\frac{z_{\mathrm{FWHM}}^2}{\lambda_z^2}\right] \tag{4}$$

The quantity $<T'>$ in equation (4) is the temperature perturbation measured by the AMTM, which is smaller than the true T' amplitude due to phase averaging over the OH layer. The Sounding of the Atmosphere using Broadband Emission Radiometry (SABER) instrument on the TIMED satellite measured the OH profile on an overpass near South Island on 13 July that indicated an OH layer height of ~87 km and an OH layer FWHM of ~7 km. With the GW λ_h and k from the AMTM, m can either be derived from lidar data (with sufficient resolution and altitude coverage) or determined from the dispersion relation

$$m^2=\frac{N^2}{(c-u)^2}-\frac{1}{4H^2}-k^2 \tag{5}$$

Here c is the observed phase speed of the GW and u is the local background wind. Using lidar data and the AMTM, the MF can be calculated for observed GWs where the background conditions can be suitably approximated. This method is used to provide MF estimates for individual GW packets in the following section.

4. Momentum Flux Estimates

4.1. Observed GW Fields

The four cross-island GV flight segments on RF22 occurred between 6:15 and 9:10 UT (18:15–21:10 local time) and were each ~530 km in length. Each flight segment was sufficiently long to identify approximately two wavelengths of a stationary, large-scale MW seen in both the Rayleigh lidar temperatures from 20 to 60 km in altitude and in the AMTM and IR camera OH brightness at the OH layer altitude (~87 km). The side-viewing OH

Journal of Geophysical Research: Atmospheres 10.1002/2015JD023197

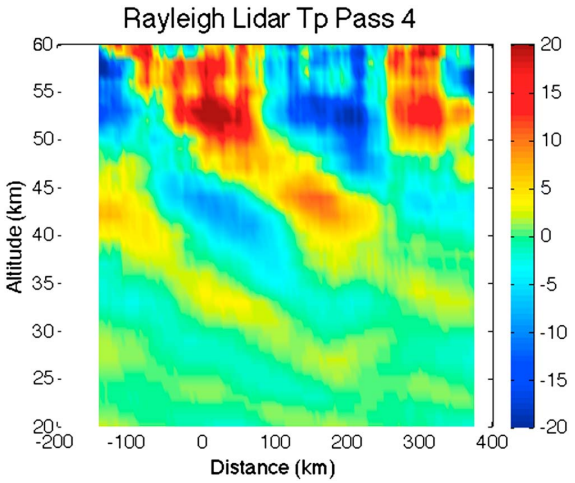

Figure 1. Rayleigh lidar temperature perturbations from the fourth pass show a vertical wavelength of ~20 km.

brightness images confirm that the phase fronts of the large-scale MW were indeed stationary along each pass. The slightly extended (east-west) imaging data suggest a MW λ_h varying from ~200 km at the eastern side of each flight segment to ~300 km at the western side, with a mean of $\lambda_h \sim 240$ km. Thus, we will assume the mean value for our analysis here.

The 240 km MW observed by the Rayleigh lidar is shown as a $T'(x,z)$ zonal-vertical cross section for flight segment 4 in Figure 1. $T'(x,z)$ was obtained by subtracting an averaged background temperature for the segment. This MW exhibits a pronounced increase in both its amplitude and its vertical wavelength with increasing altitude. T' varies from a few kelvins at the lower altitudes to ~15 K or larger at ~52 km and above. We expect amplitude growth with altitude for conservative GW propagation. At lower altitudes between ~20 and 55 km, the growth with altitude is a factor of ~8–10, which is expected for a GW with a mean scale height of $H \sim 6$–7 km that is growing in amplitude without significant dissipation. Likewise, λ_z increases with altitude from ~10 km or less below ~30 km in altitude to ~20–30 km at the higher altitudes. The changing vertical wavelength of the $\lambda_h \sim 240$ km MW is consistent with the increase in zonal wind predicted by the ECMWF model. For reference, Figure 2 shows the averaged zonal winds from ECMWF for the duration of the flight and the minimum and maximum values throughout the ECMWF domain. The increasing ECMWF zonal winds correlate with the increasing vertical wavelength observed in the Rayleigh lidar above 20 km. Additionally, we see that there was some modulation in the vertical phase structure of the $\lambda_h \sim 240$ km MW at intermediate and higher altitudes. This could have resulted from a superposition of MWs having other scales or phase slopes, or other propagating GWs, but uncertainties grow exponentially with altitude, so it is not possible to be confident of estimates based on Rayleigh lidar measurements approaching 60 km.

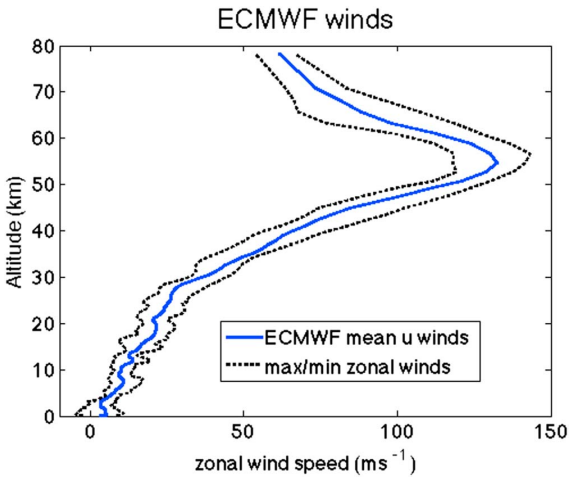

Figure 2. ECMWF winds averaged over the duration of the flight with the maximum and minimum winds included for reference.

As a guide for our inferences of MW and other GW structures seen in the AMTM data at higher altitudes, we note that a decreasing mean temperature above the stratopause would cause a smaller N and an increase in λ_z with altitude, whereas an expected reduction of the zonal wind would cause a decrease in λ_z with altitude.

DEEPWAVE forecasts by the European Center for Medium-Range Weather Forecasts (ECMWF) provided for flight planning and analysis purposes for RF22 (not shown) agree reasonably well with the T' fields obtained with the Rayleigh lidar and suggest refraction to somewhat smaller $\lambda_z \sim 20$ km above 60 km altitudes, apparently in response to the larger influences of weakening zonal winds above. Additionally,

AGU Journal of Geophysical Research: Atmospheres 10.1002/2015JD023197

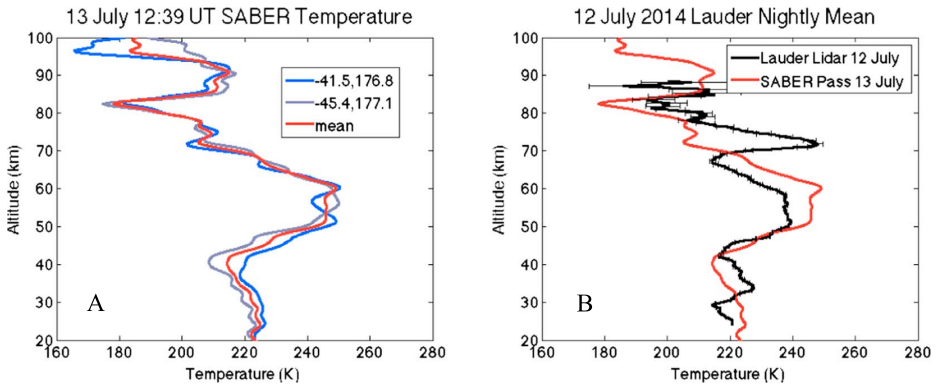

Figure 3. (a) Saber temperatures from two passes on 13 July 2014 at 12:38:21 and 12:39:31 and the averaged temperature between these passes. (b) The nightly average from the Lauder Rayleigh lidar on 12 July 2014 plotted with the averaged SABER temperature from Figure 3a.

ECMWF predicts that the particular conditions allowing the large-scale ~240 km MW to propagate to high altitudes existed for approximately 2 days, beginning on 12 July. While data from the nearby Lauder station were unavailable during the RF22 flight, Rayleigh lidar data were available from Lauder for 12 July. We believe that these data provide a good estimate of local temperatures between 60 and 85 km during RF22, given that ECMWF predicts that this event extends over these 2 days. Furthermore, SABER temperatures [*Remsberg et al.*, 2008] are available nearby at ~12:30 UT on 13 July, just a few hours after the RF22 flight. These temperatures also provide an estimate of large-scale temperature environment within which these DEEPWAVE measurements were performed. Differences of the Lauder lidar profiles from the SABER profiles then provide indications of local variations that may be largely due to MWs. Figure 3a shows the individual mean temperature profiles for the two SABER profiles. Figure 3b shows the nightly average of the Lauder Rayleigh lidar temperatures with the mean SABER temperatures. Both the lidar and SABER show a strong negative gradient in temperature between ~70 and 80 km. However, this differs in altitude between the two measurements. The lidar shows this low-stability layer to extend from ~70 to 77 km, and SABER shows it to extend from ~77 to 82 km. Both the lidar and SABER show a positive temperature gradient from ~80 to 90 km. The difference between these measurements likely indicates local influences of the MW in the lidar data, which likely makes little contribution to the limb-averaged SABER profiles. The weakly stable layer in the lidar profile between ~70 and 80 km suggests a potential for sustained MW breaking at these altitudes during these times.

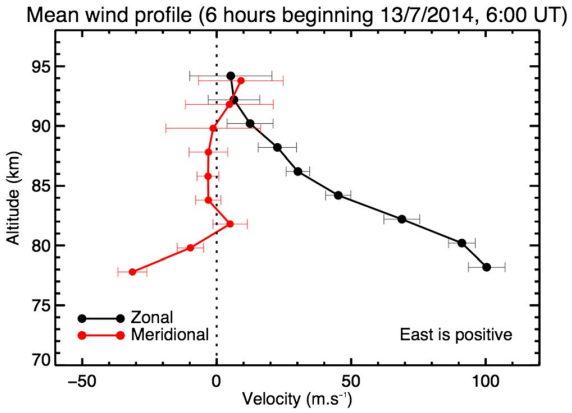

Figure 4. Kingston meteor radar wind 6 h mean starting at 6 UT on 13 July 2014 shows winds of 45 m s^{-1} toward the east at 84 km and 25 m s^{-1} toward the east at 87 km.

A rough prediction of winds for the time period of RF22 can be obtained from the Kingston radar over Tasmania. While these radar winds are ~2000 km away from the measurements over New Zealand, they provide a reasonable estimate of the mean winds and tidal influences at the altitudes, latitude, and local time of our measurement. A 6 h total wind starting at 6:00 UT is shown in Figure 4. These measurements suggest a mean wind of about ~25 ms^{-1} toward the east near 87 km at the peak of the hydroxyl layer.

Turning to the hydroxyl layer, Figure 5 shows for reference the GV AMTM and wing camera horizontal map of OH airglow brightness along and across the

AGU Journal of Geophysical Research: Atmospheres 10.1002/2015JD023197

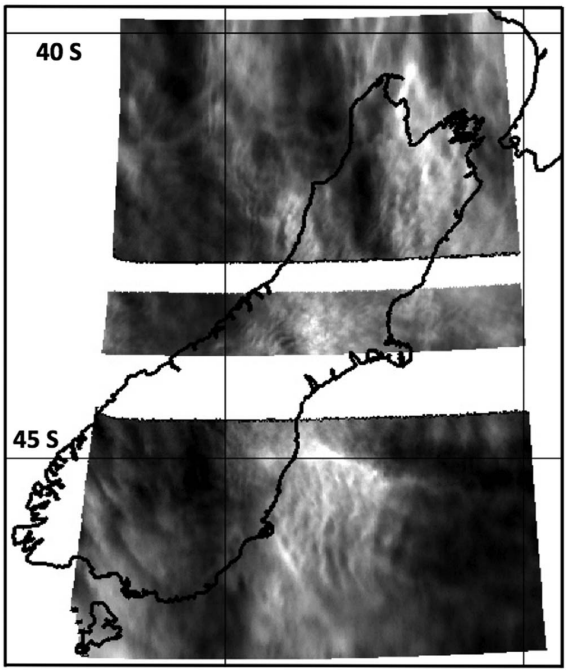

Figure 5. Imager intensities from the fourth pass of RF22 using the AMTM and side-viewing IR cameras. These intensities show the ~240 km MW positioned over the South Island of New Zealand and spanning ~900 km meridionally.

flight track for flight segment 4. The horizontal dimensions of this field are ~600 km east-west and ~900 km north-south. Seen clearly are three large-scale bright regions oriented nearly north-south, with the stronger central feature crossing the center of South Island.

Sodium mixing ratios computed along this flight provide additional insights into the evolution of the ~240 km MW in altitude and time. Figure 6 shows the sodium mixing ratio contours for each pass, for which a horizontal averaging of ~45 km has been employed. While these contours do not have the resolution to show smaller-scale GW activity, they clearly demonstrate the ~240 km MW observed on each pass. The contours show that the large-scale MW has an appreciable amplitude up to ~80 km but has largely dissipated by ~87 km. The inferred decrease of the ~240 km MW amplitude over this altitude interval and the near-vertical Na mixing ratio contours suggesting possible MW breaking and overturning appear to be consistent with the observation by both the Lauder lidar and SABER of a layer of low stability located near ~70–80 km and the observation by the Kingston radar of a critical level for MWs near 90 km altitude. Given these sodium mixing ratios, combined with the environments predicted by the Lauder Rayleigh lidar and the Kingston radar, the OH airglow measurements are likely responding to the ~240 km MW perturbations below the OH layer maximum where the amplitude and vertical wavelength are largest as opposed to the regions above 85 km where the ~240 km MW has largely dissipated.

Shown in Figure 7 are the corresponding GV AMTM along-track temperature fields for all four flight segments. These along-track field maps, also called keograms, were created using successive zenith cross sections from the AMTM that have been stitched together to create a spatial view of the temperatures along the flight path. Comparing the brightness and temperature fields for flight segment 4, we see that the regions of warmest temperatures correspond closely to the regions of maximum brightness. The particular features of greatest interest in this paper also occur in the brightest, and apparently warmest, and largest amplitude, phase of the ~240 km MW.

The along-track AMTM temperatures reveal the presence of smaller-scale GWs with $\lambda_h \sim 25$–28 km primarily within the bright and warm phases of the ~240 km MW on each flight segment. For our discussion below, we will employ the reference frame of the ~240 km MW, defining positive zonal velocities to be in the propagation direction of this MW (thus positive toward the west). We assume that the ~240 km MW is propagating approximately zonally, upward, and to the west. The following analysis yields approximate values for MF, allowing us to qualitatively estimate the MF influences of the observed GWs along this flight. We note that the corresponding MF calculations are likely an underestimate of the actual MF values. However, these values are nonetheless important in highlighting the influences of these observed GWs as they show the tendency for large magnitudes in such environments even for these underestimates. Where appropriate, upper bounds on MF are estimated or ranges of MF estimates are given based on uncertainties in observed GW amplitudes and other derived quantities.

4.2. Background Environment

The background temperature profile was estimated given the information from the Lauder Rayleigh lidar and SABER temperature measurements. Above the nearly adiabatic layer from ~70 to 80 km, we assume a slightly

Journal of Geophysical Research: Atmospheres 10.1002/2015JD023197

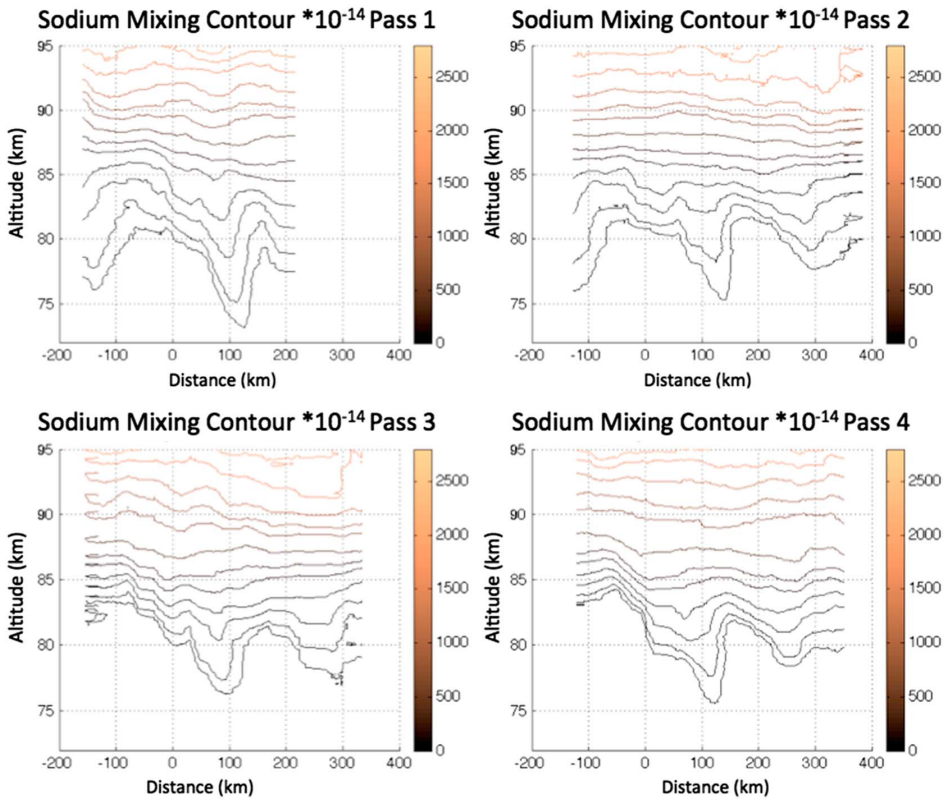

Figure 6. Sodium mixing ratios from the GV sodium lidar for the four RF22 flight segments clearly show the ~240 km MW below 85 km and strong dissipation of this MW above 85 km.

positive temperature gradient above 80 km. The nightly average from the AMTM was found to be 212 K, and that from the Lauder Rayleigh lidar at ~80 km was ~195 K. SABER provides a temperature of 194 K at 80 km and 211 K at 87 km. While both of these measurements include smaller-scale fluctuations, especially localized MWs in the Lauder lidar, we believe that a reasonable approximation to the background temperature gradient can be inferred. Using SABER and the AMTM and lidar measurements, we infer an approximate mean

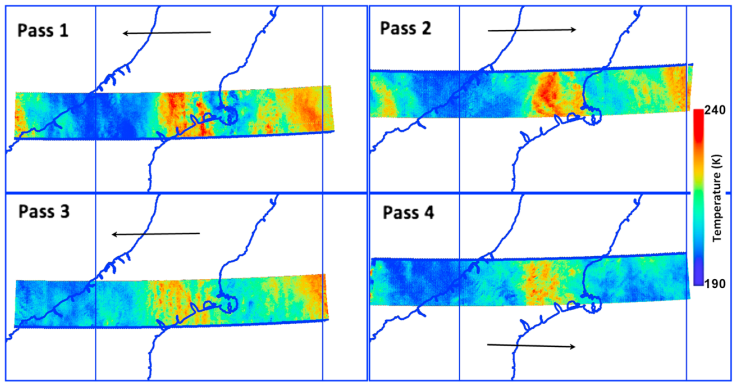

Figure 7. AMTM spatial keograms showing both the 240 km MW centered over New Zealand and several smaller-scale GWs.

AGU Journal of Geophysical Research: Atmospheres 10.1002/2015JD023197

Table 1. 240 km MW Temperature Perturbations and Corresponding MF Near 84 km

Pass Number	$<T'>$ (K)	MF ($m^2 s^{-2}$)
1	8	6
2	7	5
3	6	3
4	8	6

temperature gradient from 80 to 87 km of ~2.5 K/km. This results in an estimate of the mean buoyancy frequency between ~80 km and 87 km of $N \sim 0.023\ s^{-1}$ from equation (2).

The background wind was obtained using the Kingston radar. For the purposes of this analysis, we assume that the stationary MWs are largely observed toward the bottom side of the OH layer near 84 km, as these MWs are likely approaching a critical level near 90 km where the mean winds approach $0\ ms^{-1}$. Furthermore, the sodium mixing ratios confirm that the amplitude of the ~240 km MW decreases rapidly above 85 km. For the smaller-scale waves, we assume that those with observable phase speeds toward the east (not MWs) are weighted toward the center of the OH layer as they are not approaching a critical level. For this reason, we assume the background wind at two different altitudes depending on the GW analysis, 87 km and 84 km, where the winds are ~ −25 and $-45\ m\ s^{-1}$ respectively as shown in Figure 4.

4.3. Large-Scale MW Characterization and MF Estimation

The temperature perturbations for the ~240 km MW were found by subtracting the mean temperature for each flight segment. Smaller-scale perturbations were removed from the ~240 km GW using a smoothing spline fit to generate a low-pass characterization of the ~240 km MW and estimate the temperature perturbations associated with this MW. We assume that the temperatures measured by the AMTM are largely weighted toward the MW perturbations seen below ~85 km because of the expected strong phase averaging at higher altitudes. These temperature perturbations are likely an underestimate of the actual temperature perturbations between 80 and 85 km due to averaging within the OH layer. However, given our lack of information about the shape of the OH layer in the complex mixing environment accompanying breaking and dissipation at these altitudes, a correction factor may provide an inaccurate and potentially large overestimate of the temperature perturbation. The MF for the ~240 km MW for each pass was calculated using equation (3) and other parameters specified above. The ~240 km MW parameters and corresponding MFs calculated from the AMTM are summarized in Table 1. These varied from 3 to $6\ m^2 s^{-2}$ and are similar to the mean values at this altitude. As noted above, however, these values are likely a significant underestimate of the MF of the ~240 km MW where its amplitude is larger than the estimates from the AMTM in Table 1.

The sodium mixing ratios provide an alternate means of estimating temperature perturbations of the ~240 km MW at these altitudes. The mixing ratio yields a relative parcel displacement, and from this a temperature perturbation can be calculated. The displacements in mixing ratio contour from ~83 km for each pass are summarized in Table 2. Using an adiabatic lapse rate of 9.5 K/km and the background temperature gradient of ~2.5/km, a temperature perturbation estimation can be obtained, and these estimates are also given in Table 2. We use the winds near ~83 km, which are $55\ m\ s^{-1}$ toward the east, in order to calculate the MF here. The MF values are summarized in Table 2. These values are larger than mean MF values and range from 17 to $68\ m^2 s^{-2}$, which suggest strong variation in propagation conditions of the ~240 km MW on each pass. The difference in temperature measurements between the AMTM and sodium mixing ratio is due to the averaging associated with the AMTM and its likely small contribution from the lower altitudes where the ~240 km MW is large, given that the OH layer appears to be centered where we see little to no perturbations in the sodium mixing ratios.

Assessing uncertainties in GW MF estimates is important for defining mean values and their range of variability under various forcing and propagation conditions. Often, uncertainties in MF magnitudes are quite large due to imprecise estimates of GW amplitudes, intrinsic frequencies, and variable environments. This is especially the case in using airglow intensity measurements, where the relation between intensity and temperature perturbations may vary by a factor of up to ~10 [*Hickey and Yu*, 2005], causing MF uncertainties of up to ~100 times for slow GW phase speeds

Table 2. 240 km MW Mixing Ratio Vertical Displacements Near 83 km

Pass #	dz (km)	T' (K)	MF ($m^2 s^{-2}$)
1	2	24	68
2	1.5	18	38
3	1	12	17
4	1.5	18	38

AGU Journal of Geophysical Research: Atmospheres 10.1002/2015JD023197

Table 3. Estimated Upper Bound MF Values for the ~240 km MW Approximated From 83 to 87 km

Altitude (km)	$c-u$ (m s^{-1})	λ_z (km)	MF Limit (m^2 s^{-2})
83	55	15.2	96
84	45	12.4	52
87	25	6.8	9

and up to ~10 times for higher GW phase speeds. In particular, previous estimates using airglow brightness with claimed uncertainties of only approximately tens of percent cannot be legitimate in light of the *Hickey and Yu* [2005] analysis.

Direct estimates of T' provided by the new AMTMs largely overcome these extreme uncertainties. However, there remain significant uncertainties that could cause a traditional error analysis to imply that MFs remain almost entirely uncertain. To provide more justified bounds on MFs in such cases, we note that a well-constrained T' effectively defines a lower bound on MF in cases where measurements provide reasonable characterization of the GW intrinsic properties. Nevertheless, this always yields an underestimate, due to the phase averaging inherent in the AMTM T' estimate. Similarly, identification of GW parameters and their environments also enables an approximate upper limit imposed by a GW saturation condition, e.g., $u'_{max} \sim (c-u)$ [*Fritts*, 1984], for which there is observational, theoretical, and modeling evidence [see *Fritts and Alexander*, 2003].

In our case, MWs approaching a critical level at ~90 km imply that the peak MF will occur near where $u' = (c-u)$ and will decrease as the critical level is approached. The resulting MF estimates at 83, 84, and 87 km are summarized in Table 3. These suggest maximum MFs ranging from ~96 m^2 s^{-2} at 83 km to less than ~10 m^2 s^{-2} at 87 km. Our calculations above are within these bounds, and our data also agree with the strong dissipation that must be occurring as the MWs approach the critical level near 90 km.

Given the strong dissipation of this MW up to 85 km, and very weak influences above, we assume for further analysis that the ~240 km MW does not have large wind and temperature perturbations affecting the propagation environment of small-scale GWs observed at the altitude of the AMTM. However, it should be acknowledged that this MW most likely has an increasing influence on small-scale GW propagation at lower altitudes where its amplitude is large.

4.4. Small-Scale GW Characterization and MF Calculations

On each flight segment of the RF22 flight, there were smaller-scale dynamics observed over the South Island. Each of these occurred accompanying the central brighter, and warmer, phase of the ~240 km MW, suggesting strong influences of the ~240 km MW structure on the character and vertical propagation of these smaller-scale GWs and the potential influences of this ~240 km MW on the production of instabilities and secondary GWs. AMTM vertical views of these four events with the large-scale ~240 km MW background subtracted are shown in Figure 8. In each case, the smaller-scale dynamics were aligned principally in the zonal plane and their λ_h varied from ~25 to 28 km.

The dotted boxes in Figure 8 show the region of the image used for the calculation of T' and λ_h. To obtain T', we average the temperature meridionally as the observed GWs are aligned in the north-south direction. These averages use 10 pixels of the AMTM, so error due to AMTM noise is sufficiently reduced. The average difference between the temperature maxima and minima in the boxed areas was used to determine the approximate T'. In order to calculate a corresponding λ_h, a Lomb Scargle periodogram was used on the images in Figure 8. Our smaller-scale GW analysis is limited to the FOV of the AMTM. The images in Figure 8 are ~45 km meridionally by ~90 km zonally, and the smaller-scale GWs analyzed in this section have a $\lambda_h < 45$ km. The phase speed c for each observation was calculated by tracing phase movement across successive images in time and compensating for the speed of the GV. From these observed phase speeds, the intrinsic phase speed, $c_i = c-u$, for each event was calculated using the mean horizontal wind, u, estimated from the radar measurements. In order to account for expected uncertainties in the local mean wind, we also calculate the MF assuming that u is larger and smaller by 15 m s^{-1}. This allows for estimates of the possible range of MFs given the inherent uncertainties in the available horizontal wind information. Given the differing nature of the small-scale dynamics, each pass is described separately below.

4.4.1. Pass 1

This GW was observed to be propagating with a phase speed of ~100 m s^{-1} toward the east. The atmospheric conditions allow for this GW to propagate to higher altitudes, so we assume propagation through the entire OH layer. The measured T' is ~7 K, the horizontal wavelength is 28 km, and for a background wind of

AGU Journal of Geophysical Research: Atmospheres 10.1002/2015JD023197

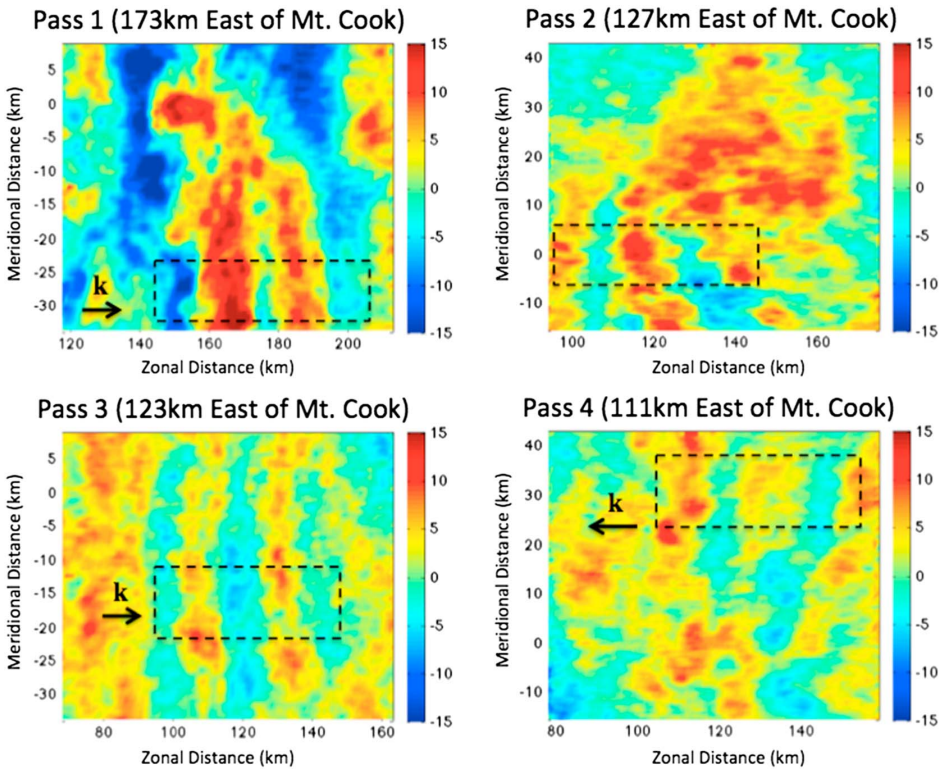

Figure 8. Overhead AMTM temperature maps of observed small-scale GWs during the four flight segments over Mount Cook, NZ. The dashed boxes show the areas used for calculating temperature perturbations and wavelength using a Lomb Scargle periodogram. The arrows denote the intrinsic direction of propagation of the observed GWs.

$-25\,m\,s^{-1}$ at 87 km, the corresponding MF is ~$105\,m^2\,s^{-2}$ which is ~10–20 times the mean at this altitude. The MF for zonal winds of $\pm 15\,m\,s^{-1}$ about the mean wind assumed above also yielded vertical propagation in each case, with MF ranging from ~70 to $200\,m^2\,s^{-2}$.

4.4.2. Pass 2

This feature appears to be largely confined to the FOV of the GV AMTM and is not seen in the side-viewing cameras, it evolves somewhat in shape over the intervals observed, and the relative motion (~ $-24\,m\,s^{-1}$) appears to be the same as the mean wind (~ $-25\,m\,s^{-1}$). Thus, we believe these features to be instabilities that simply advect with the mean wind at this altitude.

4.4.3. Pass 3

Similar to the first pass, this GW is propagating with an observed phase speed of $130\,m\,s^{-1}$ to the east. At the central OH altitude of ~87 km, the measured phase speed implies that the observed GW is evanescent. However, given the significant $T' \sim 5$ K, it is likely that this GW is ducted at a nearby eastward wind or N^2 maximum at a lower altitude, given the wind profile implied by the meteor radar and the N^2 maximum implied by SABER from ~82 to 85 km. The stronger eastward winds measured by the meteor radar just a few kilometers below 87 km would allow this GW to be in a region of vertical propagation below the evanescent region near 87 km.

Table 4. Small-Scale Parameters for Passes 1–4 Obtained From Figure 7

Pass #	$<T'>$ (K)	c ($m\,s^{-1}$)	u ($m\,s^{-1}$)	c_i ($m\,s^{-1}$)	λ_h (km)	m^2 (m^{-2})	λ_z (km)
1	7	−100	−25	−75	28	3.88E−08	31.9
2	6	−24	−25	--	28	--	--
3	5	−135	−25	−110	28	−1.23E−08	--
4	4.4	0	−45	45	25	1.96E−07	14.2

AGU Journal of Geophysical Research: Atmospheres 10.1002/2015JD023197

Table 5. Small-Scale GW MF Calculated Without Correcting for Integration Over the OH Layer for Passes 1 and 4

		MF ($m^2 s^{-2}$)		
Pass #	Altitude (km)	$u-15$ ($m s^{-1}$)	u ($m s^{-1}$)	$u+15$ ($m s^{-1}$)
1	87	68	105	212
4	84	33	21	13

4.4.4. Pass 4

The GW in this case has an observed phase speed near zero, suggesting a smaller-scale MW that is also approaching a critical level. It also appears to have small-scale structure suggesting that it may be exhibiting instability accompanying its decreasing vertical wavelength and amplitude. For this reason, we use 84 km as our analysis altitude, similar to that of the ~240 km MW. The measured T' ~ 4.4 K and horizontal wavelength of ~25 km implies a MF ~ 21 $m^2 s^{-2}$, thus with lower limits varying from 13 to 33 $m^2 s^{-2}$ due to an estimated uncertainty in the background wind of ±15 $m s^{-1}$. While we have assumed that this is a MW because of the approximately zero phase speed and the small-scale structure at higher altitudes, we note the complex environment through which this GW must propagate to reach the MLT region. This GW was observed above a region of low stability and decreasing temperature as measured by both SABER and the Lauder lidar. This region is likely a layer in which MWs are breaking, and the observed GW from this pass could either be a MW contributing to the breaking dynamics and retaining a coherent structure but with smaller amplitude as observed in modeling of GW breaking [*Fritts et al.*, 2009] or this could be a secondary GW coincidentally having the same phase speed as the source MWs. Of these possibilities, the former seems far more likely, as we are aware of no observations or modeling studies suggesting secondary GWs exhibiting this behavior.

The characteristics of each observation are summarized in Table 4. The MF calculations for passes 1 and 4 are summarized in Table 5. The MF estimates for passes 1 and 4 are very conservative as the T' is not corrected for averaging over the OH layer, which would yield a larger implied T' in all cases. As noted previously, the MW breaking environment at the bottom side of the OH layer adds complexity that makes confident estimates of the true T' challenging. We also performed these MF estimates for u increased and decreased by 15 $m s^{-1}$ relative to the estimated u in each case. The MF values computed for changes in u (and c_i) by 15 $m s^{-1}$ approximate the extrema of the possible MF values, given the uncertainties of the local horizontal wind u and phase speed c determinations from the AMTM. Nevertheless, we believe the central values to be more likely and so will use these as our best conservative estimates for these events.

5. Discussion

The MFs listed in Tables 1, 2, and 5 span a wide range of magnitudes for various observed GW scales and amplitudes. The ~240 km MW was estimated to have MFs ranging from 3 to 6 $m^2 s^{-2}$ at ~87 km by the AMTM and potentially MFs as large as 68 $m^2 s^{-2}$ from the sodium mixing ratio displacement estimates at a lower altitude where the MW amplitude is obviously much larger. This larger value is ~10 times larger than the mean values at this altitude, and this MF spans a region extending hundreds of kilometers zonally and meridionally. In comparison, the smaller-scale GWs observed in localized regions over South Island on flight segments 1 and 4 had large MFs with conservative estimates for pass 4 of ~20 $m^2 s^{-2}$ and conservative estimates for pass 1 of ~100 $m^2 s^{-2}$. Regardless of errors associated with these estimates, they may greatly underestimate the actual MF values depending on phase averaging of the small-scale GWs over the OH layer. Compared to the ~240 km MW, the smaller-scale GWs that were propagating had much larger MFs, and these range from as much as ~2–20 times typical mean magnitudes of ~5–10 $m^2 s^{-2}$ expected at these altitudes. While we note that these calculations may have large errors associated with them, even very conservative estimates show that the MF associated with the small-scale GWs is significant. These estimates demonstrate the potentially important role of such small-scale GWs in the overall momentum budget of the mesosphere and lower thermosphere.

The small-scale GWs examined here are also of interest because of the multiscale character of the environments that appeared to control where they achieved large amplitudes and MFs. During the first and third flight segments, the GWs were observed to have eastward intrinsic phase speeds. However, the observed small-scale GW on the third flight segment was evanescent, suggesting that this GW seen in the OH layer was likely ducted at a nearby layer, given its large OH layer amplitude. Observations on the fourth flight segment revealed a GW with an intrinsic phase speed toward the west and an observed phase speed of zero,

AGU Journal of Geophysical Research: Atmospheres 10.1002/2015JD023197

which was possibly a smaller-scale MW or other GW approaching a critical level. Thus, all of these GWs had apparently very different character, despite somewhat similar large-scale environments.

The different character of the three small-scale GWs discussed above suggests potentially different sources for these various GWs and/or different multiscale influences on their propagation into the MLT. One obvious potential source is the same South Island orography that generated the ~240 km MW that provided the background environment at higher altitudes. This could only be true for the small-scale GWs having $c \sim 0$ and $c_i > 0$. But this is the case for the small-scale GW on flight segment 4, which has an observed $c \sim 0$. The other small-scale GWs must have different initial c and c_i (and sources) given their large negative c and especially the $c_i < 0$ for flight segments 1 and 3.

Finally, as noted above, the small-scale GWs analyzed for the flight segments all occurred in the warm phase of the ~240 km MW, implying a significant influence of the ~240 km MW on the small-scale GW propagation and refraction with altitude. These cases are very similar to that observed at ALOMAR in northern Norway and analyzed by *Fritts et al*. [2014]. In that case, the larger GW scales within the multiscale GW field were found to strongly modulate the smaller-scale GW occurrence and amplitude, also leading to a very large momentum flux estimate. Thus, our observations of similar dynamics during DEEPWAVE appear to be further evidence of the importance of such multiscale dynamics that likely play major roles in the composition of the GW spectrum with altitude and the determination of the GWs that contribute most to momentum fluxes in the MLT.

6. Conclusions

The measurements described here occurred during the DEEPWAVE airborne measurement campaign that was performed in June and July 2014 over and around New Zealand. DEEPWAVE specifically targeted deep responses to orographic and nonorographic GW sources at lower altitudes extending to ~100 km.

GV airborne observations during DEEPWAVE Research Flight 22 on 13 July revealed a larger-scale, $\lambda_h \sim 240$ km MW extending ~600 km or more zonally and ~900 km or more meridionally. This large-scale MW yielded estimated MFs of ~ 3–6 $m^2 s^{-2}$ from AMTM altitudes and MFs of 17–68 $m^2 s^{-2}$ at altitudes near ~83 km in the sodium mixing ratios. Observations of localized smaller-scale GWs within the ~240 km MW field had $\lambda_h \sim 25$–28 km and yielded MF estimates ranging from ~20 $m^2 s^{-2}$ to 105 $m^2 s^{-2}$ that are larger, and in some cases significantly larger, than mean values in the MLT. These results demonstrate the potentially significant impacts that small horizontal-scale GWs with large λ_z can have at higher altitudes. They also emphasize the likely importance of such multiscale GW dynamics and their influences on smaller-scale GW propagation and momentum fluxes in the MLT and potentially at lower altitudes. Indeed, such multiscale dynamics may be relatively common throughout the atmosphere and suggest the value of additional efforts to quantify these dynamics and effects with further quantitative observations and parallel numerical modeling.

Acknowledgments
Research reported here was supported by NSF under grants AGS-1261619 and AGS-1338646 at GATS and AGS-1061892 and AGS-1338666 at Utah State University. Installation and operation of the Kingston radar was supported through Australian Antarctic Science project 4025. We acknowledge the SABER operations and data analysis staff, especially Greg Paxton and Tom Marshall, at GATS Inc., for their help in obtaining and understanding the SABER temperature data. We also thank the highly capable team at NCAR/EOL who made these airborne measurements aboard the GV possible. Data for the DEEPWAVE mission are stored and maintained by NCAR and can be accessed at https://www.eol.ucar.edu/field_projects/deepwave.

References

Baker, D. B., and A. T. Stair (1988), Rocket measurements of the altitude distributions of the hydroxyl airglow, *Phys. Scr.*, *37*, 611–622.
Bossert, K., D. C. Fritts, P.-D. Pautet, M. J. Taylor, B. P. Williams, and W. R. Pendelton (2014), Investigation of a mesospheric gravity wave ducting event using coordinated sodium lidar and Mesospheric Temperature Mapper measurements at ALOMAR, Norway (69°N), *J. Geophys. Res. Atmos.*, *119*, 9765–9778, doi:10.1002/2014JD021460.
Cai, X., T. Yuan, Y. Zhao, P.-D. Pautet, M. J. Taylor, and W. R. Pendelton Jr. (2014), A coordinated investigation of the gravity wave breaking and the associated dynamical instability by Na lidar and Advanced Mesospheric Temperature Mapper over Logan, UT (41.7°N, 111.8°W), *J. Geophys. Res. Space Physics*, *119*, 6852–6864, doi:10.1002/2014JA020131.
Collins, R. L., and R. W. Smith (2004), Evidence of damping and overturning of gravity waves in the Arctic mesosphere: Na lidar and OH temperature observations, *J. Atmos. Sol. Terr. Phys.*, *66*, 867–879.
Collins, R. L., X. Tao, and C. S. Gardener (1996), Gravity wave activity in the upper mesosphere over Urbana, Illinois: Lidar observations and analysis of gravity wave propagation models, *J. Atmos. Sol. Terr. Phys.*, *58*(16), 1905–1926.
Eckermann, S. D. (1997), Influence of wave propagation on the Doppler spreading of atmospheric gravity waves, *J. Atmos. Sci.*, *54*, 2554–2573.
Ejiri, M. K., M. J. Taylor, T. Nakamura, and S. J. Franke (2009), Critical level interaction of a gravity wave with background winds driven by a large-scale wave perturbation, *J. Geophys. Res.*, *114*, D18117, doi:10.1029/2008JD011381.
Ern, M., P. Preusse, J. C. Gille, C. L. Hepplewhite, M. G. Mlynczak, J. M. Russell III, and M. Riese (2011), Implications for atmospheric dynamics derived from global observations of gravity wave momentum flux in stratosphere and mesosphere, *J. Geophys. Res.*, *116*, D19107, doi:10.1029/2011JD015821.
Espy, P. J., G. O. L. Jones, G. R. Swenson, J. Tang, and M. J. Taylor (2004), Seasonal variations of the gravity wave momentum flux in the Antarctic mesosphere and lower thermosphere, *J. Geophys. Res.*, *109*, D23109, doi:10.1029/2003JD004446.
Fritts, D. C. (1984), Gravity wave saturation in the middle atmosphere: A review of theory and observations, *Rev. Geophys.*, *22*, 275–308, doi:10.1029/RG022i003p00275.

AGU Journal of Geophysical Research: Atmospheres 10.1002/2015JD023197

Fritts, D. C., and M. J. Alexander (2003), Gravity wave dynamics and effects in the middle atmosphere, *Rev. Geophys.*, *41*(1), 1003, doi:10.1029/2001RG000106.
Fritts, D. C., and R. A. Vincent (1987), Mesospheric momentum flux studies at Adelaide, Australia: Observations and a gravity wave/tidal interaction model, *J. Atmos. Sci.*, *44*, 605–619.
Fritts, D. C., S. A. Vadas, and Y. Yamada (2002), An estimate of strong local gravity wave body forcing based on OH airglow and meteor radar observations, *Geophys. Res. Lett.*, *29*(10), 1429, doi:10.1029/2001GL013753.
Fritts, D. C., L. Wang, J. Werne, T. Lund, and K. Wang (2009), Gravity wave instability dynamics at high Reynolds numbers. Part 1: Wave field evolution at large amplitudes and high frequencies, *J. Atmos. Sci.*, *66*, 1126–1148.
Fritts, D. C., D. Janches, and W. K. Hocking (2010), Southern Argentina Agile Meteor Radar: Initial assessment of gravity wave momentum fluxes, *J. Geophys. Res.*, *115*, D19123, doi:10.1029/2010JD013891.
Fritts, D. C., D. Janches, H. Iimura, W. K. Hocking, J. V. Bageston, and N. M. P. Leme (2012), Drake Antarctic Agile Meteor Radar first results: Configuration and comparison of mean and tidal wind and gravity wave momentum flux measurements with Southern Argentina Agile Meteor Radar, *J. Geophys. Res.*, *117*, D02105, doi:10.1029/2011JD016651.
Fritts, D. C., P.-D. Pautet, K. Bossert, M. J. Taylor, B. P. Williams, H. Iimura, T. Yuan, N. J. Mitchell, and G. Stober (2014), Quantifying gravity wave momentum fluxes with Mesosphere Temperature Mappers and correlative instrumentation, *J. Geophys. Res. Atmos.*, *119*, 13,583–13,603, doi:10.1002/2014JD022150.
Fritts, D. C., et al. (2015), The Deep Propagating Gravity Wave Experiment (DEEPWAVE): An Airborne and Ground-Based Exploration of Gravity Wave Propagation and Effects from their Sources throughout the Lower and Middle Atmosphere, *Bull. Am. Meteorol. Soc.*, doi:10.1175/BAMS-D-14-00269.1.
Garcia, R. R., and S. Solomon (1985), The effect of breaking gravity waves on the dynamics and chemical composition of the mesosphere and lower thermosphere, *J. Geophys. Res.*, *90*, 3850–3868, doi:10.1029/JD090iD02p03850.
Haynes, P. H., C. J. Marks, M. E. McIntyre, T. G. Shephard, and K. P. Shine (1991), On the "downward control" of extratropical diabatic circulations by eddy-induced mean zonal forces, *J. Atmos. Sci.*, *48*(657–678), 1991.
Hecht, J. H., R. L. Walterscheid, D. C. Fritts, J. R. Isler, D. C. Senft, C. S. Gardner, and S. J. Franke (1997), Wave breaking signatures in OH airglow and sodium densities and temperatures: 1. Airglow imaging, Na lidar, and MF radar observations, *J. Geophys. Res.*, *102*(D6), 6655–6668, doi:10.1029/96JD02619.
Hertzog, A., M. J. Alexander, and R. Plougonven (2012), On the intermittency of gravity wave momentum flux in the stratosphere, *J. Atmos. Sci.*, *69*, 3433–3448.
Hickey, M. P., and Y. Yu (2005), A full-wave investigation of the use of a "cancellation factor" in gravity wave-OH airglow interaction studies, *J. Geophys. Res.*, *110*, A01301, doi:10.1029/2003JA01372.
Hitchman, M., K. W. Bywaters, D. C. Fritts, L. Coy, E. Kudeki, and F. Surucu (1992), Mean winds and momentum fluxes over Jicamarca, Peru, during June and August 1987, *J. Atmos. Sci.*, *49*, 2372–2383.
Holdsworth, D. A., I. M. Reid, and M. A. Cervera (2004), Buckland Park all-sky interferometric meteor radar, *Radio Sci.*, *39*, RS5009, doi:10.1029/2003RS003014.
Holton, J. R. (1982), The role of gravity wave induced grad and diffusion in the momentum budget of the mesosphere, *J. Atmos. Sci.*, *39*, 791–799.
Holton, J. R. (1984), The generation of mesospheric planetary waves by zonally asymmetric gravity wave breaking, *J. Atmos. Sci.*, *41*, 3427–3430.
Kim, Y.-J., S. D. Eckermann, and H.-Y. Chun (2003), A overview of the past, present and future of gravity-wave drag parameterization for numerical climate and weather prediction models, *Atmos. Ocean*, *41*, 65–98.
Lieberman, R. S., et al. (2000), Comparison of mesospheric and lower thermospheric residual wind with High Resolution Doppler Imager, medium frequency and meteor radar winds, *J. Geophys. Res.*, *105*(D22), 27,023–27,035, doi:10.1029/2000JD900363.
Lieberman, R. S., D. A. Ortland, D. M. Riggin, Q. Wu, and C. Jacobi (2010), Momentum budget of the migrating diurnal tide in the mesosphere and lower thermosphere, *J. Geophys. Res.*, *115*, D20105, doi:10.1029/2009JD013684.
Lieberman, R. S., D. M. Riggin, and D. E. Siskind (2013), Stationary waves in the wintertime mesosphere: Evidence for gravity wave filtering by stratospheric planetary waves, *J. Geophys. Res. Atmos.*, *118*, 3139–3149, doi:10.1002/jgrd.50319.
Murphy, D. J., and R. A. Vincent (1993), Estimates of momentum flux in the mesosphere and lower thermosphere over Adelaide, Australia, from March 1985 to February 1986, *J. Geophys. Res.*, *98*(D10), 18,617–18,638, doi:10.1029/93JD01861.
Nakamura, T., T. Tsuda, M. Yamamoto, S. Fukao, and S. Kato (1993), Characteristics of gravity waves in the mesosphere observed with the middle and upper atmosphere radar: 1. Momentum flux, *J. Geophys. Res.*, *98*(D5), 8899–8910, doi:10.1029/92JD02978.
Namboothiri, S. P., T. Tsuda, M. Tsutsumi, and T. Nakamura (1996), Simultaneous observations of mesospheric gravity waves with the MU radar and a sodium lidar, *J. Geophys. Res.*, *101*(D2), 4057–4063, doi:10.1029/95JD03299.
Nastrom, G. D., and D. C. Fritts (1992), Sources of mesoscale variability of gravity waves. I: Topographic excitation, *J. Atmos. Sci.*, *49*, 101–110.
Nielsen, K., M. J. Taylor, R. E. Hibbins, M. J. Jarvis, and J. M. Russell III (2012), On the nature of short-period mesospheric gravity wave propagation over Halley, Antarctica, *J. Geophys. Res.*, *117*, D05124, doi:10.1029/2011JD016261.
Pautet, P.-D., M. J. Taylor, W. R. Pendelton Jr., Y. Zhao, T. Yuan, R. Esplin, and D. McLain (2014), An Advanced Mesospheric Temperature Mapper for high-latitude airglow studies, *Appl. Optics*, *53*(26), 5934–5943.
Pfister, L., S. Scott, M. Loewenstein, S. Bowen, and M. Legg (1993), Mesoscale disturbances in the tropical stratosphere excited by convection: Observations and effects on the stratospheric momentum budget, *J. Atmos. Sci.*, *50*, 1058–1075.
Reid, I. M., R. Ruster, P. Czechowsky, and G. Schmidt (1988), VHF radar measurements of momentum flux in the summer polar mesosphere over Andenes (69°N, 16°E), Norway, *Geophys. Res. Lett.*, *15*(11), 1263–1266, doi:10.1029/GL015i011p01263.
Remsberg, E. E., et al. (2008), Assessment of the quality of the version 1.07 temperature-versus-pressure profiles of the middle atmosphere from TIMED/SABER, *J. Geophys. Res.*, *113*, D17101, doi:10.1029/2008JD010013.
She, C. Y., and R. P. Lowe (1998), Seasonal temperature variations in the mesopause region at mid-latitude: Comparison of lidar and hydroxyl rotational temperatures using WINDII/UARS OH height profiles, *J. Atmos. Sol. Terr. Phys.*, *60*, 1573–1583.
Simkhada, J. B., M. J. T. Snively, and S. J. Franke (2009), Analysis and modeling of ducted and evanescent gravity waves observed in the Hawaiian airglow, *Ann. Geophys.*, *27*, 3213–3224.
Smith, A. K. (2003), The origin of stationary planetary waves in the mesosphere, *J. Atmos. Sci.*, *60*, 3033–3041.
Taylor, M. J., W. R. Pendleton, S. Clark, H. Takahashi, D. Gobbi, and R. A. Goldberg (1997), Image measurements of short-period gravity waves at equatorial latitudes, *J. Geophys. Res.*, *102*(D22), 26,283–26,299, doi:10.1029/96JD03515.
Tsuda, T., Y. Murayama, M. Yamamoto, S. Kato, and S. Fukao (1990), Seasonal variation of momentum flux in the mesosphere observed with the MU radar, *Geophys. Res. Lett.*, *17*(6), 725–728, doi:10.1029/GL017i006p00725.

AGU Journal of Geophysical Research: Atmospheres 10.1002/2015JD023197

Vincent, R. A., and I. M. Reid (1983), HF Doppler measurements of mesospheric momentum fluxes, *J. Atmos. Sci.*, *40*, 1321–1333.
Wang, D.-Y., and D. C. Fritts (1990), Mesospheric momentum fluxes observed by the MST radar at Poker Flat, Alaska, *J. Atmos. Sci.*, *47*, 1512–1521.
Williams, B. P., D. C. Fritts, C. Y. She, and R. A. Goldberg (2006), Gravity wave propagation through a large semidiurnal tide and instabilities in the mesosphere and lower thermosphere during the winter 2003 MaCWAVE rocket campaign, *Ann. Geophys.*, *24*, 1199–1208.
Wilson, R., M. L. Chanin, and A. Hauchecorne (1991), Gravity waves in the middle atmosphere observed by Rayleigh lidar: 2. Climatology, *J. Geophys. Res.*, *96*(D3), 5169–5183, doi:10.1029/90JD02610.
Yuan, T., P.-D. Pautet, Y. Zhao, X. Cai, N. R. Criddle, M. J. Taylor, and W. R. Pendleton Jr. (2014), Coordinated investigation of midlatitude upper mesospheric temperature inversion layers and the associated gravity wave forcing by Na lidar and Advanced Mesospheric Temperature Mapper in Logan, Utah, *J. Geophys. Res. Atmos.*, *119*, 3756–3769, doi:10.1002/2013JD020586.
Yue, J., S. L. Vadas, C.-Y. She, T. Nakamura, S. C. Reising, H.-L. Liu, P. Stamus, D. A. Krueger, W. Lyons, and T. Li (2009), Concentric gravity waves in the mesosphere generated by deep convective plumes in the lower atmosphere near Fort Collins, Colorado, *J. Geophys. Res.*, *114*, D06104, doi:10.1029/2008JD011244.

Appendix B

Published paper: J. Geophys. Res. Atmos., 119, 6991-7013, 2014

AGU PUBLICATIONS

JGR

Journal of Geophysical Research: Atmospheres

RESEARCH ARTICLE
10.1002/2013JD020906

Key Points:
- Fifteen years of airglow intensity measurements
- Seasonal and interseasonal variations
- Similarity to conjugate observations

Correspondence to:
I. M. Reid,
iain.reid@adelaide.edu.au

Citation:
Reid, I. M., A. J. Spargo, and J. M. Woithe (2014), Seasonal variations of the nighttime O(^{1}S) and OH (8-3) airglow intensity at Adelaide, Australia, *J. Geophys. Res. Atmos.*, *119*, 6991–7013, doi:10.1002/2013JD020906.

Received 18 SEP 2013
Accepted 19 MAY 2014
Accepted article online 23 MAY 2014
Published online 13 JUN 2014

Seasonal variations of the nighttime O(^{1}S) and OH (8-3) airglow intensity at Adelaide, Australia

Iain M. Reid[1,2], Andrew J. Spargo[1], and Jonathan M. Woithe[2]

[1]School of Chemistry & Physics, University of Adelaide, Adelaide, South Australia, Australia, [2]ATRAD Pty Ltd, Thebarton, South Australia, Australia

Abstract We analyze 15 years of atomic oxygen (OI) 558 nm and hydroxyl (OH) (8-3) 730 nm nightglow emission intensities from heights near 96 and 87 km, respectively, measured using filter photometers at the Buckland Park Field Station (34.6°S, 138.6°E) near Adelaide, Australia. The intensity of both emissions exhibits clear seasonal and interannual periodicities, with annual, semiannual, and quasi-biennial oscillations, as well as a solar cycle influence. In addition, there is a terannual and 4.1 year component in the OI airglow intensity and both a quasi-biennial and quasi-triennial oscillation in the OH intensity. The results are in very good agreement with simultaneous collocated measurements made with an imager, and with global satellite climatologies of OI and OH intensities reported for the Wind Imaging Interferometer instrument. The mean value of the OI annual oscillation intensity is the same as that of the semiannual oscillation at this location to within the experimental uncertainty. The OI annual oscillation maximizes in summer, and the semiannual oscillation maximizes in autumn and spring, with the largest maximum in autumn. The terannual component in the OI nightglow maximizes in early summer, autumn, and spring. The quasi-biennial oscillation in the OI nightglow takes its first maximum value in autumn 1996, and the 4.1 year period in this emission first maximizes in summer 1998. The OH annual and semiannual oscillation intensities also agree to within the experimental uncertainties and are observed to peak in early winter. The quasi-biennial and quasi-triennial oscillations in this emission take their first maximum value in summer 1996.

1. Introduction

The mesosphere/lower thermosphere (MLT) nightglow has been studied for some considerable time, and a massive literature exists on it and on its variability. The airglow emission rate as observed at a given location is found to change through the night and from night to night, vary with season and between years, and vary with the solar cycle. Here we are particularly interested in the atomic oxygen (OI) and hydroxyl (OH) (8-3) nightglow. *Deutsch and Hernandez* [2003] made an extensive review of ground-based observations of the OI nightglow. Its global morphology for ±40° latitude has more recently been provided by *Liu et al.* [2008], whose results are based on Wind Imaging Interferometer (WINDII) observations made during the Upper Atmosphere Research Satellite (UARS) satellite mission and cover the period from November 1991 until August 1997. Most recently, *Smith et al.* [2010] have investigated temporal variations of atomic oxygen in the upper mesosphere using the Sounding of the Atmosphere using Broadband Emission Radiometry (SABER) instrument on the Thermosphere, Ionosphere, Mesosphere Energetics and Dynamics (TIMED) satellite during the period from January 2002 to September 2009.

The variation of the OH airglow intensity has been investigated observationally from the ground in the Southern Hemisphere (SH) by *Wiens and Weill* [1973] in the SH African sector, by *Buriti et al.* [2001, 2004], *Reisin and Scheer* [2002], and *Takahashi et al.* [1995] in the SH American sector, and by *French et al.* [2000] in the Antarctic. Many more ground-based studies of OH intensities have been made in the Northern Hemisphere than in the Southern Hemisphere [see, e.g., *Pertsev and Perminov*, 2008, and references therein], but the global morphology of the OH emission has been provided by SABER instrument observations on the TIMED satellite mission [*Marsh et al.*, 2006] and by WINDII instrument observations from the UARS satellite mission [*Liu et al.*, 2008]. *Gao et al.* [2010] provide a recent overview of ground-based and satellite observations of OH intensity variability and investigate its seasonal variations using SABER.

In this work we consider the seasonal and interannual variability of the 730 nm OH (8-3) and 558 nm OI nightglow emission intensity observed over a period of 15 years from the Buckland Park (BP) (34.6°S, 138.6°E) field site located about 36 km north of Adelaide, Australia. And although their peak emission heights are different (see Table 1), the MLT region airglow emissions from the OH Meinel bands, from the O(^{1}S) level, and

AGU Journal of Geophysical Research: Atmospheres 10.1002/2013JD020906

Table 1. Summary of Optical Instruments Operated at the Buckland Park Field Site

Instrument	Parameters Measured	Peak Emission Height[a]
OH and O_2 Czerny Turner Spectrometer (Embry Riddle)	OH (6-2) temperatures	87 km
	O_2 (0,1) temperatures	94 km
	OH (6-2) and O_2 (0,1) intensities	87 and 94 km
Three-field photometer	OH (8-3) intensities three fields	87 km
	OI (558 nm) intensities in three fields	96 km
OH and O_2 Airglow Imager (Aerospace Corp)	OH (6-2) temperatures	87 km
	O_2 (0,1) temperatures	94 km
	OH (6-2) and O_2 (0-1) images	87 and 94 km

[a]Nominal peak emission heights are from *Baker et al.* [2007] for OH, *McDade* [1998] for O_2, and *Scheer et al.* [2006] for OI.

from the O_2 atmospheric band are all linked through basically the same formation mechanism [e.g., *McDade*, 1998] and by the transport of atomic oxygen into the lower thermosphere and mesosphere [e.g., *Shepherd et al.*, 2006; *Marsh et al.*, 2006]. Work by *McDade et al.* [1986, 1987] further demonstrated that OH intensities are proportional to the O density near 85 km, while O(^{1}S) intensities are proportional to the cube of the O density near 95 km.

In *Reid and Woithe* [2007, hereinafter RW07] we reported on 11 years of OI nightglow intensity made using a three-field photometer (3FP) located at the BP field site. We found the annual and semiannual oscillations to have about equal intensity, with amplitudes of between 17 (±5) % and 14 (±5) % of the mean intensity, respectively. The annual oscillation was observed to peak in summer, while the semiannual oscillation took maximum values near equinox, and the autumn enhancement was greater than the spring enhancement. The quasi-biennial oscillation had a smaller amplitude at about 5 (±1) % of the mean intensity and took a maximum value near the autumnal equinox. There was a solar cycle dependence of the airglow intensity with an amplitude of about 20 (±15) % of the mean. RW07 found agreement with the phases of the annual and semiannual oscillations from other ground- and satellite-based observations and good agreement with independent measurements of the phases of the O_2 (0-1) rotational temperature made at the same site.

Here we extend the work of RW07 for OI observations made until mid-2010, and we consider observations of the OH (8-3) airglow intensity made using the same instrument for the same period for the first time. We also extend the RW07 Lomb periodogram analysis of the major periodicities present in the intensity observations by also including a wavelet-based approach. We consider our OI observations together with OI intensity observations from the conjugate site of Kiso (35.8°N, 137.6°E) for the period 1979 to 1995 analyzed by *Das and Sinha* [2008, hereinafter DS08] and observations of the O_2 (0-1) and OH (6-2) nightglow intensity made at the BP field site for the period 2002 until 2005 by *Gelinas et al.* [2008, hereinafter G08]. G08 also included Thermosphere-Ionosphere-Mesosphere-Electrodynamics General Circulation Model (TIME-GCM) results in their analysis of BP results, and we consider them too. We also compare our results with WINDII measurements of OI and OH intensity for 35°S reported by *Liu et al.* [2008].

In addition to improving our understanding of the nightglow morphology of the MLT region, these results form a baseline for intercomparison with the other instruments at the BP field site, which provide measurements of winds and rotational temperatures, and with satellite and model results. The close link between the underlying chemistry, dynamics, and temperature structure of the MLT region and the clear interdependence of these parameters make a better understanding of the aeronomy of the MLT region particularly topical.

2. Equipment

The 3FP is the primary instrument of interest to this work, and it is described in some detail by *Reid and Woithe* [2005] and by RW07. Here we will only briefly describe it and its operation and describe the process adopted to ensure the consistency of the instrument's response across the 15 years of its operation. Apart from the 3FP, there are a number of instruments for investigating the atmosphere at the BP field site, and these have been summarized by RW07. Two of the optical instruments are of particular interest to this work because we have used them as part of the calibration process for the intensities of the OI and OH (8-3) airglow. These are the BP Aerospace imager described by *Hecht et al.* [1994] and G08, which has been used to

AGU Journal of Geophysical Research: Atmospheres 10.1002/2013JD020906

make observations of O_2 (0-1) and OH (6-2) nightglow intensities and temperatures at BP since 2002, and the BP Embry Riddle spectrometer which operated at the site from 2001 until 2006 and also made measurements of the O_2 (0-1) and OH (6-2) intensities and temperatures. This instrument is described by *Sivjee and Shen* [1997]. The optical instruments at the BP field site and the mean heights corresponding to the emissions they measure are summarized in Table 1.

2.1. The 3FP and Its Operation

The 3FP was developed for studies of short-period internal atmospheric gravity waves evident in the atomic oxygen O(^{1}S) green line nightglow using interference filters at 557.7 (±1.5) nm and in the OH (8-3) nightglow using filters at 730 (±6) nm. It was designed to simultaneously observe three different areas of the sky selected using a rotating filter wheel. The filter wheel has positions for six separate filters, any three of which can be automatically rotated over three photomultipliers as required. Each filter is always used with the same photometer channel, and so there are three independent measures of the airglow intensity for each color available. Observations are made with one filter set for 20 s, then there is a 10 s period during which the alternate filter set is rotated over the photomultipliers, and then another 20 s duration observation is made. The sequence is then repeated. This filter configuration was originally chosen to facilitate an investigation of the vertical propagation of short-period gravity waves between the two peak emission heights. These are about 87 and 96 km, respectively (see Table 1). The 3FP only operates during Moon-free periods at night, and the observing times are preprogrammed.

Reid and Woithe [2005] and *Ding et al.* [2004] presented results from this mode of operation. While the instrument was not intended for long-term studies of the nightglow intensity, RW07 successfully examined the seasonal variability of the 558 nm OI nightglow emission using data from this instrument for the period from 1995 until mid-2006.

2.2. Data Preprocessing

Three types of preprocessing were applied before the 3FP data were further analyzed. The first process removed spikes caused by various forms of external interference and occasional problems with the operation of the filter. These features are typically only present for either one or two consecutive samples and so were readily removed using linear interpolation.

The second preprocessing was the removal of data for nights obviously affected by cloud. Following the approach applied by RW07, these were identified using visual inspection of the data. We attempted to use a less tedious approach to cloud removal by using cloud cover data from Adelaide Airport to remove data for those parts of nights where cloud was present. Adelaide Airport is some 40 km from BP, and cloud cover is not always expected to be the same at both locations. Because of this, cloud cover data from the closer Edinburgh Airfield (17 km distant) were also used. These were from a closer location but were much less complete than the Adelaide Airport data. Data from neither site proved to be superior to the visual inspection approach, and so the visual inspection was the approach settled on.

The third preprocessing process was applied to remove the effect of the Milky Way in the intensity data. The feature is present in both the 557.7 nm and 730 nm time series, although it is much more evident in the 730 nm data. Figures 1 and 2 show the effect of the Milky Way on the OI and OH data, respectively. These figures show a superposed year calculated from all 15 years of observation. The Milky Way is evident as the diagonal band of higher intensity running across these plots, first appearing early in the morning around day 85 and last appearing early in the evening around day 260.

Because of the relatively wide field of view, there is a limited high-frequency component associated with the Milky Way. *Reid and Woithe* [2005] examined removal of this feature using several techniques, including standard Fourier methods, when investigating short-period atmospheric gravity waves. Because of the localized nature of the Milky Way in the data, a wavelet-based approach proved to provide the best result for their work. In this study, we found that the most effective approach when investigating long-period variations is to simply remove data records in which the Milky Way was present. For each year, the exclusion period was a 4 h interval centered on a time which tracked about 4 min earlier per day, starting at about 0600 LT on day 90 (1 April) and finishing at about 1800 LT on day 273 (1 October) (as can be approximately discerned from Figure 2).

Journal of Geophysical Research: Atmospheres 10.1002/2013JD020906

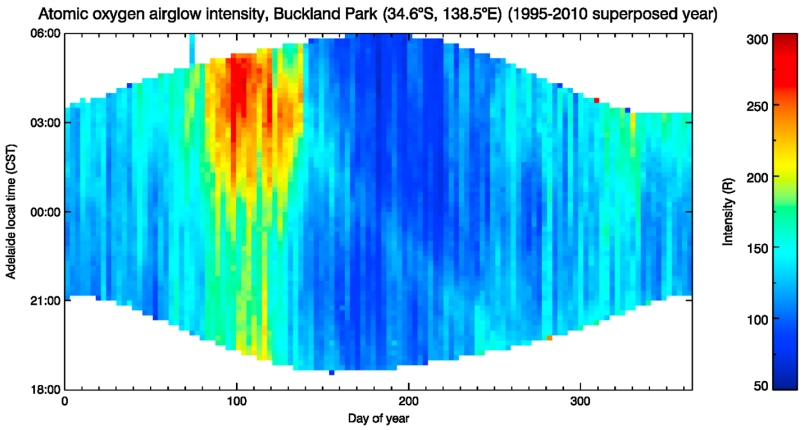

Figure 1. A superposed year of the nightly OI emission. The galactic contribution has not been removed from this image and is evident as the diagonal line running across the center of the image. Note the enhancement in the intensity at the time of the equinox, particularly the autumnal equinox (March) and its strengthening after local midnight.

2.3. Calibration

The 3FP was not calibrated absolutely. Relative calibration of the three photometer channel intensities for each of the 558 and 730 nm emissions was applied across the entire data set using the observed intensity of the Milky Way in each channel as a "standard candle." Inspection of Figures 1 and 2 indicates that the Milky Way is visible during some part of the night in the 3FP fields for about half of each year (late March through mid-September). Its peak intensity was initially calculated using the residual of the wavelet filter used to remove its amplitude from the individual OH intensity time series [*Reid and Woithe*, 2005]. These results were found to agree very well with results obtained by using the peak Milky Way intensity, and the latter was the approach subsequently adopted.

In the case of the 3FP 558 nm emission, the validity of the intensity correction was confirmed by calculating its ratio to that of the O_2 (0-1) intensity and provided by L. J. Gelinas (unpublished data, 2012) as measured in the Aerospace imager for the period from mid-2001 until mid-2010, and to the O_2 (0-1) intensity as measured using the Embry Riddle spectrometer for the 5 year period of 2001 until 2006. Although the OI and O_2 (0-1)

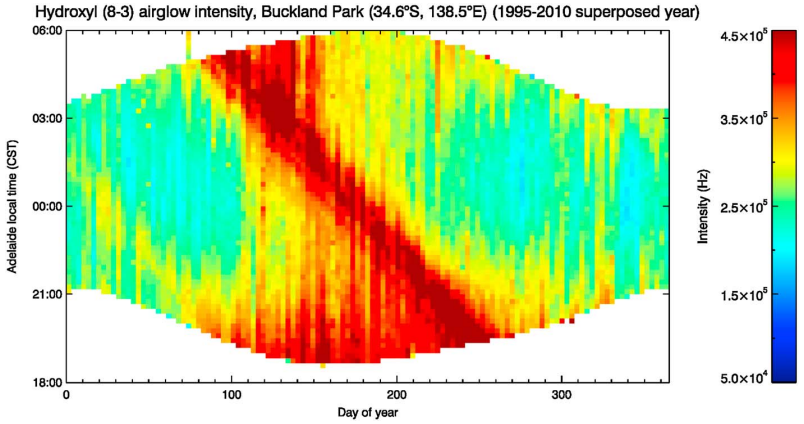

Figure 2. As for Figure 1 but for a superposed year of the nightly OH (8-3) emission. Note the brightening of the nightglow near dawn and dusk and the strong emission near March/April at the end of the night and the midyear brightening at the beginning and end of the night. The galactic influence is very clearly evident in this image, and there is a secondary feature earlier in the year. The latter feature was not used in the calibration of the 3FP.

Journal of Geophysical Research: Atmospheres 10.1002/2013JD020906

intensities are obviously from different emissions, it is not expected that their intensity ratios will vary over long time periods.

The relative calibration of the 3FP OI intensity was then compared to WINDII OI intensity observations for Adelaide provided by G. G. Shepherd (unpublished data, 2012) to obtain an absolute calibration. WINDII OI intensity data were available until late 1997 but were intermittent after mid-1996. Consequently, we have compared only the first 1.5 years of the photometer data, that is, until mid-1996, with the WINDII OI data.

The procedure used to obtain WINDII OI intensities relevant to the ground-based site can be summarized as follows. Firstly, all OI vertical emission rate (VER) profiles recorded between October 1995 and November 1996 in the latitude band 30–40°S were vertically integrated over the 80–115 km geometric height range, to encompass the entirety of the *E* region OI emission observable from the ground. Measurements taken across a group of days at similar local times (within about 1 h of each other) generally appeared to show a pronounced zonal planetary wave structure; this phenomenon observable in the WINDII OI measurements was first reported in *Shepherd et al.* [1993]. To account for this longitudinal structure in the measurements, a summation of trigonometric functions with zonal wavenumbers 1, 2, and 3 were fit via a least squares method to longitudinal profiles of measurements taken on the same UTC day within a similar band of local times. The value taken by these fits at Buckland Park's longitude (138.6°E), along with the local time at which they were recorded, was taken to be representative of the *E* region OI intensity observable at Buckland Park at that particular local time. A regression of the ground-based and resultant satellite measurements taken within 1 h of each other was then performed, and the "calibration factor" obtained from this was finally used to absolutely correct the ground-based measurements. This approach, which took advantage of the WINDII OI data recorded across a range of longitudes often encompassing the entire planet, was adopted in favor of simply taking measurements recorded in the vicinity of Buckland Park in order to reduce the scarcity of the data permissible for a comparison with the ground-based measurements.

Our corrected results agree well with the 3-monthly average zonal results published by *Liu and Shepherd* [2008] for 35°S from 1995 until the third quarter of 1997. They also agree well with the zonally averaged mean year OI intensity results for 35°S published by *Liu et al.* [2008] (see Figure 5 below). We are therefore confident that the correction based on the WINDII OI intensity data for the period of 1995 until mid-1996 and applied across the data set makes this absolute value valid across the 15 years of OI intensity observations. The overall result of this calibration process is that the mean intensity estimated across the 15 years of observation for the OI emission is 134 R. For comparison, in the preceding 16 years at the conjugate location of Kiso in Japan, DS08 found a mean intensity of 168 R.

In the case of the OH 730 nm emission, relative calibration of the photometer OH intensities was applied using the Milky Way "standard candle" in the same way as for the OI emission. This correction was again validated using the spectrometer and imager, this time using the ratio of the intensity of the photometer OH (8-3) band to that of the OH (6-2) band from the Embry Riddle spectrometer (2001 until 2006) and Aerospace imager (mid-2001 until the present). An absolute value was not estimated for this emission.

3. Results

A summary of the 558 nm and 730 nm intensity observations for the average of the three fields of the 3FP is presented for the period January 1995 to mid-2010 in Figures 3 and 4. The OI intensity is given in Rayleigh as determined by our calibration against the WINDII data. The OH optical emission brightness is referred to as "intensity" in units of "photon counts per second." Additionally, here and throughout the remainder of this paper, when a concise unit is required for clarity, Hertz (Hz) is adopted with an intensity of 1 Hz referring to "1 count per second."

To produce the averages shown in these figures, all of the data from Fields 1 and 2 were used. The original Field 3 photometer failed and was replaced in January 1998, and the data from this field have only been included from this date onward.

Figures 3 and 4 represent data that have been averaged in 5 min blocks through the night and then averaged across adjacent days. Careful inspection of these figures indicates the effect of the removal of the emission associated with the passage of the Milky Way through the field of view of the instrument. This is shown as a diagonal white band.

Journal of Geophysical Research: Atmospheres 10.1002/2013JD020906

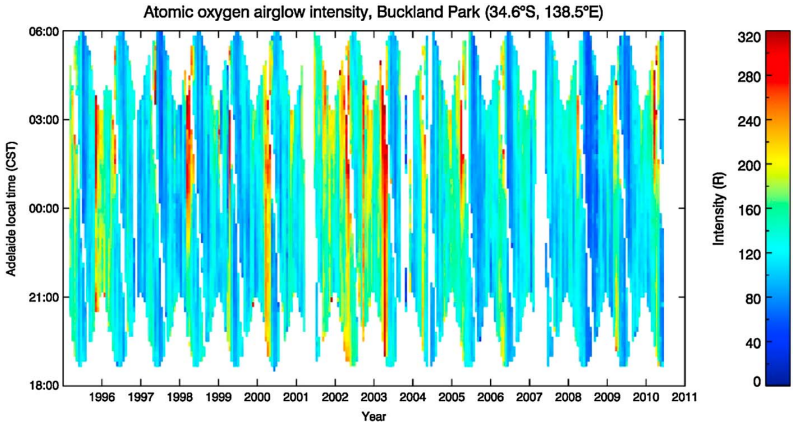

Figure 3. The intensity of the 558 nm nightglow measured throughout the night for the entire period of the observations. The emission associated with the passage of the Milky Way through the field of view has been removed from this plot and is evident as a white diagonal band within each year of observation. Note the enhancement in the intensity at the time of solar maximum.

Inspection of Figures 1–4 indicates several interesting features. In the 558 nm emission, there is an enhancement at the time of solar maximum and enhancements in emission near the equinoxes, particularly the autumnal equinox (March). At this time of the year, the enhancement brightens later in the evening/early morning. In the 730 nm emission, intensities are typically brightest in winter (midyear); there is some brightening midsummer (beginning of the year) later in the evening. There is no strong modulation of intensity consistent with the solar cycle evident in this emission.

To illustrate the development of the main features evident in Figures 1–4, through time, Figures 5 and 6 show a superposed year for each of three 4 h periods through the night starting at 1800 LT for each emission. The gaps in the data correspond to the times the Milky Way was present in the data. In Figure 5, the strengthening of the autumnal peak in the 558 nm intensity through the night is the most striking feature, and careful inspection also indicates the strengthening of the summertime maximum in the annual oscillation (AO) as the night progresses. In the 00:00–03:00 LT block in Figure 5 we have included the WINDII zonal average for 35°S for the OI volume emission rate at 96 km for 0200 LT taken from *Liu et al.* [2008]. This shows generally good agreement, although the autumnal peak is stronger in the 3FP result.

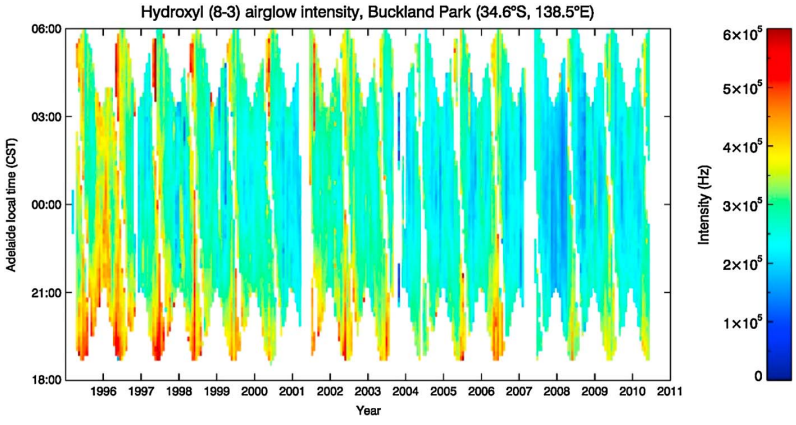

Figure 4. As for Figure 1 but for the intensity of the 730 nm nightglow measured throughout the night for the entire period of the observations. Note the brightening of the nightglow near dawn and dusk and the strong emission near March/April at the end of the night and the midyear brightening at the beginning of the night.

Journal of Geophysical Research: Atmospheres 10.1002/2013JD020906

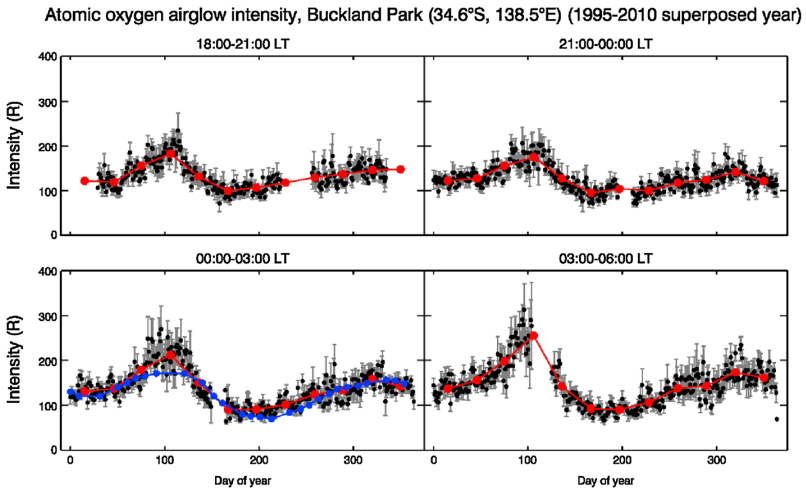

Figure 5. Superposed year of the averaged intensities for the OI emission for each of the four 3 h data blocks through the night. Error bars indicate the standard deviation. The red points indicate monthly averaged values, and the blue points are the zonally averaged VERs from *Liu et al.* [2008]. The gap in each of the time series corresponds to the time of the presence of the Milky Way in the data.

In Figure 6, the variation of the OH intensity through the night shows a clear change from a predominantly annual variation to an annual and semiannual mix as the night progresses. The WINDII zonal average for 35°S for the OH volume emission rate at 88 km for 2200 LT taken from *Liu et al.* [2008] is shown in the 21:00 to 00:00 LT time block. In this case, there is general agreement, but it is less good than that for the OI emission.

In the next section, we quantify the variations evident in the data shown in Figures 1 to 6.

4. Analysis

RW07 used harmonic fitting to the intensity time series after determining the significant periods present in the data using a Lomb periodogram analysis. Here we extend their approach by also using a continuous wavelet analysis to the data [*Torrence and Compo*, 1998]. This has the advantage of providing a measure of

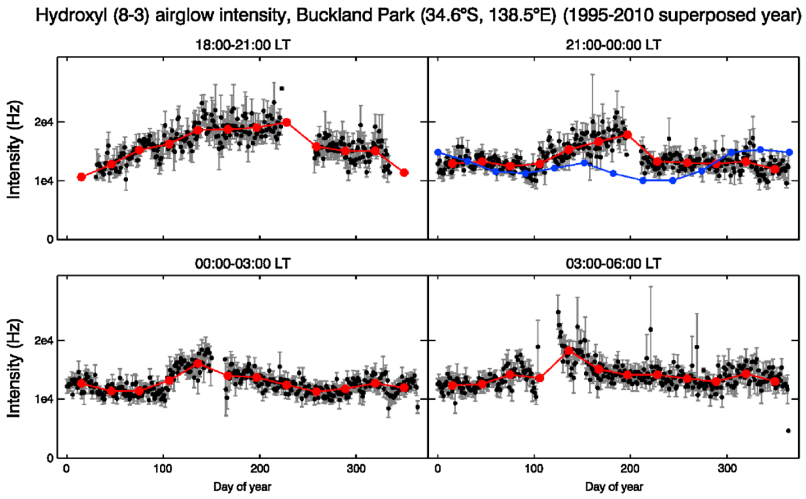

Figure 6. As for Figure 5 but for the OH (8-3) emission.

Journal of Geophysical Research: Atmospheres 10.1002/2013JD020906

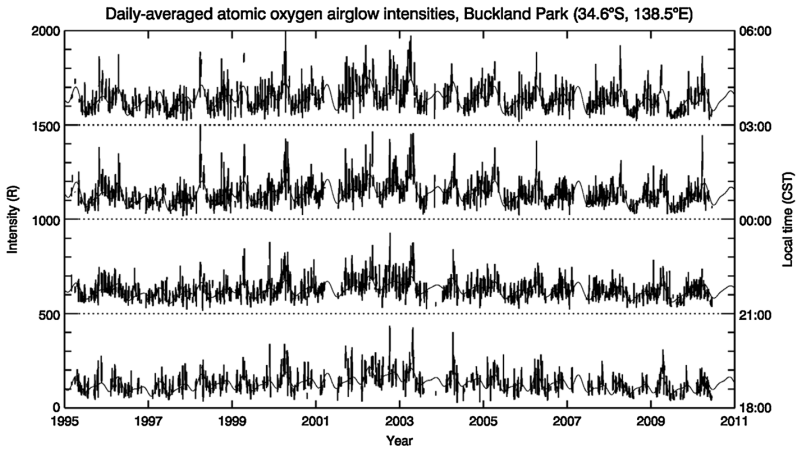

Figure 7. The average 558 nm airglow intensities for the three fields for the four 3 h data blocks measured through the night. The average has been formed from all of the Field 1 and Field 2 data, and Field 3 data from 1 January 1998 onward. The solid line indicates the result of the harmonic fit to the data based on the periods identified in the Lomb periodogram shown in Figure 9 (see the text for details).

the variation of the amplitude and mix of oscillations present through the observational period. This is important when examining variations between the quasi-biennial oscillation (QBO) and quasi-triennial oscillations (QTO) which have been observed to occur in both the Na and OH airglow at Haute Provence (44°N, 6°E) [*Fukuyama*, 1977] and in the OI airglow at Kiso [*Das and Sinha*, 2008]. We begin with a Lomb periodogram analysis to the four 3 h average blocks of the intensity data shown in Figures 7 and 8.

4.1. Lomb Periodogram Analysis

In order to identify the periodicities present in the intensity data, Lomb periodograms were calculated using the method of *Press and Rybicki* [1989] for the entire night for each of the emissions. The Lomb periodogram for the average of the three fields for the nightly mean of the 558 nm OI intensity data is shown in Figure 9 (first panel) and for the nightly mean of the 730 nm OH intensity in Figure 10 (first panel). Following the approach of RW07, data were also binned into four consecutive 3 h blocks starting at 1800 LT, and the Lomb periodograms for these data sets are shown in Figures 9 (second to fifth panels) and 10 (second to fifth

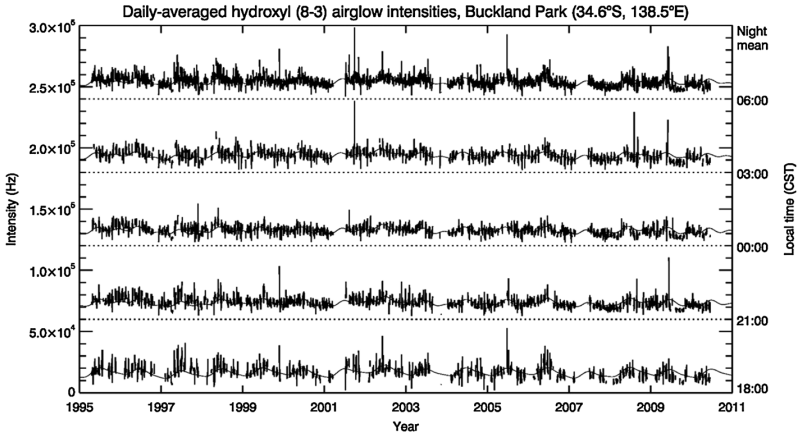

Figure 8. As for Figure 7 but for the average 730 nm airglow intensities for the three fields for the four 3 h data blocks measured through the night. The solid line indicates the result of the harmonic fit to the data based on the periods identified in the Lomb periodogram shown in Figure 10 (see the text for details).

Journal of Geophysical Research: Atmospheres 10.1002/2013JD020906

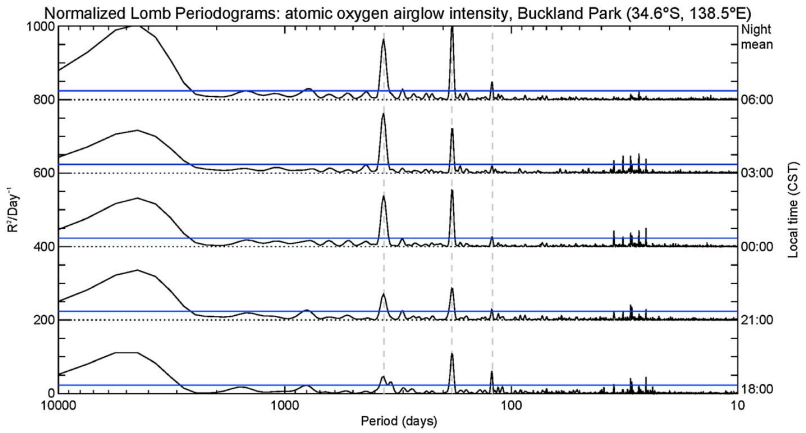

Figure 9. Lomb periodograms calculated from the four data series shown in Figure 7. Note the peaks near 122, 183, 365, 770, 1490, and 4088 days. There is power at the QTO period near 1075 days in the nightly mean, but it is not significant at the 99% level (indicated by the horizontal blue line). Also note the variation in the amplitude of the peaks for a given periodicity through the night.

panels). A 3 h average was selected in order to provide both a statistically reliable measure and the ability to investigate variations of the airglow intensity through the night. Following the discussion of *Hernandez* [1999], we have calculated the 99% significance level for the Lomb periodograms using the method of *Schuster* [1898], which agrees well with the exact *Fisher* [1929] method and to a greater extent than the method of *Press et al.* [1986], previously used by RW07. The 99% confidence level corresponding to the Schuster significance level is shown as the blue horizontal line on each of the periodograms.

Inspection of Figure 9 indicates peaks present at periods (rounded to the nearest day) near 122, 183, 365, 770, 1490, and 4088 days all confident at a level greater than 99%. A series of peaks below about 100 days particularly between 20 and 40 days period is also evident. The latter peaks have been discussed by RW07, who concluded that they did not contain useful geophysical data, and most likely resulted from the 28 day sampling period imposed by the lunar cycle. Each of the four 3 h time series through the night show similar spectral content to the nightly mean, with the 122, 183, 365, 770, 1490, and 4088 day periods all confident at a level greater than 99% in each of the four 3 h bins.

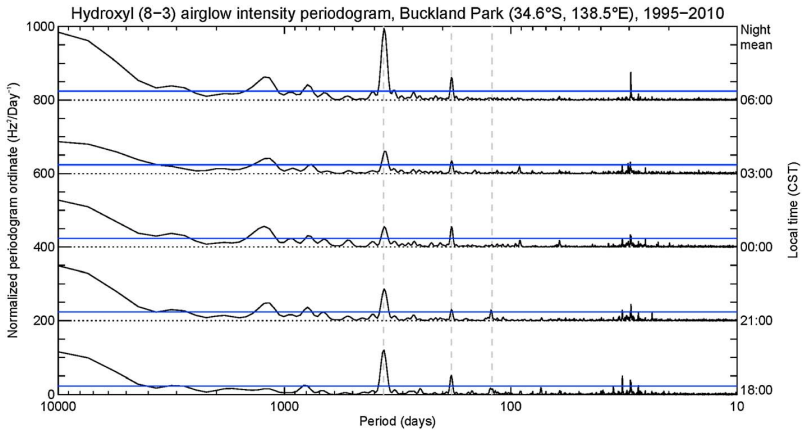

Figure 10. Lomb periodograms calculated from the four data series shown in Figure 8. Note the peaks near 183, 365, 770, 1075, and 3000 days. There are significant peaks at 90 days in the 0000 to 0300 LT and 0300 to 0600 LT periodograms and a significant 60 day peak in the 0000 to 0300 LT periodogram. Also note the variation in the amplitude of the peaks for a given periodicity through the night.

AGU Journal of Geophysical Research: Atmospheres 10.1002/2013JD020906

Figure 10 shows the Lomb periodograms for the OH emission. Peaks are present in the nightly mean at periods (rounded to the nearest day) near 183, 365, 791, 1175, and 3000 days at a level greater than 99%. Like the OI periodograms, there are peaks evident between 20 and 40 days present. Each of the four 3 h time series through the night show similar spectral content to the nightly mean, with the 183, 365, and 791 day periods all confident at a level greater than 99% in each of the four 3 h bins. Unlike the OI emission, the 122 day period is not present at a significant level in the nightly mean but is present prior to 0000 LT at a 99% significance level. The QTO is evident but not significant at the 99% level prior to 2100 LT, and the 3000 day period is not evident after 0300 LT.

4.2. Harmonic Fits

The periods identified in the Lomb periodogram as significant at the 99% level in the nightly mean were used to fit harmonic functions using least squares fitting. We will consider other components that may be present through the observing period with more variable amplitudes throughout using a wavelet approach below. The actual period of each statistically significant peak identified in Figures 7 and 8 was determined by varying the period to minimize the chi-square of the fit, and the following function was used as a basis for the least squares fit

$$f(t) = \sum_{i=1}^{N} A_i \cos \frac{2\pi(t - \theta_i)}{T_i}$$

where t is the time index in days, A_i is the calculated amplitude, θ_i is the calculated phase in days, T_i is the predetermined period in days, and N is the number of harmonic components. For the atomic oxygen emission, T_i = [4088; 1490, 770, 365; 183; 122] and for the hydroxyl emission T_i = [4088; 1175; 791, 365; 183] days. We have chosen to fit the 4088 day period to the hydroxyl data rather than the 3000 day period in order to make a direct comparison with the OI solar cycle contribution, even though this is not justified from the Lomb periodogram analysis. However, we find that when this is done, the phase corresponds to that of the 4088 day period in the OI component to within the experimental uncertainty.

In fitting, we followed the method suggested by *Hernandez* [1999]. A sequential approach was applied, where the strongest period was fitted before moving onto the next largest amplitude periodicity. The reason for fitting each periodicity in turn was to prevent the fit from getting trapped in a shallow chi-square local minimum. A component was not removed from the data before fitting the next; instead, its parameters in the harmonic series were held at their fitted values, with only the next component of interest having "variable" parameters visible to the fitting function. Hence, at all times the same data were being fitted.

Hernandez [1999] has also considered the Lomb periodogram approach when applied to similar data and suggests several limitations. To further validate the periods selected in our analysis, we note that the 122, 183, 365, and 4088 day periods are readily evident when the OI intensity time series are inspected by eye. All of the selected periods are evident in the wavelet spectra. Likewise, the 183 and 365 day periods are readily evident in the OH (8-3) intensity time series. The QTO is not as evident by visual inspection of the time series, but all of the selected periods do appear in the wavelet analysis. To further validate the periods identified, we compared the harmonically fitted function with 120 day running means for each field. These indicated good agreement and provided additional confidence that the periods identified actually exist in the data sets.

The 1800–2100 LT time bin included sunset at some times of the year, while the 0300–0600 LT time bin included sunrise at some times of the year. Data were not acquired at these times, so it might be considered that these bins were not representative for the purposes of fitting the terannual oscillation (TAO) and semiannual oscillation (SAO). However, fits were made to all four of the 3 h data sets giving a total of 12 fits per emission and yielding the same results to within the experimental error as for the two 3 h data sets from 2100 to 0300 LT. Consequently, we choose to use all four 3 h blocks in the harmonic analysis.

Table 2 summarizes the results of the harmonic fit to the 558 nm data based on the peaks identified in the Lomb periodogram shown in Figure 9. The harmonic fit is overplotted on the appropriate times series in Figure 7. The periods indicated in this table and used below have been rounded to the nearest day. The relative amplitude shown in this table indicates the mean relative amplitude of the four time series analyzed, and the amplitude in Rayleigh is that determined by the WINDII calibration. The phase is the mean phase of the four time series and indicates the day number of the first maximum relative to 1 January 1995. The largest contribution to the variability of the intensity is from the SAO with a relative value of 22 ± 4%.

AGU Journal of Geophysical Research: Atmospheres 10.1002/2013JD020906

Table 2. Results of Harmonic Fits to the BP 558 nm Emission Intensity Data

		O(^{1}S)					
Period (days)	Mean	122	183	365	770	1490	4088
Amplitude	134 R	11 ± 4%	22 ± 4%	18 ± 9%	7 ± 3%	7 ± 5%	17 ± 7%
Phase (first max after 1 Jan 1995)		103 ± 3 13 Apr Autumn	107 ± 2 17 Apr Autumn	57 ± 17 26 Feb Summer	475 ± 38 19 Apr 1996 Autumn	1437 ± 133 7 Dec 1998	2872 ± 232 11 Nov 2002

Inspection of Table 2 indicates that the amplitudes of the SAO and AO agree within the experimental uncertainties at 22 ± 4% and 18 ± 9%, respectively. The phase of the SAO takes its first maximum on 17 April 1995 (107 ± 2 days) which is midautumn. The AO takes its maximum on 26 February 1995 (57 ± 17 days) which is in late summer. The next largest contribution is from the solar component with an amplitude of 17 ± 7% maximizing on 11 November 2002 (±232 days). The terannual oscillation (TAO) has an amplitude of 11 ± 4%, which first maximizes on 13 April 1995 (103 ± 3 days), in midautumn. The QBO has an amplitude of 7 ± 3%, and there is a 4.1 year period with an amplitude of 7 ± 5% present.

Table 3 summarizes the results of the harmonic fit to the 730 nm data based on the AO and SAO, with QBO and QTO peaks identified in the Lomb periodogram shown in Figure 10. The harmonic fits are overplotted to the four 3 h blocks and the nightly mean in Figure 8. In the case of the OH intensity, the fitted 4088 day periodicity is only 6 ± 5% of the mean intensity with its maximum on 30 March 2002 (day 2646 ± 359). The annual oscillation is the largest component of the intensity time series with a relative amplitude of 15 ± 7% of the mean intensity. The phase of this oscillation takes its first maximum on 18 June (day 169 ± 22) in early winter. The semiannual oscillation has a relative amplitude of 7 ± 5% or about 47% that of the annual oscillation. Its phase maximizes on 5 June (day 156 ± 17), in early winter, which agrees with the phase of the AO to within the experimental uncertainty. The QTO has a period of 1175 days, or 3.2 years and an amplitude of 8 ± 4%, which takes its first maximum in midsummer 1996 (day 374 ± 53; 9 January 1996) and a QBO with an amplitude of 5 ± 3% with a first maximum on 17 November 1995 (day 321 ± 54).

4.3. Wavelet Analysis

The results of a wavelet analysis using IDL software provided by C. Torrence and G. Compo (freely available at http://paos.colorado.edu/research/wavelets/software.html) to 30 day averaged nightly mean intensity values are shown in Figure 11 for the 558 nm emission and in Figure 12 for the 730 nm emission. Here we have followed the presentation style used by DS08 in their analysis of Kiso OI intensity data, in that the time series of 30 day averages is shown in the lower part of the panel, the wavelet spectrum above that, and (in our case) the Lomb periodogram to the right. Note that the Lomb periodogram corresponds to nightly averages, rather than 30 day averages, and we have included it in order to be able to directly compare the wavelet results with the Lomb periodogram results shown in Figures 9 and 10 and used as the basis of the harmonic fitting. The Schuster 99% confidence level is indicated on the Lomb periodogram plot.

The mother wavelet function used was of Gaussian windowed cosine (Morlet) form, with an ω_0 value of 10. This is in slight contrast to *Torrence and Compo* [1998] and DS08, both of whom select a corresponding value of 6 for their analysis. *Farge* [1992] notes that an ω_0 value greater than 5 is required for a Morlet wavelet to have a mean of zero (and hence satisfy the admissibility condition) without additional correction terms. Increasing ω_0 to values higher than 6 offers increased resolution in the frequency domain of the wavelet transform, with the trade-offs being decreased time resolution and a more restrictive cone of influence. We

Table 3. Results of Harmonic Fits to the 730 nm Emission Intensity Data

		OH (8-3)			
Period (days)	183	365	791	1175	4088
Relative Amplitude (%)	7 ± 5%	15 ± 7%	5 ± 3%	8 ± 4%	6 ± 5%
Phase (first max after 1 Jan 1995)	156 ± 17 5 June Winter	169 ± 22 18 June Winter	321 ± 54 17 Nov Spring	374 ± 53 9 Jan 1996 Summer	2646 ± 359 30 Mar 2002

Journal of Geophysical Research: Atmospheres 10.1002/2013JD020906

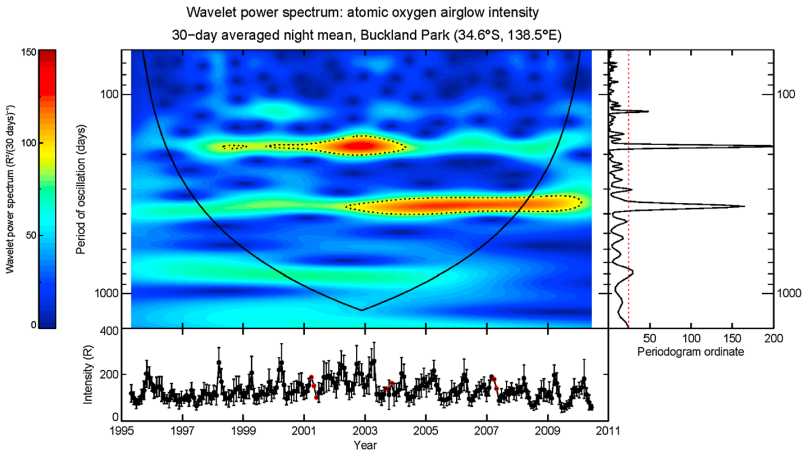

Figure 11. Wavelet spectrum of the OI 30 day average of the nightly mean intensity for the entire observational period. The intensity time series is shown below the wavelet spectrum, and the Lomb periodogram for the daily mean values is shown on the right-hand side for reference. Red points in the time series indicate missing data points which have been interpolated. Error bars indicate the standard deviation for each of the mean values. Dotted lines on the wavelet spectrum indicate the 99% confidence level. The red dotted line on the Lomb periodogram indicates the Schuster 99% confidence level.

chose an ω_0 value of 10 to more clearly display both the intermittency of the SAO and TAO during the period spanning 1997–2009 in the OI intensity and the amplitude variation in the AO of the hydroxyl emission.

Inspection of the OI intensity variations shown in Figure 11 indicates that the SAO amplitude peaks during the period 2002 to 2004. The AO takes its maximum amplitude in the second half of the observing period, strengthening after 2002. There is power at the QBO period, but it is not significant at the 99% level, and insight into its development over the observing period is limited by the cone of influence. The TAO is intermittent in amplitude and does not reach the 99% confidence level.

The OH (8-3) intensity variations shown in Figure 12 show a dominant AO. The SAO is present through the entire observing period within the cone of influence but not at a 99% significance level. There is power at the QBO period through the observing period but not at the 99% significance level. There is power at the period of the QTO, although it is mostly outside the cone of influence.

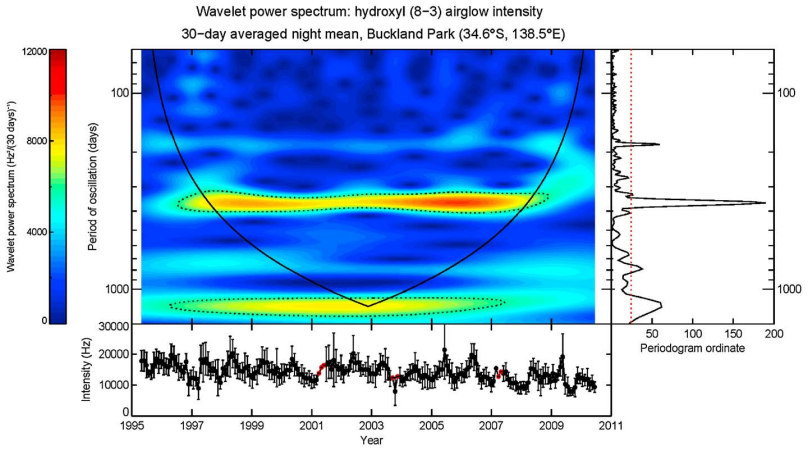

Figure 12. As for Figure 11 but for the OH (8-3) emission intensity.

Journal of Geophysical Research: Atmospheres 10.1002/2013JD020906

Table 4. Results of Harmonic Fits to the Kiso 558 nm Emission Intensity Data

		O(^{1}S) Kiso			
Period (days)	Mean	121	183	365	4088
Kiso	168 R	10%	16%	21%	18%
Kiso		45	115	210	544
After 1 Jan 1979		14 Feb Winter	25 April Spring	(30) 29 June Summer	(16 Nov 2002)

5. Discussion

5.1. OI Intensity (558 nm)

The 3FP OI 558 nm results for 1995 until 2006 have previously been discussed by RW07, and we revisit them here in the context of the additional results available from this work, the results from the significant analysis of the 16 year Kiso 558 nm intensity data set by DS08, and the O_2 (0-1) intensity results from G08 for 2002–2005 for BP.

Table 2 summarizes the OI intensity results for the entire data set. The SAO, AO, and solar cycle results are in good agreement with those of RW07, but there are a few obvious differences. We have fitted the TAO whereas they did not, and we do not find the 1650 day (4.5 year) periodicity they found. Instead, we find a 1490 day (4.1 year) periodicity which is significant at the more stringent Schuster 99% level in the nightly mean in our longer data set. We also note for completeness that RW07 only used fields 1 and 2, and only used data from 2100 until 0300 LT when fitting their results.

When considering the OI nightglow, a question arises in relation to the relative contribution of the *E* and *F* region emissions. A review of the literature indicates very little published data in relation to the nightglow relative intensities, in contrast to that for the dayglow [see, e.g., *Zhang and Shepherd*, 2005]. *Takahashi et al.* [1990] did consider the results from a rocket-borne photometer at an equatorial location and deduced an *F* region contribution of about 30 to 50 R. Examination of the 1 year of WINDII OI emission data provided by G. G. Shepherd (unpublished data, 2012) for Adelaide used for the 3FP calibration indicate an average relative emission from the *F* region of 6% of that of the *E* region with no seasonal structure. We conclude that our OI results are representative of the *E* region.

We now consider the various periodicities in more detail in the following sections.

5.1.1. TAO, SAO, and AO

As we have noted above, the amplitudes of the TAO, SAO, and AO are modulated through the period of the observations. However, the harmonic fits allow some generalizations to be made. The TAO peaks around the times of equinox and summer solstice. The SAO is an equinoctial phenomenon with the largest intensities observed in autumn. The AO peaks in late summer. Generally, the SAO is observed to dominate at lower latitudes and the AO at higher latitudes; RW07 noted that Adelaide appeared to be transitional with some low-latitude and some midlatitude characteristics, and we find that the amplitudes of these two periodicities agree to within the experimental uncertainty.

Earlier we noted the annual variation of the 558 nm volume emission rate provided by *Liu et al.* [2008], who analyzed WINDII results to provide latitudinal averages. We have shown their results for 35°S at 0200 LT in Figure 5, and we note that the agreement is very good in form, with the autumnal maxima being less prominent in the zonal average.

DS08 looked at the Kiso OI intensity data for a 16 year period from 1979 to 1995. They did not harmonically analyze their results, but we have taken their published 30 day averaged nightly mean data and analyzed them as we analyzed our own data as described in sections 4.1 and 4.2. The results are summarized in Table 4. The agreement with Table 2 is good. When the results are adjusted for the seasonal variation and the solar cycle continued into our period of observation, the agreement between the Kiso and BP results becomes very clear. This is shown in Figure 13. This confirms that at both 35°S and 35°N, there is a clear solar cycle dependence, an SAO with dominant emission at the autumnal equinox, an AO of similar amplitude to the SAO with maximum emission in late local summer, and a TAO with emission peaks at equinox and summer. The Kiso results (168 R) do appear to be brighter than the Adelaide results (134 R), but the relative amplitudes of the solar, AO, SAO, and TAO are very similar.

AGU Journal of Geophysical Research: Atmospheres 10.1002/2013JD020906

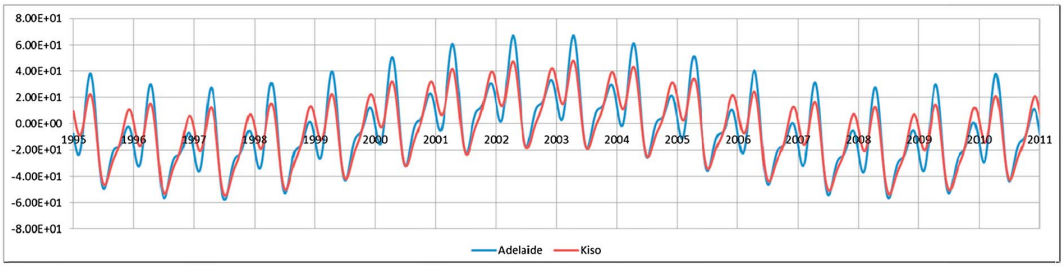

Figure 13. Adelaide solar, AO, SAO, and TAO harmonic fits with the Kiso results overplotted. In the case of the AO, SAO, and TAO, the Kiso results have been shifted 6 months in time, and in the case of the solar component calculated for Kiso, the phase has been extended in time of two solar cycles.

G08 published a comprehensive study of the annual and semiannual oscillation in the OH (6-2) and O_2 (0-1) airglow intensity and rotational temperatures measured at both Adelaide and Alice Springs during a 4 year period between 2002 and 2005. Their Adelaide observations are made using the Aerospace Imager at the Buckland Park field site, and they also compared their observations with the TIMED-GCM results for the same period. Their results refer to a superposed year for a 6 h period centered on local midnight, and so to compare their intensity results with our observations, we reanalyzed our data by binning them into a superposed year corresponding to that of G08 and then fitted only the SAO and the AO.

Table 5 summarizes our SAO and AO OI intensity results for 2002 to 2005 along with the corresponding O_2 (0-1) intensity results from G08. The phases of the SAO O_2 and OI observations agree, and the O_2 SAO amplitude is larger than that of the OI. The O_2 AO amplitude is smaller than that of the OI AO amplitude, but the phases agree to within the experimental uncertainty. We note that in the OI superposed year results, power has accumulated in the AO (from 18% in the fit to entire data set to 22% for the superposed year) although still within the experimental uncertainty, and the uncertainty in the phase has increased slightly (from ±17 to ±19 days). *Deutsch and Hernandez* [2003] have noted a similar effect when creating a superposed year when longer periods are present. Neither the G08 nor our results agree with the TIME-GCM results to within the experimental uncertainties. Our results indicate much larger intensities with our AO and SAO amplitudes 7 and 3.5 times those of the TIME-GCM, respectively, while the AO phases differ by 130 days and the SAO by 90 days.

When comparing OI and O_2 (0-1) emission intensities, it is interesting to note the work of *Buriti et al.* [2001], who reported measurements of the intensities of the OI 558 nm and the O_2 (0-1) atmospheric band made at São João do Cariri (7°S, 35°W). They note that to a first approximation, the intensity ratio between OI 558 nm and O_2 (0-1) gives an indication of the atomic oxygen mixing ratio of $[O]/[O_2]$ in the emission height range. If this can be applied to our results, it would indicate a difference in the mixing ratio between the annual and semiannual periodicities and between March and September.

Angelats i Coll and Forbes [1998] looked at the effects of the mean meridional circulation, diurnal and semidiurnal tides, and eddy and molecular diffusion on local time variations in O concentrations and 558 nm emission rates. They found that vertical winds play an important role in producing variations in these quantities and could account for the equatorial emission rate structures inferred from WINDII. They also found that smaller secondary effects are produced by tidal variations in the major species concentrations and in temperature-dependent chemical reaction rates.

Table 5. BP OI Emission Intensity Data for a Superposed Year and BP Aerospace Imager O_2(0,1) Intensity Data From G08 for the Same Years[a]

		AO		SAO	
OI and O_2 Intensity	Mean	Amplitude (%)	Phase	Amplitude (%)	Phase
This study OI superposed year (2002–2005) AO and SAO only	134 R	22 ± 5	73 ± 19	21 ± 3	108 ± 3
G08 O_2 (0-1) superposed year (2002–2005) AO and SAO only	152 ± 2 R	7 ± 2	31 ± 20	29 ± 2	111 ± 2
O_2 TIME-GCM (from G08)		3 ± 1	308 ± 17	6 ± 1	18 ± 4

[a]Only the SAO and AO have been fitted.

Journal of Geophysical Research: Atmospheres 10.1002/2013JD020906

Considerable clarity on the global airglow morphology and its relation to the dynamics of the MLT region has been provided by the studies of Shepherd and colleagues which contrast WINDII satellite and ground-based observations, and TIMED-GCM model calculations. Their studies highlight the close interplay between tidal influences and the global planetary airglow intensity and temperature morphology [e.g., *Shepherd et al.*, 2005; *Liu and Shepherd*, 2008; *Liu et al.*, 2008]. In particular, they note that the diurnal variation in intensity is associated with tidal dynamical effects and that there is a well-defined semiannual variation in emission rate of the O(^{1}S) nightglow in the tropics, consistent with the amplitude variation of the propagating diurnal tide at low latitudes [*Liu et al.*, 2008]. The low-latitude variation has emission rate maximum in both spring and autumn, which transitions to an annual variation at higher latitudes with a maximum in the autumn [*Shepherd et al.*, 2005].

More recently, *Smith et al.* [2010] have also concluded that the semiannual variation in the diurnal tidal amplitude affects the seasonal variation of daily average atomic oxygen concentration, which likely indicates that there is irreversible transport by the tides. They suggested that atomic oxygen is brought down on the tide but not returned.

Diurnal tidal winds at Adelaide are strongly influenced by the (1,1) mode, and its amplitude exhibits a strong interannual variability in amplitude [see, e.g., *Vincent et al.*, 1998]. In this, and in a number of other characteristics, Adelaide has the attributes of a lower latitude site. In terms of seasonal behavior, the diurnal tide undergoes the same behavior in zonal and meridional wind components with strong maxima in amplitude in March (SH autumn) and with secondary maxima in July/August (SH winter) and October (SH spring). *Vincent et al.* [1998] found that the diurnal tidal amplitudes are larger than the climatological average at the autumnal (March) equinox in the eastward phase of the QBO and smaller than average in the westward phase of the QBO. The phases of both the semidiurnal and diurnal tides show little interannual variability.

We note that at Adelaide there is a striking correspondence between the O_2 temperature maximum, the time of greatest 558 nm brightness (RW07), and the time of the maximum meridional wind, which would correspond to the downward phase of the diurnal tide at equinox later in the night. This is consistent with the transport of atomic oxygen down into the MLT region and the brightening of the OI and OH (8-3) airglow late in the night as observed at the autumnal equinox.

The view that it is the vertical advection of atomic oxygen rather than the variation in eddy diffusion which is responsible for the semiannual variation in airglow intensity is in contrast with the older suggestion [see, e.g., *Garcia and Solomon*, 1985] that it is the change in eddy diffusivity associated with gravity wave breaking that produces the equinoctial brightening in the 558 nm airglow emission intensity. Variances of wind velocity and airglow intensity are certainly higher at equinox, a result consistent with enhanced gravity wave activity at that time, but the relative importance of vertical advection and gravity wave mixing is yet to be determined. We will consider this further in future work.

5.1.2. QBO

The QBO is prominent in the wavelet spectrum (Figure 11) between 1997 and 2005. This corresponds approximately to the time of strongest SAO and to a weaker AO. DS08 observed that the QBO becomes a QTO during some sequences of years at Kiso and also noted that a change from QBO to QTO can occur through the night. In the present study, we do not find a significant QTO in the nightly mean 558 nm airglow emission. We do note that there is power near 1175 days in the Lomb periodogram in Figure 7, particularly earlier in the night, but not at the 99% significance level.

5.1.3. Periodicity of 4.1 Years

In this study, we find a 4.1 year periodicity with an amplitude of 7 ± 5% of the mean and which takes its first maximum in early December 1998, with the next maximum near the peak of solar cycle 23. We are uncertain as to the origin of this component, but note that it has appeared in other spectral analyses of the *Ap* index and sunspot number. For example, *Fraser-Smith* [1972] found a 4.1 year periodicity in his analysis of 457 monthly average *Ap* indices for a 38 year period and suggested that a possible origin in the solar corona is indicated for this component, and *Krivova and Solanki* [2002] found a 4.1 year periodicity in an analysis of monthly values of the sunspot number recorded between 1749 and 2001.

Periods close to half a solar cycle are relatively common and have been noted in 558 nm intensity by *Hernandez* [1976], *Mikhalev et al.* [2008], and *Semonov and Shefov* [1997; reported in *Mikhalev et al.* [2008]. *Hernandez* [1976] found a 5 year periodicity in one solar cycle of Fabry-Perot spectrometer Doppler

AGU Journal of Geophysical Research: Atmospheres 10.1002/2013JD020906

temperatures from the 558 nm emission at Fritz Peak (39.9°N), and *Mikhalev et al.* [2008] found variations in the 558 nm intensity of 5.5 years over Irkutsk (52°N). This periodicity also occurs in the OH emission. For example, *Shefov* [1969] found a 5.5 year periodicity in the intensity and rotational temperatures derived from this emission. Interestingly, *Mikhalev et al.* [2008] find a maximum in the 5.5 year periodicity in the 558 nm airglow intensity in solar cycle 23 at Irkutsk in 1998 and in 2002, a phase in agreement with the present observations. The amplitude in their observations is about 20% of the mean. More typical values from the work cited above at midlatitude sites are around 5%. Whether there is any relation between the 5 year period and our 4 year period is unclear.

5.1.4. OI Solar Cycle Dependence

We note at the beginning of this discussion that although the WINDII results for 1995 and 1996 indicate an *F* region OI intensity contribution of less than 6% of that of the *E* region, we cannot account for the *F* region green line emission solar dependence across the observational period of these data. However, we would expect 1995 and 1996 to be typical and for the relative contribution to be similar across our entire data set. With this caveat noted, we consider the solar cycle dependence of the 558 nm intensity in our data. Solar radiation directly drives the production of atomic oxygen, and so the nighttime O(^{1}S) emission rate could be expected to follow solar activity. This is typically observed [e.g., *Donahue et al.*, 1973; *Fukuyama*, 1977; *Takahashi et al.*, 1984; *Deutsch and Hernandez*, 2003; *Clemesha et al.*, 2005; *Liu and Shepherd*, 2008], although the response typically shows some hysteresis in that the decline in the emission intensity after solar maximum is slower than the decline in solar activity. *Silverman* [1970] discussed the variation of 558 nm intensity with solar cycle at some length and noted that a number of authors had found that the dependence was not symmetric over the solar cycle. Indeed, whether a sinusoid as fitted here is the best form is fit is not obvious given the form of the $F_{10.7}$ cm flux or sunspot number (rapid rise and slower falloff). *Deutsch and Hernandez* [2003] follow *Hernandez and Silverman* [1964] and find a hysteresis between the Penticton $F_{10.7}$ cm flux and the 558 nm airglow intensity at a number of sites. They find greater intensity during the decreasing phase at six sites (including Canberra at 35°S in Australia and Kiso in Japan at 36°N), which is also seen in our data, and find a lower intensity during the decreasing phase at two sites, one of which is at 33°N and the other at Mount John in New Zealand at 44°S (latitudes which bracket Adelaide's).

Campbell and Brunger [2010] modeled the RW07 long-term 558 nm intensity results and considered the kinetic, ionospheric, and auroral contributions to the 558 nm emission. They concluded that there was agreement between the observations and the kinetic contribution to the nightglow, particularly for the AO, SAO, and solar cycle variations. They also found that the observed post solar maximum enhancement was better matched to the model calculations when the auroral hemispheric power was included and so concluded that there was a contribution to the 558 nm nightglow emission associated with auroral activity rather than to direct auroral precipitation itself.

Pertsev and Perminov [2008] found an amplitude of 25% of the mean in the O_2 (0-1) intensity for the solar cycle contribution as measured in the hour immediately after local midnight at Zvenigorod (56°N, 37°E) in the years 2000 to 2006. *Scheer et al.* [2005] found a moderate positive correlation between the solar radio flux and the O_2 (0-1) intensity at the El Leoncito (32°S, 69°W).

In the present observations, the solar cycle dependence is a large contributor to the long-term variation in the 558 nm nightglow intensity with an amplitude of 17 ± 7% of the mean, which maximizes on 11 November 2002 (±232 days). *Das et al.* [2011] considered the solar cycle variation of the Kiso 558 nm emission using a Hilbert Huang transform approach. Using this method, they found a mean amplitude of around 20% over the 16 year period of the observations. We have already noted the similarity of the Kiso results summarized in Table 4 to those of the present study, and in the case of the solar cycle, we find an amplitude of 18% by using a harmonic fit to the Kiso data, with a peak 544 days after 1 January 1979. This would correspond to 16 November 2002 two solar cycles later, which is in excellent agreement with our present result of 12 November 2002 (±232 days).

5.2. OH Intensity (730 nm)

5.2.1. TAO, SAO, and AO

In the nightly averages, the AO in the OH emission is a wintertime phenomenon, and the SAO takes its first peak in the year in winter. Inspection of Figure 2 indicates that there is an autumnal enhancement in the OH intensity late in the night, which corresponds to the time of that in the OI emission. There does not appear to

AGU Journal of Geophysical Research: Atmospheres 10.1002/2013JD020906

Table 6. Summary of the *OH SAO* and *AO* Intensity Results of the Present Study for One Superposed Year and for *Gelinas et al.* [2008] (G08) for Adelaide

		AO		SAO	
OH Intensity	Mean	Amplitude (%)	Phase	Amplitude (%)	Phase[a]
This study OH (8-3) 2002–2005 superposed		14 ± 4	159 ± 15	7 ± 2	160 ± 21
G08 OH (6-2) 2002–2005 superposed	1142 ± 11 R	17 ± 1	174 ± 4	3 ± 1	134 ± 11
TIME-GCM (from G08)		6 ± 1	265 ± 6	7 ± 1	177 ± 3

[a]The phase refers to the day of first maximum after 1 January.

be a corresponding enhancement at the time of the vernal equinox. There is a TAO in the first 6 h of the night, although only at the 99% significance level between 2100 and 0000 LT. There is a greater transition in form through the night than that found in the OI emission. In the first 3 h of the night, the AO dominates; thereafter there is a mix of the AO and SAO.

Earlier, we noted the annual variation of the OH volume emission rate provided by *Liu et al.* [2008], who analyzed WINDII results to provide latitudinal averages. We have shown their results for 35°S at 2200 LT in Figure 6, and we note that there is general agreement with the WINDII zonal average underestimating the midyear annual peak in our results. *Liu et al.* [2008] note that a semiannual oscillation is not always observed in the OH emission intensity, and results from different locations are certainly variable.

The TIMED SABER OH emission results of *Gao et al.* [2010] for 2002–2008 indicate that the SAO takes a value of 12% peaking on 6 June (day 156), in very good agreement with our SAO result. There is lesser agreement for the AO, with Gao's amplitude result less than half of ours at 6% and the phase showing a 6 month difference in the time of peak emission at December 21 (day 355). Their results show that the SAO emission rates and intensity peak at the equator, and at ±35°, and that the AO peaks at ±20°.

Our results are consistent with other observations at similar northern latitudes. *Lopez-Gonzalez et al.* [2004] looked at 3 years of O_2 and OH emissions at the Sierra Nevada Observatory in Spain at 37°N. Their OH emission intensity data show high winter values, and low summer, with a superimposed midsummer peak, results similar to ours.

Table 6 summarizes our SAO and AO OH (8-3) intensity superposed year results for 2002 to 2005 along with the OH (6-2) intensity superposed year results for the same period from G08. Inspection of this table indicates that the amplitude of the AO dominates the SAO in both the results of G08 and those of the present study. The agreement between the two Adelaide studies in the case of the AO is excellent, both in terms of relative amplitude and phase. The SAO phases agree to within the experimental uncertainties, but the amplitudes do not. The SAO relative amplitude as measured in this work is about twice that of the G08 study. The SAO results of the present study do agree with the TIME-GCM results presented in G08 to within the experimental uncertainty. The TIME-GCM AO does not agree with either the present study or with G08's result.

Marsh et al. [2006] have compared SABER satellite OH observations with the Research for Ozone in the Stratosphere (ROSE) three-dimensional chemical transport model. Their work shows that much of the variability in OH emission intensity is caused by variations in the production rate of ozone. They show that at the peak height of the OH emission, variations are predominantly caused by changes in atomic oxygen concentration resulting from vertical transport. Above the emission layer peak, emission variations are driven by changes in both temperature and density, again caused by vertical transport. They further note that the differing causes manifest themselves as opposite signs in the correlations between emission and temperature, with the correlation being positive where oxygen transport is the dominant process (in the region of the sharp vertical gradient in nighttime oxygen density in the middle to upper mesosphere) and negative where changes in the density and reaction rates are more important. Confirmation of this was provided by *Xu et al.* [2010], who analyzed TIMED/SABER observations of the 2.0 mm OH Meinel brightness and observed that the emission rate is positively correlated with temperature below 94 km and negatively correlated above.

The *Marsh et al.* [2006] intercomparison of SABER OH observations with the ROSE three-dimensional chemical transport model likewise indicates that the diurnal tide has a large effect on the overall magnitude and temporal variation of the OH emission in low latitudes. They find that this tidal variability is so dominant that

AGU Journal of Geophysical Research: Atmospheres 10.1002/2013JD020906

the seasonal cycle in the nighttime emission depends very strongly on the local time of the analysis. They also find that at higher latitudes the emission has an annual cycle that they conclude is due mainly to transport of oxygen by the seasonally reversing mean circulation. It is interesting in this context to note the March brightening of the OH intensity (Figure 2) late in the night which corresponds to that evident in the OI emission (Figure 1).

5.2.2. QBO and QTO

The variation between a QBO and QTO through time has been noted by *Fukuyama* [1977], who analyzed 9 years of OH intensity data from Haute Provence. DS08 found a variation between the QBO to a QTO through the night and through the period of their observations, albeit in the 558 nm airglow intensity at Kiso. Inspection of Figure 12 suggests a similar variation between the QBO and QTO, with the QBO strongest at the beginning and end of the observing period and the QTO strong throughout but strongest at the middle of the observing period. However, the cone of influence again limits our interpretation of the behavior of the QBO.

The QTO accounts for 8 ± 4% of the long-term variability in the OH nightglow intensity and so makes a similar contribution as the SAO (7 ± 5%). *Gao et al.* [2010] found that the QBO, like the SAO, peaked at the equator and at ±35° with a peak intensity of about 8% at the equator. At 35°S, the intensity was about 6%, a result consistent with the present study. The QBO and QTO take their first maximum after 1 January 1995 at similar times around the following summer (November 1995 and January 1996, respectively). *Gao et al.* [2010] found that the QBO took a maximum value around January 2003. Our result suggests March 2002, so these results are not consistent.

5.2.3. OH Solar Cycle Dependence

As solar radiation directly drives atomic oxygen production and because of its link to the formation of OH, we expect the 730 nm emission intensity to also show a response to solar forcing. Indeed, *Wiens and Weill* [1973] determined a 25% variation in OH (9-3) intensity for Haute Provence. More recently, *Clemesha et al.* [2005] looked at monthly mean OH (6-2) band intensities at Cachoeira Paulista (23°S, 45°W) for the period 1987 to 2000. They found the amplitude of the mean oscillation to be about 14% of the mean intensity and that the maximum intensity occurred about 1.4 years before the maximum of solar cycle 22. *Pertsev and Perminov* [2008] found an amplitude of 19% of the mean in the OH (6-2) intensity for the solar cycle component as measured in the hour immediately after local midnight at Zvenigorod (56°N) in the years 2000 to 2006. In contrast, *Scheer et al.* [2005] found no correlation between the solar radio flux and the OH (6-2) airglow intensity at El Leoncito (32°S, 69°W). They did however, find a moderate positive correlation between the solar radio flux and the O_2 (0-1) intensity at the same location.

As we noted in section 4.2 above, we have chosen to fit the solar periodicity of 4088 days found in the OI intensity to the OH data, even though the OH Lomb periodogram analysis indicates a peak near 3000 days. We do this because we can find no underlying physical basis for fitting 3000 days and for ease of comparison between the results.

In the present study, the solar cycle dependence is one of the weakest long-term variations in the 730 nm nightglow intensity with an amplitude of 6 ± 5% of the mean, which maximizes in late March 2002 (±359 days) agreeing with the OI solar cycle variation phase to within the experimental uncertainty.

5.3. Intensity Variation Through the Night at 558 nm

Figure 5 shows the variation of the total OI intensity through the night. DS08 used a continuous wavelet transform to analyze the long-term Kiso 558 nm intensity data. The relative strengths of the various components they identify show a complex variation through the night over the observational period of their study.

The amplitudes and phases for each of the periodicities identified in the OI emission for each of the four 3 h blocks measured between 1800 and 0600 LT (UT + 09:30 h) are shown in Figures 14a and 14b. The major variation is in the amplitudes, with the phases remaining relatively consistent through the night. There is considerable variation in amplitude through the night for the TAO, SAO, and AO, while the 4.1 year and solar periodicities show amplitudes consistent to within the experimental uncertainties. The SAO and AO strengthen through the night, while the TAO tends to be strongest at the beginning and end of the night.

DS08 provide some general comments on their work. They find that the SAO is strongest at 2000 h JST (UT + 09:00 h), after which it weakens through the night. They note that this variation is similar to the variation

Journal of Geophysical Research: Atmospheres 10.1002/2013JD020906

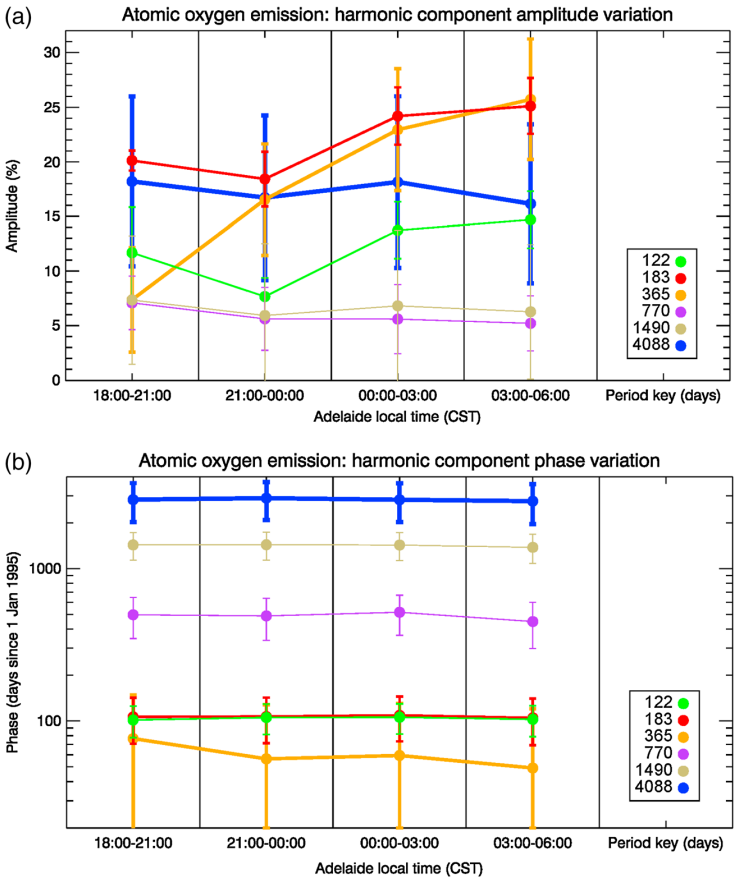

Figure 14. (a, b) The intensity variation through the night and the corresponding phase variations of the various harmonic components of the OI intensity. Note the general increase in brightness through the night. *Smith et al.* [2010] found that the local time variation of atomic oxygen concentration increased through the night at 94 km at 35°S consistent with this result.

seen in WINDII satellite data and in TIME-GCM model results as described by *Shepherd et al.* [2005]. DS08 also find that the AO takes a minimum value near local midnight. They observe the QBO at 2000 and 0200 h JST and find that its amplitude exceeds that of the SAO during some years. Our results are not generally consistent with DS08's results for the variation of amplitude through the night, but given the variability in the amplitudes of the various components through the years of observation evident in both their and our work (Figure 11), this is not particularly surprising.

5.4. Intensity Variations Through the Night at 730 nm

We expect the diurnal variation in OH intensity to be modulated by the tides [*Marsh et al.*, 2006] and so to vary through the year. This requires a more detailed investigation than is possible here, but we can make some observations based on the mean harmonic fits to the 730 nm data.

Figure 15a shows the intensity of each of the harmonic components in each 3 h block through the night, and the corresponding phases are shown in Figure 15b. The AO takes maximum values of more than 18% at the beginning and end of the night and falls to 12% later in the night. The SAO increases in amplitude through the night, peaking in the 0000 to 0300 LT time block at around 10%. The QTO shows a similar behavior to this in amplitude throughout the night. Inspection of the phases corresponding to these periods indicates consistent values to within the experimental uncertainties through the night.

Journal of Geophysical Research: Atmospheres 10.1002/2013JD020906

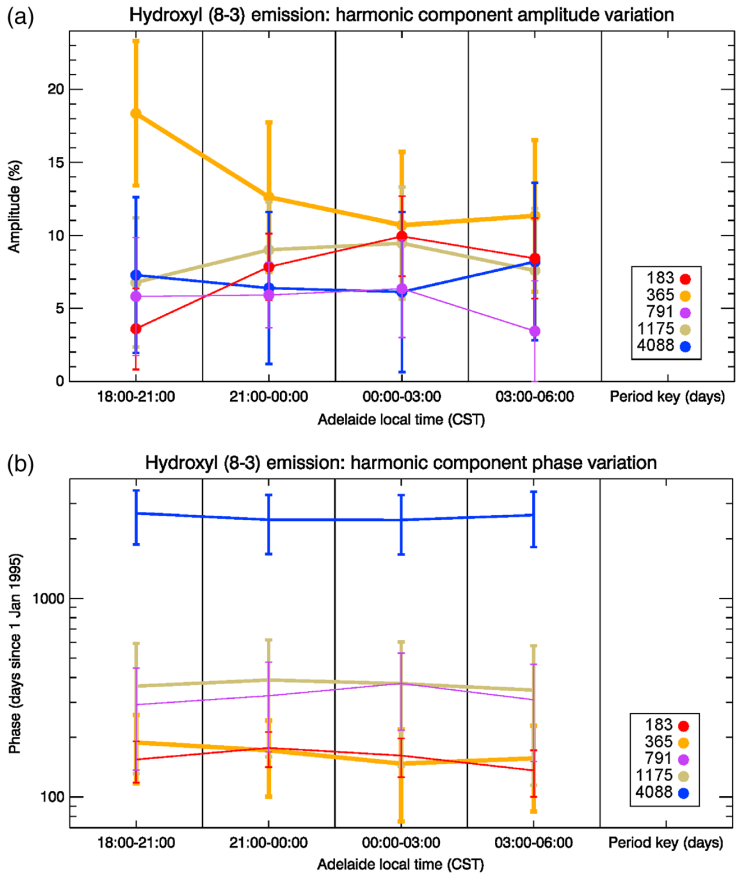

Figure 15. (a, b) as for Figure 14 but for the OH (8-3) intensity.

Moreels et al. [1974, 1977] investigated the variation in OH emission found by *Wiens and Weill* [1973] through the night and considered it in terms of eddy diffusion. Using a Fourier transform spectrometer at Maynooth (53.2°N, 6.4°W), *Mulligan et al.* [1995] found that the brightness of the OH (3-1) and OH (4-2) bands during the period January–December 1993 generally showed a steady decrease from dusk to dawn. *Parihar and Mukherjee* [2008] used a tilting-filter photometer and an all-sky scanning photometer at Kolhapur (16.8°N, 74.2°E), India, during November 2002 to May 2005 to investigate the OH (8-3), (7-2), and (6-2) Meinel bands. They found a steady decrease of emission intensities from evening to dawn hours on approximately 59% of nights. Inspection of Figures 2, 4, and 15 indicates that the variation is more complex but that there is a general tendency at Adelaide for the intensity to be greatest near dawn and dusk midyear (when the observations are available) particularly for the AO and near the autumnal equinoctial dawn. G08 found little agreement between the TIME-GCM model results and their OH intensity observations at Adelaide. Their observations showed equinoctial intensity maxima which maximized in the morning around 0330 LT and in the evening, albeit in a less well-organized fashion, around 2030 LT. The morning maximum is in broad agreement with the results shown in Figures 2 and 15.

6. Summary and Conclusions

The analysis of 15 years of photometer measurements of OH and OI nightglow emission intensities provides results consistent with previous ground-based studies and in very good agreement with simultaneous collocated measurements made with an imager and with global satellite climatologies of OI and OH

AGU Journal of Geophysical Research: Atmospheres 10.1002/2013JD020906

intensities made with the WINDII instrument. The intensities vary through the night, leading to a variation in the relative amplitudes of the various harmonic components when analyzed at different local times. This is consistent with a tidal modulation of the intensity through the night and is consistent with WINDII satellite morphologies of the OI and OH global intensities. By dividing the night up into four 3 h intervals and analyzing these as four separate time series over the entire data set, some general observations can be made. These are summarized below.

The mean value of the OI annual oscillation intensity agrees with that of the semiannual oscillation at this location, with amplitudes of 18 (±9) % and 22 (±4) % of the mean intensity, respectively, when averaged over the entire observational period and over the entire night. This is consistent with 35°S being a transition zone between the dominant SAO characteristic of low latitudes and the dominant AO characteristic of midlatitudes.

The annual and semiannual oscillations are observed to peak in late summer and midautumn, respectively. The quasi-biennial oscillation has an amplitude at about 7 (±3) % of the mean intensity and takes a maximum value in autumn. There is a 4.1 year periodicity with an amplitude of 7 (±5) %.

The Adelaide results agree very well with those of the conjugate site of Kiso from the previous 16 years of observation.

There is clear evidence of a solar cycle dependence of the OI intensity, with nightglow intensity tracking the solar cycle with some hysteresis. A harmonic fit to this period yields an amplitude of about 17 (±7) % of the mean intensity with a maximum on 11 November 2002 (±232 days). This is in very good agreement with the results from Kiso for the previous solar cycle.

The OH annual oscillation intensity dominates that of the semiannual oscillation at this location, with amplitudes of 15 (±7) % and 7 (±5) % of the mean intensity, respectively, when averaged over the entire observational period and over the entire night. The annual and semiannual oscillations are observed to peak in winter. The quasi-biennial oscillation has an amplitude at about 5 (±3) % of the mean intensity and takes a maximum value near midsummer. The QTO takes a value of 8 (±4) % and also maximizes midsummer.

There is a solar cycle dependence of the OH intensity with an amplitude of about 6 (±5) % of the mean intensity and a maximum in late March 2002.

Acknowledgments

Funding for this research was provided by the Australian Research Council grants A69943065, DP0450787, DP0878144, and DP1096901 and by the Adelaide University ARC Small Grants Scheme. We gratefully acknowledge G. G. Shepherd and L. J. Gelinas for access to the WINDII and Aerospace Imager data used in the calibration of the 3FP in this work. The IDL wavelet analysis software was provided by C. Torrence and G. Compo, and is available at URL http://atoc.colorado.edu/research/wavelets/.

References

Angelats i Coll, M., and J. M. Forbes (1998), Dynamical influences on atomic oxygen and 5577 Å emission rates in the lower thermosphere, *Geophys. Res. Lett.*, *25*(4), 461–464, doi:10.1029/98GL00130.

Baker, D. J., B. K. Thurgood, W. K. Harrison, M. G. Mlynczak, and J. M. Russell (2007), Equatorial enhancement of the nighttime OH mesospheric infrared airglow, *Phys. Scr.*, *75*, 615–619.

Buriti, R. A., H. Takahashi, and D. Gobbi (2001), Temporal variations of the volume emission rates between OI5577 and O_2 (0,1), *Adv. Space Res.*, *27*, 1159–1164.

Buriti, R. A., H. Takahashi, D. Gobbi, A. F. de Medeiros, A. A. Nepomuceno, and L. M. Lima (2004), Semiannual oscillation of the mesospheric airglow at 7.4°S during the PSMOS observation period of 1998–2001, *J. Atmos. Sol. Terr. Phys.*, *66*, 567–572.

Campbell, L., and M. J. Brunger (2010), Modeling of kinetic, ionospheric and auroral contributions to the 557.7-nm nightglow, *Geophys. Res. Lett.*, *37*, L22104, doi:10.1029/2010GL045444.

Clemesha, B., H. Takahashi, D. Simonich, D. Gobbi, and P. Batista (2005), Experimental evidence for solar cycle and long-term change in the low-latitude MLT region, *J. Atmos. Sol. Terr. Phys.*, *67*, 191–196.

Das, U., and H. S. S. Sinha (2008), Long term variations in oxygen green line emission over Kiso, Japan from ground photometric observations using continuous wavelet transform, *J. Geophys. Res.*, *113*, D19115, doi:10.1029/2007JD009516.

Das, U., C. J. Pan, and H. S. S. Sinha (2011), Effects of solar cycle variations on oxygen green line emission rate over Kiso, Japan, *Earth Planets Space*, *63*, 941–948, doi:10.5047/eps.2011.04.006.

Deutsch, K. A., and G. Hernandez (2003), Long-term behavior of the OI 558 nm emission in the night sky and its aeronomical implications, *J. Geophys. Res.*, *108*(A12), 1430, doi:10.1029/2002JA009611.

Ding, F., H. Yuan, W. Wan, I. M. Reid and J. M. Woithe (2004), Occurrence characteristics of medium scale gravity waves observed in OH and OI nightglow over Adelaide (35°S, 138°E), *J. Geophys. Res.*, *109*, D14104, doi:10.1029/2003JD004096.

Donahue, T. M., B. Guenther, and R. J. Thomas (1973), Distribution of atomic oxygen in the upper atmosphere deduced from Ogo 6 airglow observations, *J. Geophys. Res.*, *78*, 6662–6689, doi:10.1029/JA078i028p06662.

Farge, M. (1992), Wavelet transforms and their applications to turbulence, *Annu. Rev. Fluid Mech.*, *24*, 395–457.

Fisher, R. A. (1929), Tests of significance in harmonic analysis, *Proc. R. Soc. London, Ser. A*, *125*, 54–59.

Fraser-Smith, A. C. (1972), Spectrum of the geomagnetic activity index *Ap*, *J. Geophys. Res.*, *77*, 4209–4220, doi:10.1029/JA077i022p04209.

French, W. J. R., G. B. Burns, K. Finlayson, P. A. Greet, R. P. Lowe, and P. F. B. Williams (2000), Hydroxyl (6,2) airglow emission intensity ratios for rotational temperature determination, *Ann. Geophys.*, *18*, 1293–1303.

Fukuyama, K. (1977), Airglow variations and dynamics in the lower thermosphere and upper mesosphere—II: Seasonal and long-term variations, *J. Atmos. Sol. Terr. Phys.*, *39*, 1–14.

Gao H., J. Y. Xu, and Q. A. Wu (2010), Seasonal and QBO variations in the OH nightglow emission observed by TIMED/SABER, *J. Geophys. Res.*, *115*, A06313, doi:10.1029/2009JA014641.

AGU Journal of Geophysical Research: Atmospheres 10.1002/2013JD020906

Garcia, R. R., and S. Solomon (1985), The effect of breaking gravity waves on the dynamics and chemical composition of the mesosphere and lower thermosphere, *J. Geophys. Res.*, *91*, 3850–3868, doi:10.1029/JD090iD02p03850.
Gelinas, L. J., J. H. Hecht, R. L. Walterscheid, R. G. Roble, and J. M. Woithe (2008), A seasonal study of mesospheric temperatures and emission intensities at Adelaide and Alice Springs, *J. Geophys. Res.*, *113*, A01304, doi:10.1029/2007JA012587.
Hecht, J. H., R. L. Walterscheid, and M. N. Ross (1994), First measurements of the 2D horizontal wave number spectrum from CCD images of the nightglow, *J. Geophys. Res.*, *99*, 11,449–11,460, doi:10.1029/94JA00584.
Hernandez, G. J. (1976), Lower-thermosphere temperatures determined from the line profiles of the OI 17,927-K (5577 Å) emission in the night sky 1: Long-term behavior, *J. Geophys. Res.*, *81*, 5165–5172, doi:10.1029/JA081i028p05165.
Hernandez, G. J. (1999), Time series, periodograms and significance, *J. Geophys. Res.*, *104*, 10,355–10,368, doi:10.1029/1999JA900026.
Hernandez, G. J., and S. M. Silverman (1964), A re-examination of Lord Rayleigh's data on the airglow 5577A [OI] emission, *Planet. Space Sci.*, *12*, 97–112.
Krivova, N. A., and S. K. Solanki (2002), The 1.3-year and 156-day periodicities in sunspot data: Wavelet analysis suggests a common origin, *Astron. Astrophys.*, *394*, 701–706, doi:10.1051/0004-6361:20021063.
Liu, G., and G. G. Shepherd (2008), An investigation of the solar cycle impact on the lower thermosphere O(1S) nightglow emission as observed by WINDII/UARS, *Adv. Space Res.*, *42*, 933–938.
Liu, G., G. G. Shepherd, and R. G. Roble (2008), Seasonal variations of the nighttime O(^{1}S) and OH airglow emission rates at mid-to-high latitudes in the context of the large-scale circulation, *J. Geophys. Res.*, *113*, A06302, doi:10.1029/2007JA012854.
Lopez-Gonzalez, M. J., et al. (2004), Seasonal variations of O2 atmospheric and OH(6-2) airglow and temperature at mid-latitudes from SATI observations, *Ann. Geophys.*, *22*, 819–828.
Marsh, D. R., A. K. Smith, M. G. Mlynczak, and J. M. Russell III (2006), SABER observations of the OH Meinel airglow variability near the mesopause, *J. Geophys. Res.*, *111*, A10S05, doi:10.1029/2005JA011451.
McDade, I. C. (1998), The photochemistry of the MLT oxygen airglow emissions and the expected influences of tidal perturbations, *Adv. Space Res.*, *21*, 787–794.
McDade, I. C., D. P. Murtagh, R. G. H. Greer, P. H. G. Dickinson, G. Witt, J. Stegman, E. J. Llewellyn, L. Thomas, and D. B. Jenkins (1986), ETON 2: Quenching parameters for the proposed precursors of O_2(b 1) and O(^{1}S) in the terrestrial nightglow, *Planet. Space Sci.*, *34*, 789–800.
McDade, I. C., E. J. McLlewellyn, D. P. Murturgh, and R. G. H. Greer (1987), ETON 5: Simultaneous rocket measurements of the OH Meinel Delta-v = 2 sequence and (8-3) band emission profiles in the nightglow, *Planet. Space Sci.*, *35*, 1137–1147.
Mikhalev, A. V., P. Stoeva, I. V. Medvedev, B. Benev, and A. V. Medvedev (2008), Behaviour of the atomic oxygen 557.7 nm atmospheric emission in the solar cycle 23, *Adv. Space Res.*, *41*, 655–659.
Moreels, G., R. L. Gatringer, and A. Vallance Jones (1974), Comments on the paper: Diurnal, annual and solar cycle variations of hydroxyl and sodium nightglow intensities in the Europe-Africa sector, *Planet. Space Sci.*, *22*, 344–346.
Moreels, G., G. Megie, A. Vallance Jones, and R. L. Gattinger (1977), An oxygen-hydrogen atmospheric model and its application to the OH emission problem, *J. Atmos. Sol. Terr. Phys.*, *39*, 551–570.
Mulligan, F. J., D. F. Horgan, J. G. Galligan, and E. M. Griffin (1995), Mesopause temperatures and integrated band brightnesses calculated from airglow OH emissions recorded at Maynooth (53.2°N, 6.4°W) during 1993, *J. Atmos. Sol. Terr. Phys.*, *57*, 1623–1637.
Parihar, N., and G. K. Mukherjee (2008), Measurement of mesopause temperature from hydroxyl nightglow at Kolhapur (16.8°N, 74.2°E), India, *Adv. Space Res.*, *41*, 660–669.
Pertsev, N., and V. Perminov (2008), Response of the mesopause airglow to solar activity inferred from measurements at Zvenigorod, Russia, *Ann. Geophys.*, *26*, 1049–1056.
Press, W. H., and G. B. Rybicki (1989), Fast algorithm for spectral analysis of unevenly sampled data, *Astrophys. J.*, *338*, 277–280.
Press, W. H., B. P. Flannery, S. A. Teukolsky, and W. T. Vetterling (1986), *Numerical Recipes*, Cambridge Univ. Press, London.
Reid, I. M., and J. M. Woithe (2005), Three Field Photometer Observations of short period gravity wave intrinsic parameters in the 80 to 100 km height region, *J. Geophys. Res.*, *110*, D21108, doi:10.1029/2004JD005427.
Reid, I. M., and J. M. Woithe (2007), The variability of the 558 nm OI airglow intensity measured over Adelaide, Australia, *Adv. Space Res.*, *39*, 1237–1247.
Reisin, E. R., and J. Scheer (2002), Searching for trends in mesopause region airglow intensities and temperatures at El Leoncito, *Phys. Chem. Earth*, *27*, 563–569.
Scheer, J., E. R. Reisen, and C. H. Mandrini (2005), Solar activity signatures in mesopause region temperatures and atomic oxygen related airglow brightness at El Leoncito, Argentina, *J. Atmos. Sol. Terr. Phys.*, *67*, 145–154.
Scheer, J., E. R. Reisin, O. A. Gusev, W. J. R. French, G. Hernandez, R. Huppi, P. Ammosov, G. A. Gavrilyeva, and D. Offermann (2006), Use of CRISTA mesopause region temperatures for the intercalibration of ground-based instruments, *J. Atmos. Sol. Terr. Phys.*, *68*, 1698–1708.
Schuster, A. (1898), On the investigation of hidden periodicities with application to a supposed 26 day period of meteorological phenomena, *Terr. Magn.*, *3*, 13–41, doi:10.1029/TM003i001p00013.
Semenov,A. I., and N. N. Shefov (1997), Empirical model of atomic oxygen 557.7 nm emission variations in the night-time. 1. Intensity, *Geomagn. Aeron.*, *37*(2), 81–90.
Shefov, N. N. (1969), Hydroxyl emission of the upper atmosphere-I: The behaviour during a solar cycle, seasons and geomagnetic disturbances, *Planet. Space Sci.*, *17*, 797–813.
Shepherd, G. G., et al. (1993), Longitudinal structure in atomic oxygen concentrations observed with WINDII on UARS, *Geophys. Res. Lett.*, *20*, 1303–1306, doi:10.1029/93GL01105.
Shepherd, G. G., G. Liu, and R. G. Roble (2005), Large-scale circulation of atomic oxygen in the upper mesosphere and lower thermosphere, *Adv. Space Res.*, *35*, 1945–1950.
Shepherd, G. G., Y.-M. Cho, G. Liu, M. G. Shepherd, and R. G. Roble (2006), *J. Atmos. Sol. Terr. Phys.*, *68*, 2000–2011.
Silverman, S. (1970), Night airglow phenomenology, *Space Sci. Rev.*, *11*, 341–379.
Sivjee, G. G., and D. Shen (1997), Auroral optical emissions during the solar magnetic cloud event of October 1995, *J. Geophys. Res.*, *102*, 7431–7437, doi:10.1029/97JA00195.
Smith, A. K., D. R. Marsh, M. G. Mlynczak, and J. C. Mast (2010), Temporal variations of atomic oxygen in the upper mesosphere from SABER, *J. Geophys. Res.*, *115*, D18309, doi:10.1029/2009JD013434.
Takahashi, H., Y. Sahai, and P. P. Batista (1984), Tidal and solar cycle effects on the 015577 Å, NaD and OH(8-3) airglow emissions observed at 23°S, *Planet. Space Sci.*, *32*, 897–902.
Takahashi, H., B. R. Clemesha, P. P. Batista, Y. Sahai, M. A. Abdu, and P. Muralikrishna (1990), Equatorial *F*-region OI 6300 Å and OI 5577 Å emission profiles observed by rocket-borne airglow photometers, *Planet. Space Sci.*, *38*, 547–554, doi:10.1016/0032-0633(90)90148-J.

Journal of Geophysical Research: Atmospheres 10.1002/2013JD020906

Takahashi, H., B. R. Clemesha, and P. P. Batista (1995), Predominant semi-annual oscillation of the upper mesospheric airglow intensities and temperatures in the equatorial region, *J. Atmos. Sol. Terr. Phys.*, *57*(4), 407–414.

Torrence, C., and G. P. Compo (1998), A practical guide to wavelet analysis, *Bull. Am. Meteorol. Soc.*, *79*, 61–78, doi:10.1175/1520-0477(1998)079<0061:APGTWA>2.0.CO;2.

Vincent, R. A., S. Kovalam, D. C. Fritts, and J. R. Isler (1998), Long-term MF radar observations of solar tides in the low-latitude mesosphere: Interannual variability and comparisons with the GSWM, *J. Geophys. Res.*, *103*(D8), 8667–8683, doi:10.1029/98JD00482.

Wiens, R. H., and G. Weill (1973), Diurnal, annual and solar cycle variations of hydroxyl and sodium nightglow intensities in the Europe–Africa sector, *Planet. Space Sci.*, *21*, 1011–1027.

Xu, J., A. K. Smith, G. Jiang, H. Gao, Y. Wei, M. G. Mlynczak, and J. M. Russell III (2010), Strong longitudinal variations in the OH nightglow, *Geophys. Res. Lett.*, *37*, L21801, doi:10.1029/2010GL043972.

Zhang, S. P., and G. G. Shepherd (2005), On the response of the O(1S) dayglow emission rate to the Sun's energy input: An empirical model deduced from WINDII/UARS global measurements, *J. Geophys. Res.*, *110*, A03304, doi:10.1029/2004JA010887.

Appendix C

Wind field gravity wave parameters

Here, the interrelation between the parameters of linear gravity waves in a wind field are listed.

Wave scale

A wave of ground-based angular frequency ω, horizontal phase speed c_p and propagation direction ϕ (here, clockwise from North) has a horizontal wavenumber given by:

$$k_h = \frac{\omega}{c_p}\,,$$

which can be broken up into the component horizontal wavenumbers:

$$k = k_h \sin\phi\,, \text{ and}$$
$$l = k_h \cos\phi\,.$$

If the wave is propagating in a non-zero horizontal wind field of components $\overline{u}$ and $\overline{v}$, its intrinsic frequency (the wave's frequency measured in the frame of reference of the wind field) is:

$$\hat{\omega} = \omega - (k\overline{u} + l\overline{v})$$

Dispersion relation

For a specified Brunt-Väisälä frequency N, a gravity wave will have the vertical wavenumber:

$$m^2 = \frac{k_h(N^2 - \hat{\omega}^2)}{\hat{\omega}^2}$$

Polarization relations

If the wind field has a horizontal perturbation amplitude v_h associated with the wave, the component wind amplitudes are:

$$u' = v_h \sin\phi\,,$$
$$v' = v_h \cos\phi\,, \text{ and}$$
$$w' = \frac{v_h k_h}{m}\,.$$

Appendix D

Supplementary meteor radar RST climatologies

This Appendix shows climatologies of Reynolds stress tensor terms determined by the Buckland Park (55 MHz) and Darwin (33 MHz) meteor radars. Like those shown for Davis in Fig. 4.9, they were evaluated using the methodology discussed in Sect. 6.2. No attempt is made here to explain the features geophysically.

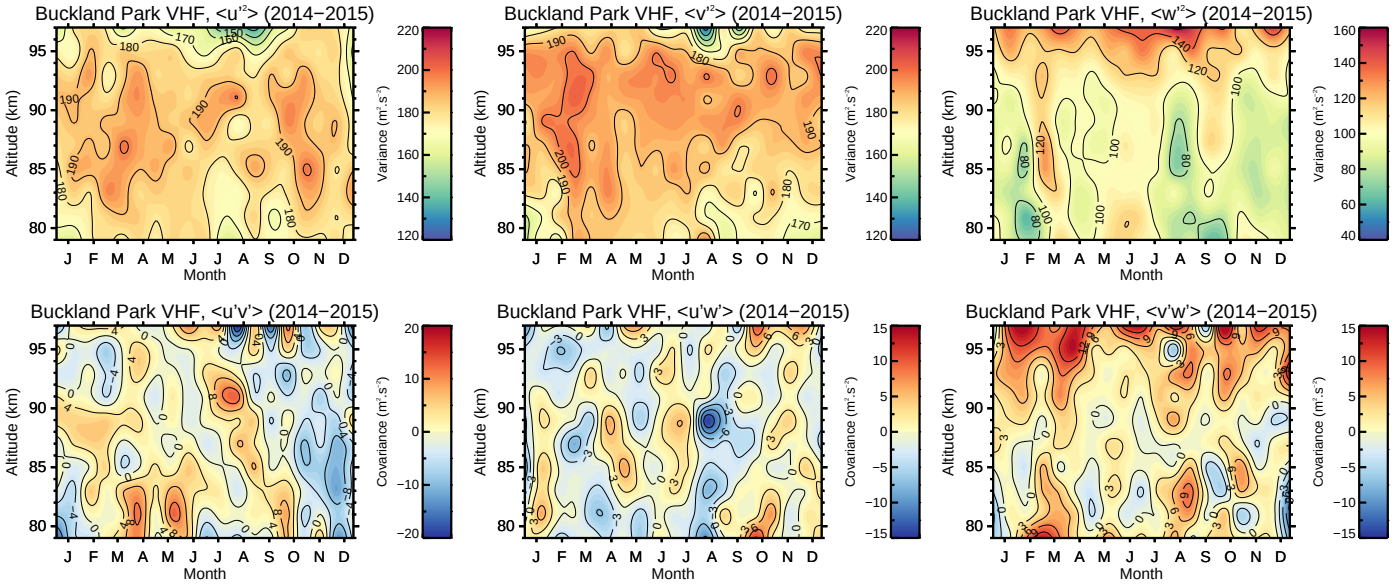

Fig. D.1: A climatology of Reynolds stress tensor components from the 55 MHz meteor radar at Buckland Park.

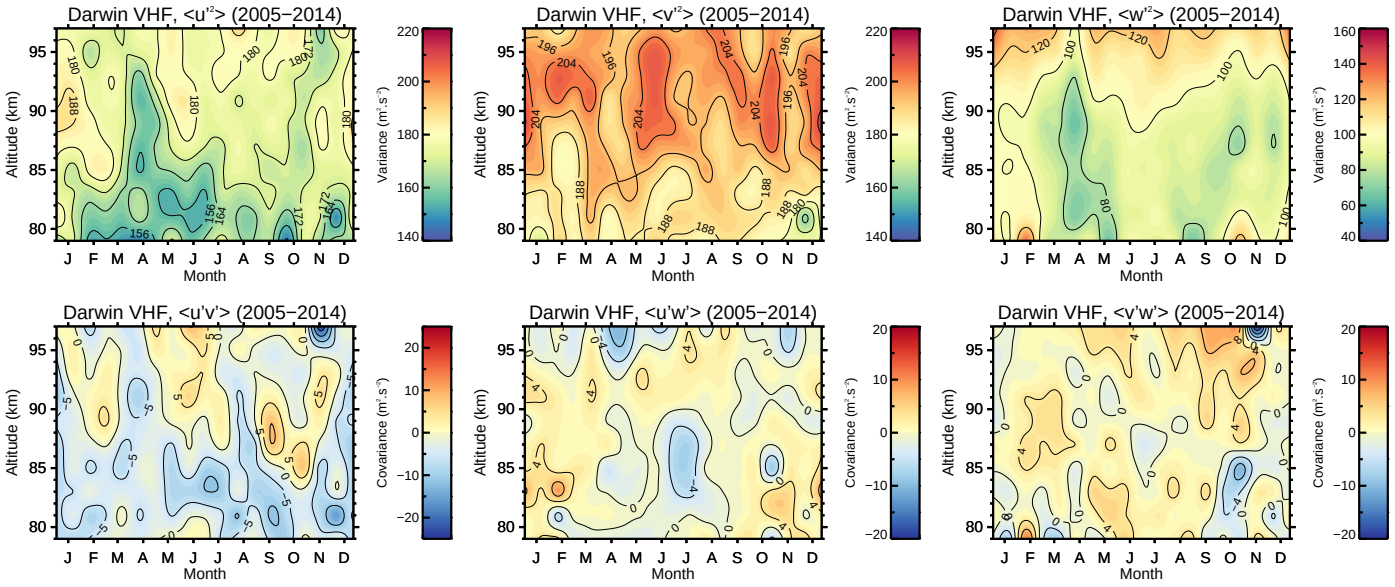

Fig. D.2: As per Fig. D.1, but for the 33 MHz meteor radar at Darwin.

Appendix E

Seasonally-averaged BP/Davis MF/meteor radar wind and variance data sets

This Appendix shows plots of the complete seasonally-averaged data sets used for the trend estimations reported in Chapter 4.

The plots shown are vectorized, and so can be enlarged to a readable size in the electronic version of this thesis.

Overplots of the F10.7 cm flux have been included at the top of each panel. Overplots of the fitted linear long-term trend function are also included as a blue dashed line.

On the right side of each plot are four figures: a, b, R_a and R_b. a represents the temporal coefficient of the regression (units/year), b the solar cycle coefficient (units/1×10^{-22} W.m^{-2}.s^{-1}), and R_a and R_b the correlation coefficients for the two regressed variables.

Standard deviations in each seasonal average are overplotted as error bars.

Results from each season are shown separately in each row (from left to right: Dec-Jan-Feb, Mar-Apr-May, Jun-Jul-Aug, Sep-Oct-Nov).

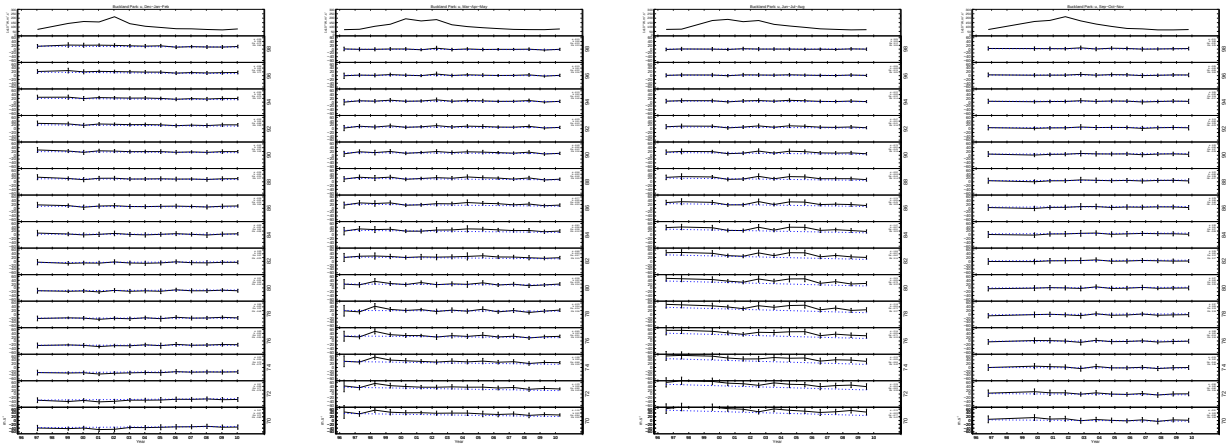

Buckland Park, zonal winds.

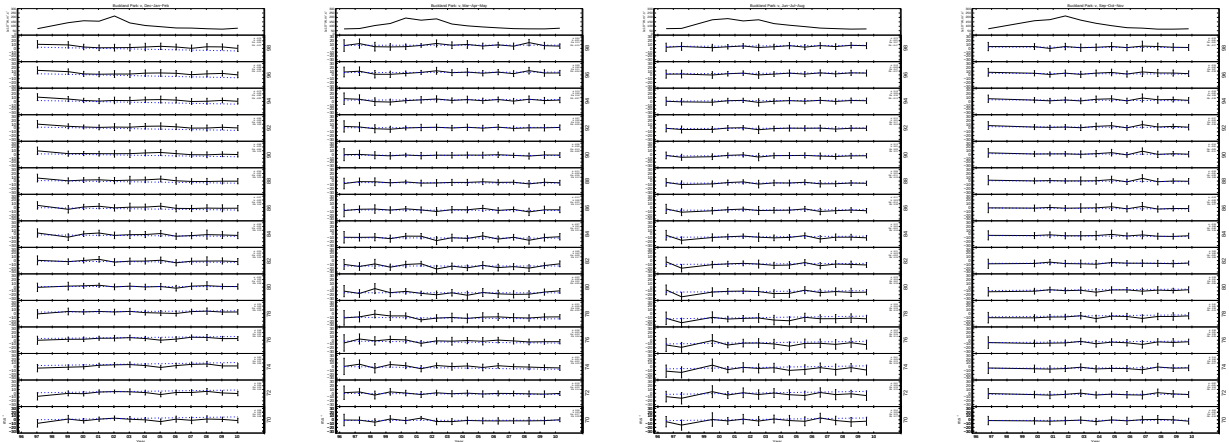

Buckland Park, meridional winds.

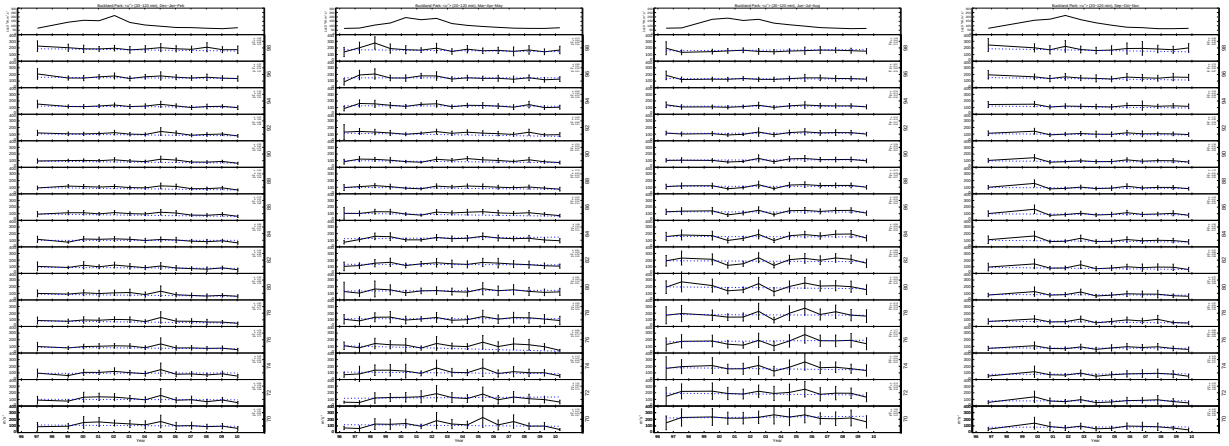

Buckland Park, 20-120 minute zonal variances.

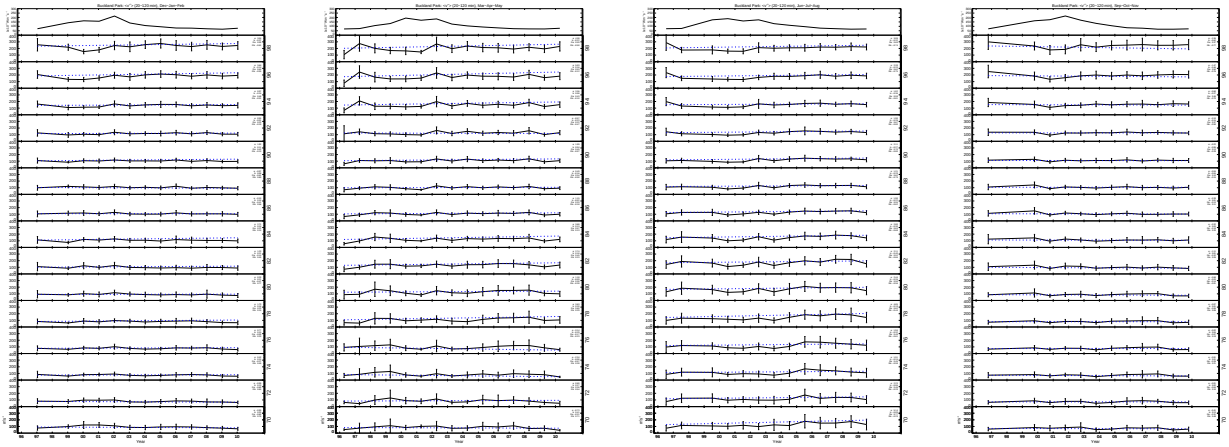

Buckland Park, 20-120 minute meridional variances.

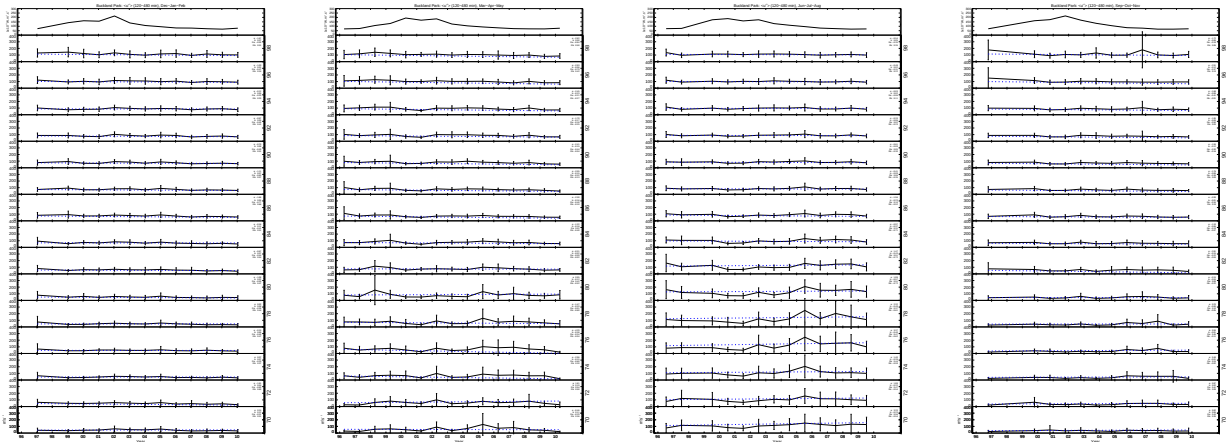

Buckland Park, 120-480 minute zonal variances.

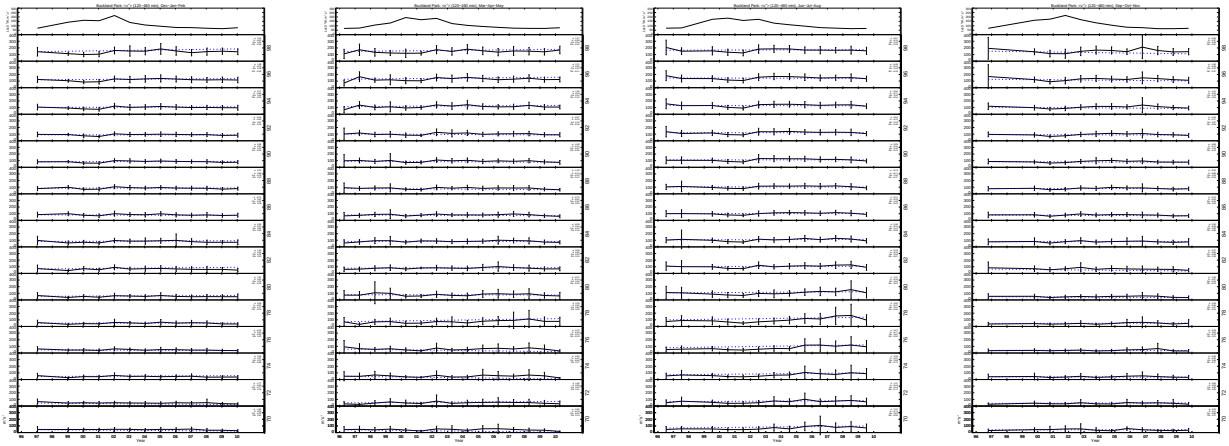

Buckland Park, 120-480 minute zonal variances.

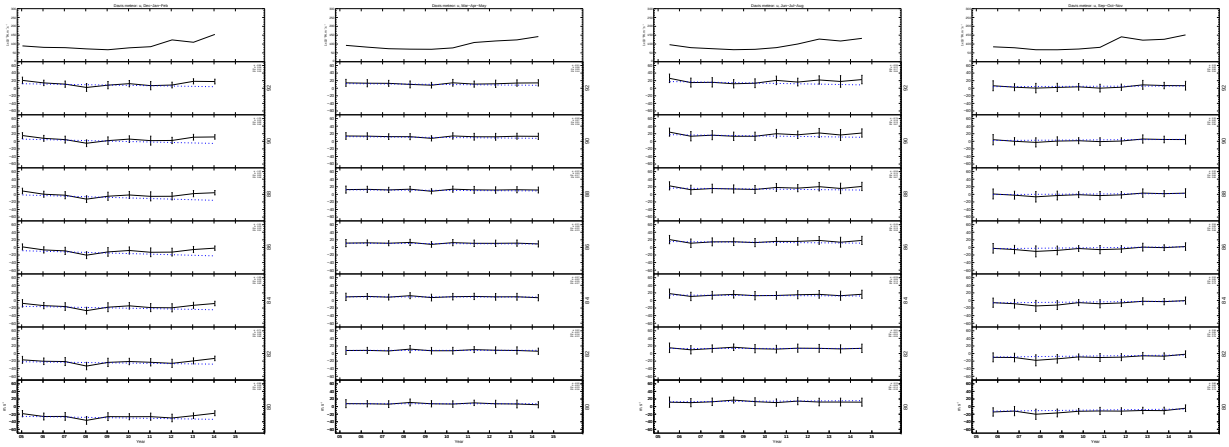

Davis, zonal winds.

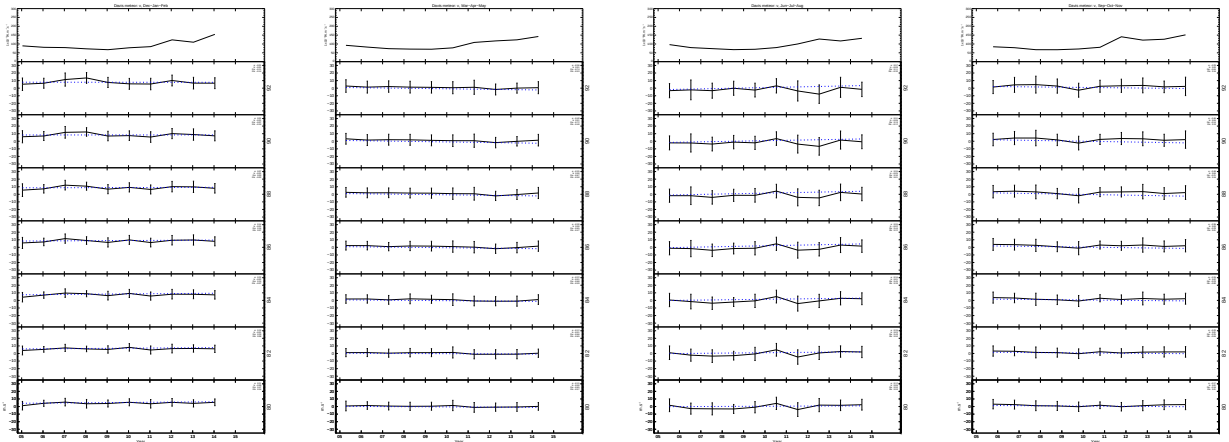

Davis, meridional winds.

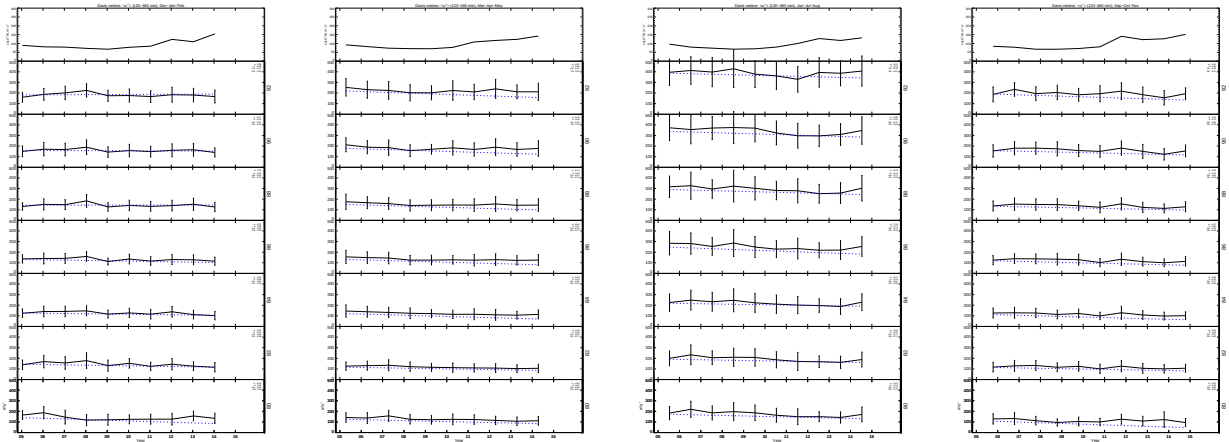

Davis, 120-480 minute zonal variances.

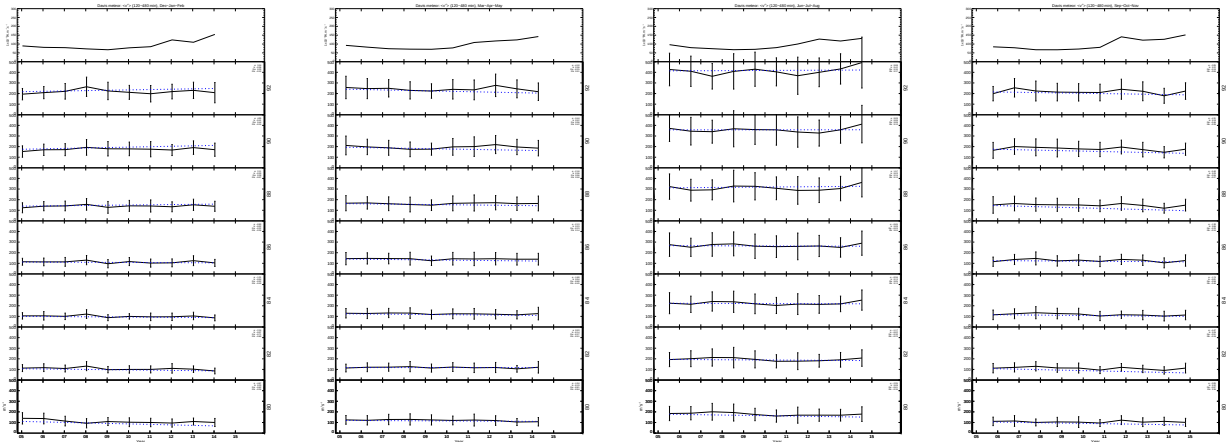

Davis, 120-480 minute meridional variances.

References

Adams, G. W., D. P. Edwards, and J. W. Brosnahan (1985). The imaging Doppler interferometer: Data analysis. *Radio Sci.* 20.6, pp. 1481–1492.

Alexander, M. J., M. Geller, C. McLandress, S. Polavarapu, P. Preusse, F. Sassi, K. Sato, S. Eckermann, M. Ern, A. Hertzog, et al. (2010). Recent developments in gravity-wave effects in climate models and the global distribution of gravity-wave momentum flux from observations and models. *Quarterly Journal of the Royal Meteorological Society* 136.650, pp. 1103–1124.

AMS Glossary (2012). *Glossary of Meteorology, American Meteorological Society*. URL: `http://glossary.ametsoc.org/wiki/Reynolds_stresses`.

Anandan, V. K., S. Kumar, V. N. Sureshbabu, T. N. Rao, M. P. Rao, and T. Tsuda (2014). Improved performance over time of integration in momentum flux estimation using Postset Beam Steering technique. *J. Atmos. Sol. Terr. Phys.* 120, pp. 132–142.

Andrews, D. G., J. R. Holton, and C. B. Leovy (1987). *Middle atmosphere dynamics*. 40. Academic press.

Andrioli, V. F., P. P. Batista, B. R. Clemesha, N. J. Schuch, and R. A. Buriti (2015). Multi-year observations of gravity wave momentum fluxes at low and middle latitudes inferred by all-sky meteor radar. 33.9, pp. 1183–1193.

Andrioli, V. F., D. C. Fritts, P. P. Batista, and B. R. Clemesha (2013a). Improved analysis of all-sky meteor radar measurements of gravity wave variances and momentum fluxes. *Ann. Geophys.* 31.5, pp. 889–908.

Andrioli, V. F., D. C. Fritts, P. P. Batista, B. R. Clemesha, and D. Janches (2013b). Diurnal variation in gravity wave activity at low and middle latitudes. *Ann. Geophys.*

Antonita, T. M., G. Ramkumar, K. K. Kumar, and V. Deepa (2008). Meteor wind radar observations of gravity wave momentum fluxes and their forcing toward the Mesospheric Semiannual Oscillation. *J. Geophys. Res.* 113.D10.

Aster, R. C., B. Borchers, and C. Thurber (2005). *Parameter Estimation and Inverse Problems. 2005*. Elsevier Academic Press: Burlington.

ATRAD Pty. Ltd. (2006). *APAC Acquisition Software, Version 5.1 (general description)*.

Becker, E. (2009). Sensitivity of the upper mesosphere to the Lorenz energy cycle of the troposphere. *J. Atmos. Sci.* 66.3, pp. 647–666.

Beldon, C. L. and N. J. Mitchell (2009). Gravity waves in the mesopause region observed by meteor radar, 2: Climatologies of gravity waves in the Antarctic and Arctic. *J. Atmos. Sol. Terr. Phys.* 71.8, pp. 875–884.

Beldon, C. L. and N. J. Mitchell (2010). Gravity wave–tidal interactions in the mesosphere and lower thermosphere over Rothera, Antarctica (68°S, 68°W). *J. Geophys. Res.* 115.D18.

Booker, J. R. and F. P. Bretherton (1967). The critical layer for internal gravity waves in a shear flow. *Journal of Fluid Mechanics* 27.03, pp. 513–539.

Bossert, K., D. C. Fritts, P.-D. Pautet, B. P. Williams, M. J. Taylor, B. Kaifler, A. Dörnbrack, I. M. Reid, D. J. Murphy, A. J. Spargo, and A. D. MacKinnon (2015). Momentum flux estimates accompanying multiscale gravity waves over Mount Cook, New Zealand, on 13 July 2014 during the DEEPWAVE campaign. *J. Geophys. Res.* 120, pp. 9323–9337.

Bretherton, F. P. (1966). The propagation of groups of internal gravity waves in a shear flow. *Quarterly Journal of the Royal Meteorological Society* 92.394, pp. 466–480.

Briggs, B. H. (1985). The analysis of spaced sensor records by correlation techniques. *Middle Atmosphere Program. Handbook for MAP. Volume 18: Extended abstracts, Presented at MAP Symposium, Kyoto, Japan, 26-30 Nov. 1984. Edited by S. Kato.* Vol. 18, p. 166.

Briggs, B. H. (1993). Observations of atmospheric dynamics using radar techniques. *Australian Journal of Physics* 46.1, pp. 127–148.

Briggs, B. H., W. G. Elford, D. G. Felgate, M. G. Golley, D. E. Rossiter, and J. W. Smith (1969). Buckland Park aerial array. *Nature* 223, pp. 1321–1325.

Briggs, B. H. and N. Holmes (1973). Ionospheric Observations using an Ultrasonic Image Forming Technique. *Nature* 243.129, pp. 111–112.

Briggs, B. H., G. J. Phillips, and D. H. Shinn (1950). The analysis of observations on spaced receivers of the fading of radio signals. *Proceedings of the Physical Society* 63.2, p. 106.

Brown, N. (1976). Radio echoes from meteor trains at a radio frequency of 1.98 MHz. *J. Atmos. Terr. Phys.* 38.1, pp. 83–87.

Browning, K. A. and R. Wexler (1968). The determination of kinematic properties of a wind field using Doppler radar. *J. Appl. Meteor.* 7.1, pp. 105–113.

Cebik, L. B. (date unknown). *Antenna Modeling: 37. Verticals: Using the MININEC Ground.* URL: `http://www.antennex.com/w4rnl/col0301/amod37.htm`.

Ceplecha, Z., J. Borovička, W. G. Elford, D. O. ReVelle, R. L. Hawkes, V. Porubčan, and M. Šimek (1998). Meteor phenomena and bodies. *Space Science Reviews* 84.3-4, pp. 327–471.

Clemesha, B. R., P. P. Batista, R. A. B. da Costa, and N. Schuch (2009). Seasonal variations in gravity wave activity at three locations in Brazil. *Ann. Geophys.* 27, pp. 1059–1065.

Clemesha, B. R. and P. P. Batista (2008). Gravity waves and wind-shear in the MLT at 23°S. *Adv. Space Res.* 41.9, pp. 1472–1477.

Crary, A. P. (1950). Stratosphere winds and temperatures from acoustical propagation studies. *Journal of Meteorology* 7.3, pp. 233–242.

Czechowsky, P., I. M. Reid, and R. Rüster (1988). VHF radar measurements of the aspect sensitivity of the summer polar mesopause echoes over Andenes (69°N, 16°E), Norway. *Geophys. Res. Lett.* 15.11, pp. 1259–1262.

Doviak, R. J. and D. S. Zrnič (1993). *Doppler Radar and Weather Observations*. Academic Press, Inc.

Dowdy, A. J., R. A. Vincent, M. Tsutsumi, K. Igarashi, Y. Murayama, W. Singer, and D. J. Murphy (2007). Polar mesosphere and lower thermosphere dynamics: 1. Mean wind and gravity wave climatologies. *J. Geophys. Res.* 112.D17.

Dunkerton, T. J. (1982). Stochastic parameterization of gravity wave stresses. *J. Atmos. Sci.* 39.8, pp. 1711–1725.

Dutta, G., P. V. Rao, M. C. Kumar, P. V. Kumar, H. A. Basha, V. K. Anandan, and A. K. Ghosh (2005). On the optimum time of integration for estimation of momentum flux from VHF radar data. *Geophys. Res. Lett.* 32.L15811.

Felgate, D. G. and M. G. Golley (1971). Ionospheric irregularities and movements observed with a large aerial array. *J. Atmos. Terr. Phys.* 33.9, pp. 1353–1369.

Frame, D. J., B. N. Lawrence, G. J. Fraser, R. A. Vincent, and A. Dudhia (2000). A new technique for evaluating mesospheric momentum balance utilizing radars and satellite data. *Ann. Geophys.* Vol. 18. 4. Springer, pp. 478–484.

Fritts, D. C., D. Janches, and W. K. Hocking (2010a). Southern Argentina Agile Meteor Radar: Initial assessment of gravity wave momentum fluxes. *J. Geophys. Res.* 115.D19123.

Fritts, D. C., D. Janches, W. K. Hocking, N. J. Mitchell, and M. J. Taylor (2012a). Assessment of gravity wave momentum flux measurement capabilities by meteor radars having different transmitter power and antenna configurations. *J. Geophys. Res.* 117.D10108.

Fritts, D. C., D. Janches, H. Iimura, W. K. Hocking, J. V. Bageston, and N. M. P. Leme (2012b). Drake Antarctic Agile Meteor Radar first results: Configuration and comparison of mean and tidal wind and gravity wave momentum flux measurements with Southern Argentina Agile Meteor Radar. *J. Geophys. Res.* 117.D02105.

Fritts, D. C., D. Janches, H. Iimura, W. K. Hocking, N. J. Mitchell, R. G. Stockwell, B. Fuller, B. G. W. Vandepeer, J. Hormaechea, C. Brunini, et al. (2010b). Southern Argentina Agile Meteor Radar: System design and initial measurements of large-scale winds and tides. *J. Geophys. Res.* 115.D18112.

Fritts, D. C. (1984). Gravity wave saturation in the middle atmosphere: A review of theory and observations. *Rev. Geophys.* 22.3, pp. 275–308.

Fritts, D. C. and R. A. Vincent (1987). Mesospheric momentum flux studies at Adelaide, Australia: Observations and a gravity wave-tidal interaction model. *J. Atmos. Sci.* 44.3, pp. 605–619.

Fritts, D. C., L. Yuan, M. H. Hitchman, L. Coy, E. Kudeki, and R. F. Woodman (1992). Dynamics of the equatorial mesosphere observed using the Jicamarca MST radar during June and August 1987. *J. Atmos. Sci.* 49.24, pp. 2353–2371.

Fritts, D. C., P. Pautet, K. Bossert, M. J. Taylor, B. P. Williams, H. Iimura, T. Yuan, N. J. Mitchell, G. Stober, et al. (2014). Quantifying gravity wave momentum fluxes with Mesosphere Temperature Mappers and correlative instrumentation. *J. Geophys. Res.* 119, pp. 13583–13603.

Fritts, D. C., R. B. Smith, M. Taylor, J. D. Doyle, S. D. Eckermann, A. Dörnbrack, M. Rapp, B. P. Williams, D. Pautet, K. Bossert, et al. (2015). The Deep Propagating Gravity Wave Experiment (DEEPWAVE): An Airborne and Ground-Based Exploration of Gravity Wave Propagation and Effects from their Sources throughout the Lower and Middle Atmosphere. *Bull. Amer. Meteor. Soc.* 119, pp. 13583–13603.

Gage, K. S. and B. B. Balsley (1980). On the scattering and reflection mechanisms contributing to clear air radar echoes from the troposphere, stratosphere, and mesophere. *Radio Sci.* 15.2, pp. 243–257.

Gavrilov, N. M., S. Fukao, and T. Nakamura (1999). Peculiarities of interannual changes in the mean wind and gravity wave characteristics in the mesosphere over Shigaraki, Japan. *Geophys. Res. Lett.* 26.16, pp. 2457–2460.

Gavrilov, N. M., A. H. Manson, and C. E. Meek (1995). Climatological monthly characteristics of middle atmosphere gravity waves (10 min-10 h) during 1979-1993 at Saskatoon. *Ann. Geophys.* Vol. 13. 3, pp. 285–295.

Gavrilov, N. M., D. M. Riggin, and D. C. Fritts (2004). Interannual variations of the mean wind and gravity wave variances in the middle atmosphere over Hawaii. *J. Atmos. Sol. Terr. Phys.* 66.6, pp. 637–645.

Golley, M. G. and D. E. Rossiter (1970). Some tests of methods of analysis of ionospheric drift records using an array of 89 aerials. *J. Atmos. Terr. Phys.* 32.7, pp. 1215–1233.

Grant, S. I. (2003). Medium frequency radar studies of meteors. PhD thesis. University of Adelaide, Department of Physics.

Hall, G. E., C. E. Meek, and A. H. Manson (1992). MF radar interferometry measurements of fluxes and Coriolis accelerations over Saskatoon (52°N, 107°W). *Geophys. Res. Lett.* 19.23, pp. 2293–2296.

Haurwitz, B. (1961). Frictional effects and the meridional circulation in the mesosphere. *J. Geophys. Res.* 66.8, pp. 2381–2391.

Hines, C. O. (1960). Internal atmospheric gravity waves at ionospheric heights. *Can. J. Phys.* 38.11, pp. 1441–1481.

Hines, C. O., G. W. Adams, J. Brosnahan, F. T. Djuth, M. P. Sulzer, C. A. Tepley, and J. S. Van Baelen (1993). Multi-instrument observations of mesospheric motions over Arecibo: comparisons and interpretations. *J. Atmos. Terr. Phys.* 55.3, pp. 241–287.

Hines, C. O. and R. R. Rao (1968). Validity of three-station methods of determining ionospheric motions. *Journal of Atmospheric and Terrestrial Physics* 30.5, pp. 979–993.

Hocking, W. K. (1979). Angular and temporal characteristics of partial reflections from the D-region of the ionosphere. *J. Geophys. Res.* 84.A3, pp. 845–851.

Hocking, W. K. (1981). Investigations of the movement and structure of D-region ionospheric irregularities. PhD thesis. University of Adelaide (Physics Department).

Hocking, W. K. (1983). Mesospheric turbulence intensities measured with a HF radar at 35°S—II. *J. Atmos. Terr. Phys.* 45.2, pp. 103–114.

Hocking, W. K. (1987). Radar studies of small scale structure in the upper middle atmosphere and lower ionosphere. *Adv. Space Res.* 7.10, pp. 327–338.

Hocking, W. K. (1989). Seasonal variation of turbulence intensities in the upper mesosphere and lower thermosphere measured by radar techniques. *Middle Atmosphere Program. Handbook for MAP, volume 27*. Vol. 27, pp. 439–442.

Hocking, W. K. (2005). A new approach to momentum flux determinations using SKiYMET meteor radars. *Ann. Geophys.* Vol. 23. 7, pp. 2433–2439.

Hocking, W. K. (2011). A review of Mesosphere–Stratosphere–Troposphere (MST) radar developments and studies, circa 1997–2008. *J. Atmos. Sol. Terr. Phys.* 73.9, pp. 848–882.

Hocking, W. K., R. Rüster, and P. Czechowsky (1986). Absolute reflectivities and aspect sensitivities of VHF radio wave scatterers measured with the SOUSY radar. *J. Atmos. Sol. Terr. Phys.* 48.2, pp. 131–144.

Hocking, W. K. and R. A. Vincent (1982). Comparative observations of D region HF partial reflections at 2 and 6 MHz. *J. Geophys. Res.* 87.A9, pp. 7615–7624.

Hoffmann, P., M. Rapp, W. Singer, and D. Keuer (2011). Trends of mesospheric gravity waves at northern middle latitudes during summer. *J. Geophys. Res.* 116.D00P08.

Hoffmann, P., M. Rapp, W. Singer, G. Kishore Kumar, E. Becker, R. Latteck, and M. Ern (2012). Trends and solar cycle variations of mesospheric winds and waves at northern middle and polar latitudes. *Trend Workshop*.

Hoffmann, P., E. Becker, W. Singer, and M. Placke (2010). Seasonal variation of mesospheric waves at northern middle and high latitudes. *J. Atmos. Sol. Terr. Phys.* 72.14, pp. 1068–1079.

Holdsworth, D. A. (1995). Signal analysis with applications to atmospheric radars. PhD thesis. University of Adelaide, Department of Physics and Mathematical Physics.

Holdsworth, D. A. and I. M. Reid (1998). Comparison of Spaced Antenna and Doppler Interferometer techniques using the Mt Gambier ST profiler. Proceedings of the Fourth International Symposium on Tropospheric Profiling: Needs and Technologies, Snowmass, Colorado, September 20-25.

Holdsworth, D. A. and I. M. Reid (2004a). Comparisons of full correlation analysis (FCA) and imaging Doppler interferometry (IDI) winds using the Buckland Park MF radar. *Ann. Geophys.* Vol. 22. 11, pp. 3829–3842.

Holdsworth, D. A. and I. M. Reid (2004b). The Buckland Park MF radar: routine observation scheme and velocity comparisons. *Ann. Geophys.* 22.11, pp. 3815–3828.

Holdsworth, D. A., R. Vuthaluru, I. M. Reid, and R. A. Vincent (2002). Differential absorption measurements of mesospheric and lower thermospheric electron densities using the Buckland Park MF radar. *J. Atmos. Sol. Terr. Phys.* 64.18, pp. 2029–2042.

Holdsworth, D. A. and I. M. Reid (1995). Spaced antenna analysis of atmospheric radar backscatter model data. *Radio science* 30.5, pp. 1417–1433.

Holdsworth, D. A. and I. M. Reid (1997). An investigation of biases in the full correlation analysis technique. *Adv. Space Res.* 20.6, pp. 1269–1272.

Holdsworth, D. A., I. M. Reid, and M. A. Cervera (2004a). Buckland Park all-sky interferometric meteor radar. *Radio Sci.* 39.RS5009.

Holdsworth, D. A., M. Tsutsumi, I. M. Reid, T. Nakamura, and T. Tsuda (2004b). Interferometric meteor radar phase calibration using meteor echoes. *Radio Sci.* 39.RS5012.

Holt, J. M. and S. R. Zhang (2008). Long-term temperature trends in the ionosphere above Millstone Hill. *Geophys. Res. Lett.* 35.L05813.

Iimura, H., D. C. Fritts, M. Tsutsumi, T. Nakamura, P. Hoffmann, and W. Singer (2011). Long-term observations of the wind field in the Antarctic and Arctic mesosphere and lower-thermosphere at conjugate latitudes. *J. Geophys. Res.* 116.D20112.

Jacobi, C. (1998). On the solar cycle dependence of winds and planetary waves as seen from mid-latitude D1 LF mesopause region wind measurements. *Ann. Geophys.* Vol. 16. 12. Springer, pp. 1534–1543.

Jacobi, C., N. M. Gavrilov, D. Kürschner, and K. Fröhlich (2006). Gravity wave climatology and trends in the mesosphere/lower thermosphere region deduced from low-frequency drift measurements 1984–2003 (52.1°N, 13.2°E). *J. Atmos. Sol. Terr. Phys.* 68.17, pp. 1913–1923.

Janches, D., C. J. Heinselman, J. L. Chau, A. Chandran, and R. Woodman (2006). Modeling the global micrometeor input function in the upper atmosphere observed by high power and large aperture radars. *J. Geophys. Res.* 111.A07317.

Jones, J., A. R. Webster, and W. K. Hocking (1998). An improved interferometer design for use with meteor radars. *Radio Sci.* 33.1, pp. 55–65.

Kellogg, W. W. and G. F. Schilling (1951). A proposed model of the circulation in the upper stratosphere. *J. Meteor.* 8.4, pp. 222–230.

Keuer, D., P. Hoffmann, W. Singer, and J. Bremer (2007). Long-term variations of the mesospheric wind field at mid-latitudes. *Ann. Geophys.* 25.8, pp. 1779–1790.

Klövekorn, P. (1992). *Radar Array Interferometry and Vertical Velocities in the Upper Atmosphere.* Honours thesis, University of Adelaide, Department of Physics and Mathematical Physics.

Kudeki, E. and S. J. Franke (1998). Statistics of momentum flux estimation. *J. Atmos. Sol. Terr. Phys.* 60.16, pp. 1549–1553.

Kudeki, E., P. K. Rastogi, and F. Sürücü (1993). Systematic errors in radar wind estimation: implications for comparative measurements. *Radio Sci.* 28.2, pp. 169–179.

Kudeki, E. and R. F. Woodman (1990). A poststatistics steering technique for MST radar applications. *Radio Sci.* 25.4, pp. 591–594.

Laštovička, J. (2015). Comment on "Long-term trends in thermospheric neutral temperatures and density above Millstone Hill" by WL Oliver et al. *J. Geophys. Res.* 120.3, pp. 2347–2349.

Laštovička, J., R. A. Akmaev, G. Beig, J. Bremer, and J. T. Emmert (2006). Global change in the upper atmosphere. *Science* 314.5803, pp. 1253–1254.

Laštovička, J., R. A. Akmaev, G. Beig, J. Bremer, J. T. Emmert, C. Jacobi, M. J. Jarvis, G. Nedoluha, Y. I. Portnyagin, and T. Ulich (2008). Emerging pattern of global change in the upper atmosphere and ionosphere. *Ann. Geophys.* Vol. 26. Copernicus Group, pp. 1255–1268.

Laštovička, J., G. Beig, and D. R. Marsh (2014). Response of the mesosphere-thermosphere-ionosphere system to global change-CAWSES-II contribution. *Progress in Earth and Planetary Science* 1.1, pp. 1–19.

Laštovička, J., S. C. Solomon, and L. Qian (2012). Trends in the neutral and ionized upper atmosphere. *Space Sci. Rev.* 168.1-4, pp. 113–145.

Leovy, C. B. (1964). Simple models of thermally driven mesopheric circulation. *J. Atmos. Sci.* 21.4, pp. 327–341.

Lesicar, D. and W. K. Hocking (1992). Studies of seasonal behaviour of the shape of mesospheric scatterers using a 1.98 MHz radar. *J. Atmos. Terr. Phys.* 54.3, pp. 295–309.

Lesicar, D., W. K. Hocking, and R. A. Vincent (1994). Comparative studies of scatterers observed by MF radars in tbe southern hemisphere mesosphere. *J. Atmos. Terr. Phys.* 56.5, pp. 581–591.

Lewallen, R. W. (1985). Baluns: What they do and how they do it. *APRL Antenna Compendium* 1, pp. 157–164.

Li, T., T. Leblanc, I. S. McDermid, D. L. Wu, X. Dou, and S. Wang (2010). Seasonal and interannual variability of gravity wave activity revealed by long-term lidar observations over Mauna Loa Observatory, Hawaii. *J. Geophys. Res.* 115.D13103.

Lindzen, R. S. (1981). Turbulence and stress owing to gravity wave and tidal breakdown. *J. Geophys. Res.* 86.C10, pp. 9707–9714.

Liu, A. Z., X. Lu, and S. J. Franke (2013). Diurnal variation of gravity wave momentum flux and its forcing on the diurnal tide. *J. Geophys. Res.* 118.4, pp. 1668–1678.

McIntosh, D. L. (2009). Comparisons of VHF meteor radar observations in the middle atmosphere with multiple independent remote sensing techniques. PhD thesis. University of Adelaide.

Merzlyakov, E. G., D. J. Murphy, R. A. Vincent, and Y. I. Portnyagin (2009). Long-term tendencies in the MLT prevailing winds and tides over Antarctica as observed by radars at Molodezhnaya, Mawson and Davis. *J. Atmos. Sol. Terr. Phys.* 71.1, pp. 21–32.

Merzlyakov, E. G., Y. I. Portnyagin, C. Jacobi, I. Fedulina, N. J. Mitchell, B. L. Kashcheyev, A. N. Oleynikov, and A. H. Manson (2005). On the day-to-day wind and semidiurnal tide variations at heights of the mid-latitude summer mesopause: Zonal wavenumber estimations and its consequences, case-study in 1998. *J. Atmos. Sol. Terr. Phys.* 67.6, pp. 535–551.

Murphy, D. J. and R. A. Vincent (1993). Estimates of momentum flux in the mesosphere and lower thermosphere over Adelaide, Australia, from March 1985 to February 1986. *J. Geophys. Res.* 98.D10, pp. 18617–18638.

Murphy, D. J. and R. A. Vincent (1998). Mesospheric momentum fluxes over Adelaide during the 2-day wave: Results and interpretation. *J. Geophys. Res.* 103.D22, pp. 28627–28636.

Murphy, D. J. (1992). Measurements of Energy and Momentum in the Mesosphere. PhD thesis. University of Adelaide, Department of Physics and Mathematical Physics.

Nakamura, T., T. Tsuda, M. Yamamoto, S. Fukao, and S. Kato (1993). Characteristics of gravity waves in the mesosphere observed with the middle and upper atmosphere radar, 1, Momentum flux. *J. Geophys. Res.* 98, pp. 8899–8899.

Nicolls, M. J., D. C. Fritts, D. Janches, and C. J. Heinselman (2012). Momentum flux determination using the multi-beam Poker Flat Incoherent Scatter Radar. *Ann. Geophys.* 30, pp. 945–962.

Offermann, D., J. Wintel, C. Kalicinsky, P. Knieling, R. Koppmann, and W. Steinbrecht (2011). Long-term development of short-period gravity waves in middle Europe. *J. Geophys. Res.* 116.D00P07.

Offermann, D. and R. Koppmann (2013). "Short Period Dynamics in the Mesosphere: Morphology, Trends, and the General Circulation". *Climate and Weather of the Sun-Earth System (CAWSES)*. Springer, pp. 517–539.

Oliver, W. L., J. M. Holt, S. R. Zhang, and L. P. Goncharenko (2014). Long-term trends in thermospheric neutral temperature and density above Millstone Hill. *J. Geophys. Res.* 119.9, pp. 7940–7946.

Oliver, W. L., J. M. Holt, S. R. Zhang, and L. P. Goncharenko (2015). Reply to comment by Jan Laštovička on "Long-term trends in thermospheric neutral temperature and density above Millstone Hill". *J. Geophys. Res.*

Oliver, W. L., S. R. Zhang, and L. P. Goncharenko (2013). Is thermospheric global cooling caused by gravity waves? *J. Geophys. Res.* 118.6, pp. 3898–3908.

Palmer, R. D., R. F. Woodman, S. Fukao, T. Tsuda, and S. Kato (1990). Three-antenna poststatistic steering using the MU radar. *Radio Sci.* 25.6, pp. 1105–1110.

Placke, M. (2014). Gravity waves and momentum fluxes in the mesosphere and lower thermosphere region. PhD thesis. Universität Rostock, Mathematisch-Naturwissenschaftlichen Fakultät.

Placke, M., P. Hoffmann, and M. Rapp (2015). First experimental verification of summertime mesospheric momentum balance based on radar wind measurements at 69°N. *Ann. Geophys.* Vol. 33. 9. Copernicus GmbH, pp. 1091–1096.

Placke, M., P. Hoffmann, E. Becker, C. Jacobi, W. Singer, and M. Rapp (2011a). Gravity wave momentum fluxes in the MLT—Part II: Meteor radar investigations at high and midlatitudes in comparison with modeling studies. *J. Atmos. Sol. Terr. Phys.* 73.9, pp. 911–920.

Placke, M., P. Hoffmann, R. Latteck, and M. Rapp (2014). Gravity wave momentum fluxes from MF and meteor radar measurements in the polar MLT region. *J. Geophys. Res.* 120.

Placke, M., G. Stober, and C. Jacobi (2011b). Gravity wave momentum fluxes in the MLT—Part I: seasonal variation at Collm (51.3 N, 13.0 E). *J. Atmos. Sol. Terr. Phys.* 73.9, pp. 904–910.

Portnyagin, Y. I., E. G. Merzlyakov, T. V. Solovjova, C. Jacobi, D. Kürschner, A. H. Manson, and C. E. Meek (2006). Long-term trends and year-to-year variability of mid-latitude mesosphere/lower thermosphere winds. *J. Atmos. Sol. Terr. Phys.* 68.17, pp. 1890–1901.

Qian, L., J. Laštovička, R. G. Roble, and S. C. Solomon (2011). Progress in observations and simulations of global change in the upper atmosphere. *J. Geophys. Res.* 116.A00H03.

Ratcliffe, J. A. (1972). *An introduction to the ionosphere and magnetosphere*. Cambridge University Press.

Reid, I. M. (2015). MF and HF radar techniques for investigating the dynamics and structure of the 50 to 110 km height region: A review. *Progress in Earth and Planetary Science* 2.33.

Reid, I. M., B. G. W. Vandepeer, S. C. Dillon, and B. M. Fuller (1995). The new Adelaide medium frequency Doppler radar. *Radio Sci.* 30.4, pp. 1177–1189.

Reid, I. M. (1987). Some aspects of Doppler radar measurements of the mean and fluctuating components of the wind field in the upper middle atmosphere. *J. Atmos. Terr. Phys.* 49.5, pp. 467–484.

Reid, I. M., R. Rüster, P. Czechowsky, and G. Schmidt (1988). VHF radar measurements of momentum flux in the summer polar mesosphere over Andenes (69°N, 16°E), Norway. *Geophys. Res. Lett.* 15.11, pp. 1263–1266.

Reid, I. M. and R. A. Vincent (1987). Measurements of mesospheric gravity wave momentum fluxes and mean flow accelerations at Adelaide, Australia. *J. Atmos. Terr. Phys.* 49.5, pp. 443–460.

Richter, J. H., F. Sassi, R. R. Garcia, K. Matthes, and C. A. Fischer (2008). Dynamics of the middle atmosphere as simulated by the Whole Atmosphere Community Climate Model, version 3 (WACCM3). *J. Geophys. Res.* 113.D08101.

Rishbeth, H. and O. K. Garriott (1969). *Introduction to Ionospheric Physics*. Vol. 14. International Geophysics Series. Academic Press.

Roble, R. G. and R. E. Dickinson (1989). How will changes in carbon dioxide and methane modify the mean structure of the mesosphere and thermosphere? *Geophys. Res. Lett.* 16.12, pp. 1441–1444.

Roper, R. G. and J. W. Brosnahan (1997). Imaging Doppler interferometry and the measurement of atmospheric turbulence. *Radio Sci.* 32.3, pp. 1137–1148.

Röttger, J. (1989). The interpretation of MST radar echoes: The present knowledge of the scattering/reflection and the irregularity generation mechanisms. *Middle Atmosphere Program. Handbook for MAP, volume 28*. Vol. 28, pp. 68–82.

Röttger, J. and H. Ierkic (1985). Postset beam steering and interferometer applications of VHF radars to study winds, waves, and turbulence in the lower and middle atmosphere. *Radio Sci.* 20.6, pp. 1461–1480.

Rousseeuw, P. J. and C. Croux (1993). Alternatives to the median absolute deviation. *J. Am. Stat. Assoc.* 88.424, pp. 1273–1283.

Sato, T. (1988). Radar principles. *Lecture notes of International School on Atmospheric Radar (ISAR)*, pp. 19–53.

Silberstein, R. (1959). The origin of the current nomenclature for the ionospheric layers. *J. Atmos. Terr. Phys.* 13, pp. 382–382.

Sprenger, K. and R. Schminder (1969). Solar cycle dependence of winds in the lower ionosphere. *J. Atmos. Terr. Phys.* 31.1, pp. 217–221.

Stubbs, T. J. (1973). The measurement of winds in the D-region of the ionosphere by the use of partially reflected radio waves. *J. Atmos. Terr. Phys.* 35.5, pp. 909–919.

Stubbs, T. J. (1976). Mean and periodic components of ionospheric drifts in the D-region at 35°S during 1972. *J. Atmos. Terr. Phys.* 38.9, pp. 979–989.

Stubbs, T. J. and R. A. Vincent (1973). Studies of D-Region Drifts During the Winters of 1970-72. *Aust. J. Phys.* 26.5, pp. 645–660.

Sürücü, F., S. J. Franke, and E. Kudeki (1995). On the influence of specular reflections in MF radar wind measurements. *Radio Sci.* 30.4, pp. 1229–1244.

Thorsen, D., S. J. Franke, and E. Kudeki (1997). A new approach to MF radar interferometry for estimating mean winds and momentum flux. *Radio Sci.* 32.2, pp. 707–726.

Thorsen, D., S. J. Franke, and E. Kudeki (2000). Statistics of momentum flux estimation using the dual coplanar beam technique. *Geophys. Res. Lett.* 27.19, pp. 3193–3196.

Vandepeer, B. G. W. (1993). A new MF Doppler radar for upper atmospheric research. PhD thesis. University of Adelaide, Department of Physics and Mathematical Physics.

Vandepeer, B. G. W. and I. M. Reid (1995). Some preliminary results obtained with the new Adelaide MF Doppler radar. *Radio Sci.* 30.4, pp. 1191–1203.

Vincent, R. A. and S. M. Ball (1981). Mesospheric winds at low-and mid-latitudes in the southern hemisphere. *J. Geophys. Res.* 86.A11, pp. 9159–9169.

Vincent, R. A., S. Kovalam, I. M. Reid, and J. P. Younger (2010). Gravity wave flux retrievals using meteor radars. *Geophys. Res. Lett.* 37.L14802.

Vincent, R. A. and I. M. Reid (1983). HF Doppler measurements of mesospheric gravity wave momentum fluxes. *J. Atmos. Sci.* 40.5, pp. 1321–1333.

Vincent, R. A. and T. J. Stubbs (1977). A study of motions in the winter mesosphere using the partial reflection drift technique. *Plan. Space Sci.* 25.5, pp. 441–455.

Walterscheid, R. L. (1981). Dynamical cooling induced by dissipating internal gravity waves. *Geophys. Res. Lett.* 8.12, pp. 1235–1238.

Weiss, A. A. and W. G. Elford (1963). An equipment for combined geophysical and astronomical measurements of meteors. *Proc. of the IRE Australia*, pp. 197–203.

de Wit, R. J., R. E. Hibbins, and P. J. Espy (2014a). The seasonal cycle of gravity wave momentum flux and forcing in the high latitude northern hemisphere mesopause region. *J. Atmos. Sol. Terr. Phys.* 127, pp. 21–29.

de Wit, R. J., R. E. Hibbins, P. J. Espy, Y. J. Orsolini, V. Limpasuvan, and D. E. Kinnison (2014b). Observations of gravity wave forcing of the mesopause region during the January 2013 major Sudden Stratospheric Warming. *Geophys. Res. Lett.* 41.13, pp. 4745–4752.

Woodman, R. F. and Y.-H. Chu (1989). Aspect sensitivity measurements of VHF backscatter made with the Chung-Li radar: Plausible mechanisms. *Radio Sci.* 24.2, pp. 113–125.

Woodman, R. F. and A. Guillen (1974). Radar observations of winds and turbulence in the stratosphere and mesosphere. *J. Atmos. Sci.* 31.2, pp. 493–505.

Younger, J. P., I. M. Reid, and R. A. Vincent (2013). Mutual coupling of antennas in a meteor radar interferometer. *Radio Sci.* 48.2, pp. 118–121.

Younger, J. P. (2011). Theory and Applications of VHF Meteor Radar Observations. PhD thesis. The University of Adelaide.